

First-Principles Study of Non-Collinear Magnetism and Spin-Orbit Driven Physics in Nanostructures at Surfaces

Dissertation
zur Erlangung des Doktorgrades
der Mathematisch-Naturwissenschaftlichen Fakultät
der Christian-Albrechts-Universität zu Kiel

vorgelegt von
Silke Schröder
aus Hamburg

Kiel

2013

Erster Gutachter:
Zweiter Gutachter:

Prof. Dr. Stefan Heinze
Prof. Dr. Eckhard Pehlke

Tag der mündlichen Prüfung:
Zum Druck genehmigt:

28.06.2013
21.10.2013

gez. Prof. Dr. Wolfgang J. Duschl, Dekan

Inhaltsangabe

In dieser Arbeit werden die strukturellen, elektronischen und magnetischen Eigenschaften von Nanostrukturen an Oberflächen, insbesondere für ultradünne Filme und einzelne Adatome, untersucht. Hierzu wird die Dichtefunktionaltheorie mittels der implementierten 'Full-Potential Linearized Augmented Plane Wave' (FLAPW) Methode verwendet. Im Schwerpunkt dieser Arbeit liegen komplexe nichtkollineare Spinstrukturen, die aufgrund von konkurrierenden Wechselwirkungen und dem Effekt der Spin-Bahn-Kopplung auftreten können.

Zunächst wird die Herkunft von solchen Strukturen untersucht. In nichtkollinearen magnetischen Ordnungen sind die Spins benachbarter Atome weder parallel noch antiparallel zueinander ausgerichtet, sondern können jeden beliebigen Winkel einschließen. Solch eine Spinkonfiguration findet sich z. B. in einer Monolage von Cr auf Pd(111). Diese weist einen Néel-Zustand auf, welcher sich durch einen Winkel von 120° zwischen den magnetischen Momenten benachbarter Atome auszeichnet. Es wird gezeigt, dass dieser magnetische Grundzustand durch die topologische Frustration der antiferromagnetischen Austauschkopplung zwischen nächsten Nachbarn hervorgerufen wird. Die Simulation von Bildern der spinpolarisierten Rastertunnelmikroskopie (RTM) erlaubt den direkten Vergleich mit dem Experiment und ermöglicht so die erste Beobachtung eines theoretisch vorhergesagten sowie experimentell nachgewiesenen Néel-Zustandes. Ein noch interessanterer nichtkollinearer Grundzustand tritt in der Doppellage Mn auf W(110) auf. Hier sind die magnetischen Momente einer antiparallelen Spinanordnung senkrecht zur Oberfläche verkippt und rotieren auf einem Kegel mit einem Öffnungswinkel von 30° . Es wird demonstriert, dass dieser transversale konische Spinspiralenzustand von Spinwechselwirkungen höherer Ordnung verursacht wird. Der erste Fund einer solchen komplexen magnetischen Struktur an einer Oberfläche verdeutlicht die Relevanz der Spinwechselwirkungen über den paarweisen Heisenberg-Austausch hinaus.

Weiterhin enthält diese Arbeit eine Studie des Tunnel-Anisotropie-Magnetowiderstandes (TAMR) von einzelnen Atomen, die auf magnetischen dünnen Filmen auf W(110) adsorbiert sind. Aufgrund der Austauschwechselwirkung zwischen dem magnetischen Moment des Adatoms und der darunter befindlichen Spinstruktur der Probe, ist es möglich, den Spin zu rotieren ohne ein externes Magnetfeld anzulegen. Somit kann ein direkter Vergleich zwischen dem berechneten TAMR und den RTM Experimenten stattfinden. Es wird gezeigt, dass der TAMR vom Mischen von d -Zuständen mit unterschiedlicher Orbitalsymmetrie aufgrund der Spin-Bahn-

Kopplung herrührt. Dieses Mischen verursacht magnetisierungsrichtungsabhängige Änderungen in der Vakuumzustandsdichte, die für ein einzelnes Co-Atom auf einer Doppellage Fe auf W(110) in etwa 20% betragen. Tauscht man dieses Co-Atom durch ein Ir-Atom mit stärkerer Spin-Bahn-Kopplung aus, so kann der TAMR um einen Faktor von bis zu vier erhöht werden. Für Co-Atome, die auf einem Film adsorbieren, welcher wie die Mn-Monolage auf W(110) einen Spinspiralenzustand auf atomarer Skala besitzt, rangiert der TAMR im Bereich von -25% bis $+25\%$.

Abstract

In this thesis, the structural, electronic, and magnetic properties of nanostructures at surfaces, such as ultra-thin films and single adatoms, are explored based on density functional theory as implemented within the full-potential linearized plane wave (FLAPW) method. The focus of this work are complex non-collinear spin structures due to competing magnetic interactions and the effect of spin-orbit coupling.

First, the origin of non-collinear magnetic structures is examined, i.e., structures in which the spins of neighboring atoms are aligned neither parallel nor antiparallel to each other but can take arbitrary angles. Such a non-collinear spin texture is found in a monolayer of Cr on Pd(111), which exhibits a Néel state with angles of 120° between adjacent magnetic moments. It is demonstrated that this magnetic ground state arises due to topological frustration of the antiferromagnetic nearest-neighbor exchange coupling. Spin-polarized scanning tunneling microscopy (STM) images are simulated and allow for a direct comparison with experimental results leading to the first theoretically predicted and experimentally confirmed observation of a Néel state. An even more intriguing non-collinear magnetic state occurs in the double layer of Mn on W(110), where the magnetic moments of an antiparallel spin arrangement are canted with respect to the surface plane and rotate on a cone with an opening angle of about 30° . It is shown that this transverse conical spin-spiral state is induced by higher-order spin interactions. The first finding of such a complex magnetic structure at a surface demonstrates the relevance of spin interactions beyond pair-wise Heisenberg exchange.

Furthermore, this thesis contains a study of the tunneling anisotropic magnetoresistance (TAMR) of single atoms adsorbed on magnetic thin films on W(110). Due to the exchange coupling of the magnetic moment of the adatom to the underlying sample's spin structure, it is feasible to rotate the spin without an external magnetic field and allow a direct comparison of the calculated TAMR with STM experiments. It is demonstrated that the TAMR stems from the mixing of d states with different orbital symmetry due to the spin-orbit interaction. This mixing induces magnetization-direction dependent changes in the vacuum density of states that are on the order of 20% for a single Co adatom on the double layer Fe on W(110). By replacing the Co atom with an Ir atom, which exhibits a stronger spin-orbit coupling, the TAMR can be enhanced by a factor of up to four. For Co adatoms adsorbed on the Mn monolayer on W(110), which shows an atomic-scale spin spiral state, the TAMR is found to be in the range of -25% to $+25\%$.

Contents

1	Introduction	1
2	Density functional theory	9
2.1	The Hohenberg-Kohn theorem	9
2.2	The Kohn-Sham equations	12
2.3	Exchange-correlation potentials	14
2.4	The self-consistency cycle	15
3	Solving the Kohn-Sham equations with FLAPW	17
3.1	APW method	17
3.2	LAPW method	19
3.3	The FLAPW method	20
3.3.1	Film Calculations With FLAPW	21
3.3.2	The Representation of the Density and the Potential	23
3.3.3	The Generalized Eigenvalue Problem	24
3.3.4	Brillouin Zone Integration within FLAPW	25
3.3.5	Determination of the Total Energy	26
4	Modeling Magnetic Systems	29
4.1	Stoner Model	29
4.2	Heisenberg Model	34
4.2.1	The classical Heisenberg model on a Bravais lattice	36
4.3	Simulation of Spin-Polarized Scanning Tunneling Microscopy Images	38
4.3.1	The Tersoff-Hamann Approximation	40
4.3.2	The Spin-Polarized Tersoff Hamann Theory	42
4.3.3	Independent-Orbital Approximation	45
5	Non-collinear Magnetism within DFT	47
5.1	Constrained Magnetic Moments	48
5.2	Spin Spirals	49
5.3	The Generalized Bloch Theorem	50
5.4	Non-collinear magnetism in FLAPW	52
6	Spin-Orbit Coupling	55
6.1	The Relativistic Density Functional Theory	56

6.2	Spin-Orbit Coupling	57
6.3	The Magnetocrystalline Anisotropy and the Orbital Moment	59
6.4	Perturbation Theory	60
6.5	Spin-Orbit Coupling in FLAPW	62
	6.5.1 Local Force Theorem	62
	6.5.2 Variational Methods	63
6.6	The Dzyaloshinskii-Moriya Interaction	65
7	Spin Frustration on a Triangular Lattice: Cr/Pd(111)	71
7.1	Computational Details	72
7.2	Structural Properties of Cr/Pd(111)	73
7.3	The Néel state of Cr/Pd(111)	74
7.4	Experimental Verification of the Néel State	78
	7.4.1 Experimental Details	78
	7.4.2 Spin-Polarized STM Images: Theory vs. Experiment	79
	7.4.3 Tip Magnetization Switching Events	81
7.5	Conclusions	83
8	Conical Spin-spiral State Driven by Higher-Order Spin Interactions	85
8.1	Experimental Observations	86
8.2	Explaining the STM images	88
8.3	Computational Details	90
8.4	Magnetic Properties of the Mn Double Layer on W(110)	91
8.5	Conical Spin Spirals Induced by Spin-Orbit Coupling	95
8.6	Conical Spin Spirals Induced by Higher-Order Spin Interactions	98
8.7	Simulation of spin-polarized STM images	102
8.8	Corrugation Amplitudes	105
8.9	The Tunneling Anisotropic Magnetoresistance Effect in a Conical Spin-Spiral State	108
8.10	Conclusions	110
9	Tunneling Anisotropic Magnetoresistance at the Single Atom Limit	113
9.1	TAMR of the Fe Double-Layer on W(100)	115
	9.1.1 Calculation of the TAMR of the Double Layer Fe on W(110)	117
9.2	Co Adatom on Fe/W(110)	119
	9.2.1 TAMR of the Co Adatom on the Double Layer Fe on W(110)	122
	9.2.2 Model of the TAMR	126
9.3	Non-magnetic Single Iridium Adatom on the Double Layer Fe on W(110)	129
	9.3.1 Spin-Polarization of the Ir Adatom on the Double Layer Fe on W(110)	130

9.3.2	The TAMR Effect of the Ir Adatom on the Double Layer Fe on W(110)	132
9.4	Co Adatom on the Mn monolayer on W(110)	143
9.4.1	Spin Analysis of the Co Adatom on the Single Layer Mn on W(110)	144
9.4.2	The TAMR of the Co Adatom on the Single Layer Mn on W(110)	146
10	Summary	151
11	Bibliography	157
	List of Abbreviations	171

1 Introduction

Nowadays, the fast processing and storage of huge amounts of data play a key role in information technology. In today's hard-disk drives the information is stored in terms of magnetic bits or domains, i.e., small patches exhibiting a certain magnetic polarization that can be read as a logical '1' or '0'. A quantity that presents the benchmark for technology achievements in this area is the so-called areal density, i.e., the number of bits that can be stored per surface area. For instance, in state-of-the-art laptop type products released by Hitachi GST an areal density of about 375 Gbits/in² is achieved [1]. In comparison to the first commercial hard-disk drive that has been produced by IBM in 1956 this number has been improved of about 200,000,000 times. A major breakthrough in this field has been the discovery of the Giant Magnetoresistance (GMR) in 1988 by P. Grünberg and A. Fert [2, 3], who were honored by the 2007 Nobel Prize in Physics. It triggered the development of a new research field - *Spin(elec)tronics*. In 1997, only 10 years after the discovery of the GMR, the magnetoresistive read heads based on the GMR hit the market as first generation spintronic devices and accelerated the technology improvement with annual growth rates of up to 100% for the areal density [4].

Spintronics aims at exploiting the electronic spin degree of freedom by either adding it to conventional charge based electronic devices or by using it alone. Concerning the performance of non-volatile spintronic devices in comparison to conventional semiconductor devices, one expects an increased data processing speed and increased integration densities while the power consumption decreases [5]. However, on the path towards quantum information processing there are several topics to be dealt with such as the microscopic mechanisms of spin transport and coherence as well as the understanding of the magneto- and spindynamics concerning magnetic switching processes. Furthermore, the reduced dimensions of the magnetic elements require the investigation of magnetism on the nanoscale, which is in the focus of this thesis.

The spin is a fundamental property of the electron, such as its mass and charge. It can lead to the formation of a magnetic moment in a solid, and the exchange coupling can give rise to magnetic ordering, such as ferro- or antiferromagnetism. Furthermore, the spin and the crystal lattice can couple due to the relativistic effect of spin-orbit coupling (SOC). It is a well-known fact that this leads to a preferred magnetization direction within the lattice denoted as magnetocrystalline anisotropy. Due to the inversion asymmetry at surfaces and interfaces spin-orbit coupling can also give rise to a coupling of spins known as Dzyaloshinskii-Moriya interaction

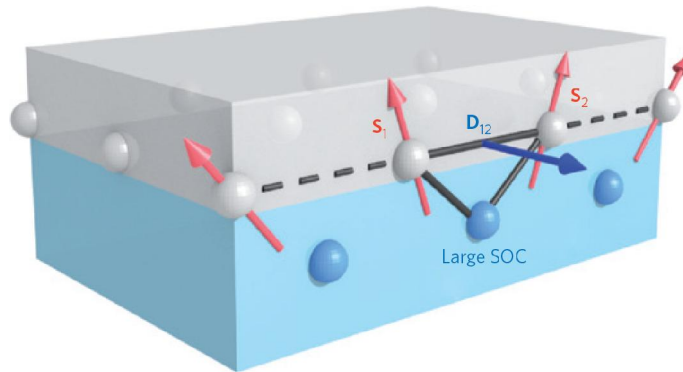


Figure 1.1: Schematic illustration of the Dzyaloshinskii-Moriya interaction at the interface between a ferromagnet (gray) and a metallic substrate with strong spin-orbit coupling (blue). The Dzyaloshinskii vector \mathbf{D}_{12} is related to the triangle spanned by the two interface spins \mathbf{S}_1 and \mathbf{S}_2 and a substrate atom with large spin-orbit coupling. \mathbf{D}_{12} is perpendicular to the plane of the triangle. Figure taken from reference [6].

(DMI) [7, 8]. It takes the form

$$H_{\text{DMI}} = -\mathbf{D}_{12} \cdot (\mathbf{S}_1 \times \mathbf{S}_2),$$

where \mathbf{S}_1 and \mathbf{S}_2 are two atomic spins and \mathbf{D}_{12} denotes the Dzyaloshinskii vector. At the interface between a ferromagnetic thin layer and a metallic substrate with strong spin-orbit interaction, the atomic spins and the Dzyaloshinskii vector present a relative orientation as it is schematically illustrated in Fig. 1.1. The interface spins and a substrate atom span a triangle that has the Dzyaloshinskii vector as normal due to symmetry considerations [7, 8]. From Fig. 1.1 as well as the equation above it is evident that the DMI stabilizes magnetic structures of non-collinear order, such as spin spirals, where the spins of neighboring magnetic moments are neither parallel or antiparallel aligned but canted by a constant angle. The impact of this effect on surface magnetism has been demonstrated for the first time in 2007 by means of spin-polarized scanning tunneling microscopy (SP-STM) in a single layer Mn on W(110) [9], where a long-range modulation superimposed to the pattern of the local antiferromagnetic order was observed. It was identified as a spin spiral with a periodicity of about 12 nm and a unique rotational sense, also known as chirality. The latter cannot be ascribed to the exchange coupling but is a characteristic of the DMI. Further observations of the DMI have been made in 2008 while studying a bilayer Fe film on W(110), which exhibits a magnetic domain structure [10]. Domains are sections of opposite magnetization direction that are separated by domain walls, which provide a transition from an 'up' magnetized domain to a 'down' magnetized domain and *vice versa*. Many properties of a domain wall such as the orientation of the magnetic domains relative to the crystal lattice as well as the type of the

domain wall and its chirality can be governed by the DMI. Thus, this effect needs to be taken into consideration for the development of novel spintronic devices. For instance, in Pt/CoFe/MgO and Ta/CoFe/MgO it was observed that the domain walls are driven into opposite directions by applying a current. This behavior has been explained based on the left-handed chirality induced by the DMI [11]. Hence, it can be suggested that current-controlled spintronic devices could be tailored by selecting the materials adjacent to the ferromagnet.

A very promising nanoscale magnetic structure that is driven likewise by the DMI and could be used as an information carrier in ultra-dense memory and logic devices is the *skyrmion* – a chiral spin structure with a whirling configuration that is topologically protected and exhibits particle-like properties (cf. Fig. 1.2 (a)) [6, 12]. It has been first observed in 2009 in bulk magnets such as MnSi [13, 14, 15]. Recently, the occurrence of a skyrmion lattice in a magnetic thin film has been reported for a monolayer of Fe on the (111) surface of Ir [16]. It was shown that the two-dimensional square lattice of skyrmions is enforced by the four-spin interaction, i.e., a spin interaction beyond the pair-wise Heisenberg exchange. Later in this thesis, a second example will be presented where it is demonstrated that the higher-order terms are crucial for the magnetic ground state.

In contrast to the situation in the bulk systems, the skyrmion phase in the Fe monolayer does not need a magnetic field in order to be stabilized, since it presents the magnetic ground state of the system. Skyrmions can be moved with electrical currents of very small density ($\approx 10^6 \text{ Am}^{-2}$) [17, 18] in comparison to current densities of approximately 10^{11} to 10^{12} Am^{-2} [6] needed for the motion of domain walls. Besides the current-induced motion of the skyrmions their small size of only a few nanometers (or atoms) allows for a significant reduction of the spacing between bits with respect to that of domains. While the domain wall width can be as small as a few nanometers, too, the size of a domain has a lower limit of 30 to 40 nm, which can hardly be reduced. However, up to now the formation of skyrmions has been exclusively studied at temperatures below room temperature, although from the theoretical point-of-view it is expected that skyrmions are also stable at room temperature [6, 16].

Finally, another route towards novel spintronic devices is given by the tunneling anisotropic magnetoresistance (TAMR). This effect occurs if two metallic electrodes are separated by an insulating barrier such as a vacuum layer. The resistance depends on the magnetization directions of one of those electrodes with respect to the current flow. For instance, in a double layer Fe film [19] it has been demonstrated that the domain walls can be detected using a nonmagnetic STM tip since the local density of states of the sample depends on the magnetization direction. This result was explained by means of *ab initio* calculations and could be ascribed to the hybridization of states with different orbital character. It leads to a differential conductivity that depends on the magnetization direction and allows for the resolution of magnetic structures at the nanometer scale.

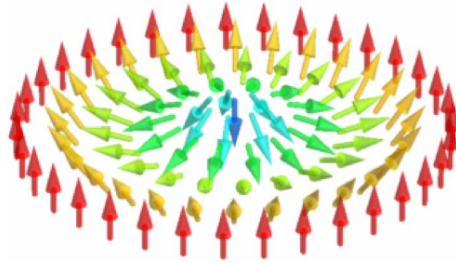


Figure 1.2: Sketch of a cycloidal skyrmion in a two-dimensional ferromagnet. The magnetic moments rotate around an axis perpendicular to the diameter from pointing up at the edges to pointing down at the center. This figure is taken from reference [6].

The above examples demonstrate the importance of the investigation and understanding of nanoscale magnetic structures for future spintronic devices. Therefore, this thesis focuses on the study of nanomagnetism in terms of magnetic and electronic properties of nanostructures at surfaces and the interpretation of spin-polarized STM experiments. In particular, non-collinear magnetic structures in thin films as well as the TAMR effect at the single-atom limit were investigated. For this purpose, calculations were carried out within the density functional theory [20, 21], which is the most successful *ab initio* theory for real solid state materials. Its implementation in the FLEUR code [22] is based on the full-potential linearized augmented plane wave method (FLAPW) [23, 24], one of the most precise density functional methods and particularly suited for open structures and surfaces as they are studied in the present work. Based on the first-principles results several issues will be tackled: What kind of a magnetic ground state does an antiferromagnetic single atomic layer exhibit on a triangular lattice? Which mechanism can give rise to a conical spin-spiral state in a magnetic thin film? How large is the influence of the spin-orbit coupling in such a complex magnetic structure? How does the TAMR scale in the ultimate single-atom limit? What happens to the TAMR if single magnetic adatoms are replaced by nonmagnetic atoms that have a larger spin-orbit interaction?

In density functional theory the electron-electron interaction is incorporated in the so-called exchange-correlation potential, which implicitly includes all of the magnetic exchange interactions. Therefore, it is helpful to map the *ab initio* results to model Hamiltonians, such as that of an extended Heisenberg model, in order to identify the magnetic exchange interaction giving rise to the ground state of a system. In the present work, it is demonstrated that frustration of exchange interactions leads to a 120° -Néel state of a Cr monolayer on Pd(111). Since Pd exhibits only minor hybridization with the overlying magnetic film, the tendency towards antiferromagnetism is preserved in the Cr monolayer leading to a spin frustration in this system and thus to a non-collinear magnetic ground state. The occurrence of this spin structure, which has been verified by spin-polarized STM measurements for Cr on

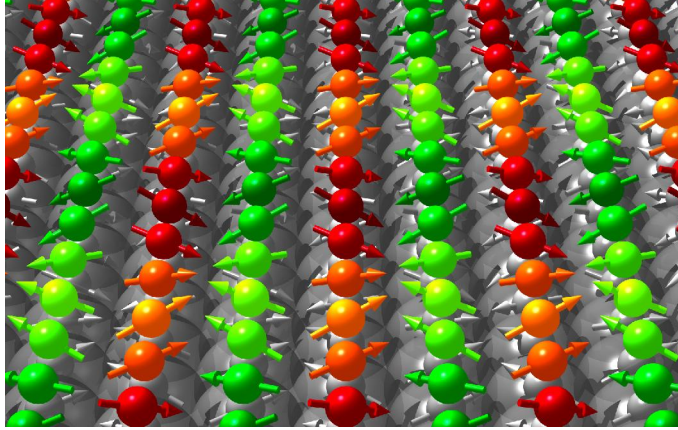


Figure 1.3: Conical spin-spiral state in the double layer of Mn on the (110) surface of W. The topmost Mn layer has been colorized with respect to the components of the magnetization. The magnetic moments are rotated from atom to atom by a constant angle around the rotation axis that is perpendicular to the propagation direction of the spin spiral. In addition, the magnetic moments are canted with respect to the rotation axis by a cone angle. Here, green and red indicate a positive and negative alignment, respectively, of the magnetic moments within the film plane. The variation of the magnetization direction perpendicular to the film plane is denoted by dark and bright colors. The Mn subsurface atoms as well as the W substrate atoms are presented as gray spheres.

Pd(111), can be explained on the basis of the Heisenberg exchange coupling.

However, it is not *a priori* clear if the Heisenberg model is suitable for itinerant magnets such as transition metals. Therefore, it is necessary to consider exchange interactions beyond pair-wise interactions such as the four-spin interaction and the biquadratic exchange. Typically, these are neglected to interpret the magnetic order in transition metals, but in the present work it will be demonstrated that these higher-order spin interactions can play a crucial role in surface magnetism. In particular, they can induce a canting of the magnetic moments leading to a transverse conical spin spiral as observed in this thesis for two monolayers of Mn on the W(110) surface. As illustrated in Fig. 1.3 this spin structure is characterized by a nearly antiparallel alignment of neighboring magnetic moments and an additional rotation on a cone perpendicular to the propagation axis of the spiral. The finding of such a complex spin structure at a surface emphasizes the importance of higher-order spin interactions.

As mentioned in the beginning, spin coherent transport is one of the main topics that needs to be dealt with on the path towards novel spintronic devices. The TAMR represents an excellent possibility to circumvent this problem, since it needs only one magnetic electrode [25]. So far, the TAMR has been studied almost exclusively for tunnel junctions that comprise planar structures such as multilayers and nonmagnetic materials of a few nanometer thickness. Therefore, it is still under

debate how the TAMR scales down in the single-atom limit. This thesis addresses the smallest nanostructure that could be used as a potential spintronic device – the single atom on a magnetic surface. However, the direct comparison of theoretical and experimental results is a major issue in the investigation of the TAMR in single atoms, since the techniques used so far for the fabrication of nanoscale contacts did not allow for a well-defined microscopic structure of the contacts. Here, a system will be introduced for the first time that is suited for a direct comparison of theory and experiment. It comprises a single atom, such as a Co or an Ir atom, that is adsorbed on a magnetic surface. The magnetization direction of the adatom aligns to that of the nearest magnetic atoms of the film below due to the strong exchange coupling. This allows for an adjustment of the spin direction without the use of an external magnetic field. Here, different magnetic templates are chosen such as the domain wall structure in a double layer of Fe on W(110) [19, 26, 27] or the atomic scale spin-spiral state of a monolayer of Mn on W(110) [9]. In a nanoscale domain structure the magnetic moment of the adatom can be aligned perpendicular or parallel to the film plane depending on its position on the domain or the domain wall. In an atomic-scale spin-spiral state, on the other hand, it can take every angle that is provided by the magnetic moments of the underlying film. Then, the TAMR can be studied by comparing the local vacuum density of states above the adatom for different magnetization directions. Since the spin-orbit coupling is imprinted onto the electronic structure via the magnetization direction dependent hybridization of different d orbitals in the adatom, the density of states becomes anisotropic and induces the TAMR. This allows for the use of nonmagnetic STM tips and a direct comparison of theoretical and experimental results. Furthermore, the basic principle of the TAMR, namely the magnetization dependent hybridization of d states with different orbital character, can be explained based on a simple model that is introduced in this work.

This thesis is structured into two parts:

In chapters 2 to 6 the methods and underlying theory of the electronic structure calculations are introduced. The idea and concept of the *density functional theory* to solve the quantum mechanical many-particle problem are presented in chapter 2. The *Full Potential Linearized Augmented Plane Wave* (FLAPW) method, which ranks amongst the most accurate implementations of the density functional theory, is described in chapter 3. In the present thesis the program code FLEUR [22] has been used, which is based on the FLAPW method. It is particularly suited to treat systems with complex magnetic structure. Chapter 4 deals with elementary models of magnetism that provide a basis for the understanding of the *ab initio* results. The Stoner model describes the occurrence of ferromagnetism and antiferromagnetism in terms of the nonmagnetic density of states. The Heisenberg model offers a simple description of the magnetic interactions in terms of the exchange parameters and thus discusses the tendency of a system towards non-collinear magnetism. For a direct comparison of the *ab initio* calculations and the spin-polarized STM results,

the spin-polarized Tersoff-Hamann model is introduced that provides a formulation of the spin-polarized tunneling current. The implementation of non-collinear magnetism in the FLAPW method is presented in chapter 5. Finally, in chapter 6 the relativistic effect of *spin-orbit coupling* is presented as well as its implementation in the FLEUR code.

The results of this thesis are organized in chapters 7 to 9. As a first example of a non-collinear magnetic structure the 120° Néel state is discussed in chapter 7. It has been observed in a monolayer of Cr on the (111) surface of Pd and is driven by the topological spin frustration. A much more complex magnetic structure, namely a three-dimensional conical spin-spiral state, is presented in chapter 8. It has been discovered in a double layer of Mn on the (110) surface of W, and it is demonstrated here that it can be ascribed to the higher-order spin interactions. Furthermore, the influence of spin-orbit coupling effects onto a non-collinear magnetic structure in terms of the *Dzyaloshinskii-Moriya interaction* (DMI) and the *tunneling anisotropic magnetoresistance* (TAMR) has been studied in this system. In chapter 9 the TAMR is studied systematically for different Cr and Ir ad-atoms on ultrathin films on the (110) surface of W. It is explained on the basis of a simple model that describes the mixing of surface states with different orbital character.

2 Density functional theory

The quantum mechanical treatment of a solid constitutes a complex many-particle problem. In order to calculate the total energy and the ground state properties of such a system the non-relativistic Schrödinger equation

$$\mathcal{H}|\Psi(\mathbf{r}_1, \mathbf{r}_2, \dots, \mathbf{r}_N)\rangle = E|\Psi(\mathbf{r}_1, \mathbf{r}_2, \dots, \mathbf{r}_N)\rangle \quad (2.1)$$

needs to be solved for a multi-dimensional N -particle wave function Ψ . Since this is a nontrivial task, approaches like the Born-Oppenheimer approximation have been made to simplify the problem. The Born-Oppenheimer approximation is based upon the fact that due to the large difference in mass, the electrons move much faster than the nuclei and therefore considers the latter ones as point charges at fixed positions. In this way, the total system can be reduced to a many-electron system in an external potential v_{ext} generated by the atomic nuclei.

Due to the antisymmetry and the multi-dimensionality of the N -electron wave function $\Psi(\mathbf{r}_1, \mathbf{r}_2, \dots, \mathbf{r}_N)$, the remaining many-electron problem is still very complex and computationally demanding. Typical approaches to solve the resulting Schrödinger equation, such as the full diagonalization, lead to an exponential increase in the computational effort with the number of electrons. In order to treat this problem in an efficient way, the density functional theory (DFT) chooses the electron density $n(\mathbf{r})$ as the basic quantity. This theory has been established by Hohenberg and Kohn [20] as well as Kohn and Sham [21] and will be explained in more detail in this chapter.

2.1 The Hohenberg-Kohn theorem

The basic idea of the DFT is to describe the ground state energy of a many-electron system and its properties by the electron density solely without the loss of information. Inspired by the Thomas-Fermi model [28, 29], P. Hohenberg and W. Kohn stated that in the case of a system with a nondegenerate ground-state

- *the total energy is a unique functional of the ground-state electron density $n(\mathbf{r})$,*

and

- *the exact ground-state density minimizes the energy functional $E[n(\mathbf{r})]$.*

In order to prove the first theorem, an electronic system is considered that is influenced by an external potential $v_{ext}(\mathbf{r})$ and the Coulomb repulsion. In this case, the Hamiltonian has the form

$$\mathcal{H} = \hat{T} + \hat{U} + \hat{V} \quad (2.2)$$

where \hat{T} is the operator of the kinetic energy of the system, \hat{U} is the operator of the electron-electron interaction energy, and \hat{V} is the operator of the interaction with an external potential. The electron density of the ground-state Ψ is denoted as

$$n(\mathbf{r}) = \langle \Psi | \sum_{i=1}^N \delta(\mathbf{r} - \mathbf{r}_i) | \Psi \rangle. \quad (2.3)$$

In the following, it is demonstrated that different external potentials $v_{ext}(\mathbf{r})$ and $v'_{ext}(\mathbf{r})$ with $v_{ext}(\mathbf{r}) \neq v'_{ext}(\mathbf{r}) + const$ must generate different ground state densities $n(\mathbf{r})$ and $n'(\mathbf{r})$. The ground-state energies are given as

$$E_0 = \langle \Psi | \mathcal{H} | \Psi \rangle \quad (2.4)$$

and

$$E'_0 = \langle \Psi' | \mathcal{H}' | \Psi' \rangle \quad (2.5)$$

with $\mathcal{H} = \hat{T} + \hat{U} + \hat{V}$ and $\mathcal{H}' = \hat{T} + \hat{U} + \hat{V}'$, respectively. Due to the Ritz variational principle it applies that

$$E_0 = \langle \Psi | \mathcal{H}' | \Psi \rangle - \langle \Psi | \hat{V}' - \hat{V} | \Psi \rangle > \langle \Psi' | \mathcal{H}' | \Psi' \rangle - \langle \Psi' | \hat{V}' - \hat{V} | \Psi' \rangle \quad (2.6)$$

leading to

$$E_0 > E'_0 - \int (v'_{ext}(\mathbf{r}) - v_{ext}(\mathbf{r}))n(\mathbf{r})d^3r. \quad (2.7)$$

Interchanging the primed and unprimed quantities and assuming $n'(\mathbf{r}) = n(\mathbf{r})$, it is obtained analogously that

$$E'_0 > E_0 - \int (v_{ext}(\mathbf{r}) - v'_{ext}(\mathbf{r}))n(\mathbf{r})d^3r. \quad (2.8)$$

Adding Eq. (2.7) and (2.8) results in

$$E_0 > E'_0 - \int (v'_{ext}(\mathbf{r}) - v_{ext}(\mathbf{r}))n(\mathbf{r})d^3r \quad (2.9)$$

$$> E_0 - \int (v_{ext}(\mathbf{r}) - v'_{ext}(\mathbf{r}))n(\mathbf{r})d^3r - \int (v'_{ext}(\mathbf{r}) - v_{ext}(\mathbf{r}))n(\mathbf{r})d^3r$$

$$> E_0 \quad (2.10)$$

which is wrong. Thus, it can be concluded that $v_{ext}(\mathbf{r})$ is a unique functional of $n(\mathbf{r})$. Moreover, the full ground-state energy is a unique functional of $n(\mathbf{r})$, since the kinetic energy T and the electron-electron interactions U are known. Only the external potential $v_{ext}(\mathbf{r})$ defines the Hamiltonian \mathcal{H} . Therefore, the energy is rewritten as a functional of the electron density $n(\mathbf{r})$:

$$\begin{aligned} E[n(\mathbf{r})] &= T[n(\mathbf{r})] + U[n(\mathbf{r})] + \int v_{ext}(\mathbf{r})n(\mathbf{r})d^3r \\ &= F_{HK}[n(\mathbf{r})] + \int v_{ext}(\mathbf{r})n(\mathbf{r})d^3r \end{aligned} \quad (2.11)$$

In order to prove the second theorem, it is assumed that for a given external potential $v_{ext}(\mathbf{r})$ the ground-state density is $n_0(\mathbf{r})$ and the ground state wave function is Ψ_0 . In this case, the expression in Eq. (2.11) is written as

$$\begin{aligned} E_{v_{ext}}[n] &= F_{HK} + \int v_{ext}(\mathbf{r})n(\mathbf{r})d^3r \\ &= \langle \Psi_0 | \hat{T} + \hat{U} + \hat{V}_0 | \Psi_0 \rangle \end{aligned} \quad (2.12)$$

where $n(\mathbf{r})$ denotes an arbitrary density. By applying the variational principle it follows that

$$\begin{aligned} E_{v_{ext}}[n] &\geq \langle \Psi_0 | \hat{T} + \hat{U} + \hat{V}_0 | \Psi_0 \rangle \\ &= F_{HK}[n_0] + \int v_{ext}(\mathbf{r})n_0(\mathbf{r})d^3r \\ &= E_{v_{ext}}[n_0] = E_0[n_0]. \end{aligned} \quad (2.13)$$

This means that the correct ground-state density indeed minimizes the energy functional. In this way, the determination of the electronic ground state for a given external potential v_{ext} has been reduced to the minimization of the energy functional $E_{v_{ext}}[n]$.

Furthermore, the Hohenberg-Kohn theorem can be extended in order to describe degenerate [30] and spin-polarized systems [31, 32]. The extension to spin-polarized DFT is carried out by including an external magnetic field $\mathbf{B}(\mathbf{r})$ in the Hamilton operator, and introducing spin-dependent electron densities $n_\uparrow(\mathbf{r})$ and $n_\downarrow(\mathbf{r})$ as well as a magnetization density $\mathbf{m}(\mathbf{r}) = n_\uparrow(\mathbf{r}) - n_\downarrow(\mathbf{r})$. Then, the energy functional reads

$$E[n(\mathbf{r}), \mathbf{m}(\mathbf{r})] \geq E[n_0(\mathbf{r}), \mathbf{m}_0(\mathbf{r})]. \quad (2.14)$$

The proof for the spin-polarized case is similar to the one performed in the nonmagnetic case. Hence, the Hohenberg-Kohn theorem also applies for magnetic systems.

In order to make use of this simplification, a reasonable representation of the energy functional is necessary, which will be introduced in the next section.

2.2 The Kohn-Sham equations

A promising representation of the energy functional $E[n(\mathbf{r})]$ is ascribed to W. Kohn and L. J. Sham [21]. They decided to map the many-electron problem onto a system of non-interacting particles in an effective potential v_{eff} . Then, the many-electron density can be written in terms of single-particle wave functions:

$$n(\mathbf{r}) = 2 \sum_{i=1}^{N/2} |\psi_i(\mathbf{r})|^2, \quad (2.15)$$

with the factor '2' originating from the spin degeneracy. In order to describe it as correctly as possible, the energy functional is split into several contributions:

$$\begin{aligned} E[n] &= \int v_{ext} n(\mathbf{r}) d^3r + \frac{1}{2} \int \int \frac{n(\mathbf{r})n(\mathbf{r}')}{|\mathbf{r} - \mathbf{r}'|} d^3r d^3r' + G[n] \\ &= E_{ext}[n] + E_H[n] + G[n]. \end{aligned} \quad (2.16)$$

The first term, $E_{ext}[n]$, includes the potential energy caused by the atomic nuclei. The second term $E_H[n]$ arises from the Coulomb interaction of the electrons within the approximation of Hartree. The universal functional $G[n]$ itself splits into two further contributions:

$$G[n] = T_S[n] + E_{xc}[n] \quad (2.17)$$

where $T_S[n]$ is the kinetic energy of a system of non-interacting electrons:

$$T_S[n] = -2 \sum_{i=1}^N \int \psi_i^*(\mathbf{r}) \frac{\hbar}{2m} \nabla^2 \psi_i(\mathbf{r}) d^3r, \quad (2.18)$$

and the functional $E_{xc}[n]$ contains all the exchange and correlation effects. The accurate description of the kinetic energy is a benefit of this formalism as $T_S[n]$ contributes significantly to the total energy. Since there is no exact expression of $E_{xc}[n]$, approximations need to be made. Some of them will be introduced in section 2.3.

From section 2.1 it can be concluded that the energy functional is not only minimized by the ground state electron density $n(\mathbf{r})$, but also with respect to the ground state wave function ψ_i . Due to the conservation of the number of particles, the wave functions need to be normalized in this case:

$$\int |\psi_i(\mathbf{r})|^2 d^3r = 1 \quad \longrightarrow \quad \sum_{i=1}^N \int |\psi_i(\mathbf{r})|^2 d^3r = N. \quad (2.19)$$

This condition is taken into account by introducing Lagrange multipliers ϵ_i . After applying the variational principle to Eq. (2.16), the Kohn-Sham equations result in

$$\left(-\frac{\hbar^2}{2m}\nabla^2 + v_{\text{eff}}(\mathbf{r})\right)\psi_i(\mathbf{r}) = \epsilon_i\psi_i(\mathbf{r}) \quad (2.20)$$

resembling the single-particle Schrödinger equation with the eigenfunctions ψ_i . Besides the external potential v_{ext} , the Hartree potential

$$v_H = \int \frac{n(\mathbf{r}')}{|\mathbf{r} - \mathbf{r}'|}, \quad (2.21)$$

and the exchange correlation potential

$$v_{xc} = \frac{\delta E_{xc}[n]}{\delta n(\mathbf{r})} \quad (2.22)$$

contribute to the effective potential v_{eff}

$$v_{\text{eff}}(\mathbf{r}) = v_{\text{ext}}(\mathbf{r}) + v_H(\mathbf{r}) + v_{xc}(\mathbf{r}). \quad (2.23)$$

Since v_H and v_{xc} depend on the electronic density and, at the same time, are required to solve the Kohn-Sham equations, this problem needs to be tackled by means of a self-consistency method.

The generalization of the Kohn-Sham equations with respect to spin-polarized systems is carried out by replacing the spin-dependent electron densities, $n_{\uparrow}(\mathbf{r})$ and $n_{\downarrow}(\mathbf{r})$, as well as the magnetization density $\mathbf{m}(\mathbf{r})$ with the density matrix $\rho_{\alpha\beta}(\mathbf{r})$. In order to obtain the generalized Kohn-Sham equations, the electronic and magnetization densities need to be reproduced by Pauli spinors:

$$\boldsymbol{\psi}_i(\mathbf{r}) = \begin{pmatrix} \psi_i^{\uparrow}(\mathbf{r}) \\ \psi_i^{\downarrow}(\mathbf{r}) \end{pmatrix}. \quad (2.24)$$

Then, the electronic and the magnetization densities can be written as

$$n(\mathbf{r}) = \sum_{i=1}^N |\boldsymbol{\psi}_i(\mathbf{r})|^2, \quad (2.25)$$

and

$$\mathbf{m}(\mathbf{r}) = \sum_{i=1}^N \boldsymbol{\psi}_i^*(\mathbf{r})\boldsymbol{\sigma}\boldsymbol{\psi}_i(\mathbf{r}), \quad (2.26)$$

respectively. The components of $\boldsymbol{\sigma}$ are the Pauli-spin matrices. The Application of the variational principle yields the generalized Kohn-Sham equations exhibiting the

form of the Schrödinger-Pauli equation:

$$\left(-\frac{\hbar^2}{2m}\nabla^2 + v_{eff} + \boldsymbol{\sigma} \cdot \mathbf{B}_{eff}\right)\psi_i = \epsilon_i\psi_i(\mathbf{r}). \quad (2.27)$$

There are two terms contributing to the additional effective magnetic field \mathbf{B}_{eff} in Eq. (2.27). The first one is originating from the variation of the exchange-correlation energy with respect to the magnetization density \mathbf{m} . The other one is due to an external magnetic field \mathbf{B}_{ext} :

$$\mathbf{B}_{eff}(\mathbf{r}) = \mathbf{B}_{xc}(\mathbf{r}) + \mathbf{B}_{ext}(\mathbf{r}) \quad (2.28)$$

with

$$\mathbf{B}_{xc}(\mathbf{r}) = \frac{\delta E_{xc}[n(\mathbf{r}), \mathbf{m}(\mathbf{r})]}{\delta \mathbf{m}(\mathbf{r})}. \quad (2.29)$$

Further simplifications of Eq. (2.27) can be made regarding the spin direction. In a collinear magnetic ordering, as in the ferromagnetic or the antiferromagnetic case, the parallel or antiparallel magnetic moments may coincide with a certain axis, such as the z -axis, without loss of generality. Thus, the Hamilton operator becomes diagonal in both spin components of the spinor, which can be decoupled and the problem becomes independently solvable for the spin-up and the spin-down component. Furthermore, the total energy and other ground state properties of the system remain functionals of the spin-up and the spin-down density $n_{\uparrow}(\mathbf{r})$ and $n_{\downarrow}(\mathbf{r})$. These are expressed in terms of spin-dependent single-particle wave functions:

$$n_{\sigma=\uparrow,\downarrow}(\mathbf{r}) = \sum_{i=1}^N |\psi_i^{\sigma}(\mathbf{r})|^2. \quad (2.30)$$

2.3 Exchange-correlation potentials

In principle, the DFT enables the exact determination of a solid's ground state properties except for the exchange-correlation effects contained in the energy functional $E_{xc}[n]$. There is no accurate representation of this functional, and therefore, it needs to be approximated. The simplest approach is to assume the exchange-correlation energy to be locally represented by a uniform electron gas of the same electronic and magnetic density. In this case the exchange-correlation energy has the following form:

$$E_{xc}[n(\mathbf{r}), |\mathbf{m}(\mathbf{r})|] = \int n(\mathbf{r})\epsilon_{xc}(n(\mathbf{r}), |\mathbf{m}(\mathbf{r})|)d^3r. \quad (2.31)$$

Here, ϵ_{xc} is not a functional but a function of the electron density $n(\mathbf{r})$ and the absolute value of the magnetization density $|\mathbf{m}(\mathbf{r})|$, which is due to the parallel alignment of the exchange-correlation field \mathbf{B}_{xc} and the magnetization density $\mathbf{m}(\mathbf{r})$.

This approach is called the local density approximation (LDA) [31] or local spin-density approximation (LSDA) if the spin-polarization is considered as in the present work. The exchange-correlation potential, on the other hand, is written as

$$v_{xc}(\mathbf{r}) = \epsilon_{xc}(n(\mathbf{r}), |\mathbf{m}(\mathbf{r})|) + n(\mathbf{r}) \frac{\partial \epsilon_{xc}(n(\mathbf{r}), |\mathbf{m}(\mathbf{r})|)}{\partial n(\mathbf{r})}, \quad (2.32)$$

and the magnetic field results as below

$$\mathbf{B}_{xc}(\mathbf{r}) = n(\mathbf{r}) \frac{\partial \epsilon_{xc}(n(\mathbf{r}), |\mathbf{m}(\mathbf{r})|)}{\partial |\mathbf{m}(\mathbf{r})|} \hat{\mathbf{m}}(\mathbf{r}). \quad (2.33)$$

The validity of the LSDA is assumed only in the case of a slowly varying density, which is rare for atomic systems. Nevertheless, the LSDA yields extremely good results even in the case of inhomogeneous systems. Further optimization can be achieved by considering spatially varying electronic densities and introducing local gradients of the electron and magnetization density. This method is known as the 'Generalized Gradient Approximation' (GGA) [33]. The LDA and GGA are the most common approximations for the exchange-correlation potential.

2.4 The self-consistency cycle

As outlined above, solving the Kohn-Sham equations is performed within a self-consistency method. At first, a starting electronic density n_{in} is constructed. Then, the self-consistency cycle is run through iteratively (see Fig. 2.1):

Based on the density $n_{in}^N(\mathbf{r})$, the Hartree and the exchange-correlation potential, $v_H(n_{in})$ and $v_{xc}(n_{in})$, are computed, and the effective potential $v_{eff}(n_{in})$ is calculated. The latter one is inserted into the Kohn-Sham equations, which can be solved by means of exploiting the periodicity of a crystal via the Bloch's theorem. The Hamilton matrix is set up and diagonalized for every single Bloch vector \mathbf{k} that covers the Brillouin zone. In the next step, the eigenvalues and -states of the Hamilton matrix are used to determine the Fermi energy employing the occupation of bands assigned to the energy E_ν . It starts at the lowest energy and continues until the sum of the weights $w(\mathbf{k}, E_\nu(\mathbf{k}_\parallel) - E_F) = w(\mathbf{k}_\parallel)(e^{(E_\nu(\mathbf{k}_\parallel) - E_F)/k_B T} + 1)^{-1}$ equals the total number N of electrons per unit cell. The resulting condition fixes the Fermi energy. The calculation of the electronic density n_{out}^N is carried out by a sum over all occupied states:

$$n(\mathbf{r}) = \sum_{\mathbf{k}} \sum_{\nu} |\psi_{k\nu}(\mathbf{r})|^2. \quad (2.34)$$

In the last step, a new starting density n_{in}^{N+1} results from mixing the densities n_{in}^N and n_{out}^N . It is done in order to improve the numerical stability of the calculation. The simplest mixing method is the straight mixing $n_{in}^{N+1} = (1 - \alpha)n_{in}^N + \alpha n_{out}^N$, where

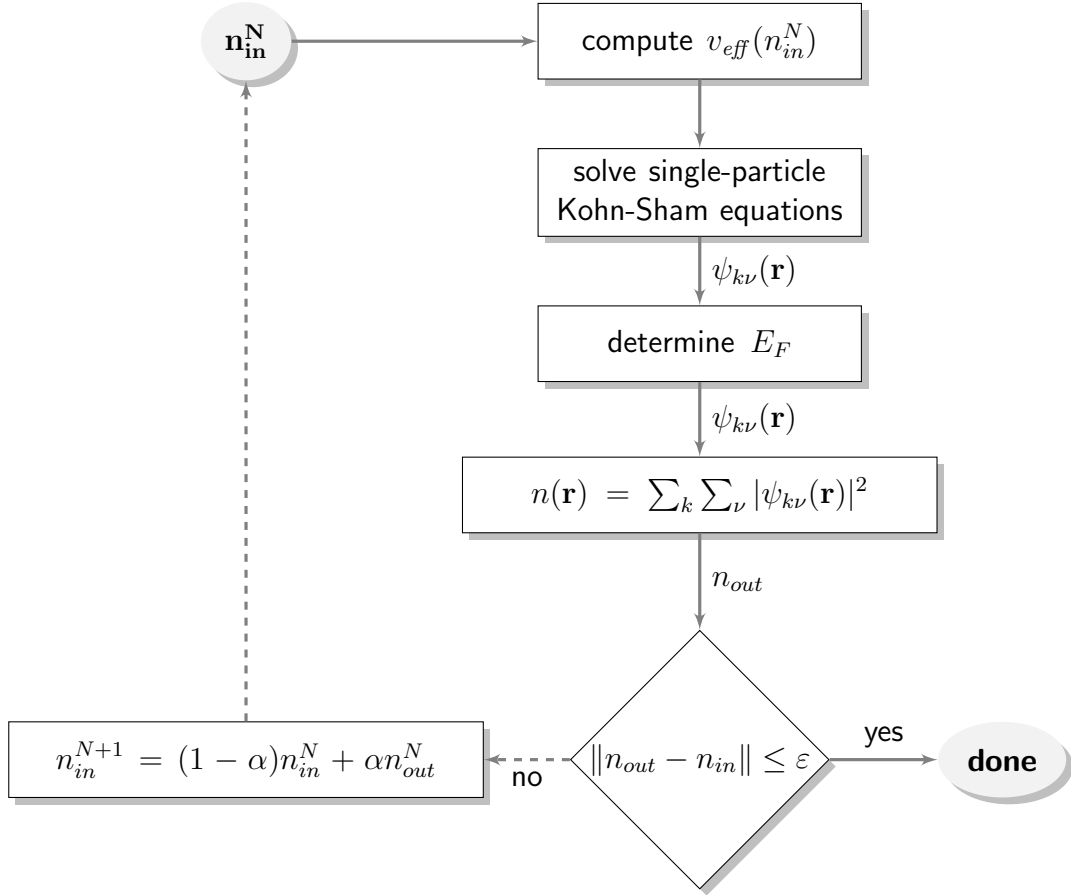


Figure 2.1: Schematic flow-chart of the self-consistency cycle in DFT calculations.

α is the mixing parameter. As α needs to be sufficiently small for the systems under consideration, it takes many iterations until the criterion of convergence is satisfied, i.e., the difference between n_{in} and n_{out} is lower or equal to a limit ε of choice:

$$\|n_{out} - n_{in}\| \leq \varepsilon. \quad (2.35)$$

Besides the straight mixing there are other mixing methods that achieve a more rapid convergence [34].

3 Solving the Kohn-Sham equations with FLAPW

In the previous chapter, the complex many-particle problem has been transferred into a single-particle problem by means of the DFT. In the following, several basis sets are discussed that allow for the solution of the Kohn-Sham equations. Therefore, a method will be introduced that provides the proper basis set as well as a good description of the potential. This method is called the 'full-potential linearized augmented plane wave' method (FLAPW) [35].

The easy implementation of plane waves qualifies them as a clearly promising basis set, since they are orthogonal and at the same time diagonal in the momentum, i.e., they are eigenfunctions of the kinetic energy operator. Their major drawback is the description of the electrons' wave functions near the atomic nuclei. Here, the latter ones are heavily oscillating due to the $1/r$ dependency of the Coulomb potential. Hence, large wave vectors are needed to reproduce the total wave function correctly. A common approach to avoid the oscillations, is the application of so-called pseudopotentials [36], where the core states are projected out of the Hamilton operator leading to weaker binding potentials. Therefore, they are describing the structure of the valence electrons only. Furthermore, the pseudo-wave functions may be represented using fewer Fourier components than the all-electron wave functions at the same time. But the construction of pseudopotentials is often very complicated, therefore, an alternative way of representing the oscillations near the nuclei is chosen here, which is the application of radial wave functions. This procedure has been suggested by J. C. Slater [37] and is called the 'augmented plane wave' method (APW).

3.1 APW method

In order to reproduce the wave functions correctly throughout the space, the APW method separates the volume into two distinct regions. At the positions of the atomic nuclei the potential is assumed to be spherically symmetric within non-overlapping spheres, which are called *muffin tins* (MT). In between the muffin tins the *interstitial region* (IR) extends, where the potential is set to a constant value, i.e.,

$$v(\mathbf{r}) = \begin{cases} v_{IR}^0 = const & \text{interstitial region} \\ v_{MT}^0(r) & \text{muffin tin.} \end{cases} \quad (3.1)$$

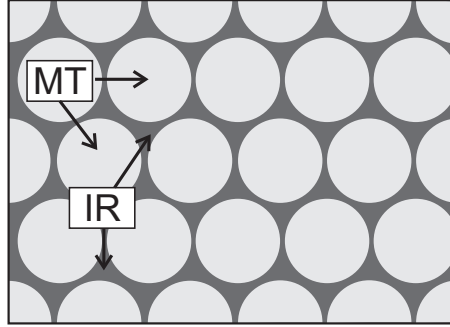


Figure 3.1: The division of the space in the APW method. Spheres represent the muffin tins centered at the position of the atomic nuclei. The dark region denotes the interstitial region in between the muffin tins.

It is known that for a constant potential the fundamental solutions of the Schrödinger equation are plane waves, whereas the radial Schrödinger equation in a spherical potential is solved by radial functions times spherical harmonics. Therefore, the present approximation of the potential allows for the expansion of the single-particle wave functions as below:

$$\varphi_{\mathbf{G}}(\mathbf{k}, \mathbf{r}) = \begin{cases} e^{i(\mathbf{G}+\mathbf{k})\mathbf{r}} & \text{interstitial region} \\ \sum_L A_L^{\mu\mathbf{G}}(\mathbf{k}) u_l(r) Y_L(\hat{\mathbf{r}}) & \text{muffin tin } \mu, \end{cases} \quad (3.2)$$

where \mathbf{k} denotes the Bloch vector and \mathbf{G} the reciprocal lattice vector. L abbreviates the quantum numbers l and m , and $\hat{\mathbf{r}}$ specifies the location inside the muffin tin μ with respect to its center. The functions u_l are solutions of the radial Schrödinger equation, including the energy parameter E_l and the spherical component of the potential $v(r)$:

$$\left(-\frac{\hbar^2}{2m} \frac{\partial^2}{\partial r^2} + \frac{\hbar^2}{2m} \frac{l(l+1)}{r^2} + v(r) \right) r u_l(r) = E_l r u_l(r). \quad (3.3)$$

The condition of continuous wave functions at the transition from the muffin tin spheres to the interstitial region determines the coefficients $A_{\mu L}^{\mathbf{G}}(\mathbf{k})$. Thus, the APW form a set of continuous basis functions covering all space. Nevertheless, this choice of a basis set has several disadvantages:

- The APW offer only little variational freedom, since the energy parameters E_l and the quantum numbers l , m need to be kept fixed. Furthermore, a correct description of the system is obtained solely, if E_l equals the band energies. At the same time the u_l 's depend on the band energies and thus a simple diagonalization of the Hamilton matrix is impossible and leads to a nonlinear

problem.

- For infinitesimal u_l at the boundary of the muffin tin spheres the matching condition is not satisfied anymore, and as a result, the plane waves and radial functions decouple. This is called the asymptotic problem.

3.2 LAPW method

In order to eliminate the problems listed in the section above, O. Krogh Andersen [38] as well as D. D. Koelling and G. O. Arbman [39] linearized the APW basis by adding the energy derivative $\dot{u}_l(r) = \frac{\partial u_l(E,r)}{\partial E}$ to the radial solution $u_l(E, r)$ of the Schrödinger equation. Therefore, u_l is expanded into a Taylor-series around E_l

$$u_l(E, r) = u_l(E_l, r) + \dot{u}_l(E_l, r)(E - E_l) + \mathcal{O}[(E - E_l)^2]. \quad (3.4)$$

Here, $\mathcal{O}[(E - E_l)^2]$ is due to the fact that the linearized APW (LAPW) basis functions are constructed from linear combinations of u_l and \dot{u}_l to obtain an energy independent basis. The errors introduced in the wave functions are of the order of $(E - E_l)^2$. After the application of the variational principle the errors in the computed band energies result in the order of $(E - E_l)^4$. For this reason, the linearization works well for a wide energy range.

In comparison to the APW method the extra coefficients $B_L^{\mu\mathbf{G}}(\mathbf{k})$ are added to the LAPW basis guaranteeing that the basis functions inside the muffin tin spheres match continuously and differentially onto the plane waves in the interstitial region:

$$\varphi_{\mathbf{G}}(\mathbf{k}, \mathbf{r}) = \begin{cases} e^{i(\mathbf{G}+\mathbf{k})\mathbf{r}} & \text{interstitial region} \\ \sum_L \left(A_L^{\mu\mathbf{G}}(\mathbf{k})u_l(r) + B_L^{\mu\mathbf{G}}(\mathbf{k})\dot{u}_l(r) \right) Y_L(\hat{\mathbf{r}}) & \text{muffin tin } \mu. \end{cases} \quad (3.5)$$

The \dot{u}_l are obtained by taking the energy derivative of Eq. (3.3) resulting in

$$\left(-\frac{\hbar^2}{2m} \frac{\partial^2}{\partial r^2} + \frac{\hbar^2}{2m} \frac{l(l+1)}{r^2} + v(r) - E_l \right) r\dot{u}_l(r) = ru_l(r). \quad (3.6)$$

Furthermore, they have to meet the normalization requirement

$$\int_0^{R_{MT}} u_l^2(r)r^2 dr = 1. \quad (3.7)$$

By differentiating Eq. (3.7) with respect to the energy, it is shown that the u_l and \dot{u}_l need to fulfill the requirement of orthogonalization at the same time

$$\int_0^{R_{MT}} u_l(r)\dot{u}_l(r)r^2 dr = 0, \quad (3.8)$$

since every linear combination of u_l and \dot{u}_l solves Eq. (3.6). Thus, they form a complete and orthogonal basis set inside the muffin tin spheres as the spherical harmonics Y_{lm} are orthogonal by definition. Unfortunately, the core states still need a separate treatment considering that the plane waves are nonorthogonal to them. This causes a problem for so-called semi-core states, i.e., energetically high states of the electrons close to the nuclei. Due to their strong delocalization they do not reside completely within the muffin tin spheres. As a result, the energy parameter E_l , which is originally assigned to those states, is used for the description of the higher valence electrons. This is for instance the case for the p -states of the early transition metals. In order to avoid this problem local orbitals can be introduced [40].

The introduction of the LAPW basis fixes the main issues of the APW method:

- Since E_l no longer equals the band energies, the Hamilton matrix is energy independent, and the energies can be determined within a single diagonalization.
- The extension of the muffin-tin potentials to non-spherical potentials is easily performed, since the LAPW basis set offers a large variational freedom. This results in the full-potential linearized augmented plane wave method (FLAPW).
- If the u_l vanish at the muffin-tin boundaries, their radial derivatives and the \dot{u}_l are generally nonzero. Therefore, the continuity condition at the boundaries is always satisfied and there is no asymptote problem.

Since both, the APW and the LAPW method, have the representation of the basis as plane waves in common, the nonlinearity of the APW basis can only be avoided by a large eigenvalue problem. The basis functions inside the muffin-tin spheres are coupled to the plane waves in the interstitial region via the matching condition at the boundary. Thus, they can only be varied indirectly by manipulating the plane wave coefficients. The variation becomes independent with a finite number of plane waves and at maximum the same number of functions in the muffin tin spheres. In order to exploit the larger variational freedom of the LAPW method compared with the APW method, the number of plane waves needs to be increased.

3.3 The FLAPW method

In the case of close packed metallic systems the LAPW method provides a good description. However, for open structures, i.e., structures of reduced symmetry like semiconductors, surfaces and interfaces, the shape-approximations applied to the potential become difficult to justify. The FLAPW method [23] considers the

inclusion of a warped potential in the interstitial region and non-spherical terms in the muffin tin rather than approximating the potential:

$$v(r) = \begin{cases} \sum_{\mathbf{G}} v_I^{\mathbf{G}} e^{i\mathbf{G}\mathbf{r}} & \text{interstitial region,} \\ \sum_L v_{MT}^{\mathbf{G}}(r) Y_L(\hat{\mathbf{r}}) & \text{muffin tin spheres.} \end{cases} \quad (3.9)$$

The charge density may be phrased analogously:

$$v(r) = \begin{cases} \sum_{\mathbf{G}} \rho_I^{\mathbf{G}} e^{i\mathbf{G}\mathbf{r}} & \text{interstitial region,} \\ \sum_L \rho_{MT}^{\mathbf{G}}(r) Y_L(\hat{\mathbf{r}}) & \text{muffin tin spheres.} \end{cases} \quad (3.10)$$

3.3.1 Film Calculations With FLAPW

Since there is great interest in studying phenomena at surfaces and thin films, the exact computation of those systems has become more and more important nowadays. Unfortunately, they exhibit a lack of the translational symmetry, and since only Bloch vectors \mathbf{k}_{\parallel} parallel to the surface are used, the description of these systems is numerically very demanding. An attempt to tackle this problem has been provided by reintroducing the periodicity perpendicular to the surface by means of a periodically repeating film in the direction of the symmetry break. This thin-slab approximation only yields reasonable results if the vacuum layer is chosen sufficiently large. Otherwise, the interaction between the films becomes too strong and the system loses its features of the semi-infinite crystal.

Another approach is to divide the space into three distinct regions, which is made use of by the FLAPW method for thin films. In addition to the muffin tin spheres and interstitial region already known from the FLAPW method, a vacuum region is introduced (cf. Fig. 3.2). As a result, the interstitial region spreads from $-\frac{D}{2}$ to $+\frac{D}{2}$ along the z -direction, which is defined to be perpendicular to the film surface. Due to the lack of periodicity along the z -axis, the computed unit cell stretches from $-\infty$ to $+\infty$. In consequence of this partitioning, the wave functions in the interstitial region may be kept the same as in the FLAPW method for bulk systems. They can still be expanded in terms of plane waves, but instead of D the parameter \tilde{D} is used to define wave vectors perpendicular to the film. Here, \tilde{D} needs to satisfy the condition $D < \tilde{D}$ in order to gain a larger variational freedom. In this way, the plane waves are written as

$$\varphi_{\mathbf{G}_{\parallel}G_{\perp}}(\mathbf{k}, \mathbf{r}) = e^{i(\mathbf{G}_{\parallel} + \mathbf{k}_{\parallel})\mathbf{r}_{\parallel}} e^{iG_{\perp}z} \quad \text{with} \quad G_{\perp} = \frac{2\pi n}{\tilde{D}}. \quad (3.11)$$

\mathbf{k}_{\parallel} and \mathbf{G}_{\parallel} represent the two-dimensional Bloch and wave vectors, respectively. \mathbf{r}_{\parallel} is the component of \mathbf{r} that is aligned parallel to the film, whereas G_{\perp} is the wave vector

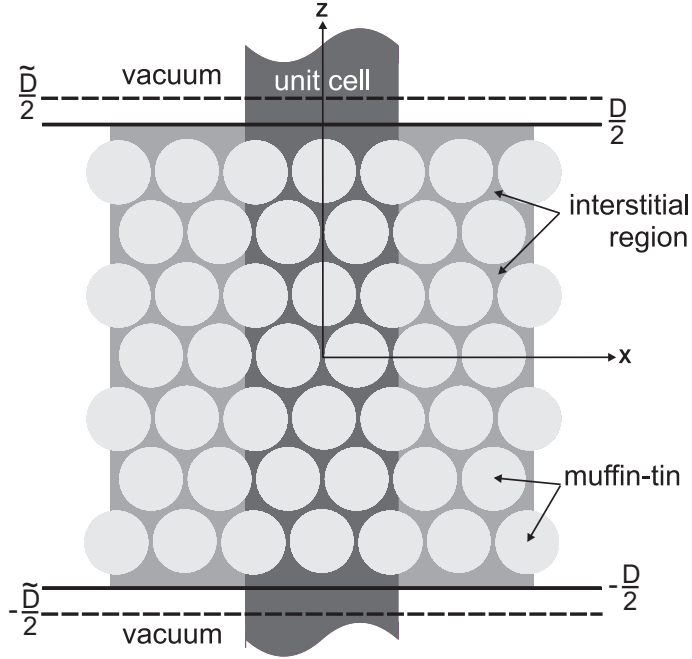


Figure 3.2: The unit cell in a film calculation with FLAPW

perpendicular to the film. The basis functions of the vacuum region are constructed analogously to the basis functions of the muffin-tin spheres. They consist of plane waves parallel to the film and a function $u_{\mathbf{G}_{\parallel}}(\mathbf{k}, z)$ solving the corresponding one-dimensional Schrödinger equation

$$\left(-\frac{\hbar^2}{2m} \frac{\partial^2}{\partial z^2} + v_0(z) - E_{vac} + \frac{\hbar^2}{2m} (\mathbf{G}_{\parallel} + \mathbf{k}_{\parallel})^2 \right) u_{\mathbf{G}_{\parallel}}(\mathbf{k}, z) = 0. \quad (3.12)$$

E_{vac} denotes the energy parameter of the vacuum and v_0 the planar averaged part of the vacuum potential. Again, deriving Eq. (3.12) with respect to the energy

$$\left(-\frac{\hbar^2}{2m} \frac{\partial^2}{\partial z^2} + v_0(z) - E_{vac} + \frac{\hbar^2}{2m} (\mathbf{G}_{\parallel} + \mathbf{k}_{\parallel})^2 \right) \dot{u}_{\mathbf{G}_{\parallel}}(\mathbf{k}, z) = u_{\mathbf{G}_{\parallel}}(\mathbf{k}, z) \quad (3.13)$$

yields the equation that determines the energy derivative $\dot{u}_{\mathbf{G}_{\parallel}}(\mathbf{k}, z)$. Then, the basis functions of the vacuum region are given by

$$\varphi_{\mathbf{G}_{\parallel} \mathbf{G}_{\perp}}(\mathbf{k}, \mathbf{r}) = \left(A_{\mathbf{G}_{\parallel} \mathbf{G}_{\perp}}(\mathbf{k}_{\parallel}) u_{\mathbf{G}_{\parallel}}(\mathbf{k}_{\parallel}, z) + B_{\mathbf{G}_{\parallel} \mathbf{G}_{\perp}}(\mathbf{k}_{\parallel}) \dot{u}_{\mathbf{G}_{\parallel}}(\mathbf{k}_{\parallel}, z) \right) . \quad (3.14)$$

Similar to the coefficients used for the wave functions within the muffin-tin spheres, the coefficients $A_{\mathbf{G}_{\parallel} \mathbf{G}_{\perp}}(\mathbf{k}_{\parallel})$ and $B_{\mathbf{G}_{\parallel} \mathbf{G}_{\perp}}(\mathbf{k}_{\parallel})$ are obtained by requiring the continuous and differential match at the transition to the vacuum region. Since the number

of basis functions is significantly lower in the vacuum, its basis provides a smaller variational freedom compared to the basis of the interstitial region. Due to the work function, the energy spectrum of electrons is smaller in the vacuum and therefore, it is convenient to use a whole series of energy parameters instead of the energy parameter E_{vac}

$$E_{vac}^{G_{\perp}} = E_{vac} - \frac{\hbar^2}{2m} G_{\perp}^2 \quad (3.15)$$

to increase the variational freedom. This allows for basis functions $u_{\mathbf{G}_{\parallel}}(\mathbf{k}, z)$, which are depending on G_{\perp} .

For thin films the FLAPW basis set takes the form

$$\varphi_{\mathbf{G}_{\parallel}G_{\perp}}(\mathbf{k}_{\parallel}, \mathbf{r}) = \begin{cases} e^{i(\mathbf{G}_{\parallel}+\mathbf{k}_{\parallel})\mathbf{r}_{\parallel}} e^{iG_{\perp}z} & \text{interstitial region} \\ \left(A_{\mathbf{G}_{\parallel}G_{\perp}}(\mathbf{k}_{\parallel})u_{\mathbf{G}_{\parallel}}(\mathbf{k}_{\parallel}, z) \right. \\ \left. + B_{\mathbf{G}_{\parallel}G_{\perp}}(\mathbf{k}_{\parallel})\dot{u}_{\mathbf{G}_{\parallel}}(\mathbf{k}_{\parallel}, z) \right) e^{i(\mathbf{G}_{\parallel}+\mathbf{k}_{\parallel})\mathbf{r}_{\parallel}} & \text{vacuum} \\ \sum_L \left(A_L^{\mu\mathbf{G}}(\mathbf{k})u_l(r) + B_L^{\mu\mathbf{G}}(\mathbf{k})\dot{u}_l(r) \right) Y_{l,m}(\hat{\mathbf{r}}) & \text{muffin-tin } \mu. \end{cases} \quad (3.16)$$

It traces back to H. Krakauer, M. Posternak and A. J. Freeman [24].

3.3.2 The Representation of the Density and the Potential

The charge density ρ and the potential v resemble the wave functions in the FLAPW method. In the interstitial region they consist of three-dimensional plane waves, in the muffin tin they are represented by spherical harmonics and radial functions. In the vacuum region two-dimensional plane waves in combination with z -dependent functions describe the density and the potential, respectively. In general, the charge density is given by

$$\rho = e \sum_i^N |\psi_i(\mathbf{r})|^2 \quad (3.17)$$

with the sum over all occupied states. Since the expansion of the wave functions is restricted by a wave vector cut-off $k_{max} > |\mathbf{k}_{\parallel} + \mathbf{G}|$ that is included quadratically in the charge density, it is necessary to consider a cut off $G_{max} = 2k_{max}$ for the density and the potential. According to this, many coefficients need to be computed and stored. In order to minimize the computational effort, the symmetry of the system has to be exploited due to the fact that the potential and the density possess the symmetry of the lattice. For this reason, the plane waves may be substituted by symmetrized plane waves, which are called star functions. In the interstitial region

the star functions have the form

$$\Phi_s^{3D}(\mathbf{r}) = \frac{1}{N_{op}} \sum_{op} e^{i\mathbf{R}\mathbf{G}(\mathbf{r}-\boldsymbol{\tau})}. \quad (3.18)$$

$\{\mathbf{R}|\boldsymbol{\tau}\}$ denotes a symmetry operation of the three-dimensional space group. N_{op} is assigned to the number of performable symmetry operations. By means of this representation, plane waves that are equivalent in symmetry can be combined to a so-called star. Analogously, the two-dimensional plane waves in the vacuum region are merged in two-dimensional star functions $\Phi_s^{2D}(\mathbf{r})$ with regard to the symmetry operations of the two-dimensional space group. In a similar way, the expansion of the charge density and the potential in the muffin tin is performed by benefitting from the point symmetry of the atoms. In this case the symmetrized wave functions are called lattice harmonics instead of star functions. They result from the linear combinations of the spherical harmonics

$$K_\nu(\hat{\mathbf{r}}) = \sum_m c_{\nu,m}^\alpha Y_L(\hat{\mathbf{r}}). \quad (3.19)$$

The lattice harmonics are real, orthonormal and invariant concerning symmetry operations of the point group.

In summary, the expansion of the charge density in all of the three distinct regions is specified as follows

$$\rho(\mathbf{r}) = \begin{cases} \sum_s \rho_s \Phi_s^{3D}(\mathbf{r}) & \text{interstitial region,} \\ \sum_s \rho_s(z) \Phi_s^{2D}(\mathbf{r}) & \text{vacuum region,} \\ \sum_\nu \rho_\nu^\mu(r) K_\nu(\hat{\mathbf{r}}) & \text{muffin tin sphere } \mu. \end{cases} \quad (3.20)$$

The potential is expanded in the same way.

3.3.3 The Generalized Eigenvalue Problem

Despite the fact that plane waves form an orthogonal basis set, the FLAPW functions behave different due to the spatial division into specific regions. The muffin tins are cut out from the unit cell in which the orthogonality is defined. Therefore, the basis functions of different regions are able to overlap, but at the same time they are non-orthogonal. The degree of non-orthogonality is given by the overlap matrix \mathbf{S} , and in the FLAPW basis it results in the overlap matrix \mathbf{S} not being diagonal, but Hermitian:

$$S^{\mathbf{G}\mathbf{G}'} = \int \varphi_{\mathbf{G}'}^*(\mathbf{r}) \varphi_{\mathbf{G}}(\mathbf{r}) d^3r. \quad (3.21)$$

Here, and in the rest of this section, the index \mathbf{k} for the Bloch vector is dropped for reasons of simplicity even though setting up the basis set as well as the Hamiltonian matrix is done for every Bloch vector independently. However, inserting the non-orthogonal basis set $|\phi_i\rangle = \sum_{\mathbf{G}} \mathbf{G} c_{i\mathbf{G}} |\varphi_{\mathbf{G}}\rangle$ in the secular equation (2.20) yields

$$(\mathcal{H} - \epsilon_i \mathbf{S}) \mathbf{c}_i = 0, \quad (3.22)$$

where \mathbf{c}_i denotes the coefficient vector corresponding to the i th eigenvalue. Equation (3.22) is called a *generalized eigenvalue problem*. It can be reduced to a standard eigenvalue problem by applying the Cholesky decomposition. In order to achieve this, the overlap matrix is split into a matrix product of a lower triangular matrix \mathbf{L} with only positive diagonal elements and its Hermitian conjugate \mathbf{L}^\dagger . This procedure is correct as it applies for every Hermitian and positive definite matrix [41]:

$$\mathbf{S} = \mathbf{L}\mathbf{L}^\dagger. \quad (3.23)$$

After the insertion of Eq. (3.23) in Eq. (3.22) and multiplying with \mathbf{L}^{-1} from the left, the eigenvalue problem gains the following simple form

$$\begin{aligned} \mathbf{L}^{-1}\mathcal{H}(\mathbf{L}^{-1})^\dagger \mathbf{L}^\dagger \mathbf{c}_i &= \epsilon_i \mathbf{L}^\dagger \mathbf{c}_i \\ \Leftrightarrow \mathbf{P}\mathbf{x}_i &= \epsilon_i \mathbf{x}_i. \end{aligned} \quad (3.24)$$

The eigenvectors \mathbf{c}_i can be obtained by back-transforming the \mathbf{x}_i

$$\mathbf{c}_i = (\mathbf{L}^\dagger)^{-1} \mathbf{x}_i. \quad (3.25)$$

3.3.4 Brillouin Zone Integration within FLAPW

The computation of certain quantities such as the electronic density in an infinite periodic solid happens in terms of the integration of periodic functions over the Brillouin zone described by the Bloch vector \mathbf{k} and the band energy ν . These integrations are carried out over those parts of the Brillouin zone, where the band energy $\epsilon_\nu(\mathbf{k})$ is lower than the Fermi energy, i.e., the states need to be occupied. Then, the integrals have this form

$$\frac{1}{V_{BZ}} \int_{BZ} \sum_{\nu, \epsilon_\nu(\mathbf{k}) < E_F} f_\nu(\mathbf{k}) d^3k. \quad (3.26)$$

Here, V_{BZ} denotes the volume of the Brillouin zone and f is the function to be integrated. The computational effort caused by the Brillouin zone integration is decreased by the exploitation of the point symmetry, which restricts the integration to the irreducible part of the Brillouin zone only. There are several methods to perform the integration like the tetrahedron method [42] or the special point methods

of Chadi and Cohen [43] as well as Monkhorst and Pack [44]. The latter are methods in order to integrate slowly varying periodic functions of \mathbf{k} . Then, the function needs to be calculated on a discrete mesh of \mathbf{k} points, each one of them featuring a specific weight. In this way, the integration is transformed into a sum of a set of \mathbf{k} points. In order to permit only those states, which are located below the Fermi energy, an energy cut off parameter is assigned to every \mathbf{k} point. Due to the discretization in momentum space the charge density undergoes sudden changes, which might prevent a convergence. Therefore, the chosen step function is replaced by the Fermi function

$$f(\epsilon_\nu) = \frac{1}{(e^{(\epsilon_\nu(\mathbf{k}) - E_F)/k_B T} + 1)} \quad (3.27)$$

introducing a temperature broadening. Choosing the appropriate temperature T accelerates the convergence.

3.3.5 Determination of the Total Energy

An important ground-state property of a solid state system is the total energy. It depends on many parameters such as the structure of the lattice, the lattice constant, the magnetic order, and the orientation of the magnetization in space if spin-orbit coupling (SOC) is taken into account. The minimum energy determines the ground state and, consequently, the other properties of the system. Therefore, it is of importance to compute this quantity as exact as possible. The total energy consists of the term describing the energy of the electrons, Eq. (2.16), and an additional term E_{ii} as a result of the Coulomb interaction of the atomic nuclei:

$$E[n] = T_S[n] + E_{ext}[n] + E_H[n] + E_{xc} + E_{ii}. \quad (3.28)$$

E_{ii} is given as

$$E_{ii} = e^2 \sum_{\substack{\mu, \mu'=1 \\ \mu \neq \mu'}}^M \frac{Z^\mu Z^{\mu'}}{\|\mathbf{R}^\mu - \mathbf{R}^{\mu'}\|}. \quad (3.29)$$

μ denotes the atoms of the crystal at the position \mathbf{R}^μ . The Nabla operator ∇^2 included in the kinetic energy T_S should not be applied explicitly due to numerical reasons. Therefore, T_S is rewritten in terms of single-particle eigenvalues ϵ_i

$$T_S[n] = \sum_{i=1}^N \epsilon_i - \int n(\mathbf{r}) v_{eff}(\mathbf{r}) d^3r - \int \mathbf{m}(\mathbf{r}) \cdot \mathbf{B}_{eff}(\mathbf{r}) d^3r. \quad (3.30)$$

This representation is obtained from the Kohn-Sham equations (2.20). Another problem are the Coulomb singularities originating from the atomic nuclei. As M. Weinert, E. Wimmer and A. J. Freeman showed [35], the occurrence of the singu-

larities is avoided by combining the contributions of the kinetic and the potential energy. Assuming that the external potential arises from the atomic nuclei solely and excluding the existence of an external magnetic field, i.e.,

$$v_{ext}(\mathbf{r}) = - \sum_{\mu=1}^M \frac{Z^{\mu}}{|\mathbf{r} - \mathbf{R}^{\mu}|}, \quad \mathbf{B}_{ext} = 0, \quad (3.31)$$

the total energy may be obtained via Eq. (3.28). During the iterative procedure Eq. (3.28) depicts only an approximation. The ground state energy $E_0[n_0]$ is obtained after achieving the self-consistency.

4 Modeling Magnetic Systems

In order to provide a framework to interpret the results obtained from *ab initio* calculations, it is convenient to develop model concepts based on relatively simple assumptions. Since the present thesis deals with magnetic systems, this chapter focuses on the Stoner model, the Heisenberg model as well as the spin-polarized Tersoff-Hamann model.

4.1 Stoner Model

The Stoner model [45, 46, 47, 48] expresses the competition between the exchange interaction in terms of the exchange integral I and the kinetic energy in terms of the density of states (DOS) $n(E_F)$ at the Fermi energy E_F . It is based upon the fact that within the spin density functional theory the magnetization density $m(\mathbf{r}) = |\mathbf{m}(\mathbf{r})|$ of a solid is usually much smaller than the electronic density $n(\mathbf{r})$. Thus, performing a Taylor expansion of the exchange-correlation energy $\epsilon_{xc}(n(\mathbf{r}), m(\mathbf{r}))$ with $\zeta = \frac{m}{n}$ results in:

$$\epsilon(n, \zeta) = \epsilon(n, 0) + \frac{1}{2}\epsilon''_{xc}(n, 0)\zeta^2 + \dots \quad (4.1)$$

The magnetic field \mathbf{B}_{xc} (cf. Eq. (2.29)) is written as follows

$$\mathbf{B}_{xc} = \frac{1}{n^2}\epsilon''_{xc}(n, 0)\mathbf{m}. \quad (4.2)$$

\mathbf{B}_{xc} acts as an additional spin-dependent contribution \tilde{v}_{xc} to the nonmagnetic exchange-correlation potential v_{xc}^0 . This extra term has the same absolute value in both spin channels. It is attractive for the majority spin (+) and repulsive for the minority spin (-):

$$v_{xc}^{\pm} = v_{xc}^0 \mp \tilde{v}_{xc}(\mathbf{r})m(\mathbf{r}). \quad (4.3)$$

The Stoner model neglects the spatial variation and uses the approximation

$$v_{xc}^{\pm} = v_{xc}^0 \mp \frac{1}{2}IM. \quad (4.4)$$

Here, the magnetic moment per atom is given as the integral of the magnetization density over the muffin tin, $\int_{MT} m(\mathbf{r})d^3r$. \tilde{v}_{xc} is replaced by the exchange integral I which is also called *Stoner parameter*. Due to the constant shift of $\mp \frac{1}{2}IM$ the potential has the same spatial shape as in the non-magnetic case. Therefore, the

wave functions $\psi_i^\pm(\mathbf{r})$ remain unchanged while the eigenvalues ϵ_i^\pm are rigidly shifted by $\mp\frac{1}{2}IM$ as well:

$$\psi_i^\pm(\mathbf{r}) = \psi_0(\mathbf{r}) \quad \text{and} \quad \epsilon_i^\pm = \epsilon_i^0 \mp \frac{1}{2}IM. \quad (4.5)$$

The subscript i is the abbreviation of $\mathbf{k}\nu$, namely the wave vectors \mathbf{k} and the band indices ν . The constant shift in the energy eigenvalues gives rise to a spin split in the bandstructure, whereas the shape of the bands remains unaltered. As a consequence, the local spin densities of states keep the shape of the non-magnetic DOS with a simultaneous shift of $\pm\frac{1}{2}IM$:

$$n^\pm(E) = \sum_\nu \int_{BZ} \delta(E - \epsilon_i^\pm) d^3k = n^0(E \pm \frac{1}{2}IM), \quad (4.6)$$

where the integrated volume is the Brillouin zone (BZ). The criterion for the existence of ferromagnetism can be derived from Eq. (4.6). The number N of electrons per atom and the magnetic moment M of the unit cell are yielded by integrating the DOS over all occupied states up to the Fermi energy E_F :

$$N = \int_{E < E_F} \left[n^0\left(E + \frac{1}{2}IM\right) + n^0\left(E - \frac{1}{2}IM\right) \right] dE, \quad (4.7)$$

and

$$M = \int_{E < E_F} \left[n^0\left(E + \frac{1}{2}IM\right) - n^0\left(E - \frac{1}{2}IM\right) \right] dE. \quad (4.8)$$

Assuming charge neutrality, Eq. (4.7) can be applied to determine the Fermi energy $E_F = E_F(M)$ given that $n^0(E)$ and N are known. In that case, the magnetic moment M is obtained by substituting E_F with $E_F(M)$ leading to a nonlinear equation:

$$\begin{aligned} M &= F(M) \\ &= \int_{E < E_F(M)} \left[n^0\left(E + \frac{1}{2}IM\right) - n^0\left(E - \frac{1}{2}IM\right) \right] dE. \end{aligned} \quad (4.9)$$

From Eq. (4.9) it can be deduced that the function $F(M)$ satisfies the following conditions:

- $F(0) = 0$,
- $F(M) = -F(-M)$,
- $F(\pm\infty) = \pm M_\infty$,
- $F'(M) > 0$.

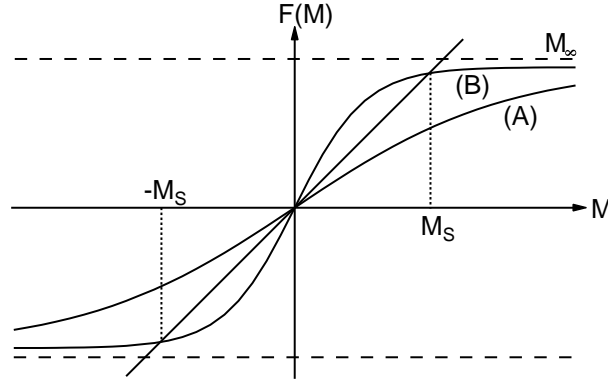


Figure 4.1: Graphical solution of Eq. (4.9).

The last condition is owing to the fact that $n^0(E) > 0$. Here, M_∞ is the saturation magnetization for full spin-polarization according to Hund's rule, i.e., all the majority spin states are occupied and the minority states are empty.

Equation (4.9) can be solved graphically as it is shown in Fig. 4.1. There are two kinds of functions $F(M)$ satisfying the conditions above. In the first case (A) the trivial paramagnetic solution $F(M) = M = 0$ is considered. The function denoted with (B) has three solutions of which only the nontrivial ones for $M = \pm M_S$ have a finite spontaneous magnetization. The nonmagnetic solution $M = 0$ is unstable. Fig. 4.1 shows that there always exists a solution with finite magnetization if the slope of $F(M)$ at $M = 0$ is larger than one. Therefore, the necessary and at the same time sufficient condition for the existence of a ferromagnetic solution is

$$F'(0) > 1. \quad (4.10)$$

The derivation of Eq. (4.9) with respect to M reads

$$F'(M) = \frac{I}{2} \left[n^0 \left(E_F + \frac{1}{2}IM \right) + n^0 \left(E_F - \frac{1}{2}IM \right) \right] + \left[n^0 \left(E_F + \frac{1}{2}IM \right) - n^0 \left(E_F - \frac{1}{2}IM \right) \right] \frac{dE_F}{dM}, \quad (4.11)$$

and setting $M = 0$ in Eq. (4.11) results in the Stoner criterion of ferromagnetism:

$$F'(0) = In^0(E_F) > 1. \quad (4.12)$$

This criterion represents an instability condition. It states that for a large exchange integral I and a large nonmagnetic DOS $n^0(E_F)$ at the Fermi energy the ferromag-

netic phase is more stable than the paramagnetic one.

In a simple approximation the DOS is proportional to the inverse of the bandwidth. This is the case for the d -bands in transition metals. Therefore, the probability of exhibiting a magnetic ground state increases for a small bandwidth. In the limiting case of single atoms the smallest bandwidth, i.e., zero bandwidth is achieved. Hence, atoms do always satisfy the Stoner criterion. The more common elements that fulfill the Stoner criterion also in bulk are Fe, Co and Ni, which are the typical bulk ferromagnets. Another example are surface systems, where due to the reduction of the coordination the bandwidth becomes smaller and thus elements that are non-magnetic in bulk might become magnetic at the surface.

The extension to the Stoner model for antiferromagnetism is performed by including the influences of an external magnetic field $\mathbf{H} = (0, 0, H)$ [49, 50]. From first order perturbation theory it follows that the relation between the external magnetic field and the induced magnetism is given by the susceptibility χ_{AF} :

$$M = \chi_{AF} H. \quad (4.13)$$

Since antiferromagnetism features alternating magnetic moments M and $-M$, the magnetic field and the magnetic moments generate the following exchange-correlation potentials:

$$\begin{aligned} v_{xc,1}^{\pm} &= v_{xc}^0 \pm \Delta v_{xc,1}^{\pm} = v_{xc}^0 \pm \left(\frac{1}{2} I M + \mu_B H \right) \\ v_{xc,2}^{\pm} &= v_{xc}^0 \pm \Delta v_{xc,2}^{\pm} = v_{xc}^0 \mp \left(\frac{1}{2} I M + \mu_B H \right) \end{aligned} \quad (4.14)$$

grouping the atoms into two sublattices 1 and 2. Similar to Eq. (4.9) the present problem has to be solved self-consistently. Unfortunately, the paramagnetic densities n^{\pm} cannot be obtained by a simple shift of $\pm \frac{1}{2} I M$ anymore. Using the basic features of the Green's functions the magnetic moment is calculated as below

$$\begin{aligned} M &= \int^{E_F(M)} [n_0^+(E) - n_0^-(E)] dE \\ &= -\frac{1}{\pi} \Im \left(\int^{E_F(M)} [G_{00}^+(E) - G_{00}^-(E)] dE \right) \\ &= -\frac{1}{\pi} \sum_i \Im \left(\int^{E_F(M)} G_{0i}^0(E) [\Delta v_i^+ - \Delta v_i^-] G_{i0}^0(E) dE + \mathcal{O}(\Delta v_i^3) dE \right). \end{aligned} \quad (4.15)$$

Written in terms that are linear in Δv_{xc}^\pm the moment M is given as follows

$$M = \chi_{AF}^0 \left(\frac{IM}{2\mu_B} + H \right). \quad (4.16)$$

The spin susceptibility χ_{AF}^0 is defined as

$$\begin{aligned} \chi_{AF}^0 &= \frac{2\mu_B}{\pi} \Im \int^{E_F(M)} \left[\sum_{\text{even } i} G_{0i}^0(E) G_{i0}^0(E) - \sum_{\text{odd } i} G_{0i}^0(E) G_{i0}^0(E) \right] \\ &= \frac{2\mu_B}{\pi} \Im \int^{E_F(M)} \left[\sum_{\text{all } i} G_{0i}^0(E) G_{i0}^0(E) - 2 \sum_{\text{odd } i} G_{0i}^0(E) G_{i0}^0(E) \right] \\ &= 2\mu_B [-n_0(E_F) + a(E_F)] \\ &= 2\mu_B [a(E_F) - n_0(E_F)]. \end{aligned} \quad (4.17)$$

Solving Eq. (4.16) with respect to M yields

$$M = \chi_{AF} H = \left(1 - \frac{I\chi_{AF}^0}{2\mu_B} \right)^{-1} \chi_{AF}^0 H = S_{AF} \chi_{AF}^0 H, \quad (4.18)$$

where the spin susceptibility χ_{AF} is enhanced by a factor S_{AF} . The Stoner criterion of antiferromagnetism results from Eq. (4.18)

$$\frac{I\chi_{AF}^0}{2\mu_B} > 1, \quad (4.19)$$

which can be rewritten as

$$I [a(E_F) - n^0(E_F)] > 1 \quad (4.20)$$

by using the expression in Eq. (4.17). In conclusion, it can be stated that a small non-magnetic DOS $n^0(E_F)$ at the Fermi energy favors antiferromagnetism even if the coefficient $a(E_F)$ is unknown.

In order to illustrate the Stoner criterion, it is useful to consider a simple DOS exhibiting for example a rectangular form:

$$n^0(E_F) = \begin{cases} W^{-1} & -\frac{W}{2} < E < \frac{W}{2} \\ 0 & |E| > \frac{W}{2}, \end{cases} \quad (4.21)$$

where the bandwidth is given by the parameter W . In this case, $a(E_F)$ may be evaluated approximately from the Green function $G^0(E)$. The main contribution arises

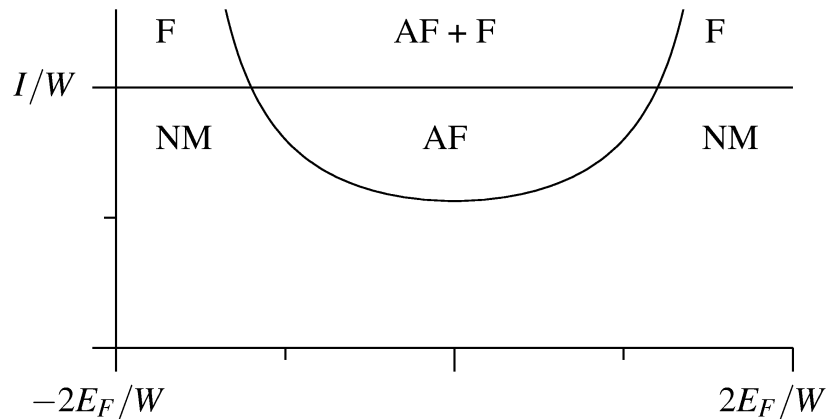


Figure 4.2: Phase diagram for the Stoner criterion of antiferromagnetism using the example of a rectangular model DOS. The area denoted with NM represents the stability region for the nonmagnetic state, whereas AF and F indicate the stability regions for the antiferromagnetic and the ferromagnetic state, respectively. Figure is taken from [50].

from the atom $i = 0$ while the contributions for atoms beyond nearest neighbors, that means $i \neq 0$, are neglected due to the decay with increasing distance. Then, the stability criterion Eq. (4.20) takes this form

$$\frac{I}{W} = \left[2 \int_{-1}^{E_F/W} \ln \left| \frac{x-1}{x+1} \right| dx - 1 \right]^{-1} \quad (4.22)$$

with x as a substitute for $2E/W$. Plotting the left-hand side of Eq. (4.22) (straight line) and the right-hand side as a function $f(2E_F/W)$ (bended curve) in a phase diagram (cf. Fig. 4.2), it turns out that antiferromagnetism is favorable in the case of a half filled band ($E_F \approx 0$).

4.2 Heisenberg Model

In the previous section the possibility of a system to form a ferromagnetic or antiferromagnetic ground state has been discussed in terms of the non-magnetic DOS. However, the ferromagnetic and antiferromagnetic configurations represent only an infinitesimal part of the magnetic phase space. The major part consists of non-collinear magnetic configurations with arbitrarily aligned moments. This happens for instance, when all exchange interactions between neighboring atoms cannot be satisfied at the same time. The resulting frustrated exchange can give rise to a multitude of possible spin structures. A model that discusses the tendency of a system towards non-collinear magnetism and has been used almost exclusively in the last few years is the Heisenberg model. It can be derived from the Hubbard model via

perturbation theory by expanding it into a spin model and replacing the spin operators by classical spin vectors [51]. The Hubbard model is the simplest model to describe the short-range repulsive interactions between fermions in a lattice. There are two contributions to the Hamilton operator $\mathcal{H} = \hat{T} + \hat{U}$: the kinetic energy \hat{T} of electrons hopping between atoms of adjacent lattice sites, and the Coulomb energy \hat{U} arising from the on-site repulsion of the charges on the electrons. In second order the perturbative treatment results in the Hamilton operator of the classical Heisenberg model:

$$\mathcal{H} = - \sum_{i,j} J_{ij} \mathbf{S}_i \cdot \mathbf{S}_j \quad (4.23)$$

where the sum is over all magnetic atoms of the system. The J_{ij} represent the Heisenberg exchange parameters of the magnetic moments (referred to as spins) \mathbf{S}_i and \mathbf{S}_j that are located at the lattices sites i and j . In general the \mathbf{S}_i and \mathbf{S}_j are operators, which are usually treated as classical vectors assuming that

$$\mathbf{S}_i^2 = S^2, \quad \text{for all } i. \quad (4.24)$$

That means all the spins have the same magnitude S . The Heisenberg model is especially suitable for the description of the isotropic exchange interaction between highly localized spins that are typically found in systems such as metal oxides. In these systems J_{ij} can be restricted to the ferromagnetic ($J_1 > 0$) and the antiferromagnetic ($J_1 < 0$) nearest-neighbor interaction, since the pair interaction between nearest neighbors dominates over the rest of the farther distant pairs. For itinerant systems the exchange constants J_{ij} follow the characteristic oscillatory decaying asymptotic behavior of the Ruderman-Kittel-Kasuya-Yoshida (RKKY) interaction [52], which describes the coupling of localized magnetic moments by means of the indirect exchange via the conducting electrons. However, in itinerant magnets it is not always the case that the Heisenberg model reproduces the correct magnetic ground state due to its restriction as a localized model. Therefore, it is necessary to consider the terms of higher order resulting from the perturbation of the Hubbard model. While the second order perturbation treatment reproduces the Heisenberg model, the next nonzero term, which is of fourth order, yields to two additional terms: the biquadratic interaction

$$\mathcal{H}_{biq} = - \sum_{ij} B_{ij} (\mathbf{S}_i \cdot \mathbf{S}_j)^2 \quad (4.25)$$

arising from the hopping of electrons over the two lattice sites $i \rightarrow j \rightarrow i \rightarrow j \rightarrow i$ and the four-spin interaction

$$\mathcal{H}_{4\text{-spin}} = - \sum_{ijkl} K_{ijkl} [(\mathbf{S}_i \cdot \mathbf{S}_j)(\mathbf{S}_k \cdot \mathbf{S}_l) + (\mathbf{S}_i \cdot \mathbf{S}_l)(\mathbf{S}_k \cdot \mathbf{S}_j) - (\mathbf{S}_i \cdot \mathbf{S}_k)(\mathbf{S}_j \cdot \mathbf{S}_l)] \quad (4.26)$$

resulting from the hopping over four lattice sites $i \rightarrow j \rightarrow k \rightarrow l \rightarrow i$.

The parameter J_{ij} , B_{ij} and K_{ijkl} depend on the electronic structure, and it is known [53] that in thin films $B_1 S^4$ and $K_1 S^4$ are typically one order of magnitude smaller than $J_1 S^2$. The energetic degeneracy between magnetic states within the Heisenberg model for two spins may be lifted if the higher-order spin interactions are taken into account.

4.2.1 The classical Heisenberg model on a Bravais lattice

The periodicity of a lattice plays an important role in the computation of the physical properties of a magnetic crystal. Hence, a great advantage is the expression of quantities in terms of their Fourier components. The discrete Fourier components of the spins at the N lattice sites are given as

$$\mathbf{S}_j = \sum_{\mathbf{q}} \mathbf{S}_{\mathbf{q}} e^{i\mathbf{q}\mathbf{R}_j}, \quad (4.27)$$

and their back-transform as

$$\mathbf{S}_{\mathbf{q}} = \frac{1}{N} \sum_j \mathbf{S}_j e^{-i\mathbf{q}\mathbf{R}_j}, \quad (4.28)$$

where \mathbf{q} is the reciprocal lattice vector and \mathbf{R}_j represents the coordinates of the lattice site j in the real space. The spins' Fourier components obviously meet the condition $\mathbf{S}_{\mathbf{q}} = \mathbf{S}_{-\mathbf{q}}^*$. Inserting them into Eq. (4.23) and exploiting that $\sum_j e^{i(\mathbf{q}+\mathbf{q}')\mathbf{R}_j} = N\delta_{\mathbf{q},-\mathbf{q}'}$ for all lattice sites, results in

$$\begin{aligned} \mathcal{H} &= - \sum_{ij} J_{ij} \sum_{\mathbf{q}, \mathbf{q}'} \mathbf{S}_{\mathbf{q}} \cdot \mathbf{S}_{\mathbf{q}'} e^{i\mathbf{q}\mathbf{R}_i} e^{i\mathbf{q}'\mathbf{R}_j} \\ &= - \sum_{ij} J_{ij} \sum_{\mathbf{q}, \mathbf{q}'} \mathbf{S}_{\mathbf{q}} \cdot \mathbf{S}_{\mathbf{q}'} e^{i(\mathbf{q}+\mathbf{q}')\mathbf{R}_i} e^{i\mathbf{q}'(\mathbf{R}_j - \mathbf{R}_i)} \\ &= -N \sum_{\mathbf{q}} \mathbf{S}_{\mathbf{q}} \cdot \mathbf{S}_{-\mathbf{q}} \left(\sum_{\delta} J_{0\delta} e^{-i\mathbf{q}\mathbf{R}_{\delta}} \right). \end{aligned} \quad (4.29)$$

Here, \mathbf{R}_{δ} is defined as $\mathbf{R}_{\delta} = \mathbf{R}_i - \mathbf{R}_j$. Since the exchange interaction is symmetric, it is necessary that $J_{ij} = J_{ji}$, and as a consequence of the translational symmetry

$J_{0\delta} = J_{0-\delta}$. The Fourier transform of the exchange parameters in Eq. (4.29) are then specified as

$$J(\mathbf{q}) = \sum_{\delta} J_{0\delta} e^{-i\mathbf{q}\mathbf{R}_{\delta}} = J(-\mathbf{q}) = J(\mathbf{q})^*. \quad (4.30)$$

Rewriting the Hamilton operator in Eq. (4.23) in terms of $J(\mathbf{q})$ and using the expression in Eq. (4.28) gives

$$\mathcal{H} = -N \sum_{\mathbf{q}} J(\mathbf{q}) \mathbf{S}_{\mathbf{q}} \cdot \mathbf{S}_{-\mathbf{q}}, \quad (4.31)$$

where N denotes the number of lattice sites in the crystal. The energy defined by Eq. (4.31) can be minimized under the condition that the magnitude of the spins is kept constant, i.e., $\mathbf{S}_i^2 = S^2$. This leads to a system of N independent equations. The lowest energy

$$E = -NS^2 J(\mathbf{Q}) \quad (4.32)$$

is found for the spin state, which is described by the wave vector \mathbf{Q} . It is characterized by the following equation

$$\mathbf{S}_n = S (\cos(\mathbf{Q} \cdot \mathbf{R}_n), \sin(\mathbf{Q} \cdot \mathbf{R}_n), 0). \quad (4.33)$$

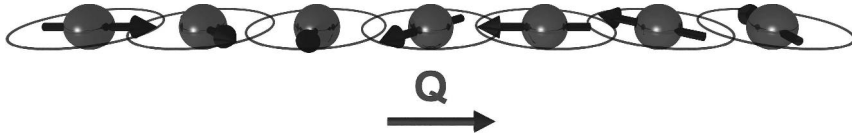


Figure 4.3: Example of a flat spin spiral. The spin-spiral vector \mathbf{Q} defines the propagation direction within the crystal lattice.

In Fig. 4.3 the spin structure defined by Eq. (4.33) is illustrated, which is a so-called *flat spin spiral*. These and their linear combinations represent the fundamental solutions of the classical Heisenberg model on a periodic lattice. Since the SOC is neglected in the Hamiltonian, lattice and spin coordinates remain decoupled, and therefore, the rotational axis may coincide, e.g, with the z -axis. Thus, the spins rotate around the z -axis (and within the xy -plane) while proceeding from lattice site to lattice site in the direction given by \mathbf{Q} . The cycloidal spin spiral shown in Fig. 4.3 is a special case since the angle between rotational axis and the magnetic moment is of 90° .

4.3 Simulation of Spin-Polarized Scanning Tunneling Microscopy Images

The construction of the first scanning tunneling microscope (STM) by Binnig, Rohrer, Gerber and Weibel in 1982 [54] marked the beginning of a new era in surface science, since it allows for the imaging of surfaces down to the atomic scale in real space. Its principle is based on the quantum-mechanical effect of tunneling, where a particle with a certain kinetic energy E_{kin} , e.g., an electron penetrates a barrier with a potential $v > E_{kin}$, which it would classically never get past (cf. Fig. 4.4). While propagating through the tunneling barrier, the wave functions $\psi(z)$ of the

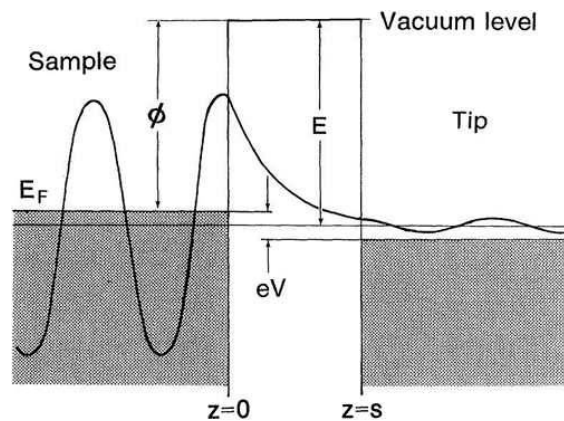


Figure 4.4: The one-dimensional tunneling effect in a metal-vacuum-metal tunneling junction. The z -axis is perpendicular to the surface. The sample and tip are modeled as semi-infinite pieces of metal with equal work function ϕ and the temperature is assumed to be $T = 0$ K. The decay of the amplitude of the sample wave function in the vacuum barrier is sketched. Figure taken from reference [55].

electrons decay according to

$$\psi(z) \propto e^{-\kappa z} \quad \text{with} \quad \kappa = \sqrt{2m|E|/\hbar^2}. \quad (4.34)$$

κ denotes the decay constant, m is the electron mass and E the energy of the electronic state that participates in the tunneling process. In the simplest case, E is equal to the vacuum level. For states at the Fermi energy it is equal to the work function ($E = E_F \propto \phi = 4 - 5\text{eV}$)¹, i.e, the minimum energy needed to remove an electron from the solid to a point at infinity. It determines the height of the tunneling barrier. Then, the numerical value of the decaying constant results in

$$\kappa = 0.51\sqrt{\phi(\text{eV})}\text{\AA}^{-1} \quad (4.35)$$

¹Most metals reveal typical values of 4 to 5 eV.

with eV being the unit of the wave function and \AA^{-1} being the unit of the decay constant.

The knowledge of the wave function allows for the calculation of the probability to find an electron of the sample at the location of the tip ($z = s$):

$$w = |\psi(s)|^2 = |\psi(0)|^2 e^{-2\kappa s}. \quad (4.36)$$

By decreasing the distance between tip and sample to the order of a few \AA , the wave functions overlap and electrons can tunnel from the sample to the tip and *vice versa*. The average net tunneling current is zero. Therefore, a small bias voltage can be applied that raises the Fermi niveau of the sample with respect to that of the tip. In the case of a positive bias the electrons can tunnel through the vacuum from the tip to the sample. A negative bias voltage leads to the reversal of the tunneling direction. Thus, one can conclude that only those electronic states contribute to the tunneling current that are available within a small energy range close to the Fermi level. By summing over all electronic states μ of the sample this assumption leads to

$$I(s, V) \propto e^{-2\kappa s} \sum_{E_\mu = E_F - eV}^{E_F} |\psi(0)|^2. \quad (4.37)$$

Equation (4.37) reveals the origin of the high resolution in STM experiments: if one sets the work function in Eq. (4.35) to $\phi = 4$ eV, the decay constant is about $\kappa \approx 1 \text{\AA}^{-1}$ and the current in Eq. (4.37) decays with $e^2 \approx 7.4$ per \AA , so that even a small change in height causes an increase in the tunneling current of almost one order of magnitude. This sensitivity allows for a vertical resolution of the order of 0.01\AA and can be exploited in the *constant-current mode*, i.e., while the tunneling current is kept constant by adjusting the vertical position of the STM tip, the lateral (\mathbf{r}_{\parallel}) scan of the tip over the sample surface generates a topographic STM image.

Typically, the STM probe tip is fabricated from metal wires such as W, Pt-Ir alloys or Au. By coating such non-magnetic STM tips with a magnetic material, e.g., Fe, Gd or Cr [27, 56, 57, 58], or producing them from magnetic bulk material [59], an additional contribution to the tunneling current can be measured that originates from the imbalance of majority and minority electrons close to the Fermi level. It depends on the angle between the local magnetization direction of the sample and the tip, also known as TMR effect [60]. The spin-dependent tunneling allows for the investigation of magnetic structures down to the atomic scale. Since the present thesis focuses on nanoscale magnetic order, an expression for the spin-dependent tunneling current will be derived based on the spin-polarized Tersoff-Hamann model [61] and the independent orbital approximation [55, 62].

4.3.1 The Tersoff-Hamann Approximation

In order to describe the tunneling current, several theoretical models have been developed – most of them follow the tunneling-Hamiltonian formalism that has been established by J. Bardeen [63]. Within this approach, which is derived via the time-dependent perturbation theory, the tunneling current I is given to first order. It is obtained from the eigenstates of the unperturbed subsystems, i.e., the sample (S) and the STM tip (T). In the non-spin-polarized case it is defined as

$$I(V, \mathbf{R}_T) = \frac{2\pi e}{\hbar} \sum_{\mu\nu} [f(E_\mu^S - E_F^S) - f(E_\nu^T - E_F^T)] |M_{\mu\nu}|^2 \delta(E_\mu^T - E_\nu^S - eV), \quad (4.38)$$

where I is a function of the sample bias voltage V and the position of the tip \mathbf{R}_T . The occupation is included by means of the Fermi-Dirac function $f(E - E_F) = \{1 + e^{(E - E_F)/k_B T}\}^{-1}$. $E_F^{(T/S)}$ is the Fermi energy of the tip/sample and $M_{\mu\nu}$ is the tunneling matrix element between the states Ψ_μ^S of the sample and Ψ_ν^T of the tip. Note that Ψ_μ and Ψ_ν are nonorthogonal eigenstates of different Hamiltonians. Finally, $E_{\mu/\nu}^{(S/T)}$ represents the energy of state $\Psi_{\mu/\nu}^{(S/T)}$ in the absence of tunneling. The conservation of energy during the tunneling process, i.e., elastic tunneling is guaranteed by the δ function. The major issue in handling Eq. (4.38) is the evaluation of the matrix elements

$$M_{\mu\nu}(\mathbf{R}_T) = \langle \Psi_\nu^T | U_T | \Psi_\mu^S \rangle = \int_{V_T} dV \Psi_\nu^T U_T \Psi_\mu^S \quad (4.39)$$

for the potential U_T of the tip. According to Bardeen's theory [63] the matrix elements can be transformed into a surface integral over any surface lying entirely within the vacuum barrier by means of the Green's theorem:

$$M_{\mu\nu} = -\frac{\hbar^2}{2m} \int d\mathbf{S} (\Psi_\nu^* \nabla \Psi_\mu - \Psi_\mu \nabla \Psi_\nu^*). \quad (4.40)$$

The expression in parentheses in Eq. (4.40) is also known as the current operator $\mathbf{j}_{\mu\nu}$. The calculation of the matrix elements $M_{\mu\nu}$ in (4.40) requires explicit expressions for the wave functions Ψ_μ and Ψ_ν of the sample and the tip. Since the atomic structure of the tip is generally unknown, Tersoff and Hamann [64, 65] made several assumptions in order to simplify the modeling of the tip: According to Eq. (4.37) the tunneling current decays exponentially with the tip-sample distance s . Therefore, it can be assumed that only the outermost tip apex atom contributes significantly to the tunneling current and the matrix elements can be calculated by approximating

the wave function of the tip as s wave, i.e.,

$$\Psi_\nu^T = C \frac{e^{-\kappa\rho}}{\kappa\rho}, \quad (4.41)$$

where the normalization coefficient C fits the wave functions in the vacuum continuously to those in the tip potential. $\rho = |\mathbf{r} - \mathbf{R}_T|$ is the radial distance from the center \mathbf{R}_T of the tip apex atom. Then, the matrix elements result in

$$M_{\nu\mu}(\mathbf{R}_T) = -\frac{2\pi C\hbar^2}{\kappa m} \Psi_\mu^S(\mathbf{R}_T). \quad (4.42)$$

Hence, the approximation of the tip in the vacuum as s wave leads to a direct proportionality of the matrix elements to the value of the sample wave functions at the position of the tip, \mathbf{R}_T . Inserting the matrix elements into Eq. (4.38) and considering the limit $k_B T \rightarrow 0$ the tunneling current is given as

$$I(\mathbf{R}_T, V) = \frac{16\pi^3 C^2 \hbar^3 e}{\kappa^2 m^2} V n^T \int_E^{E+eV} d\epsilon n^S(\mathbf{R}_T, \epsilon). \quad (4.43)$$

Here, the DOS of the tip has been assumed to be constant, since it is basically destructured with respect to that of the sample. In the limit of small bias voltages the current reduces further to

$$I(\mathbf{R}_T, V) = \frac{16\pi^3 C^2 \hbar^3 e}{\kappa^2 m^2} V n^T n^S(\mathbf{R}_T, E_F + eV). \quad (4.44)$$

Deriving Eq. (4.44) with respect to the bias voltage V defines the differential conductivity

$$\frac{dI}{dV} = \frac{16\pi^3 C^2 \hbar^3 e^2}{\kappa^2 m^2} n^T n^S(\mathbf{R}_T, E_F + eV). \quad (4.45)$$

It is directly proportional to the local DOS of the sample $n^S(\mathbf{R}_T, E_F + eV)$ at the position of the tip \mathbf{R}_T at the energy $E_F + eV$. It is measured in the *spectroscopy mode* of the STM. By varying the bias voltage eV the local DOS of the sample can be investigated. This approximation has been likewise successfully applied to semiconductor [66] and transition-metal surfaces [67, 68].

As mentioned above, STM tips are usually fabricated from W or Pt-Ir alloys. These elements belong to the class of transition metals that exhibit some d -like states close to the Fermi level. Therefore, it is convenient to consider tip states with $l \neq 0$ as proposed by Chen [55, 69, 70]. He established the *derivative rule* that relates the matrix element to the orbital character of the tip wave function. For instance, if the tip wave function is approximated by a p_z orbital, the resulting

matrix element is given as

$$M_{\mu,p_z}(\mathbf{R}_T) = -\frac{2\pi C_{p_z} \hbar^2}{\kappa m} \frac{\partial}{\partial z} \Psi_{\mu}^S(\mathbf{R}_T), \quad (4.46)$$

where C_{p_z} is the normalization constant². The matrix element reveals a proportionality to the spatial derivative of the tip wave function at the position \mathbf{R}_T . In general, it can be derived by rewriting the angular dependence of the tip wave function in terms of x, y, z and replace them by the derivative, i.e.,

$$x \rightarrow \frac{\partial}{\partial x}, \quad y \rightarrow \frac{\partial}{\partial y}, \quad z \rightarrow \frac{\partial}{\partial z}. \quad (4.47)$$

By means of the matrix elements obtained for ($m = 0$) orbitals Chen demonstrated for close packed metal surfaces [71] that instead of following the contour of the local DOS at the Fermi level, the tip rather traces the contour of a fictitious surface that is determined by the derivatives of the sample surface wave functions. This behavior results in a stronger atomic corrugation than that of the charge density. Orbitals with $m \neq 0$ such as p_x or p_y , on the other hand, exhibit a particular charge distribution with a node at the center of the tip. While scanning a surface that shows maxima in the local DOS above the atomic positions the overlap of the tip and the sample wave functions is minimized on top of a surface atom and maximized above a hollow site. Thus, the topographic STM image shows anti-corrugation, i.e., atoms are detected as depressions and hollow sites as protrusions.

4.3.2 The Spin-Polarized Tersoff Hamann Theory

The extension to the spin-polarized case [61] is carried out by replacing the wave function Ψ_{μ}^T of the tip by two component spinors with respect to the magnetization axis $\hat{\mathbf{e}}_M^T$ of the tip:

$$\Psi_{\nu}^T = \begin{pmatrix} \psi_{\nu\uparrow}^T \\ 0 \end{pmatrix} \quad \text{or} \quad \Psi_{\nu}^T = \begin{pmatrix} 0 \\ \psi_{\nu\downarrow}^T \end{pmatrix}, \quad (4.48)$$

where \uparrow (\downarrow) denotes the electrons of majority (minority) spin. Since the tip is assumed to reveal collinear magnetism, i.e., ferromagnetic or antiferromagnetic order, it is possible to express the tip states in terms of pure spin up and pure spin down states. The magnetic structure in the sample, on the other, hand may exhibit a variety of different possible spin arrangements, such as non-collinear magnetic order or spin-density waves, leading to a mixing of the spin up and spin down states. Furthermore, a coupling of both spin components can be expected even for a collinear magnetic sample if the quantization axes of the tip and the sample are not parallel

²The expression in Eq. (4.46) is derived analogously to the Tersoff Hamann model. For details refer to references [55, 69, 70].

aligned. Thus, the spinor of the electronic states of the sample reads

$$\Psi_\mu^S = \begin{pmatrix} \psi_{\mu\uparrow}^S \\ \psi_{\mu\downarrow}^S \end{pmatrix}. \quad (4.49)$$

Analogously to the non-spin-polarized case, where scattering processes are neglected, i.e., elastic single-particle tunneling, the extension to the spin-polarized current assumes a spin conservation during the tunneling process. Thus, the matrix elements can be expressed as

$$M_{\nu\mu}^\sigma(\mathbf{R}_T) = \langle \Psi_\nu^T | \mathbf{U}_T | \Psi_\mu^S \rangle = \langle \psi_{\nu\sigma}^T | U_{T\sigma\sigma} | \psi_{\mu\sigma}^S \rangle, \quad (4.50)$$

where the matrix of the tip potential \mathbf{U}_T is diagonal in spin space. $\sigma = \uparrow, \downarrow$ denotes the spin index of the tip state that is involved in the tunneling. Thus, tip wave functions with higher quantum numbers, $l \neq 0$, have been neglected. For both, the spin-up and spin-down s states, the decay constant κ is assumed to be the same. Also the same normalization coefficient will be applied. Assuming that the spin-up, n_T^\uparrow , and the spin-down, n_T^\downarrow DOS of the tip are constant in energy, they have to be different in size in order to account for the magnetization of the tip, $\mathbf{m}_T = (n_T^\uparrow - n_T^\downarrow) \hat{\mathbf{e}}_M^T$. Insertion of $M_{\nu\mu}^\sigma$ in Eq. (4.38) leads to

$$\begin{aligned} I(\mathbf{R}_T, V, \theta) &= \frac{8\pi^3 C^2 \hbar^3 e}{\kappa^2 m^2} \int d\epsilon g_V(\epsilon) \sum_\mu \delta(E_\mu - \epsilon) \\ &\times \left[n_T^\uparrow |\psi_{\mu\uparrow}^S(\mathbf{R}_T)|^2 + n_T^\downarrow |\psi_{\mu\downarrow}^S(\mathbf{R}_T)|^2 \right] \end{aligned} \quad (4.51)$$

with $g_V(\epsilon) = f(\epsilon - E_F) - f(\epsilon + eV - E_F)$. The angle enclosed by the magnetization direction of the tip and the sample at the position \mathbf{R}_T is denoted as $\theta(\mathbf{R}_T, V)$. The expression in (4.51) is maximal for a parallel and minimal for an antiparallel alignment of the tip and the sample magnetization ($\theta = 0^\circ$ and $\theta = 180^\circ$).

For general magnetic structures the spin-polarized tunneling current I can be decomposed into a nonmagnetic and a magnetic part:

$$\begin{aligned} I(\mathbf{R}_T, V, \theta) &= I_0(\mathbf{R}_T, V) + I_P(\mathbf{R}_T, V, \theta) \\ &= \frac{4\pi^3 C^2 \hbar^3 e}{\kappa^2 m^2} [n_T \tilde{n}_S(\mathbf{R}_T, V) + \mathbf{m}_T \tilde{\mathbf{m}}_S(\mathbf{R}_T, V)]. \end{aligned} \quad (4.52)$$

Here, $\tilde{n}_S(\mathbf{R}_T, V) = \tilde{n}_S^\uparrow(\mathbf{R}_T, V) + \tilde{n}_S^\downarrow(\mathbf{R}_T, V)$ represents the energy-integrated local DOS of the sample and $\tilde{\mathbf{m}}_S(\mathbf{R}_T, V)$ is the corresponding vector of the energy-integrated local magnetization DOS $\tilde{n}_S(\mathbf{R}_T, V) = \tilde{n}_S^\uparrow(\mathbf{R}_T, V) + \tilde{n}_S^\downarrow(\mathbf{R}_T, V)$ of the

sample³. It is given as

$$\mathbf{m}_S(\mathbf{R}_T, \epsilon) = \sum_{\mu} \delta(\epsilon_{\mu} - \epsilon) \Psi_{\mu}^{S\dagger}(\mathbf{R}_T) \boldsymbol{\sigma} \Psi_{\mu}^S(\mathbf{R}_T) \quad (4.53)$$

$$\tilde{\mathbf{m}}_S(\mathbf{R}_T, V) = \int (f(\epsilon - \epsilon_F) - f(\epsilon + eV - \epsilon_F)) \mathbf{m}_S(\mathbf{R}_T, \epsilon) d\epsilon. \quad (4.54)$$

Here, $\boldsymbol{\sigma}$ is the known Pauli's spin matrix. $n_S(\mathbf{R}_T, V)$ and $\tilde{n}_S(\mathbf{R}_T, V)$ are defined analogously by replacing σ by the unity matrix. Apparently, the spin-polarized contribution of the tunneling current (second term in Eq. (4.52)) depends on the projection of $\tilde{\mathbf{m}}_S$ onto the tip magnetization \mathbf{m}_T and thus scales with the cosine of the angle between the magnetization directions of the tip and the sample. In the case of a nonmagnetic sample or an non-spin-polarized tip, the second term in Eq. (4.52) vanishes and the model resembles the original Tersoff-Hamann model.

Based on the results derived above the differential conductivity that is measured in the spectroscopy mode of a spin-polarized STM (SP-STM) is obtained as

$$\frac{dI}{dV}(\mathbf{R}_T, V) \propto n_T n_S(\mathbf{R}_T, E_F + eV) + \mathbf{m}_T \mathbf{m}_S(\mathbf{R}_T, E_F + eV). \quad (4.55)$$

In contrast to the spin-polarized tunneling current in Eq. (4.52) it is directly proportional to the local DOS, n_S , and the magnetization DOS, \mathbf{m}_S , of the sample at the energy $E_F + eV$.

It is possible to decouple the spin-polarized and the non-spin-polarized tunneling current via the constant current image mode of the spin-polarized STM [61]. The constant current image results from the vertical adjustment $\Delta z(\mathbf{r}_{\parallel}, V, \theta)$ of the tip in order to keep the tunneling current constant. For a sample surface with two-dimensional translational symmetry the change in both, the non-spin-polarized and the spin-polarized part of the current I , can be written in terms of a two-dimensional Fourier expansion with respect to the reciprocal surface lattice vectors \mathbf{G}_{\parallel}^n :

$$\Delta I(\mathbf{r}_{\parallel}, z, V, \theta) = \sum_{n \neq 0} \Delta I_{\mathbf{G}_{\parallel}^n}(z, V, \theta) e^{i\mathbf{G}_{\parallel}^n \mathbf{r}_{\parallel}}. \quad (4.56)$$

Here, the $\Delta I_{\mathbf{G}_{\parallel}^n}(\mathbf{r}_{\parallel}, z, V, \theta)$ are the tip-sample distance (z) dependent expansion coefficients. They decay exponentially with increasing length of the reciprocal lattice vectors \mathbf{G}_{\parallel}^n [67]. Therefore, the STM image is primarily dominated by the smallest nonvanishing reciprocal lattice vector \mathbf{G}_{\parallel}^1 :

$$\Delta I(\mathbf{r}_{\parallel}, z, V, \theta) \propto e^{-2z \sqrt{2m/\hbar^2 |E_F + eV| + (\mathbf{G}_{\parallel}^1/2)^2}}. \quad (4.57)$$

³ n_T as well as \mathbf{m}_T refer to the densities of states of the tip.

In comparison to a nonmagnetic state any magnetic superstructure lowers the translational symmetry and leads to a larger periodicity in the real space. Accordingly, the corresponding reciprocal lattice vector becomes smaller with respect to that of the chemical unit cell. Due to the filtering effect of the vacuum, waves with the smallest lattice vector \mathbf{G}_{\parallel}^n extend furthest into the vacuum and thus contribute most to the STM image. Therefore, a topographic spin-polarized STM image obtained in the constant-current mode reflects rather the magnetic superstructure than the atomic structure. This has been first demonstrated for the two-dimensional antiferromagnetism at surfaces [72].

4.3.3 Independent-Orbital Approximation

The expression for the spin-polarized tunneling current in Eq. (4.52) is derived for general magnetic structures. However, since it requires the exact information about the electronic structure of the sample in the vacuum, the simulation of complex magnetic structures is difficult within the spin-polarized Tersoff-Hamann model. In the following, a simple method will be introduced that allows for the calculation of spin-polarized STM images of an arbitrary complex magnetic structure without the accurate knowledge of the electronic structure [62]. It is based on the atomic superposition as presented in [55, 64, 65, 73].

In the limit of low bias voltage the integrated local DOS of the sample can be replaced by the local DOS at the Fermi energy resulting in

$$n^s(\mathbf{R}_T, E_F) = \sum_{\alpha} (n_{\alpha}^{\uparrow} + n_{\alpha}^{\downarrow}) \exp(-2\kappa |\mathbf{R}_T - \mathbf{R}_{\alpha}|), \quad (4.58)$$

where the atomic superposition is expressed as the sum over all surface atoms α at the position \mathbf{R}_{α} . It is assumed that the local DOS from each surface atom contributes to the tunneling current of the STM tip at the position \mathbf{R}_T with an exponential decay. κ denotes the decay constant as given in Eq. (4.34) with $\kappa = \sqrt{2m\phi/\hbar^2}$ using the work function ϕ . n_{α}^{\uparrow} and n_{α}^{\downarrow} represent the DOS of the surface atom α at the Fermi level in the majority and minority spin channel, respectively.

The local magnetization DOS is given as

$$\hat{\mathbf{e}}_T \mathbf{m}(\mathbf{R}_T, E_F) = \sum_{\alpha} (n_{\alpha}^{\uparrow} - n_{\alpha}^{\downarrow}) \cos \theta_{\alpha} \exp(-2\kappa |\mathbf{R}_T - \mathbf{R}_{\alpha}|), \quad (4.59)$$

where the angle θ_{α} specifies the rotation of the local magnetization axis at the atom α with respect to the tip magnetization direction $\hat{\mathbf{e}}_T$.

Under the assumption that the electronic structure of all surface atoms α is the

same, the spin-polarized tunneling current in the simple model can be expressed as

$$I(\mathbf{R}_T) \propto \sum_{\alpha} [1 + P_T P_S \cos \theta_{\alpha}] \exp(-2\kappa |\mathbf{R}_T - \mathbf{R}_{\alpha}|). \quad (4.60)$$

Here, the spin-polarization of the tip and the sample is given by

$$P_T = \frac{n_T^{\uparrow} - n_T^{\downarrow}}{n_T^{\uparrow} + n_T^{\downarrow}} \quad \text{and} \quad P_S = \frac{n_S^{\uparrow} - n_S^{\downarrow}}{n_S^{\uparrow} + n_S^{\downarrow}}, \quad \text{respectively.} \quad (4.61)$$

The product of the spin-polarization of the tip and the sample, $P_{\text{eff}} = P_T P_S$, is the effective spin-polarization of the system, which remains as the only unknown parameter in the approach presented above.

Finally, the simple model of the spin-polarized tunneling current allows for a direct comparison of constant-current and constant-height images as well as quantitative values of the corrugation amplitude. The corrugation amplitude, i.e., the difference Δz in the tip height as a function of the lateral tip position \mathbf{r}_{\parallel} is given as

$$\Delta z(\mathbf{r}_{\parallel}) = -\frac{\Delta I(\mathbf{r}_{\parallel}, z_0)}{dI_0/dz(z_0)} = \frac{\Delta I(\mathbf{r}_{\parallel}, z_0)}{2\kappa I_0(z_0)}. \quad (4.62)$$

Here, z_0 denotes an average tip-sample distance, where the tunneling current can be split into a lateral constant part $I_0(z_0)$ and a small variation $\Delta I(\mathbf{r}_{\parallel}, z_0)$ leading to the expression above.

5 Non-collinear Magnetism within DFT

Collinear magnetic configurations, i.e., the parallel and antiparallel alignment of neighboring magnetic moments, represent only a small number of possible magnetic arrangements. The major part of spin structures reveals an arbitrary alignment of neighboring magnetic moments, i.e., non-collinear magnetism. Within the DFT it is possible to go beyond collinear magnetism by adjusting the representation of the density in order to describe non-collinear magnetic orders. Therefore, the electron and magnetization densities n and \mathbf{m} are replaced by the Hermitian 2×2 density matrix $\boldsymbol{\rho}$. Both concepts are completely equivalent.

The density matrix is defined as

$$\boldsymbol{\rho} = \frac{1}{2}n \cdot \mathbf{I}_2 + \boldsymbol{\sigma} \cdot \mathbf{m} = \frac{1}{2} \begin{pmatrix} n + m_z & m_x - im_y \\ m_x + im_y & n - m_z \end{pmatrix}, \quad (5.1)$$

where \mathbf{I}_2 is the unity matrix and $\boldsymbol{\sigma}$ is the vector of the Pauli spin matrices. Similarly, the Hermitian 2×2 potential matrix is defined as

$$\mathbf{v} = v \cdot \mathbf{I}_2 + \mu_B \boldsymbol{\sigma} \cdot \mathbf{B} = \begin{pmatrix} v + \mu_B B_z & \mu_B (B_x - iB_y) \\ \mu_B (B_x + iB_y) & v - \mu_B B_z \end{pmatrix}. \quad (5.2)$$

The components of the density matrix are given in terms of the solutions of the Kohn-Sham equation:

$$\rho_{\alpha\beta} = \sum_{\nu=1}^N \psi_{\nu\alpha}^* \psi_{\nu\beta}. \quad (5.3)$$

Including the potential matrix (Eq. (5.2)) the Kohn-Sham equations (Eq. (2.20)) take the following form:

$$\left(-\frac{\hbar^2}{2m} \nabla^2 \mathbf{I}_2 + \mathbf{v} \right) \boldsymbol{\psi}_\nu = \epsilon_\nu \boldsymbol{\psi}_\nu. \quad (5.4)$$

The kinetic energy part of the Hamiltonian is diagonal in both spin directions. However, the off-diagonal part of the potential matrix, i.e., $v_{12} = \mu_B (B_x - iB_y)$ and $v_{21} = \mu_B (B_x + iB_y)$, couples the two components $\boldsymbol{\psi}_\nu$ of the Pauli spinor. In the collinear case this behavior is unproblematic, since the quantization axis of the spin can be chosen parallel to the z -axis without loss of generality. Thus, B_x and B_y become zero and the off-diagonal elements v_{12} and v_{21} vanish. Both spin

directions decouple and Eq. (5.4) can be solved for every direction separately, i.e., treating $v^\uparrow = \mu_B(B_x + iB_y)$ and $v^\downarrow = \mu_B(B_x - iB_y)$ like the nonmagnetic problem. In a non-collinear magnetic calculation the computational effort to diagonalize the Hamilton matrix increases with the third power of the number of basis functions in comparison with a collinear calculation. Another drawback is the reduction of the symmetry of the system due to the non-collinearity, resulting in an increase of the irreducible wedge of the Brillouin zone and, in addition, a larger number of Bloch vectors \mathbf{k} . Since the computational effort increases linearly with the number of Bloch vectors, too, the calculation of non-collinear systems is highly time-consuming. It is recommended to start the studies with the collinear calculations and use them as a starting point for the non-collinear ones afterwards.

5.1 Constrained Magnetic Moments

Non-collinear magnetic configurations do not necessarily represent extrema of the energy functional $E[n(\mathbf{r}), \mathbf{m}(\mathbf{r})]$. Therefore, Dederichs et al. [74] extended the DFT to systems that tend to exhibit arbitrary constraints. This is done by introducing boundary conditions to keep the local magnetic moments of the atoms fixed in a specific direction. Hence, Lagrange multipliers are needed to pin the magnetic moment of the atom in the direction $\hat{\mathbf{e}}_\alpha$ within the muffin tin sphere α . They have the form of local magnetic fields. The energy functional reads then

$$\begin{aligned}
 E_{constr}[n(\mathbf{r}), \mathbf{m}(\mathbf{r}), \{\hat{\mathbf{e}}_\alpha\}] &= E[n(\mathbf{r}), \mathbf{m}(\mathbf{r})] \\
 &+ \mu_B \sum_\alpha \mathbf{B}_c^\alpha \left(\int_{MT_\alpha} \mathbf{m}(\mathbf{r}) d^3r - \hat{\mathbf{e}}_\alpha \left(\hat{\mathbf{e}}_\alpha \cdot \int_{MT_\alpha} \mathbf{m}(\mathbf{r}) d^3r \right) \right) \\
 &= E[n(\mathbf{r}), \mathbf{m}(\mathbf{r})] + \mu_B \sum_\alpha \mathbf{B}_c^\alpha \cdot (\mathbf{M}^\alpha - \mathbf{M}_\parallel^\alpha) \\
 &= E[n(\mathbf{r}), \mathbf{m}(\mathbf{r})] + \mu_B \sum_\alpha \mathbf{B}_c^\alpha \cdot \mathbf{M}_\perp^\alpha. \tag{5.5}
 \end{aligned}$$

The minimum of the energy functional provides the state of lowest energy meeting simultaneously the condition of constrained magnetic moments. The minimization of Eq. (5.5) with respect to the wave functions yields the Kohn-Sham equations within the muffin-tin sphere α plus an additional term:

$$\epsilon_i \psi_i(\mathbf{r}) = \left\{ -\frac{\hbar^2}{2m} \nabla^2 + v_{eff}(\mathbf{r}) + \mu_B \left[\boldsymbol{\sigma} \cdot \mathbf{B}_{eff}(\mathbf{r}) + \boldsymbol{\sigma} \cdot \left(\mathbf{B}_c^\alpha - \hat{\mathbf{e}}_\alpha (\hat{\mathbf{e}}_\alpha \cdot \mathbf{B}_c^\alpha) \right) \right] \right\} \psi_i(\mathbf{r}). \tag{5.6}$$

The contribution $\mu_B \boldsymbol{\sigma} \cdot (\mathbf{B}_c^\alpha - \hat{\mathbf{e}}_\alpha (\hat{\mathbf{e}}_\alpha \cdot \mathbf{B}_c^\alpha))$ is always perpendicular to $\hat{\mathbf{e}}_\alpha$, i.e., $\mathbf{B}_c^\alpha \perp \hat{\mathbf{e}}_\alpha$. Hence, the problem is apparently solved if \mathbf{M}_\perp^α becomes zero during the self-consistency cycle. Besides the presented method there are other approaches to phrase the condition of the constrained magnetic moments. For instance, the requirement of a vanishing vector product $\mathbf{M}_\perp^\alpha \times \hat{\mathbf{e}}_\alpha$ causes a torsional moment acting on the magnetic moment [75, 76]. The additional contribution to the total energy generated by the constrained magnetic moments compensates with the one caused by the effective \mathbf{B} field included in the kinetic energy (Eq. (3.30)). Thus, the total energy (Eq. (3.28)) remains unchanged.

5.2 Spin Spirals

In section 4.2 it was pointed out that the general solutions of the Heisenberg Hamiltonian on a periodic lattice are flat spin-spiral states, i.e., the magnetic moments rotate homogeneously within a plane either perpendicular or parallel to the film plane. But beside those two-dimensional spin structures there are more complicated spin arrangements such as conical spin spirals, which will be introduced in the following.

The main characteristic of a homogeneous spin spiral is the rotation of magnetic moments by a constant angle ϕ proceeding from atom to atom along a certain direction of the crystal. The reciprocal lattice vector \mathbf{q} , which describes this configuration, is called *spin-spiral vector*. The n th atom is located at the site \mathbf{R}_n and the rotation angle is given by $\phi = \mathbf{q} \cdot \mathbf{R}_n$. Then, the magnetic moment of this atom is defined by

$$\mathbf{S}_n = S (\cos(\phi + \tau) \sin \theta, \sin(\phi + \tau) \sin \theta, \cos \theta), \quad (5.7)$$

where θ denotes the *cone angle*, i.e. a relative angle between the magnetic moment and the rotational axis, and τ is an eventual phase factor. Obviously, there are three parameters defining a spin spiral:

- the spin-spiral vector \mathbf{q} ,
- the rotational axis and
- the cone angle θ .

Neglecting SOC the angle between the spin-spiral vector \mathbf{q} and the rotational axis is of no relevance since \mathbf{q} is a vector of the real space coordinate frame, while the spin-rotation axis is defined in the spin-coordinate frame. Excluding SOC means the decoupling of the lattice and the spin lattice. In that case, the top and the bottom spin spiral in Fig. 5.1 become energetically equivalent. The same applies for the two spirals in between. Spin spirals of different θ , on the other hand, are energetically nonequivalent, since θ is still a well defined quantity while SOC is neglected.

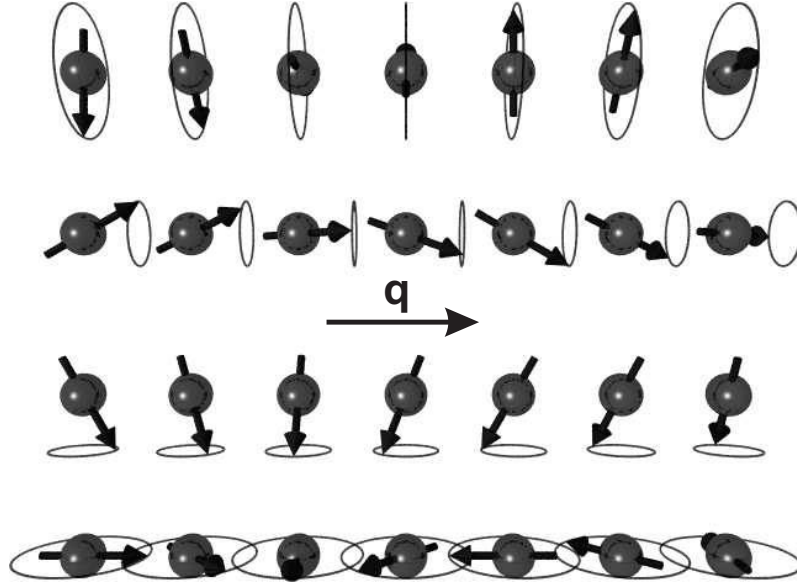


Figure 5.1: Spin spirals assigned to different cone angles θ . The upper two examples show spirals with a rotation plane perpendicular to \mathbf{q} . In the lower two illustrations the rotation plane includes \mathbf{q} . Special cases are the first and the last example since $\theta = 90^\circ$, i.e., they are flat spin spirals, whereas the other two are so-called conical spin spirals.

Besides the high symmetry states, such as the ferromagnetic state ($\mathbf{q} = 0$), the spin spirals cover a vast part of the magnetic phase space. Another benefit of spin spirals is their suitability for the simulation of domain walls or temperature effects in magnetic systems. In general, the discovery of the spin spiral inspired many theoreticians [77, 78].

Depending on the size of the spin-spiral vector \mathbf{q} , the description of spin spirals might require large magnetic unit cells. Therefore, their calculation is computationally very demanding. In order to treat spin spirals in first-principles calculations without using large unit cells, the generalized Bloch theorem can be exploited [79, 80, 81]. However, the Bloch theorem is only valid while SOC is neglected.

5.3 The Generalized Bloch Theorem

Spin spirals break the translational symmetry of the lattice along the direction of the spin-spiral vector \mathbf{q} . In particular for *ab-initio* methods relying on the translational symmetry, this is a severe problem. For instance, a large number of atoms is needed in order to describe a spin-spiral state with a small rotation angle, which leads to a large unit cell. Since the computation of the latter is very time-consuming, it is necessary to find a formulation similar to the Bloch theorem in order to reduce the computational effort for those configurations.

Neglecting SOC the atoms of a homogeneous spin-spiral structure are all equivalent since they experience the same local environment. Their magnetic moments have the same magnitude and angles with respect to the neighboring magnetic moments. This local equivalence will be exploited to generalize the Bloch theorem [79, 80, 81]. Concerning the lack of translational invariance so-called generalized translations $\mathcal{T}_m = \{-\mathbf{q}\mathbf{R}_m|\epsilon|\mathbf{R}_m\}$ are introduced, which are combinations of a spin translation and spin rotation. They link the lattice vectors \mathbf{R}_n in the real space and the spin rotations with the rotation angle $\phi = \mathbf{R}_n \cdot \mathbf{q}$ in the spin space. ϵ denotes the identity operation. The generalized translations belong to the spin-space group.

The Hamilton operator of a spin spiral without an external magnetic field, but with a counterclockwise rotating angle $\phi = \mathbf{q} \cdot \mathbf{R}_n$ and an exchange-correlation magnetic field \mathbf{B}_{xc} changing from site to site, fulfills the relation as below

$$\mathcal{H}(\mathbf{r} + \mathbf{R}_n) = \mathbf{U}(\mathbf{q} \cdot \mathbf{R}_n) \mathcal{H}(\mathbf{r}) \mathbf{U}^\dagger(\mathbf{q} \cdot \mathbf{R}_n). \quad (5.8)$$

The spin-rotation axis coincides with the z -axis of the spin without loss of generality. In that case the spin-rotation matrix reads

$$\mathbf{U}(\mathbf{q} \cdot \mathbf{R}_n) = \begin{pmatrix} e^{-i\phi/2} & 0 \\ 0 & e^{i\phi/2} \end{pmatrix}. \quad (5.9)$$

The application of a generalized translation onto $\mathcal{H}(\mathbf{r}) \psi(\mathbf{r})$ yields:

$$\begin{aligned} \mathcal{T}_n \mathcal{H}(\mathbf{r}) \psi(\mathbf{r}) &= \mathbf{U}(-\mathbf{q} \cdot \mathbf{R}_n) \mathcal{H}(\mathbf{r} + \mathbf{R}_n) \mathbf{U}^\dagger(-\mathbf{q} \cdot \mathbf{R}_n) \mathbf{U}(-\mathbf{q} \cdot \mathbf{R}_n) \psi(\mathbf{r} + \mathbf{R}_n) \\ &= \mathcal{H}(\mathbf{r}) \mathbf{U}(-\mathbf{q} \cdot \mathbf{R}_n) \psi(\mathbf{r} + \mathbf{R}_n) \\ &= \mathcal{H}(\mathbf{r}) \mathcal{T}_n \psi(\mathbf{r}). \end{aligned} \quad (5.10)$$

Thus, the generalized translation commutes with the Hamilton operator.

In a similar fashion to the proof of the Bloch theorem [82] the eigenstates can be chosen such that

$$\mathcal{T}_m \psi(\mathbf{k}, \mathbf{r}) = \mathbf{U}(-\mathbf{q} \cdot \mathbf{R}_m) \psi(\mathbf{k}, \mathbf{r} + \mathbf{R}_m) = e^{i\mathbf{k} \cdot \mathbf{R}_m} \psi(\mathbf{k}, \mathbf{r}). \quad (5.11)$$

Eq. (5.11) is the generalized Bloch theorem. An equivalent formulation represents the eigenfunctions of the Hamiltonian as follows

$$\psi(\mathbf{k}, \mathbf{r}) = \begin{pmatrix} e^{-i\mathbf{q} \cdot \mathbf{r}/2} f^\uparrow(\mathbf{k}, \mathbf{r}) \\ e^{+i\mathbf{q} \cdot \mathbf{r}/2} f^\downarrow(\mathbf{k}, \mathbf{r}) \end{pmatrix}, \quad (5.12)$$

where $f^\uparrow(\mathbf{k}, \mathbf{r})$ and $f^\downarrow(\mathbf{k}, \mathbf{r})$ have the generalized periodicity of the Hamiltonian,

i.e., $f^\uparrow(\mathbf{k}, \mathbf{r}) = f^\uparrow(\mathbf{k}, \mathbf{r} + \mathbf{R}_m)$. The fact of f^\uparrow and f^\downarrow being periodic is of great advantage for the implementation of spin spirals in the FLAPW method, since it is expressed in terms of plane waves and Fourier transforms.

5.4 Non-collinear magnetism in FLAPW

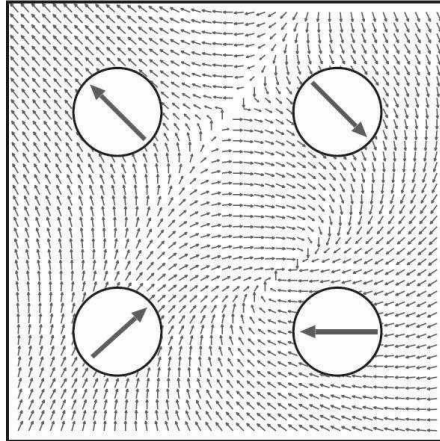


Figure 5.2: Schematic illustration of the magnetization density in the program code FLEUR [22]. In the interstitial region the magnetization is represented as a continuous vector field. Within the muffin-tin spheres the magnetization is assumed to be collinear and varying in its magnitude only. For reasons of clarity the muffin-tins spheres were chosen smaller in this picture than in the actual calculations. This figure is taken from [83].

There are two approaches to implement the non-collinear magnetism into an *ab initio* method. The first non-collinear calculations were carried out in methods like the Korringa-Kohn-Rostocker method [84, 85], the Augmented Spherical Wave method [86, 87, 88] and the Linear Muffin Tin Orbital method [77, 89]. All of these methods have in common that they make use of spheres at the positions of the nuclei. It is therefore convenient to assume the magnetization direction as fixed within the spheres and varying only from sphere to sphere. Inside of such a sphere the magnetization does not necessarily need to be homogeneous. This approach agrees with the intuitive picture that every atom carries a magnetic moment generated from the strong intra-atomic exchange. The moments of different atoms, on the other hand, interact via the inter-atomic exchange giving them the opportunity to arrange arbitrarily. Therefore, this approach describes the inter-atomic non-collinearity only.

In general, the magnetization direction is continuously varying from site to site, although in many cases the deviation from the main atomic direction is only found in those regions, where the magnetization is small, i.e., the interstitial as well as the

vacuum region. Therefore, the magnetization density \mathbf{m} has the form of a continuous vector field. This approach has been applied by Nordström and Singh [90], who published the first calculation investigating the intra-atomic non-collinearity. However, the intra-atomic exchange is not of interest for the study of the surfaces and interfaces of the 3d transition metals, since the non-collinearity in the intra-atomic exchange is expected to be rather small in those systems.

The concept used for the implementation in the FLEUR program code [22] is a "hybrid" approach, which handles the magnetization direction in the interstitial and the vacuum region continuously, whereas the magnetization direction is kept fixed within the muffin-tin spheres (cf. Fig. 5.2) [83, 91]. As mentioned above, the FLAPW method makes use of the augmented plane waves as basis functions. In order to extend this method onto spin dependent collinear systems, the spinors $\chi_{\sigma=\uparrow,\downarrow}^g$ are introduced analogously to the Pauli spinors in Eq. (2.24):

$$\chi_{\uparrow}^g = \begin{pmatrix} 1 \\ 0 \end{pmatrix} \quad \chi_{\downarrow}^g = \begin{pmatrix} 0 \\ 1 \end{pmatrix}, \quad (5.13)$$

where the index g refers to the fact that the χ_{σ}^g are defined relatively to the global quantizations axis (for example the z -axis). Hence, the basis functions in the interstitial region are written as

$$\varphi_{\mathbf{G}}(\mathbf{k}, \mathbf{r}) = e^{i(\mathbf{k}+\mathbf{G})\cdot\mathbf{r}} \chi_{\sigma}^g. \quad (5.14)$$

Generalizing this expression for the case of non-collinear magnetism means that the potential matrix \mathbf{v} is not a diagonal matrix anymore. Thus, the Hamilton operator in Eq. (5.4) needs to be fully diagonalized.

Since the local spin coordinate frame is used solely in the muffin-tin spheres, the basis set does not need to be changed in the interstitial and the vacuum region, where the basis functions are represented by the global spin frame. A transformation of the spinors χ_{σ}^g into the local coordinate frame of the χ_{σ}^l is performed by means of a unitary transformation \mathbf{U}^{gl} :

$$\chi_{\sigma}^l = \mathbf{U}^{gl} \chi_{\sigma}^g = \begin{pmatrix} e^{i\frac{\alpha}{2}} \cos\left(\frac{\beta}{2}\right) & e^{-i\frac{\alpha}{2}} \sin\left(\frac{\beta}{2}\right) \\ -e^{i\frac{\alpha}{2}} \sin\left(\frac{\beta}{2}\right) & e^{-i\frac{\alpha}{2}} \cos\left(\frac{\beta}{2}\right) \end{pmatrix} \chi_{\sigma}^g. \quad (5.15)$$

Considering the local and the global quantization axis the basis set now takes the

following form:

$$\varphi_{\mathbf{G},\sigma}(\mathbf{k}, \mathbf{r}) = \begin{cases} e^{i(\mathbf{G}+\mathbf{k})\mathbf{r}} \chi_{\sigma}^g & \text{interstitial region} \\ \left\{ A_{\sigma}^{\mathbf{G}_{\parallel}G_{\perp}}(\mathbf{k}_{\parallel}) u_{\sigma}^{\mathbf{G}_{\parallel}}(\mathbf{k}_{\parallel}, z) \right. \\ \left. + B_{\sigma}^{\mathbf{G}_{\parallel}G_{\perp}}(\mathbf{k}_{\parallel}) \dot{u}_{\sigma}^{\mathbf{G}_{\parallel}}(\mathbf{k}_{\parallel}, z) \right\} e^{i(\mathbf{G}_{\parallel}+\mathbf{k}_{\parallel})\mathbf{r}_{\parallel}} \chi_{\sigma}^g & \text{vacuum region} \\ \sum_{\sigma^{\alpha}} \sum_L \left(A_{L\sigma\sigma^{\alpha}}^{\mu\mathbf{G}}(\mathbf{k}) u_l(r) + B_{L\sigma\sigma^{\alpha}}^{\mu\mathbf{G}}(\mathbf{k}) \dot{u}_l(r) \right) Y_L(\hat{\mathbf{r}}) \chi_{\sigma^{\alpha}} & \text{muffin tin } \alpha \end{cases} \quad (5.16)$$

Again, L abbreviates lm and the sum in the muffin tins considers the local spin directions. The $A_L^{\mu\mathbf{G}}$ and $B_L^{\mu\mathbf{G}}$ have to meet the following boundary condition

$$e^{i(\mathbf{k}+\mathbf{G})\mathbf{r}} \chi_{\sigma} = \sum_{\sigma^{\alpha}} \sum_L \left(A_{L\sigma\sigma^{\alpha}}^{\mu\mathbf{G}}(\mathbf{k}) u_{l\sigma^{\alpha}}^{\alpha}(r) + B_{L\sigma\sigma^{\alpha}}^{\mu\mathbf{G}}(\mathbf{k}) \dot{u}_{l\sigma^{\alpha}}^{\alpha}(r) \right) Y_L(\hat{\mathbf{r}}) \chi_{\sigma^{\alpha}}^{\alpha g}. \quad (5.17)$$

Thus, the global spin-coordinate frame can be transformed into the local frame by a rotation given via the Euler angles α and β . In the present case, the Euler angles are equivalent to the polar angles of the local quantization axis in the global coordinate frame, namely $\alpha = \phi$ and $\beta = \theta$.

As a result of the matching condition at the boundary of the interstitial region and the muffin-tins, the spin up and spin down basis functions couple. Nevertheless, a non-collinear calculation can be transferred into a collinear one by transforming the non-collinear coefficients A and B as below

$$A_{L,\mathbf{G},\uparrow}^{\text{noco}}(\mathbf{k}) = \chi_{\uparrow g}^T U^{gl} \chi_{\uparrow g} A_{L,\mathbf{G},\uparrow}(\mathbf{k}) \quad (5.18)$$

$$B_{L,\mathbf{G},\uparrow}^{\text{noco}}(\mathbf{k}) = \chi_{\uparrow g}^T U^{gl} \chi_{\uparrow g} B_{L,\mathbf{G},\uparrow}(\mathbf{k}) \quad (5.19)$$

$$A_{L,\mathbf{G},\downarrow}^{\text{noco}}(\mathbf{k}) = \chi_{\downarrow g}^T U^{gl} \chi_{\downarrow g} A_{L,\mathbf{G},\downarrow}(\mathbf{k}) \quad (5.20)$$

$$B_{L,\mathbf{G},\downarrow}^{\text{noco}}(\mathbf{k}) = \chi_{\downarrow g}^T U^{gl} \chi_{\downarrow g} B_{L,\mathbf{G},\downarrow}(\mathbf{k}). \quad (5.21)$$

In this way, the calculation can be performed as in the collinear case, which is much simpler to solve.

6 Spin-Orbit Coupling

Relativistic effects play a more important role at surfaces and in ultra-thin films than in bulk systems. Néel explained this behavior with the reduced number of neighbors at the surface giving rise to the so-called *magnetocrystalline surface anisotropy* [92]. It describes the difference in the magnetic energy found for different magnetization directions, and leads to the distinction between an easy magnetization axis (minimal energy) and a hard magnetization axis (maximal energy). The magnetic anisotropy is caused by the spin-orbit coupling (SOC) and the magnetic dipolar interaction. The latter senses the outer boundaries of the sample and gives rise to the shape anisotropy, while the SOC couples the spin and the lattice, which leads to the magnetocrystalline anisotropy. In small magnetic systems, such as the magnetic mono- or double layers studied in the present work, the contribution of the magnetic dipole-dipole energy to the magnetic anisotropy is of the order of ~ 0.1 meV, which is small compared to the contribution of the magnetocrystalline anisotropy (~ 1 meV). Therefore, the dipole-dipole interaction is neglected in the following.

Further consequences of the SOC are the Rashba effect [93, 94], which will not be discussed in this thesis, and the *Dzyaloshinskii-Moriya interaction* (DMI) [7, 8], which are both effects of a lack of inversion symmetry in the considered system. The latter favors non-collinear magnetic structures with a unique rotational sense. Thus, left and right rotating spin structures that are degenerate within the Heisenberg model exhibit a difference in energy in the presence of the Dzyaloshinskii-Moriya interaction. This has been demonstrated in crystals, i.e., bulk systems, without inversion symmetry (cf. [95]). However, since surfaces always lack inversion symmetry, the Dzyaloshinskii-Moriya interaction needs to be considered in such systems. Recently, it has been shown that the DMI plays a crucial role in surface magnetism [9]. Furthermore, the strength of the SOC and thus the strength of the DMI depends on the atomic number, i.e., it has to be considered in systems comprising heavy elements, such as W or Ir.

In this chapter, the SOC and its effects are presented. The relativistic description of many-electron systems is introduced as well as the treatment of the SOC in the density functional theory and its implementation in the FLAPW method. Finally, the Dzyaloshinskii-Moriya interaction will be explained in more detail.

6.1 The Relativistic Density Functional Theory

The Kohn-Sham equation reads as a single-particle Dirac equation if the relativistic effects are taken into account:

$$\left(c\boldsymbol{\alpha} \cdot \mathbf{p} + (\beta - 1)mc^2 + V_{\text{eff}}(\mathbf{r}) \right) \boldsymbol{\Psi}_i = \epsilon_i \boldsymbol{\Psi}_i, \quad (6.1)$$

where $\boldsymbol{\alpha}$ and β are the Dirac matrices,

$$\boldsymbol{\alpha} = \begin{pmatrix} 0 & \boldsymbol{\sigma} \\ \boldsymbol{\sigma} & 0 \end{pmatrix} \quad \text{and} \quad \beta = \begin{pmatrix} \mathbf{I}_2 & 0 \\ 0 & -\mathbf{I}_2 \end{pmatrix}. \quad (6.2)$$

Here, $\boldsymbol{\sigma}$ is the vector of the Pauli matrices σ_x , σ_y and σ_z , and \mathbf{p} denotes the momentum operator. \mathbf{I}_2 is the (2×2) identity matrix and $\boldsymbol{\Psi}_i$ identifies the four-component Dirac spinor represented by large and small components $\varphi_i(\mathbf{r})$ and $\chi_i(\mathbf{r})$, respectively. The index i abbreviates the Bloch vector \mathbf{k} , the band index i and the spin-quantum number σ . Written in terms of the Dirac spinors, the charge and magnetization density of the ground state have the following form

$$n(\mathbf{r}) = \sum_i^N \left(\varphi_i^\dagger(\mathbf{r})\varphi_i(\mathbf{r}) + \chi_i^\dagger(\mathbf{r})\chi_i(\mathbf{r}) \right) \quad (6.3)$$

and

$$\mathbf{m}(\mathbf{r}) = \sum_i^N \left(\varphi_i^\dagger(\mathbf{r})\boldsymbol{\sigma}\varphi_i(\mathbf{r}) + \chi_i^\dagger(\mathbf{r})\boldsymbol{\sigma}\chi_i(\mathbf{r}) \right). \quad (6.4)$$

A straight and, at the same time, accurate procedure to solve Eq. (6.1) is the extension of the FLAPW basis set to all four components. The basis would then contain four times as many functions as the non-relativistic and nonmagnetic basis set. In that case the computational time needed for the diagonalization of the Hamilton matrix would increase by a factor of $4^3 = 64$. But as long as no SOC effects are treated, it is sufficient to include only those correction terms into the non-relativistic calculation that contribute to the diagonal elements of the Hamilton matrix. This method is called the *scalar-relativistic* calculation, and it has been suggested by D. Koelling and B. Harmon [96]. In this approach only the electrons within the muffin tin spheres are treated relativistically, since the kinetic energy of the electrons is large near the nuclei and the relativistic effects become stronger. In the vacuum and the interstitial region the basis functions remain non-relativistic.

6.2 Spin-Orbit Coupling

In the limiting case of small velocities $v^2/c^2 \ll 1$ of the valence electrons, Eq. (6.1) can be reduced to a Pauli equation. To achieve this, the Dirac operator is expanded in v^2/c^2 and transformed afterwards (cf. e.g. [97]). The resulting equation is a Schrödinger-like equation including the first relativistic corrections of the order of $\mathcal{O}(1/c^2)$. The corresponding Hamilton operator is called *Pauli operator* and takes the form

$$\mathcal{H}_{Pauli} = \frac{\mathbf{p}^2}{2m} - e \cdot v - \frac{\mathbf{p}^4}{8m^3c^2} + \frac{e\hbar^2}{8m^2c^2} \nabla \cdot \mathbf{E} + \frac{e\hbar}{4m^2c^2} \boldsymbol{\sigma} \cdot (\mathbf{E} \times \mathbf{p}). \quad (6.5)$$

The first and the second contribution represent the non-relativistic kinetic energy and the electrostatic potential energy, respectively. They form the non-relativistic Hamilton operator. The third and the fourth term do not depend on the spin $\mathbf{S} = \boldsymbol{\sigma}/2$ and, in addition to the first two contributions, result in the scalar-relativistic Hamilton operator. The third term in Eq. (6.5) is a correction term due to the kinematical mass enhancement. Here, the fourth summand can be interpreted as a smearing out of the electrostatic interaction between the electron and the nuclei due to rapid quantum oscillations. That means that the expectation value of \mathbf{r} does not possess sharp eigenfunctions because of the zitterbewegung that the electron performs, which is of the order of the Compton wave length $\lambda_C = \hbar/mc$. As a result the electron responds sensitively to the electric field \mathbf{E} . The very last contribution in Eq. (6.5) is finally the spin-orbit interaction \mathcal{H}_{SOC} . It originates from the coupling of the electronic spin with the magnetic field that the electron experiences while it moves in the vicinity of the nuclei. This orbital movement is coupled directly with the crystal lattice via the electric potential of the ions. It contributes to the magnetocrystalline anisotropy .

As mentioned above, the SOC effect occurs mainly close to the nuclei, since the kinetic energy of the electron and thus the gradient of the potential is largest in this region. The potential may be spherically approximated in the vicinity of the nuclei: $v(\mathbf{r}) \simeq v(r)$. According to J. C. Maxwell the electric field reads then as follows (cf. e.g. [98]):

$$\mathbf{E} = -\nabla v(\mathbf{r}) = -\frac{\mathbf{r}}{r} \frac{dv}{dr}, \quad (6.6)$$

and gives the SOC Hamiltonian the following form

$$\begin{aligned} \mathcal{H}_{SOC} &= -\frac{e\hbar}{4m^2c^2r} \frac{dv}{dr} \boldsymbol{\sigma} \cdot (\mathbf{r} \times \mathbf{p}) \\ &= \frac{-e\hbar^2}{2m^2c^2r} \frac{dv}{dr} \mathbf{L} \cdot \mathbf{S} \\ &= \underbrace{\frac{-e\hbar^2}{2m^2c^2r} \frac{dv}{dr}}_{\xi(r)} \mathbf{L} \cdot \mathbf{S}. \end{aligned} \quad (6.7)$$

\mathbf{L} represents the operator of the angular momentum and $\xi(r)$ is the SOC constant as a function of the radial distance r from the position of the nuclei. Since the magnetism in the $3d$ transition metals is originating from the d -electrons, it is reasonable to average the SOC constant over the d -orbitals in order to reduce ξ to a simple constant.

Regarding the representation of the basis functions in Eq. (5.16), the expectation value of the SOC operator \mathcal{H}_{SOC} may be separated into a matrix element of the position space and the spin space, respectively. In position space the matrix element $\xi_{\mathbf{k},\nu,\nu'}^{L,\sigma,\sigma'} = \langle \nu, L, \sigma | \xi(\mathbf{r}) | \nu', L, \sigma' \rangle$ provides the strength of the SOC. The radial part $\xi_{\mathbf{k},\nu,\nu'}^{L,\sigma,\sigma'}$ can be evaluated directly from the scalar-relativistic approximation. An estimation of the coupling strength is obtained by assuming the Coulomb potential to be $v(r) = -Z \cdot e/r$ and using the non-relativistic radial functions $R_{nl}(r) \propto r^l$. This results in

$$\xi_{nl} \propto \left\langle nl \left| \frac{1}{r} \frac{Z}{r^2} \right| nl \right\rangle \frac{Z^4}{a_B^3} \frac{1}{n^3 l^2}. \quad (6.8)$$

The proportional relation (6.8) shows that ξ_{nl} increases with the fourth order of the atomic number, Z^4 . In the case of the $3d$ transition metals ξ_{nl} is of the order of about 50 meV [99].

In spin space the matrix element $\mathbf{L} \cdot \mathbf{S}$ describes the angular dependency of the SOC, which is the main contribution to the anisotropy. The matrix element depends on the spin-quantization axis $\mathbf{\Omega}$, which has been aligned parallel¹ to the magnetization direction $\mathbf{\Omega}_M$ of the effective magnetic field \mathbf{B}_{eff} . The angular dependence of $\mathbf{L} \cdot \mathbf{S}$ in the 2×2 spin space obtained for an arbitrary spin orientation $\mathbf{\Omega} = (\sin \phi \sin \theta, \cos \phi \sin \theta, \cos \theta)$ is yielded after the computation of the $\mathbf{\Omega}_z = (0, 0, 1)$ direction and a subsequent unitary transformation \mathbf{U} (cf. Eq. (5.15)):

$$\langle lm_l \sigma | \mathbf{L} \cdot \mathbf{S} | lm'_l \sigma' \rangle (0, 0) \longrightarrow \langle lm_l \sigma | \mathbf{U}^\dagger(\vartheta, \varphi) (\mathbf{L} \cdot \mathbf{S}) \mathbf{U}(\vartheta, \varphi) | lm'_l \sigma' \rangle (\vartheta, \varphi) \quad (6.9)$$

$$\begin{aligned} \implies & \begin{pmatrix} \langle \uparrow | \mathbf{L} \cdot \mathbf{S} | \uparrow \rangle & \langle \uparrow | \mathbf{L} \cdot \mathbf{S} | \downarrow \rangle \\ \langle \downarrow | \mathbf{L} \cdot \mathbf{S} | \uparrow \rangle & \langle \downarrow | \mathbf{L} \cdot \mathbf{S} | \downarrow \rangle \end{pmatrix} (\vartheta, \varphi) = \\ & = \begin{pmatrix} \cos \vartheta & -\sin \vartheta \\ -\sin \vartheta & -\cos \vartheta \end{pmatrix} L_z \\ & + \begin{pmatrix} \frac{1}{2} \sin \vartheta (e^{i\varphi} L^+ + e^{-i\varphi} L^-) & \cos^2(\frac{\vartheta}{2}) e^{i\varphi} L^- - \sin^2(\frac{\vartheta}{2}) e^{-i\varphi} L^+ \\ \cos^2(\frac{\vartheta}{2}) e^{-i\varphi} L^+ - \sin^2(\frac{\vartheta}{2}) e^{i\varphi} L^- & -\frac{1}{2} \sin \vartheta (e^{i\varphi} L^+ + e^{-i\varphi} L^-) \end{pmatrix}, \end{aligned} \quad (6.10)$$

where the operators $L^\pm \equiv L_x \pm iL_y$ are applied onto the Y_L .

¹Technically, the spin and its magnetic moment are aligned antiparallel. However, for reasons of simplification both are assumed parallel and μ_B is set to a negative value.

6.3 The Magnetocrystalline Anisotropy and the Orbital Moment

In order to estimate the magnitude of the SOC effect on the basis of density functional theory, it is useful to consider a quantity that is directly related to this effect. The magnetocrystalline anisotropy is such a quantity, since it introduces a preferred magnetization direction within the crystal and breaks the rotational invariance of the Hamilton operator with respect to the spin quantization axis. Rotating the energy from a direction of low energy (easy axis) towards a direction of high energy (hard axis) is typically of the order 10^{-6} to 10^{-3} eV/atom and represents a very small correction to the total magnetic energy [100].

Bruno suggested a simple physical model that relates the orbital moment $\mathbf{m}_l = \mu_B \mathbf{L}$ to the magnetocrystalline anisotropy K [100, 101]. The spin splitting $\epsilon_i^\pm \approx IM$ of the bands is assumed to be much larger than the bandwidth W due to exchange. The off-diagonal elements of the spin-orbit interaction matrix \mathcal{H}_{SOC} , which mix both spin channels, may then be neglected. This results in the resemblance of the SOC to an effective magnetic field \mathbf{H}_{orb} acting merely onto the orbital moment \mathbf{m}_l :

$$\mathcal{H}_{SOC} = -\mathbf{m}_l \cdot \mathbf{H}_{orb} \quad \text{with} \quad \mathbf{H}_{orb} = \frac{\pm \xi}{2\mu_B} \boldsymbol{\Omega}_M. \quad (6.11)$$

Here, the sign \pm represents the d band filling with more or less than five electrons and $\boldsymbol{\Omega}_M$ is the magnetization direction.

The effect of this field is described by a second degree tensor of the orbital susceptibility $\chi_{orb}^{(2)}$. The expectation value of the orbital moment $\langle \mathbf{m}_l \rangle$ and the SOC energy E_{SOC} are then given in the lowest order of \mathbf{H}_{orb} as follows

$$\begin{aligned} \langle \mathbf{m}_l \rangle &= \chi_{orb}^{(2)} \cdot \mathbf{H}_{orb} \\ &= \frac{\pm \xi}{2\mu_B} \chi_{orb}^{(2)} \cdot \boldsymbol{\Omega}_M \end{aligned} \quad (6.12)$$

and

$$\begin{aligned} E_{SOC} &= -\frac{1}{2} \mathbf{H}_{orb} \cdot \chi_{orb}^{(2)} \cdot \mathbf{H}_{orb} \\ &= -\frac{1}{2} \frac{\xi^2}{4\mu_B^2} \boldsymbol{\Omega}_M \cdot \chi_{orb}^{(2)} \cdot \boldsymbol{\Omega}_M. \end{aligned} \quad (6.13)$$

In crystals, which feature uniaxial magnetic anisotropy, the symmetry axis may be aligned to the z axis without loss of generality. This applies for instance in ultrathin

films and at surfaces². Hence, the susceptibility has the form of a diagonal matrix:

$$\chi_{orb}^{(2)} = \begin{pmatrix} \chi_{orb}^{(2)11} & 0 & 0 \\ 0 & \chi_{orb}^{(2)22} & 0 \\ 0 & 0 & \chi_{orb}^{(2)33} \end{pmatrix}. \quad (6.14)$$

The orbital moment and the SOC energy result in

$$m_{l,z} = \pm \frac{\xi}{2\mu_B} \left[\chi_{orb}^{(2)33} + \left(\chi_{orb}^{(2)11} - \chi_{orb}^{(2)33} \right) \sin^2 \theta \right] \quad (6.15)$$

$$(6.16)$$

and

$$E_{SOC} = -\frac{1}{2} \frac{\xi^2}{4\mu_B^2} \left[\chi_{orb}^{(2)33} + \left(\chi_{orb}^{(2)11} - \chi_{orb}^{(2)33} \right) \sin^2 \theta \right], \quad (6.17)$$

respectively, where θ is the angle between the normal of the plane and the magnetization. According to this model the magnetic anisotropy energy K is directly proportional to the anisotropy of the orbital moments $\Delta m = m_l(\mathbf{\Omega}_{M_2}) - m_l(\mathbf{\Omega}_{M_1})$ for two different magnetizations $\mathbf{\Omega}_{M_2}$ and $\mathbf{\Omega}_{M_1}$:

$$K = \frac{\xi}{4\mu_B} \Delta m_l. \quad (6.18)$$

Equation (6.18) expresses that the anisotropy of the magnetic moment is of about $0.1 \mu_B/\text{atom}$ if an anisotropy energy of $1 \text{ meV}/\text{atom}$ and a spin-orbit coupling constant of $\xi = 50 \text{ meV}$ is considered, which is a typical value in ultrathin films.

6.4 Perturbation Theory

Since the SOC effect is rather small in $3d$ transition metals compared to the bandwidth or the exchange splitting, it is convenient to treat it within the framework of perturbation theory.

The energy difference due to SOC results from the second order perturbation theory:

$$\Delta E_{SOC} = \sum_{\Psi^1 \neq \Psi^0} \frac{|\langle \Psi^1 | \mathcal{H}_{SOC} | \Psi^0 \rangle|^2}{E^0 - E^1}. \quad (6.19)$$

²An extension to cubic systems is possible without further ado, but since they are isotropic in this order of \mathbf{H}_{orb} , i.e., $\chi_{orb}^{(2)11} = \chi_{orb}^{(2)22} = \chi_{orb}^{(2)33}$, the non-linear orbital susceptibility needs to be considered, which is given by a fourth degree tensor $\chi_{orb}^{(4)}$. For further details refer to [100, 102, 103].

Ψ^0 and Ψ^1 denote the unperturbed ground state and the excited state, respectively. The corrections to the wave functions are given by the first order perturbation theory:

$$\delta|\Psi^0\rangle = \sum_{\Psi^1 \neq \Psi^0} \frac{\langle \Psi^1 | \mathcal{H}_{SOC} | \Psi^0 \rangle | \Psi^1 \rangle}{E^0 - E^1}. \quad (6.20)$$

The considered excited states are located above the Fermi energy, and may be populated by electrons characterized by a certain momentum \mathbf{k} from an occupied state via an excitation with or without a spin flip. In particular, the denominator of Eq. (6.19) shows that states close in energy give large contributions. At the same time it has to be kept in mind that

$$|E^0 - E^1| \gg |\langle \Psi^1 | \mathcal{H}_{SOC} | \Psi^0 \rangle|^2. \quad (6.21)$$

This condition is not fulfilled by pairs of states, whose energy difference is in the range of ξ . In that case the perturbation theory of quasi degenerate states needs to be applied.

The anisotropy K_1 of uniaxial systems may be estimated roughly from the bandwidth W of the d electrons via second order perturbation theory:

$$K_1 \sim \frac{\xi^2}{W}. \quad (6.22)$$

The anisotropy constants of n th order are characterized by the proportionality of the direction dependency of the energy with respect to the n th power of the directional cosines. This leads to the linking between the anisotropy constants and the matrix element $(\mathbf{L} \cdot \mathbf{S})^n$ resulting from the n th order perturbation theory. In the case of uniaxial systems, which are discussed in this thesis, the first non vanishing terms occur in second order, whereas for cubic systems the fourth order perturbation theory needs to be considered [100, 102, 103]. In general, the anisotropy constants of n th order are proportional to $W \cdot \left(\frac{\xi}{W}\right)^n$ leading to a rapid convergence of the anisotropy energy as a function of the order n .

After the expansion of the eigenstates via the exploitation of the symmetry of the matrix elements $\mathbf{L} \cdot \mathbf{S}$, the energy difference due to SOC reads

$$\Delta E_{SOC} = -\xi^2 \sum_{m_1, m_2, m_3, m_4} \langle \uparrow | \langle m_1 | \mathbf{L} \cdot \mathbf{S} | m_2 \rangle | \uparrow \rangle \langle \uparrow | \langle m_3 | \mathbf{L} \cdot \mathbf{S} | m_4 \rangle | \uparrow \rangle G(m_1, m_2, m_3, m_4). \quad (6.23)$$

Here, $G(m_1, m_2, m_3, m_4)$ depends on the unperturbed band structure only and the matrix elements $\mathbf{L} \cdot \mathbf{S}$ are functions of the magnetization direction $\boldsymbol{\Omega}_M$. The evaluation of the matrix elements yields

$$\Delta E_{SOC} = K_0 + K_1 \sin^2 \theta, \quad (6.24)$$

where K_1 is the so-called *magnetocrystalline anisotropy*. The great advantage of the perturbation theory is that the anisotropy constants can be calculated without evaluating the total energy of the system explicitly in dependence of the magnetization direction. On the other hand, it fails in treating degenerate states properly.

6.5 Spin-Orbit Coupling in FLAPW

As mentioned at the beginning of this chapter the diagonalization of the full relativistic Hamilton matrix is numerically very challenging and therefore the methods introduced so far require huge computational effort in order to solve the Kohn-Sham-Dirac equation (6.1). Hence, the scalar-relativistic approximation is considered first and the SOC is included in an additional step. Bearing in mind that it is only a small quantity, the Brillouin zone integration requires a dense mesh of Bloch vectors \mathbf{k} . This results in another increase in computing time. A further drawback occurs if SOC and spin spiral calculations are combined. The generalized Bloch theorem only holds in the absence of SOC. Due to the coupling of the spin and the lattice, the translational symmetry is broken leading to necessarily large magnetic unit cells. Thus, it is preferable to minimize this effort via one of the following methods.

In the present thesis the SOC has been taken into account in two different ways. Since it is a small effect, it can be treated as a perturbation based on the *local force theorem* as a first approximation (cf. reference [104]). This method provides good results for magnetic configurations in many cases. However, for non-collinear magnetic systems no conclusion can be drawn due to the small number of published results so far. Alternatively, the SOC may be computed self-consistently, for which there are two different implementations available: collinear configurations are calculated self-consistently in *second variation* [105]. Non-collinear states are investigated in *first order perturbation theory*.

6.5.1 Local Force Theorem

A. R. Mackintosh and O. K. Andersen established the basic principle of this theorem [106]. The extension to magnetic systems was carried out by A. Oswald et al. [107] and further generalized by A. I. Liechtenstein et al. [108]. It is based on the idea that in a linear approximation the total energies show only little difference before and after the application of small perturbations to a system. In the case of SOC, the unperturbed (\mathcal{H}_0) and the perturbed Hamiltonian ($\mathcal{H}_1 = \mathcal{H}_0 + \mathcal{H}_{SOC}$) have to be considered. Regarding Eqs. (3.28) to (3.30) the total energies of the states can be split into two contributions:

$$E_0 = \sum_i^N \epsilon_{i,0} + E_{\text{rest},0} \quad \text{and} \quad E_1 = \sum_i^N \epsilon_{i,1} + E_{\text{rest},1}, \quad \text{respectively.} \quad (6.25)$$

The first term is formed by the sum of the single-particle energies ϵ_i , and the second one, E_{rest} , contains the remaining energy contributions. It can be demonstrated that in first order perturbation the second terms cancel each other and leave the single-particle energies solely (for further details refer to [104]). That means that the interaction 'drops' out of the total energy difference. Obviously, it is sufficient to compare the sum over the single-particle eigenvalues of both systems in order to observe a change in total energy if the perturbation is small enough. In the case of spin-orbit interaction the single-particle energies of different magnetization directions are compared in order to estimate the magnetic anisotropy energy:

$$\Delta E_{SOC} = \sum_i^N \epsilon_{i,1}(\mathbf{\Omega}_{M2}) - \sum_i^N \epsilon_{i,1}(\mathbf{\Omega}_{M1}). \quad (6.26)$$

Thus, the change in the total energies of the initial and the perturbed state can be substituted with the difference of the sums of the single-particle eigenvalues of the two states.

6.5.2 Variational Methods

The *second variational* treatment of the spin-orbit interaction [105] is based on the idea that the eigenfunctions of the scalar-relativistic Hamilton operator represent a more efficient basis set for the diagonalization of the relativistic Hamilton operator than the original LAPW basis. Therefore, fewer basis functions can be used without introducing a large error. After having determined the scalar-relativistic eigenvectors $\varphi_{\mathbf{k}\nu'\sigma'} = \sum_n c_{\mathbf{k}\nu'\sigma'}^n \phi_{\mathbf{k}\sigma'}^n$ the wave functions $\Psi_{\mathbf{k}\nu}(\mathbf{r})$ are expanded as follows

$$\Psi_{\mathbf{k}\nu}(\mathbf{r}) = \sum_{\nu'\sigma'}^{2N_S} C_{\mathbf{k}\nu'\sigma'}^\nu \varphi_{\mathbf{k}\nu'\sigma'}(\mathbf{r}). \quad (6.27)$$

N_S represents the number of basis functions per spin. The expansion coefficients $C_{\mathbf{k}\nu'\sigma'}^\nu$ have been multiplied with the Pauli spinor related to σ' . They are given via the following eigenvalue problem:

$$\sum_{\nu'',\sigma''}^{2N_S} \langle \mathbf{k}\nu'\sigma' | \mathcal{H} | \mathbf{k}\nu''\sigma'' \rangle C_{\mathbf{k}\nu''\sigma''}^\nu = \epsilon_{\mathbf{k}\nu} C_{\mathbf{k}\nu'\sigma'}^\nu. \quad (6.28)$$

Since the spin-orbit contribution is negligible, the overlap matrix remains diagonal. The Hamilton matrix, on the other hand, consists of the scalar-relativistic eigenval-

ues $\epsilon_{\mathbf{k}\nu\sigma}^0$ as diagonal elements and matrix elements resulting from the SOC:

$$\begin{aligned} \langle \mathbf{k}\nu\sigma | \mathcal{H} | \mathbf{k}\nu'\sigma' \rangle &= \epsilon_{\mathbf{k}\nu\sigma}^0 \delta_{\nu,\nu'} \delta_{\sigma,\sigma'} + \langle lm_l\sigma | \mathbf{L} \cdot \mathbf{S} | lm_l'\sigma' \rangle \times \\ &\times c_{\mathbf{k}\nu\sigma}^{n*} (A_{l\sigma}^{*\alpha} A_{l\sigma'}^\alpha \xi_{l\sigma\sigma'}^\alpha + A_{l\sigma}^{*\alpha} B_{l\sigma'}^\alpha \dot{\xi}_{l\sigma\sigma'}^\alpha + B_{l\sigma}^{*\alpha} A_{l\sigma'}^\alpha \dot{\xi}_{l\sigma\sigma'}^\alpha + B_{l\sigma}^{*\alpha} B_{l\sigma'}^\alpha \ddot{\xi}_{l\sigma\sigma'}^\alpha) c_{\mathbf{k}\nu'\sigma'}^{n'} \end{aligned} \quad (6.29)$$

A^α and B^α still represent the coefficients of the LAPW basis in the muffin tin α . The $\xi_{l\sigma\sigma'}^\alpha$, $\dot{\xi}_{l\sigma\sigma'}^\alpha$ and $\ddot{\xi}_{l\sigma\sigma'}^\alpha$ denote the radial spin-orbit interaction coefficients of the atom type α belonging to the fundamental unit cell. They are given by the radial scalar-relativistic wave functions u and their derivatives with respect to the energy, \dot{u} . The spin-quantization axis $\boldsymbol{\Omega}$ is chosen parallel to the effective magnetic field \mathbf{B}_{eff} (cf. Eq. (6.29)). Equation (6.10) is then diagonalized in the 2×2 spin space and the resulting eigenfunctions are projected onto APW's:

$$\begin{aligned} \Psi_{\mathbf{k}\nu}(\mathbf{r}) &= \sum_i^N \sum_{\nu'\sigma'}^{2N_S} C_{\mathbf{k}\nu'\sigma'}^\nu c_{\mathbf{k}\nu'\sigma'}^n \phi_{\mathbf{k}\sigma'}^n(\mathbf{r}) \\ &= \sum_{\sigma'}^2 \sum_i^N \tilde{c}_{\mathbf{k}\nu\sigma'} \phi_{\mathbf{k}\sigma'}^n(\mathbf{r}). \end{aligned} \quad (6.30)$$

Afterwards, the new charge and magnetization densities are calculated from Eqs. (6.3) and (6.4).

The advantage of the second variational method is the decrease of the size of the Hamilton matrix compared with the one of the LAPW basis without causing a large error. This is due to the employment of the scalar-relativistic wave functions. It needs to be kept in mind that this method does not represent a perturbative treatment of the SOC but a self-consistent consideration of relativistic effects.

In contrast to the second variation that first considers the scalar-relativistic Hamilton matrix in order to treat the SOC with its solutions afterwards, the *first variation* starts with the solution of the complete Hamiltonian. The use of the scalar-relativistic basis set in the case of non-collinear calculations would be inconvenient, since the non-collinearity already leads to a coupling of minority and majority spin. Thus, the full Hamilton matrix needs to be diagonalized, and cannot be split into two separate calculations for spin up and spin down (cf. Eq. (5.4)). The reduction of the computational effort may be accomplished by the calculation of the matrix elements of the SOC operator via simplified analytic formulae developed by S. J. Youn et al. [109]. In the following, the Bloch vector \mathbf{k} and the reciprocal lattice vector \mathbf{G} are abbreviated as $\mathbf{k}_n = \mathbf{k} + \mathbf{G}$. Based on the spin-orbit Hamiltonian (Eq. (6.7)) and the FLAPW basis set (Eq. (3.16)) the matrix elements of the SOC

now read as follows (cf. Eq. (6.29))

$$\begin{aligned}
 \langle \mathbf{k}_n \sigma | \mathcal{H}_{SOC} | \mathbf{k}_n \sigma' \rangle &= \tag{6.31} \\
 &= \langle l m_l \sigma | \mathbf{L} \cdot \mathbf{S} | l m_l' \sigma' \rangle \times \\
 &\quad \times c_{\mathbf{k}_n \sigma}^* (A_{l\sigma}^* A_{l\sigma'} \xi_{l\sigma\sigma'} + A_{l\sigma}^* B_{l\sigma'} \dot{\xi}_{l\sigma\sigma'} + B_{l\sigma}^* A_{l\sigma'} \dot{\xi}_{l\sigma\sigma'} + B_{l\sigma}^* B_{l\sigma'} \ddot{\xi}_{l\sigma\sigma'}) c_{\mathbf{k}_n \sigma'} \\
 &= \sum_l R_{k_n k_n'}^l \sum_{m_l m_l'} Y_{l m_l}(\hat{k}_n) \langle l m_l \sigma | \mathbf{L} \cdot \mathbf{S} | l m_l' \sigma' \rangle Y_{l m_l'}^*(\hat{k}_n).
 \end{aligned}$$

The magnetic quantum numbers m_l and m_l' are added analytically by means of the operators $L_{\pm} = L_x \pm iL_y$. For further details refer to [109]. Having introduced the Legendre polynomials $P_l(x)$ and their derivatives $P_l'(x)$ with respect to x and y followed by the integration of the spins over the angle yields

$$\langle \mathbf{k}_n \sigma | \mathcal{H}_{SOC} | \mathbf{k}_n' \sigma' \rangle = i \frac{\mathbf{S} \cdot (\mathbf{k}_n \times \mathbf{k}_n')}{k_n k_n'} \sum_l \frac{2l+1}{4\pi} R_{k_n \sigma k_n' \sigma'}^l P_l'(\cos \vartheta), \tag{6.32}$$

in which the vector product of \mathbf{k}_n and \mathbf{k}_n' has been employed. In Eq. (6.32) the following relation has been applied:

$$\begin{aligned}
 \mathbf{S} \cdot (\mathbf{k}_n \times \mathbf{k}_n') &= \langle \sigma | S_x | \sigma' \rangle [\mathbf{k}_n \times \mathbf{k}_n']_x \\
 &\quad + \langle \sigma | S_y | \sigma' \rangle [\mathbf{k}_n \times \mathbf{k}_n']_y \\
 &\quad + \langle \sigma | S_z | \sigma' \rangle [\mathbf{k}_n \times \mathbf{k}_n']_z. \tag{6.33}
 \end{aligned}$$

The contribution to Eq. (6.33), that contains the spins can be derived via the application of the eigenspinors of $\mathbf{S} \cdot \mathbf{B}$ onto both sides of the spin matrices. Here, \mathbf{B} represents an infinitesimal magnetic field. Furthermore, this formula cannot be used if the absolute value of \mathbf{k}_n or \mathbf{k}_n' becomes zero, since this would result in the disappearance of the spin-orbit matrix elements and at the same time the orbital moment in the muffin tin spheres. A benefit of this approach is the omission of the summation over the magnetic quantum numbers m_l and m_l' for the spherical harmonics, which further contributes to the simplification of the computation.

6.6 The Dzyaloshinskii-Moriya Interaction

In the case of two electrons that are localized at the lattice sites i and j , the Hubbard like Hamiltonian may be written as below [110]

$$\mathcal{H} = \mathcal{H}_0^i + \mathcal{H}_0^j + T^{ij} + \mathcal{H}_{SOC}^i + \mathcal{H}_{SOC}^j. \tag{6.34}$$

The first two terms \mathcal{H}_0^i and \mathcal{H}_0^j correspond to the states of the electrons and are composed of the kinetic energy of the particular electron due to its movement around

the nuclei and the Coulomb repulsion. T^{ij} represents the electron hopping between the lattice sites and the spin-orbit contributions at the lattice sites i and j are contained in $\mathcal{H}_{SOC}^i = \xi \mathbf{L}_i \cdot \mathbf{S}_i$ and $\mathcal{H}_{SOC}^j = \xi \mathbf{L}_j \cdot \mathbf{S}_j$, respectively. The three last terms in Eq. (6.34), namely T^{ij} , \mathcal{H}_{SOC}^i and \mathcal{H}_{SOC}^j , may be regarded as a perturbation giving the Hamiltonian of the interactions between the spins \mathbf{S}_i and \mathbf{S}_j the following form

$$\mathcal{H}_{eff} = -J_{ij} \mathbf{S}_i \cdot \mathbf{S}_j + \mathbf{D}_{ij} \cdot (\mathbf{S}_i \times \mathbf{S}_j) + \mathbf{S}_i \mathbf{\Gamma}_{ij} \mathbf{S}_j. \quad (6.35)$$

From second order perturbation theory the Hamilton operator $\mathcal{H}_0^i + \mathcal{H}_0^j + T^{ij}$ results in the well-known isotropic exchange interaction J_{ij} (cf. section 4.2). This symmetric interaction causes, e.g., the energy degeneracy between spin spirals of opposite rotational sense in the absence of SOC. It is of the order of (t_{ij}^2/U) in the expansion of the Hubbard Hamiltonian. Here, U is the Coulomb repulsion and t is the hopping integral. In the next non-vanishing highest order, where SOC is included, the Hamiltonian results in the antisymmetric exchange interaction with the Dzyaloshinskii-vector \mathbf{D}_{ij} . It corresponds to $\xi(t_{ij})^2/U\Delta$ with Δ being an energy difference between two atomic levels. The presence of SOC in systems lacking inversion symmetry causes an anisotropic exchange interaction in the form as below

$$E_{DM} = \mathbf{D}_{ij} \cdot (\mathbf{S}_i \times \mathbf{S}_j), \quad (6.36)$$

where \mathbf{D}_{ij} is a vectorial coupling constant. \mathbf{S}_i and \mathbf{S}_j are the spins at the lattice sites i and j . The interaction in Eq. (6.36) is referred to as *Dzyaloshinskii-Moriya interaction*. It was first suggested as a phenomenological model by I. Dzyaloshinskii [7] in order to motivate the 'weak' ferromagnetism in hematite. T. Moriya provided the theoretical justification of this interaction as an actual effect [8]. Based on the formalism of P. W. Anderson [111] the theory may be comprehended as an extension of the super exchange interaction to spin-orbit coupling. As a consequence the energetic degeneracy of spin spirals with opposite rotational sense is lifted. T. Moriya determined another anisotropic exchange interaction $\mathbf{\Gamma}_{ij}$ in the order of $\xi^2(t_{ij})^2/U\Delta^2$, which will be neglected in the following. Further details of the derivation of the exchange interactions may be found in [8].

In order to estimate the magnitude of the antisymmetric exchange interaction the gyromagnetic ratio g is used. The variation from the value of a free electron is denoted with Δg . The magnitude of \mathbf{D}_{ij} is then given via $|\mathbf{D}|/J \sim \Delta g/g$. Typically, $\Delta g/g$ is smaller than 0.1.³

The behavior of the antisymmetric coupling is motivated likewise via the crystal symmetry without going into detail concerning a particular exchange mechanism. For this purpose I. Dzyaloshinskii and T. Moriya established some rules:

³For $\mathbf{\Gamma}$ applies $|\mathbf{\Gamma}|/J \sim (\Delta g/g)^2$. If $\Delta g/g \leq 0.1$, then $\mathbf{\Gamma}$ obtains a magnitude of about 0.01. From this it follows that the antisymmetric exchange interaction \mathbf{D}_{ij} is the strongest and, therefore, the most important anisotropic coupling of the spins. Hence, the neglect of $\mathbf{\Gamma}$ is justified.

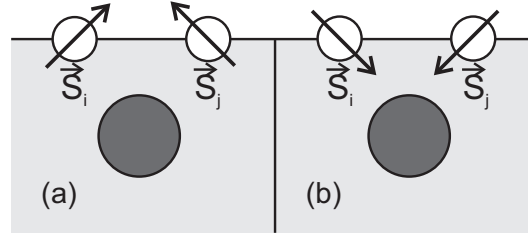


Figure 6.1: Example of the chiral symmetry breaking. The sketch shows two atoms assigned to the spins \mathbf{S}_i and \mathbf{S}_j and a nonmagnetic substrate atom. There is a change in sign of the angle that is enclosed by the spins from configuration (a) to (b). As a result of the spin-orbit interaction the spin and the lattice coordinates couple and (a) and (b) lose their equivalency since the alignment of their spins changes with respect to the third atom.

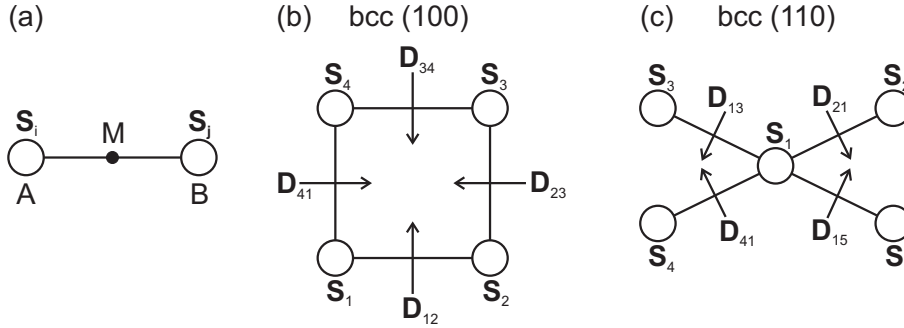


Figure 6.2: (a) Sketch of the points A and B at the lattice sites of the spins \mathbf{S}_i and \mathbf{S}_j and the point M , which bisects the straight line \overline{AB} . (b) \mathbf{D}_{ij} vectors for two lattice sites in the case of a bcc (100) surface. (c) \mathbf{D}_{ij} vectors for two lattice sites in the case of a bcc (110) surface.

The points A and B are located at the lattice sites of the spins \mathbf{S}_i and \mathbf{S}_j and connected via the straight line \overline{AB} (cf. Fig. 6.2 (a)). The point bisecting the straight line \overline{AB} is labeled M . For \mathbf{D}_{ij} applies the following:

- When a center of inversion symmetry is located at M , then $\mathbf{D}_{ij} = 0$.
- When a mirror plane that is perpendicular to \overline{AB} passes through M , then $\mathbf{D}_{ij} \parallel$ mirror plane or $\mathbf{D}_{ij} \perp \overline{AB}$.
- When there is a mirror plane including A and B , then $\mathbf{D}_{ij} \perp$ mirror plane.
- When a two-fold rotation axis that is perpendicular to \overline{AB} passes through M , then $\mathbf{D}_{ij} \perp$ two-fold axis.
- When there is a n -fold axis with $n \geq 2$ along \overline{AB} , then $\mathbf{D}_{ij} \parallel \overline{AB}$.

The first rule reveals that a lack of inversion symmetry is in general a basic condition for the existence of the antisymmetric exchange interaction in a crystal lattice. This plays an important role in particular for surfaces of magnetic materials as they are studied within this thesis, which always lack inversion symmetry. This has been recently demonstrated in experiment and theory for a monolayer of Mn on W(110) [9]. From the above symmetry considerations the direction of the Dzyaloshinskii vector \mathbf{D}_{ij} between two lattice sites can be derived for any crystal symmetry such as in the case of the bcc (110) and (110) surfaces in Fig. 6.2 (b) and (c).

The methods to include SOC in the FLAPW method (cf. section 6.5) cannot be applied directly to spin spirals. The generalized Bloch theorem (Eq. (5.11)) does not hold in the presence of SOC, since the atoms with different magnetization direction are not equivalent anymore, and the translational symmetry is broken. Alternatively, the first variational method is employable in order to calculate the spin structure via the super cell approach. However, the unit cell corresponding to a small spin-spiral vector \mathbf{q} can become very large and, therefore, those calculations may become unfeasible even for today's supercomputers. Therefore, the calculation of the Dzyaloshinskii-Moriya interaction is treated via first order perturbation theory in the FLEUR code [112], since it is linear in the SOC constant ξ . That means the corrections to the band energies are approximately given by the expectation values

$$\langle \psi_{\mathbf{k}',\nu'} | \mathcal{H}_{SOC} | \psi_{\mathbf{k},\nu} \rangle = \left(\langle \psi_{\mathbf{k}',\nu'}^\uparrow | \langle \psi_{\mathbf{k}',\nu'}^\downarrow | \right) \begin{pmatrix} \mathcal{H}_{SOC}^{\uparrow\uparrow} & \mathcal{H}_{SOC}^{\uparrow\downarrow} \\ \mathcal{H}_{SOC}^{\downarrow\uparrow} & \mathcal{H}_{SOC}^{\downarrow\downarrow} \end{pmatrix} \begin{pmatrix} |\psi_{\mathbf{k},\nu}^\uparrow\rangle \\ |\psi_{\mathbf{k},\nu}^\downarrow\rangle \end{pmatrix} \quad (6.37)$$

of the SOC operator \mathcal{H}_{SOC} and the eigenstates $\Psi_{\mathbf{k},\nu}$ to the unperturbed Hamiltonian. This approach only allows for the computation of the antisymmetric exchange as the expectation values vanish for collinear magnetic states. The components of the SOC Hamilton matrix possess the periodicity of the lattice. Therefore, it applies that

$$\begin{aligned} \mathcal{H}_{SOC}^{\sigma\sigma'} \left(e^{\mp i\mathbf{q}\cdot\mathbf{r}/2} f^{\sigma'}(\mathbf{k}, \mathbf{r}) \right) &= e^{\mp i\mathbf{q}\cdot\mathbf{r}/2} f_{SOC}^{\sigma'}(\mathbf{k}, \mathbf{r}) \\ \mathcal{H}_{SOC}^{\sigma\sigma'} \psi_{\nu'}^{\sigma'}(\mathbf{k}, \mathbf{r}) &= e^{\mp i\mathbf{q}\cdot\mathbf{r}/2} f_{SOC}^{\sigma'}(\mathbf{k}, \mathbf{r}), \end{aligned} \quad (6.38)$$

where the $f^{\sigma'}(\mathbf{k}, \mathbf{r})$ and $f_{SOC}^{\sigma'}(\mathbf{k}, \mathbf{r})$ represent any lattice periodic functions. σ denotes the spin alignment \uparrow and \downarrow , respectively. Then, the matrix elements of \mathcal{H}_{SOC} can be expressed as follows

$$\begin{aligned} \langle \psi_{\mathbf{k}',\nu'}^\uparrow | \mathcal{H}_{SOC}^{\uparrow\uparrow} | \psi_{\mathbf{k},\nu}^\uparrow \rangle &= \int d^3 e^{i(\mathbf{k}-\mathbf{k}')\cdot\mathbf{r}} f^{\uparrow\uparrow}(\mathbf{r}), \\ \langle \psi_{\mathbf{k}',\nu'}^\downarrow | \mathcal{H}_{SOC}^{\downarrow\downarrow} | \psi_{\mathbf{k},\nu}^\downarrow \rangle &= \int d^3 e^{i(\mathbf{k}-\mathbf{k}')\cdot\mathbf{r}} f^{\downarrow\downarrow}(\mathbf{r}), \end{aligned} \quad (6.39)$$

$$\begin{aligned}
 \langle \psi_{\mathbf{k}',\nu'}^\downarrow | \mathcal{H}_{SOC}^\downarrow | \psi_{\mathbf{k},\nu}^\uparrow \rangle &= \int d^3 e^{i(\mathbf{k}-\mathbf{k}'-\mathbf{q})\cdot\mathbf{r}} f^{\downarrow\uparrow}(\mathbf{r}), \\
 \langle \psi_{\mathbf{k}',\nu'}^\uparrow | \mathcal{H}_{SOC}^\uparrow | \psi_{\mathbf{k},\nu}^\downarrow \rangle &= \int d^3 e^{i(\mathbf{k}-\mathbf{k}'+\mathbf{q})\cdot\mathbf{r}} f^{\uparrow\downarrow}(\mathbf{r}).
 \end{aligned} \tag{6.40}$$

They are only nonzero if the exponents become zero. Thus, it is sufficient to consider only the diagonal elements, and the Hamilton matrix takes the following form:

$$\langle \psi_{\mathbf{k}',\nu'} | \mathcal{H}_{SOC} | \psi_{\mathbf{k},\nu} \rangle = N (\langle f^\uparrow | f^\uparrow \rangle + \langle f^\downarrow | f^\downarrow \rangle), \tag{6.41}$$

where N specifies the number of chemical unit cells. The Bloch factors cancel each other and as a result the correction to the band energies holds for all atoms.

Then the \mathcal{H}_{SOC} matrix elements for spin-spiral states are expressed explicitly in terms of the LAPW basis. Since the spin-orbit contribution is rather small in the interstitial region, the calculation of the \mathcal{H}_{SOC} matrix elements is performed within the muffin tins, where the basis functions are given in Eq. (3.5) and (3.16):

$$\varphi_{\mathbf{G}}^{\tilde{\sigma}}(\mathbf{k}, \mathbf{r}) = \sum_L \left(A_L^{\mu\mathbf{G}\tilde{\sigma}}(\mathbf{k}) u_l^{\tilde{\sigma}}(r) + B_L^{\mu\mathbf{G}\tilde{\sigma}}(\mathbf{k}) \dot{u}_l^{\tilde{\sigma}}(r) \right) Y_L(\hat{\mathbf{r}}). \tag{6.42}$$

Here, L abbreviates the quantum numbers l and m . In order to distinguish the spin indices of the local (muffin tin dependent) spin coordinate frame from the ones defined in the global coordinate frame, the first are marked with tildes ($\tilde{}$). Then, the expansion of the wave functions $\tilde{\psi}_{\mathbf{k},\nu}$ reads:

$$\tilde{\psi}_{\mathbf{k},\nu} = \sum_{\mathbf{G}} \begin{pmatrix} C_{\mathbf{G},\mathbf{k},\nu}^{\uparrow} \varphi_{\mathbf{G}}^{\uparrow} \\ C_{\mathbf{G},\mathbf{k},\nu}^{\downarrow} \varphi_{\mathbf{G}}^{\downarrow} \end{pmatrix} = \sum_L Y_L(\vartheta, \varphi) \begin{pmatrix} a_{\mathbf{k},\nu,L}^{\uparrow} u_l^{\uparrow}(r) + b_{\mathbf{k},\nu,L}^{\uparrow} \dot{u}_l^{\uparrow}(r) \\ a_{\mathbf{k},\nu,L}^{\downarrow} u_l^{\downarrow}(r) + b_{\mathbf{k},\nu,L}^{\downarrow} \dot{u}_l^{\downarrow}(r) \end{pmatrix} \tag{6.43}$$

where the coefficients $A_L^{\mu\mathbf{G}\tilde{\sigma}}(\mathbf{k})$ and $B_L^{\mu\mathbf{G}\tilde{\sigma}}(\mathbf{k})$ are introduced via

$$a_{\mathbf{k},\nu,L}^{\tilde{\sigma}} = \sum_{\mathbf{G}} c_{\mathbf{k},\nu,\mathbf{G}}^{\tilde{\sigma}} A_L^{\mu\mathbf{G}\tilde{\sigma}}(\mathbf{k}) \quad \text{and} \quad b_{\mathbf{k},\nu,L}^{\tilde{\sigma}} = \sum_{\mathbf{G}} c_{\mathbf{k},\nu,\mathbf{G}}^{\tilde{\sigma}} B_L^{\mu\mathbf{G}\tilde{\sigma}}(\mathbf{k}). \tag{6.44}$$

Then, the wave functions are rotated from the local to the global coordinate frame. The A and B coefficients of the muffin tin in the global frame read

$$a_{\mathbf{k},\nu,L}^{\sigma'\tilde{\sigma}} = \mathbf{U}_{MT}^{\sigma'\tilde{\sigma}} \sum_{\mathbf{G}} a_{\mathbf{k},\nu,L}^{\tilde{\sigma}} \quad \text{and} \quad b_{\mathbf{k},\nu,L}^{\sigma'\tilde{\sigma}} = \mathbf{U}_{MT}^{\sigma'\tilde{\sigma}} \sum_{\mathbf{G}} b_{\mathbf{k},\nu,L}^{\tilde{\sigma}}. \tag{6.45}$$

The wave functions are further rotated until their coordinate frame corresponds to

the real-space coordinate frame denoted with the index rs :

$$\langle \psi_{\mathbf{k}',\nu'} | \mathbf{U}_{rs}^\dagger \mathcal{H}_{SOC} \mathbf{U}_{rs} | \psi_{\mathbf{k},\nu} \rangle = \int_{MT} \psi_{\mathbf{k}',\nu'}^\dagger(\mathbf{r}) \mathbf{U}_{rs}^\dagger \mathcal{H}_{SOC} \mathbf{U}_{rs} \psi_{\mathbf{k},\nu}(\mathbf{r}) d^3r. \quad (6.46)$$

Since the angular momentum operator \mathbf{L} commutes with the spherically symmetric functions, the real-space integration of the matrix elements is split into an angular and a radial part. Employing Eq. (6.9) gives the following expression of the angular integrals

$$\mathcal{A}_{l,m',m}^{\sigma'\sigma} = \int_0^\pi d\vartheta \int_0^{2\pi} d\varphi (-\sin\vartheta) Y_{l,m}(\vartheta, \varphi)^* L^{\sigma'\sigma} Y_{l,m}(\vartheta, \varphi). \quad (6.47)$$

The radial integrals are given as

$$\begin{aligned} \mathcal{R}_{l,u,u}^{\tilde{\sigma}'\tilde{\sigma}} &= \int_0^{R_{MT}} dr r^2 \xi u_l^{\tilde{\sigma}'}(r) u_l^{\tilde{\sigma}}(r) \quad , \quad \mathcal{R}_{l,u,\dot{u}}^{\tilde{\sigma}'\tilde{\sigma}} = \int_0^{R_{MT}} dr r^2 \xi u_l^{\tilde{\sigma}'}(r) \dot{u}_l^{\tilde{\sigma}} \\ \mathcal{R}_{l,\dot{u},u}^{\tilde{\sigma}'\tilde{\sigma}} &= \int_0^{R_{MT}} dr r^2 \xi \dot{u}_l^{\tilde{\sigma}'}(r) u_l^{\tilde{\sigma}}(r) \quad , \quad \mathcal{R}_{l,\dot{u},\dot{u}}^{\tilde{\sigma}'\tilde{\sigma}} = \int_0^{R_{MT}} dr r^2 \xi \dot{u}_l^{\tilde{\sigma}'}(r) \dot{u}_l^{\tilde{\sigma}}(r) \end{aligned} \quad (6.48)$$

Introducing

$$\begin{aligned} \mathcal{T}^{\sigma',\sigma} &= \sum_{l,m',m} \sum_{\tilde{\sigma}'\tilde{\sigma}} \mathcal{A}_{l,m',m}^{\tilde{\sigma}'\tilde{\sigma}} \left(a_{\mathbf{k}',\nu',l,m'}^{\sigma'\tilde{\sigma}'*} a_{\mathbf{k},\nu,l,m}^{\sigma\tilde{\sigma}} \mathcal{R}_{l,u,u}^{\tilde{\sigma}'\tilde{\sigma}} \quad + \quad a_{\mathbf{k}',\nu',l,m'}^{\sigma'\tilde{\sigma}'*} b_{\mathbf{k},\nu,l,m}^{\sigma\tilde{\sigma}} \mathcal{R}_{l,u,\dot{u}}^{\tilde{\sigma}'\tilde{\sigma}} \right. \\ &\quad \left. + b_{\mathbf{k}',\nu',l,m'}^{\sigma'\tilde{\sigma}'*} a_{\mathbf{k},\nu,l,m}^{\sigma\tilde{\sigma}} \mathcal{R}_{l,\dot{u},u}^{\tilde{\sigma}'\tilde{\sigma}} \quad + \quad b_{\mathbf{k}',\nu',l,m'}^{\sigma'\tilde{\sigma}'*} b_{\mathbf{k},\nu,l,m}^{\sigma\tilde{\sigma}} \mathcal{R}_{l,\dot{u},\dot{u}}^{\tilde{\sigma}'\tilde{\sigma}} \right) \end{aligned} \quad (6.49)$$

the expectation value results in

$$\Delta E = \langle \psi_{\mathbf{k}',\nu'} | \mathbf{U}_{rs}^\dagger \mathcal{H}_{SOC} \mathbf{U}_{rs} | \psi_{\mathbf{k},\nu} \rangle = \begin{cases} \mathcal{T}^{\uparrow\uparrow} + \mathcal{T}^{\downarrow\downarrow} & \mathbf{k}' = \mathbf{k}, \\ \mathcal{T}^{\uparrow\downarrow} & \mathbf{k}' = \mathbf{k} + \mathbf{q}, \\ \mathcal{T}^{\downarrow\uparrow} & \mathbf{k}' = \mathbf{k} - \mathbf{q}, \\ 0 & \text{else.} \end{cases} \quad (6.50)$$

7 Spin Frustration on a Triangular Lattice: Cr/Pd(111)

Among the $3d$ transition metals only Cr and Mn exhibit antiferromagnetism. In particular, Cr is not only a prototypical antiferromagnet, but, in addition, it also reveals an antiferromagnetic spin-density wave in its bulk bcc phase due to Fermi-surface nesting. The spin-density wave in Cr can give rise to the formation of magnetic superstructures. For instance, at the Cr(001) surface an enhancement of magnetic moments is observed due to the reduction of the coordination number. This causes topological antiferromagnetism between ferromagnetic terraces that are separated by monoatomic steps as it has been theoretically predicted by *ab initio* calculations [113] and detected by spin-polarized scanning tunneling microscopy [114, 115]. For ultrathin films the magnetic properties of Cr depend on the exchange coupling between neighboring magnetic moments. Therefore, they are sensitive to the in-plane lattice constant of the surface as well as the hybridization with the substrate. It was reported that a monolayer (ML) of Cr on the (110) surface of W shows a local antiferromagnetic order [116]. On the other hand, a Cr monolayer adsorbed to the (001) surface of W was predicted to exhibit a ferromagnetic alignment [117].

Evidently, the surface orientation plays a crucial role for the magnetism in Cr. This has been further predicted for Cr monolayers on (111) surfaces of the noble metals Ag and Cu [118, 119]. In such triangular lattices the main characteristic of a two-dimensional antiferromagnet, i.e., the antiparallel alignment of neighboring magnetic moments, is no longer satisfied (see Fig. 7.1). This leads to a topological frustration of the spins giving rise to a row-wise antiferromagnetic state or more

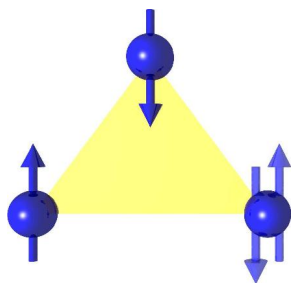


Figure 7.1: Topologically frustrated two-dimensional antiferromagnet on a triangular lattice.

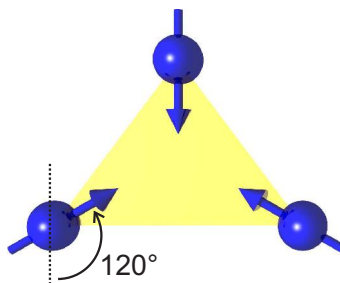


Figure 7.2: The Néel state on a triangular lattice. The magnetic moments enclose an angle of 120° .

complex magnetic structures, such as spin spirals or the Néel state – a configuration that is characterized by magnetic moments enclosing an angle of 120° as illustrated in Fig. 7.2. The Néel state has first been observed experimentally only in a Mn monolayer on the (111) surface of Ag [120]. However, this discovery conflicts with theoretical calculations performed within the DFT, which predict a row-wise anti-ferromagnetic state [118].

In systems such as the monolayers of Mn or Cr on Ag(111) the formation of alloys due to intermixing is problematic. This difficulty can be avoided by choosing substrates such as Pd(111), where the surface energy and thus the hybridization of the magnetic thin film with the substrate is different. The difference in hybridization and the in-plane lattice constant leads to a change in the exchange coupling of the system, which can induce non-collinear magnetic order such as the Néel state.

In order to shed light onto this issue, in this chapter the magnetism of a single monolayer of Cr on Pd(111) is investigated. This happens by means of DFT calculations that are compared to experimental results obtained by spin-polarized STM. First, the stacking of the film as well as the collinear magnetic ordering, i.e., ferromagnetic or antiferromagnetic, is examined. By studying the energy dispersion of spin-spiral structures on a freestanding monolayer of Cr(111) and Cr deposited on Pd(111) the influence of the substrate onto the magnetic exchange interactions will be analyzed that results in a non-collinear magnetic ground state. The comparison of simulated spin-polarized STM images of the spin-spiral state with the experimental data allows for the identification of the $(\sqrt{3} \times \sqrt{3})$ superstructure as Néel state. Moreover, the direct comparison of the simulated spin-polarized STM images with the experimental results allows for the estimation of the magnetization direction of the tip with respect to the magnetization direction of the sample.

Parts of this chapter have been published in Physical Review B [58].

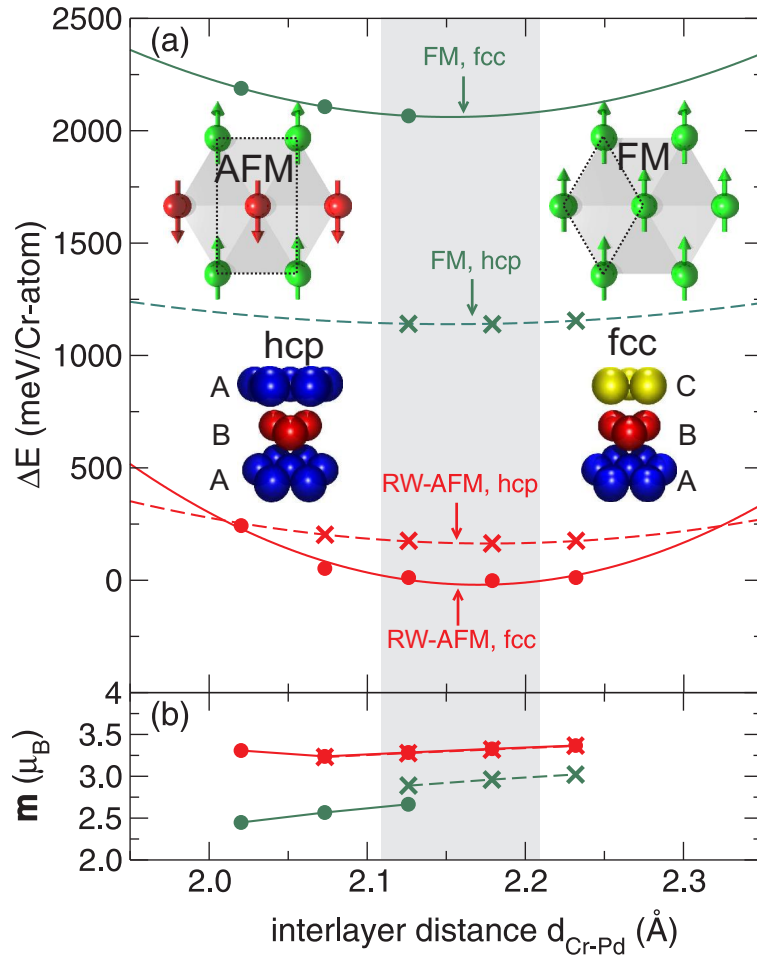
7.1 Computational Details

The *ab initio* calculations have been carried out within the GGA [33] if not stated otherwise. For the structural relaxation the theoretical lattice constant of Pd ($a_{Pd} = 3.981 \text{ \AA}$ [121]) has been used. A symmetric film consisting of seven monolayers Pd(111) with one monolayer Cr on each side has been applied. A mesh of 72 \mathbf{k}_{\parallel} points in the irreducible wedge of the two-dimensional Brillouin zone has been employed as well as about 160 basis functions per atom. To calculate the spin spirals an asymmetric film consisting of six layers of Pd(111) and one layer of Cr in fcc stacking has been employed. The structural relaxations were adopted from the row-wise antiferromagnetic state and it was made use of 1024 \mathbf{k}_{\parallel} points in the entire two-dimensional Brillouin zone as well as about 110 basis functions per atom.

7.2 Structural Properties of Cr/Pd(111)

First, the Cr stacking on the Pd(111) substrate was checked. The stacking types differ by the sequence of the layers, i.e., in the *face-centered cubic* (fcc) stacking the atoms alternate between three positions, while in the *hexagonal close-packed* (hcp) stacking the atoms of every other layer reside above the atoms of the first layer (cf. sketches in Fig. 7.3 (a)). For both stacking types the parallel (FM) and the antiparallel (RW-AFM) alignment of the magnetic moments have been investigated (see insets in Fig. 7.3 (a)). Then, the Cr monolayer has been geometrically relaxed by varying the interlayer distance for the FM and the RW-AFM configuration in both stackings. From Fig. 7.3 (a) it can be directly concluded that a parallel alignment of the magnetic moments, i.e., ferromagnetic order, is energetically highly unfavorable with about 1 eV difference in total energy compared to the antiparallel arrangement. The fcc stacking is more favorable in the RW-AFM structure than the hcp stacking with an energy difference of 162 meV. This is consistent with the results of the

Figure 7.3: (a) Total energy calculations depending on the interlayer distance d_{Cr-Pd} between Cr and Pd for collinear antiferromagnetic (RW-AFM) and ferromagnetic (FM) configurations depicted in the sketches. The abbreviations “hcp” and “fcc” refer to “hexagonal close packed” and “face centered cubic”, respectively. (b) The magnetic moments depending on the interlayer distance, the magnetic configuration and the stacking.



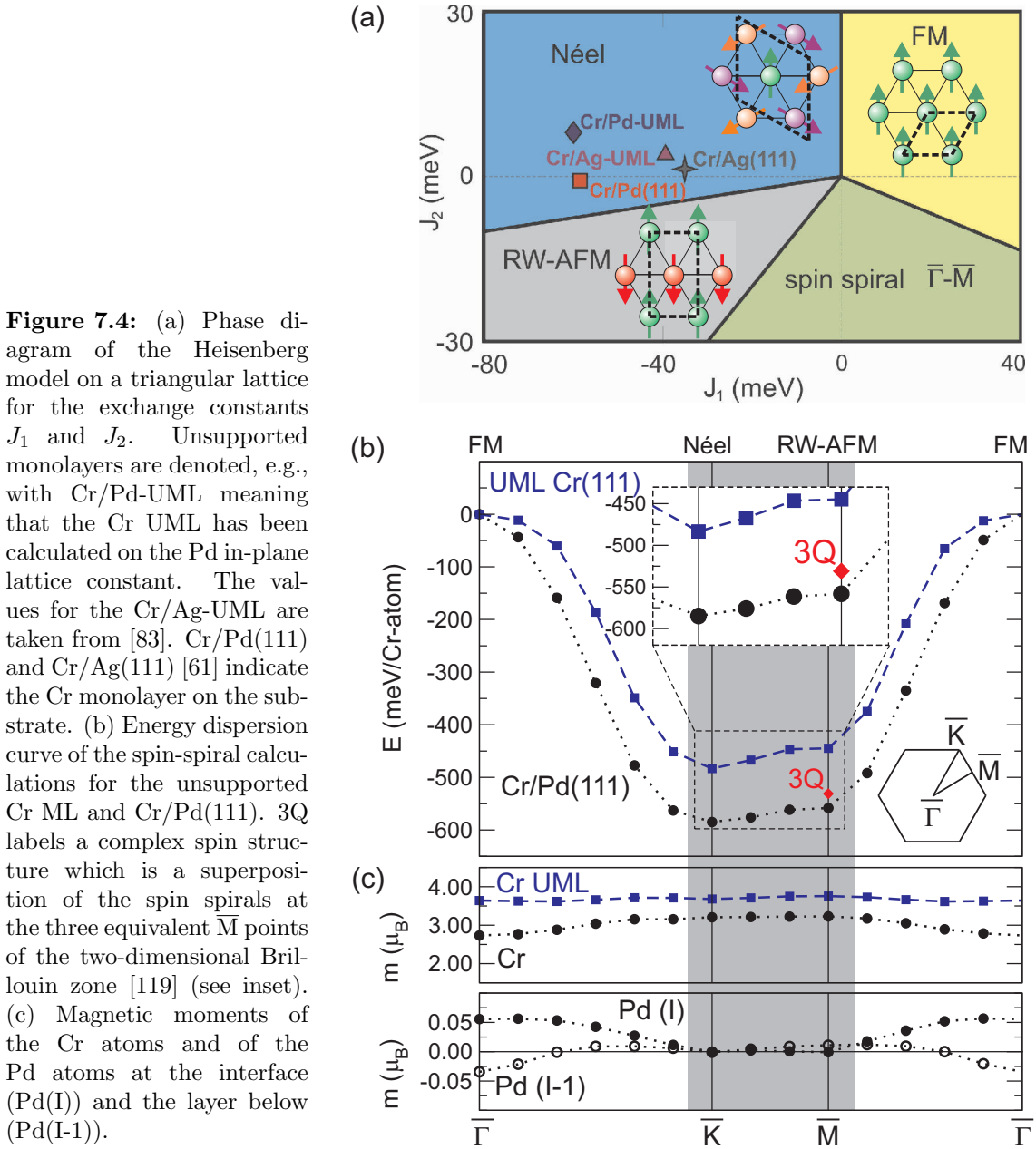
spin-polarized STM measurements, where the fcc stacking of the Pd(111) surface was observed to be continued in the Cr monolayer [58]. Finally, the results of the structural relaxations in Fig. 7.3 (a) yield an inward relaxation by 1.7 % leading to an interlayer distance of 2.17 Å for the RW-AFM state and the fcc stacking in Cr on Pd(111).

Fig. 7.3 (b) displays the magnetic moments of the FM and the RW-AFM state in both stacking types as a function of the interlayer distance. For the FM configurations in both stackings the magnetic moments are relatively small ($\approx 2.5 \mu_B$ and $\approx 2.9 \mu_B$) compared with those obtained for the RW-AFM configurations. Obviously, the stacking has no strong influence on the magnetic moments, since they are identical in the RW-AFM configuration for both, the hcp and the fcc stacking, with an absolute value of about $3.3 \mu_B$. However, the different values obtained for the magnetic moments of the FM and the RW-AFM configurations hint at a strong intra-atomic exchange, and explain the large energy difference of about 1 eV between those states.

7.3 The Néel state of Cr/Pd(111)

In order to investigate the magnetic behavior of the Cr monolayer on the Pd(111) surface, spin spirals have been considered, since they allow to explore a vast part of the magnetic phase space. The spin-spiral vector \mathbf{q} has been chosen along the high symmetry lines of the two-dimensional Brillouin zone sketched in Fig. 7.4 (b). The resulting energy dispersion curve $E(\mathbf{q})$ is plotted in Fig. 7.4 (b) for Cr on Pd(111) as well as for the unsupported monolayer (UML) of Cr on the Pd in-plane lattice constant. Both curves display a global minimum at the \bar{K} point, which corresponds to the Néel state. While the Cr UML shows an energy difference of about -39 meV/Cr-atom compared to the row-wise antiferromagnetic state (RW-AFM), the Cr monolayer on Pd has a slightly smaller difference in energy between \bar{K} and \bar{M} of -27 meV, which is due to the hybridization with the substrate. The magnetic moments of Cr (Fig. 7.4 (c)) also decrease from $3.68 \mu_B$ in the Cr UML to $3.21 \mu_B$ in Cr on the Pd(111) surface due to the hybridization. Additionally, the hybridization leads to induced magnetic moments in the Pd that are significant in the vicinity of the ferromagnetic state solely. Considering that they are equidistant from antiparallel magnetic moments of atoms in the Cr monolayer they become zero in the RW-AFM state and the Néel state. Furthermore, it has been checked that the predicted ground state does not depend on the exchange-correlation potential. Using the LDA [122] the Néel state is still in favor with an energy difference of -55 meV with respect to the RW-AFM state.

Spin-spiral calculations are not only useful to determine the system's magnetic ground state, but also they offer the opportunity to learn more about the exchange mechanisms. The exchange interaction is studied by fitting Eq. (4.30), i.e., $E(\mathbf{q}) =$



$-NS^2J(\mathbf{q})$, to the energy dispersion curve. According to Eq. (4.32) the Fourier transforms of the Heisenberg exchange parameters have the following form:

$$J(\mathbf{q}) = \sum_{\delta} J_{0\delta} e^{-i\mathbf{q}\mathbf{R}_{\delta}}. \quad (7.1)$$

The spin-spiral vector can be expressed as $\mathbf{q} = (q_1, q_2)$. For the direction $\bar{\Gamma} - \bar{K} - \bar{M}$ it applies that $q_1 = q$ and $q_2 = \frac{1}{2}q$ with $0 \leq q \leq 1$ and $q \in \mathbb{Q}$. Here, $q = \frac{2}{3}$ corresponds

	$J_1 S^2$ (meV)	$J_2 S^2$ (meV)	$J_3 S^2$ (meV)	$J_4 S^2$ (meV)
Cr UML	-59.9	+7.9	+7.2	+1.1
Cr/Pd(111)	-58.4	-1.5	+3.4	+0.7

Table 7.1: Heisenberg exchange parameters of an unsupported monolayer of Cr on the Pd(111) lattice constant (Cr-UML) and a monolayer deposited on the Pd(111) surface obtained by fitting the expression in (7.2) to the curves in Fig. 7.4.

to \bar{K} and $q = 1$ to \bar{M} . Performing the summation and making use of the relation $\mathbf{R}_i \cdot \mathbf{G}_k = 2\pi\delta_{ik}$ results in

$$\begin{aligned}
J_{\Gamma-K-M}(q) = & 2J_2 + 2J_6 \\
& + \cos(\pi q) [4J_1 + 4J_5] \\
& + \cos(2\pi q) [2J_1 + 4J_3 + 4J_7] \\
& + \cos(3\pi q) [4J_2 + 4J_5] \\
& + \cos(4\pi q) [2J_3 + 4J_4] \\
& + \cos(5\pi q) [4J_4 + 4J_7] \\
& + \cos(6\pi q) [2J_5 + 4J_6] \\
& + \cos(7\pi q) [4J_7].
\end{aligned} \tag{7.2}$$

By fitting this expression to the energy dispersion curve in Fig. 7.4 (b) the Heisenberg exchange parameters can be obtained. The nearest-neighbor exchange in both, the Cr UML on the Pd(111) lattice constant and the Cr monolayer on Pd(111), is rather large and negative, i.e., antiferromagnetic, with values of $J_{1,Cr} = -59.9$ meV and $J_{1,Cr/Pd} = -58.4$ meV, respectively. This is reflected in the large energy difference between the FM state, the RW-AFM and the Néel state, observed in the spin-spiral dispersion curve. The second-nearest-neighbor exchange results in $J_{2,Cr} = +7.9$ meV and $J_{2,Cr/Pd} = -1.5$ meV and for the third-nearest neighbors values of $J_{3,Cr} = +7.2$ meV and $J_{3,Cr/Pd} = +3.4$ meV are found. The first-nearest-neighbor exchange clearly dominates the exchange beyond nearest neighbors. Moreover, the presence of the Pd(111) surface keeps it nearly unaffected, while the exchange interactions beyond nearest neighbors decrease for Cr on Pd(111) compared to the Cr UML. The $J_1 - J_2$ phase diagram drawn in Fig. 7.4 (a) has been used to interpret the results of the spin-spiral calculations. It is separated into four phases: a ferromagnetic phase, an antiferromagnetic phase, a phase of the Néel state and a phase containing spin spirals occurring along the $\bar{\Gamma} - \bar{M}$ high symmetry line. The Cr monolayer on Pd(111) is located close to the $J_2 = 0$ axis. By enlarging the lattice constant, for instance, by choosing the in-plane lattice constant of the Ag(111) surface, the antiferromagnetic nearest-neighbor exchange is reduced [61, 83].

Besides topological frustration of antiferromagnetic exchange interaction on a tri-

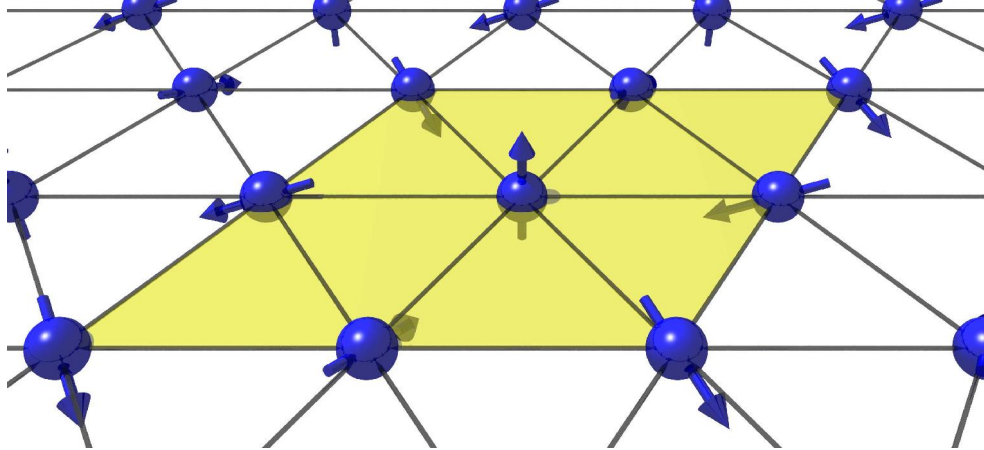


Figure 7.5: A sketch of the $3Q$ state.

angular lattice, which can lead to the occurrence of the Néel state, there are other mechanisms that can give rise to complex magnetic structures. In section 4.2 higher-order spin interactions have been introduced. These interactions can lower the energy of so-called multi- Q states with respect to spin spirals. Multi- Q states represent magnetic configurations that are superpositions of spin-spirals under the constraint of a constant magnetic moment for each atom. For example, the $3Q$ -state which is a linear combination of the spin spirals at the three equivalent \bar{M} points of the hexagonal two-dimensional Brillouin zone. This state has previously been proposed as the magnetic ground state of Mn on Cu(111) [123]. It is characterized by the tetrahedron angle ($\theta = 109.5^\circ$) between the magnetic moments (cf. Fig. 7.5). Within the Heisenberg model the $3Q$ state and the row-wise antiferromagnetic structure (spin-spiral with \mathbf{q} at \bar{M} point) are degenerate. However, higher-order spin interactions, which in a DFT calculation are implicitly included in the exchange-correlation potential, lift this degeneracy. In the case of the monolayer Cr on Pd(111) the $3Q$ state is by about 24 meV/Cr-atom unfavorable compared with the RW-AFM state (cf. Fig. 7.4 (b)). This shows that higher-order spin interactions are non-negligible in this system. However, the $3Q$ state is +51 meV/Cr-atom higher in energy than the Néel state, which is the state with the lowest energy among all the explored configurations.

7.4 Experimental Verification of the Néel State

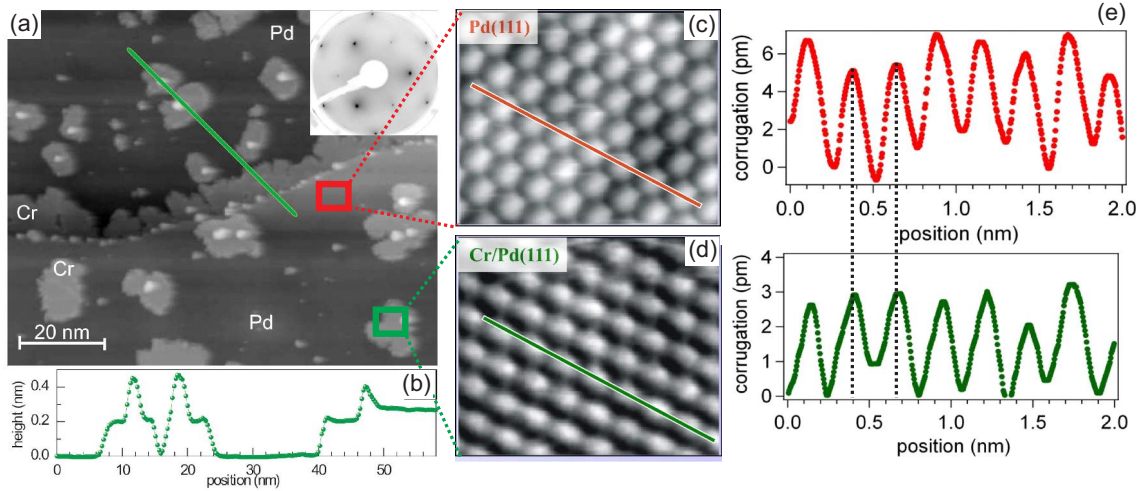


Figure 7.6: (a) A topography image of the Pd(111) surface with about 30% coverage of Cr at $T=200$ K. The inset shows the LEED pattern of the Cr submonolayer immediately after the deposition at $E = 140$ eV. (b) Line profile along the line in (a). (c) Atomically resolved STM image of the Pd(111) surface and (d) the monolayer of Cr on the Pd(111) surface at $T=200$ K. (e) The panels show the corresponding line profiles along the lines indicated in the STM images in (c) and (d).

7.4.1 Experimental Details

The spin-polarized scanning tunneling microscopy experiments were performed in an ultrahigh vacuum system with a base pressure below 1×10^{-10} mbar. The Pd(111) crystal was prepared by annealing to 870 K. Afterwards, the Cr was deposited by molecular-beam epitaxy while the sample was held at a temperature of 200 K. It was immediately transferred to the STM in order to avoid intermixing between the Cr and Pd atoms. For the measurements with atomic resolution chemically etched tungsten tips were employed. By evaporating Cr on these tips with a layer thickness of about 50 monolayers the STM tips for the magnetic measurements were prepared. They are sensitive to an in-plane magnetization. All STM images were measured in the constant current mode at a temperature of 5 K.

At a temperature of 200 K the submonolayer coverage of Cr grows in irregular shaped islands continuing the fcc stacking of the Pd substrate (Fig. 7.6 (a)). On top of these islands the second monolayer of Cr appears, which is also observed in the line profile displayed in Fig. 7.6 (b). Furthermore, it provides the fact that the steps of the Pd substrate act as sinks for the Cr atoms. In order to investigate if the Cr monolayer arranges pseudomorphically, i.e., it grows with the same in-plane

lattice constant as the Pd substrate, low-energy electron-diffraction (LEED) has been applied at an energy of $E=140$ eV. These measurements reveal that the Cr layer is free from dislocation network (compare with inset in Fig. 7.6 (a)), since they show a clear $p(1 \times 1)$ pattern lacking of any additional structures around the spots. The atomically resolved Pd(111) surface and an island of the submonolayer deposition of Cr on the Pd(111) surface presented in Fig. 7.6 (c) and (d) exhibit a structure that clearly corresponds to the chemical unit cell illustrated in Fig. 7.3. It demonstrates the pseudomorphic growth of the Cr monolayer on top of the Pd(111) surface. This is further emphasized by the line profiles shown in Fig. 7.6 (e), where the maxima correspond to the atoms of Pd and Cr, respectively. The distance between the maxima agrees with the interatomic distance of 2.71 \AA between Pd atoms in the single crystal.

7.4.2 Spin-Polarized STM Images: Theory vs. Experiment

Based on the DFT results the Néel state is proposed as the magnetic ground state of the monolayer Cr on Pd(111). In order to confirm this prediction, the images obtained in the spin-polarized STM experiments are compared with those computed by means of first-principles calculations (cf. Fig. 7.7). The simulated STM images have been calculated within the framework of the spin-polarized Tersoff-Hamann model [61] introduced in section 4.3.

Figure 7.7 (a) displays the STM measurement of the Cr monolayer on Pd(111) with a bare W tip, i.e., it shows the nonmagnetic chemical contrast. The comparison with the line profiles in Fig. 7.7 (e) as well as with the simulated STM image in Fig. 7.7 (i) allows for attributing the observed protrusions to the Cr atoms. The spin-polarized STM measurements carried out with magnetically sensitive Cr coated W tips produce three qualitatively different contrasts (Fig. 7.7 (b)-(d)). While two images, Fig. 7.7 (b) and (c), show a hexagonal pattern, Fig. 7.7 (d) features a threefold symmetry. Compared to the chemical unit cell these images are rotated by 30° . From the line profiles in Fig. 7.7 (f) and (g), respectively, it follows that the distance between protrusions is of 0.46 nm corresponding to a $\sqrt{3} \times \sqrt{3}$ unit cell of the Pd(111) surface.

While it is known that the Cr coated W tips are sensitive to an in-plane magnetization [124] the actual orientation within the plane is uncertain and can change from one measurement to the other. On the one hand, this is an advantage in order to observe different spin-polarized STM contrasts of a spin structure. On the other hand, a comparison with the theoretical calculations is needed in order to identify the real tip's in-plane magnetization direction. This has been done for the STM images in Fig. 7.7 (b)-(d). Depending on the magnetization direction \hat{e}_T of the tip with respect to the sample's magnetization the spin-polarized STM images of the Néel structure exhibit three different spin-polarized STM contrasts [61, 118]. For instance, if the tip magnetization is fully aligned to one of the Cr moments of

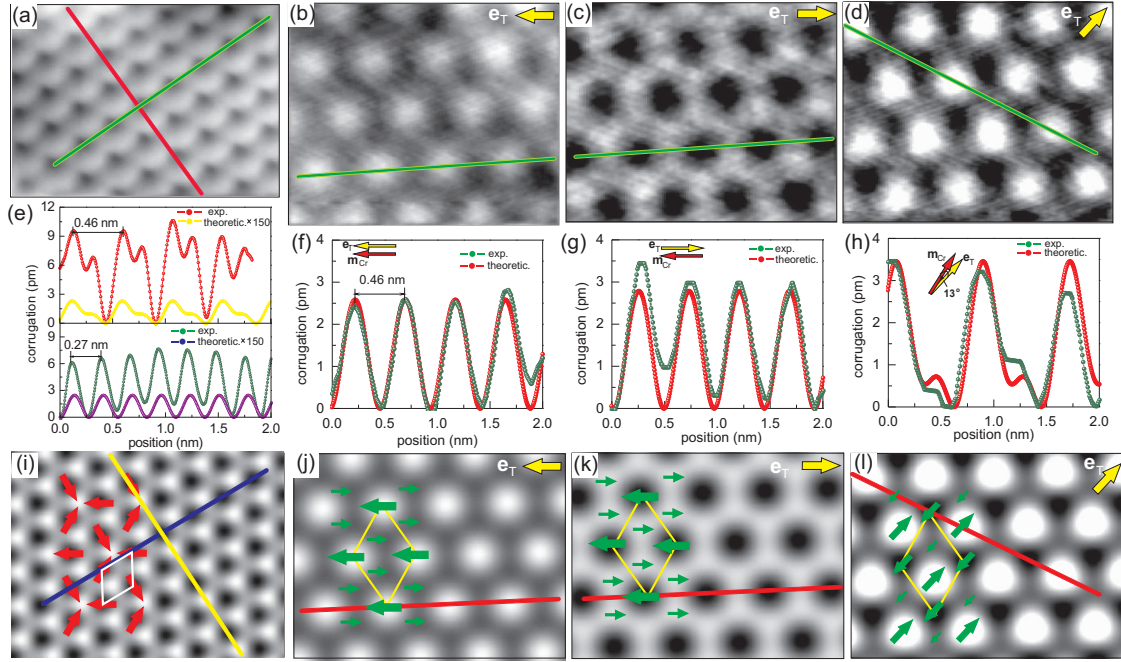


Figure 7.7: STM images of the Cr monolayer on Pd(111) measured with a bare W tip (a) (nonmagnetic) and three different Cr coated W tips ((b)-(d)) (magnetic). In every image the scan size is about $2.0 \text{ nm} \times 1.7 \text{ nm}$, and the tunneling parameters are $U = 14.1 \text{ mV}$ and $I = 6.7 \text{ nA}$. (e)-(h) Line sections along the lines indicated in (a)-(d) in comparison with the theoretical line sections obtained from [(i)-(l)]. The theoretical STM images (i)-(l) were calculated within the framework of the spin-polarized Tersoff-Hamann model [61] assuming a tip-spin polarization of $P_T = 0.18$ and a tip-sample distance of 4.2 \AA . The arrangement of the magnetic moments assumed in the calculation of the Néel state is indicated in (i) by red arrows representing the magnetic moments of the Cr atoms and enclosing an angle of 120° . For (j)-(k) the projection of the magnetic moments onto the tip magnetization direction ($\hat{e}_T \mathbf{m}_{Cr} \hat{e}_T$) is denoted by green arrows. The chemical and the magnetic unit cell are shown as a white and a yellow rhombus, respectively.

this threefold spin arrangement, the magnetic moments of the other two Cr atoms project equally onto the tip (compare with the green arrows in Fig. 7.7 (j)). This leads to a maximum in the contrast of the spin-polarized STM image, Fig. 7.7 (b) and (j). The same applies for an antiparallel alignment of the tip magnetization direction with one of the Cr magnetic moments. But instead of a maximum at the position of the Cr atom, the pattern of the spin-polarized STM contrast is inverted and exhibits a minimum (cf. Fig. 7.7 (c) and (k)). Finally, a tip that is neither parallel nor antiparallel magnetized with respect to one of the Cr moments causes a threefold pattern, since the Cr moments are all projected differently onto the tip magnetization (cf. Fig. 7.7 (d) and (l)).

In Fig. 7.7 (f) - (h) the quantitative comparison between the theoretical and the

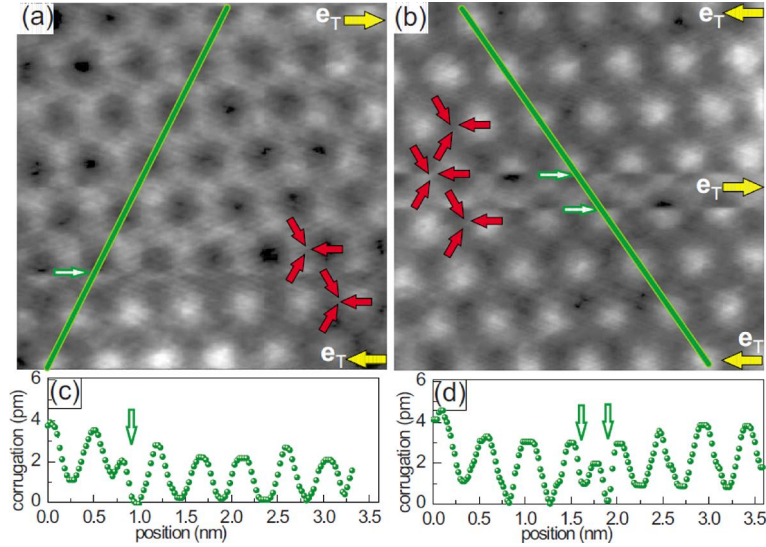


Figure 7.8: (a) and (b) Spin-polarized STM images exhibiting a magnetic switching event of the spin-polarized STM tip resulting in a sudden reversal of the magnetic contrast. The scan size is about $3 \text{ nm} \times 3 \text{ nm}$ and the tunneling parameters are $U = 14.1 \text{ mV}$ and $I = 7.7 \text{ nA}$. Arrows indicate the magnetization direction of the tip (yellow) and the Cr moments (red), respectively. (c) and (d) show the line profiles taken along the green lines in (a) and (b), respectively.

experimental line profiles is displayed. Due to identical tunneling parameters used for all spin-polarized STM images a constant tip-sample distance may be expected. For a tip-sample distance of 4.2 \AA a tip-spin polarization of $P_T = 0.18$ is needed in order to reproduce the experimental results quantitatively. Increasing the tip-sample distance to 5 \AA , for example, results in a tip-spin polarization of $P_T = 0.4$, while the choice of the bias voltage between -50 and $+50 \text{ mV}$ has only little effect onto the tip's polarization. Furthermore, the good agreement between the experimental results and the theoretical calculations allows the estimation of the angle between the tip magnetization and the magnetic moment of one of the Cr atoms for the tip alignment drawn in Fig. 7.7 (d). In the case of 4.2 \AA as tip-sample distance and a polarization of $P_T = 0.18$ the best fit is given by an angle of 17° between the tip and the Cr magnetization. This result provides also a good agreement for the spin-polarized STM images displayed in Fig. 7.7 (d) and Fig. 7.7 (l).

7.4.3 Tip Magnetization Switching Events

As mentioned in the previous section the Cr coated tips may change their magnetization direction while scanning. Furthermore, it was observed that the magnetization of the tip's apex atom reversed during the measurement as displayed in the lower part of Fig. 7.8 (a). There are several mechanisms that can cause the magnetic switching of the tip such as the magnetic exchange interaction between the tip and

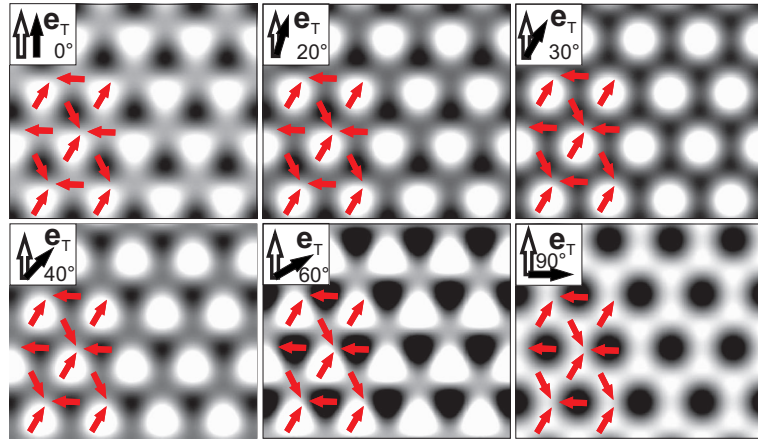


Figure 7.9: Different spin-polarized STM contrasts for varying tip magnetization directions simulated within the spin-polarized Tersoff-Hamann model [61]. The rotation angle of the tip magnetization ranges from 0° to 90° .

the sample [125] or the spin-transfer torque induced by a spin-polarized tunneling current [126]. In the upper part of Fig. 7.8 (a) the tip magnetization is aligned antiparallel to the magnetic moment of one of the Cr atoms and the Cr atoms appear as protrusions like in Fig. 7.7 (c). In the lower part the spin-polarized STM tip experiences a magnetic switching event leading to an inverted contrast with respect to the upper part due to the parallel alignment of the tip magnetization and the Cr moments. The magnetic switching event also shows in the line profiles taken along the lines in Fig. 7.8 (a) and (b) and displayed in Fig. 7.8 (c) and (d).

In order to study the effects of the tip magnetization direction onto the magnetic contrast, spin-polarized STM images were simulated within the spin-polarized Tersoff-Hamann model [61]. The results of these simulations are displayed in Fig. 7.9 starting from the alignment in which all the Cr moments have different projection onto the tip (0°). Varying the angle enclosed by the magnetization direction of the tip and the Cr moments between 0° and 90° produces basically two contrasts: (i) one with a threefold symmetry and triangular shaped moments at 0° and (ii) one with a hexagonal symmetry and circular shaped magnetic moments for 30° and 90° . For a tip magnetization aligned to any direction in between those values, the magnetic contrast takes the form of a superposition of both contrasts.

In conclusion, the switching of the tip magnetism reverses the magnetic contrast. Therefore, switching events of the tip magnetization can be further regarded as an additional evidence in order to demonstrate the origin of the magnetic contrast.

7.5 Conclusions

In this chapter the magnetism of a Cr monolayer on the triangular lattice provided by pseudomorphic growth on Pd(111) has been investigated. Structural relaxations have been taken into account for the DFT study, which reveal that the Cr monolayer prefers the fcc stacking and an antiferromagnetic exchange coupling of the magnetic moments. The tendency towards an antiparallel alignment of the neighboring magnetic moments results in the occurrence of the 120° Néel state as found by spin-spiral calculations along the high-symmetry lines of the two-dimensional Brillouin zone. Testing the influence of higher-order spin interactions onto the system by considering the $3Q$ state in the calculations confirmed the Néel state as the magnetic ground state. The good agreement between simulated spin-polarized STM images of this magnetic structure with the experimental results allowed the proof of the Néel state as the magnetic ground state. Further, evidence for the switching of the tip magnetization directions was found by a detailed analysis of the tip magnetization direction in the spin-polarized STM measurements.

8 Conical Spin-spiral State Driven by Higher-Order Spin Interactions

In this chapter, it will be demonstrated for a Mn double layer on W(110) how a truly three-dimensional spin structure can arise due to the interplay of exchange interaction, Dzyaloshinskii-Moriya interaction and higher-order spin interactions. This presents the first report of a transverse conical spin-spiral state at a surface, which is driven by the higher-order spin interactions. The latter are typically neglected in transition metal systems. Here, it will be shown that the spin interactions beyond the Heisenberg picture can play a crucial role in surface magnetism. Over the past few years thin magnetic Mn films on W substrates have turned out to be promising candidates for exhibiting non-collinear magnetic ground states. For instance, in 2007 the first spin-spiral ground state driven by the Dzyaloshinskii-Moriya interaction has been observed for a monolayer Mn on the W(110) surface [9]. This spin-spiral state exhibits a canting by about 7° of the antiparallel aligned magnetic moments of adjacent atomic rows, which leads to a period of about 12 nm. The results of spin-polarized STM experiments were explained on the basis of first-principles calculations, and demonstrate for the first time the important role of the Dzyaloshinskii-Moriya interaction at surfaces. Only one year later, in 2008, a left-handed cycloidal spin-spiral was observed in one monolayer of Mn on the W(001) surface rotating with an angle of 36° between adjacent magnetic moments [127]. Based on first-principles calculations the Dzyaloshinskii-Moriya interaction was identified as the driving force of this magnetic ground state and thus proved once again its relevance in spin structures at surfaces. These two examples as well as many others, such as the double layer of Fe on W(110) [10, 128, 129], demonstrate the important influence of the Dzyaloshinskii-Moriya interaction onto the magnetism in thin films at surfaces.

However, besides the Dzyaloshinskii-Moriya interaction higher-order spin interactions are also capable of inducing complex magnetic structures. As pointed out in section 4.2, they appear in the expansion of the Hubbard model up to fourth order in t/U . Typically, they are not considered in transition metal systems as they are believed to be negligible. However, their relevance is known in high T_C superconductors [130] and spin liquid states [131]. Furthermore, their importance has been predicted theoretically for bulk systems [132, 133] as well as ultrathin films [121, 123]. Recently, it was demonstrated for a monolayer of Fe on the Ir(111) surface that the four-spin interaction competes with the Dzyaloshinskii-Moriya interaction and the

Heisenberg exchange and gives rise to a skyrmion state, which is a highly complex magnetic structure [16].

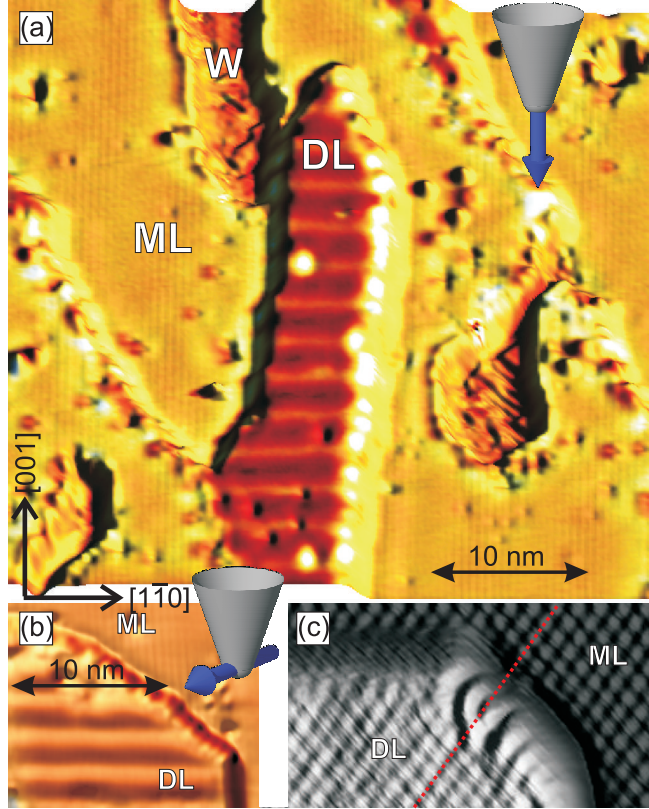
In this chapter, the Mn double layer on the W(110) surface is studied by means of the FLAPW method, and the results are compared with spin-polarized scanning tunneling microscopy experiments. A three-dimensional spin structure, i.e., a conical spin spiral is proposed as the magnetic ground state and it is shown to be consistent with the experiments. The study of collinear magnetic configurations and flat spin spirals demonstrates that the Mn double layer tends towards antiferromagnetism but shows instabilities against non-collinear magnetic order at the same time. DFT calculations of conical spin spirals, which implicitly include all magnetic interactions in the exchange-correlation potential, reveal an energy gain due to the canting of the magnetic moments. A further energy gain is observed by introducing a rotation of the spins. By investigating the possible origins of a conical spin spiral it is found that the three-dimensional magnetic ground state of this system is driven by higher-order spin interactions and the Heisenberg exchange interaction. The Dzyaloshinskii-Moriya interaction further stabilizes the non-collinear magnetic order and leads to a unique rotational sense of the spin spiral. Spin-polarized STM images of the conical spiral, which are simulated based on the spin-polarized Tersoff-Hamann model [61], agree well with the experimental results. Furthermore, the influence of the tip magnetization direction on the simulated STM contrasts is investigated. The corrugation amplitudes, i.e., the maximum change of the STM tip while scanning the surface, are analyzed concerning their applicability as a tool in order to determine the cone angle experimentally. Finally, the tunneling anisotropy magnetoresistance, which is caused by spin-orbit interaction, is studied for the conical spin-spiral state.

Parts of this chapter have been published in Physical Review Letters [56] and Physical Review B [134].

8.1 Experimental Observations

The measurements were performed in the group of Prof. R. Wiesendanger at the University of Hamburg with a homebuilt low-temperature ($T = 8 \pm 1$ K) microscope installed in a split-coil magnet (magnetic field \mathbf{B} perpendicular to the sample surface up to 2.5 T) [135]. Samples and tips were prepared *in situ* in the attached multi-chamber ultra-high vacuum system. Mn was deposited on the clean W(110) surface at moderate temperature. Chemically etched polycrystalline W-tips were flashed *in vacuo* to high temperature and used for the atomically resolved measurements. The spin-resolved measurements have been carried out by coating the W-tips with a thin film of Fe [9]. The typical magnetization direction of those tips is perpendicular to the tip axis leading to a sensitivity to an in-plane sample magnetization component. In order to measure the sample's out-of-plane magnetization component, the tip

Figure 8.1: Spin-polarized scanning tunneling microscopy images of the Mn monolayer (ML) and double layer (DL) measured in constant-current mode and colored with the simultaneously obtained differential conductance signal taken at 9 K. The W tip coated with Fe is sensitive to the (a) out-of-plane and (b) the in-plane sample magnetization component ($I = 2$ nA, $U = +60$ mV, $B = +2$ T and $U = +10$ mV, $B = 0$ T, respectively). (c) Atomically resolved topography of the Mn monolayer and the double layer ($I = 2$ nA, $U = -40$ mV, $B = -2.5$ T). The red line shows the agreement of atomic positions in the monolayer and the double layer. Thus, it demonstrates the pseudomorphic growth.



magnetization was aligned along its axis by an external magnetic field of 2 T. The sample reported in this work is not influenced by the magnetic fields available in this setup.

In Fig. 8.1 (a) a spin-polarized scanning tunneling microscopy experiment is displayed showing the sample of 1.15 monolayers of Mn on the W(110) surface obtained with a tip sensitive to the out-of-plane magnetization component. From reference [9] it is known that the Mn monolayer on the W(110) surface exhibits a spin-spiral ground state with an almost antiparallel alignment of magnetic moments along the $[1\bar{1}0]$. The angle of 173° between adjacent atomic rows leads to a pattern of fine lines along the $[001]$ direction. The elongated double-layer island located at the center of Fig. 8.1 (a), on the other hand, presents distinct stripes with a periodicity of 2.4 nm along the $[1\bar{1}0]$ direction and thus perpendicular to the stripes found in the monolayer. The atomically resolved image of the monolayer and the double layer displayed in Fig. 8.1 (c) demonstrates the pseudomorphic growth of the double layer and the monolayer. Therefore, a structural origin of the stripes on the double layer can be excluded. Since the measurement in Fig. 8.1 (a) was taken with an out-of-plane magnetized STM tip, the dark and the bright regions in the stripes can be interpreted as magnetic moments of the Mn atoms being either parallel or antiparallel aligned to surface normal. Rotating the STM tip magnetization from

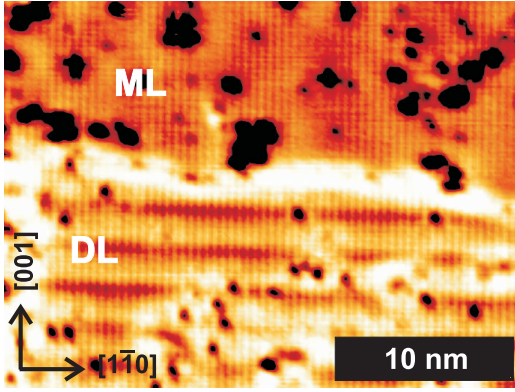


Figure 8.2: Constant-current image of the Mn monolayer and double layer connecting at a step edge of the W substrate (bright horizontal line). The spin-polarized STM tip is sensitive to the in-plane magnetization component of the sample. ($I = 2$ nA, $U = -10$ mV, $B = 0$ T, $T = 8$ K)

perpendicular to the surface into the surface plane exhibits the same periodic stripe pattern (see 8.1 (b)). By considering solely these measurements it seems that the magnetic ground state of the Mn double layer on W(110) is a spin-spiral state with almost parallel magnetic moments enclosing an angle of 24° and propagating along the $[001]$ direction. However, choosing a spin-polarized tip with a different in-plane magnetization direction exhibits a different magnetic contrast. In Fig. 8.2 the constant current image of the Mn monolayer (top) and the double layer (bottom) grown across the step edge of W reveals that beside the characteristic horizontal stripes the double layer also features fine vertical lines matching those of the Mn monolayer and indicating an antiparallel alignment of magnetic moments. However, there is a qualitative difference between the fine lines of the monolayer and the double layer: while they vanish periodically on the monolayer due to the spin-spiral state they have a periodicity of twice the atomic lattice on the double layer.

8.2 Explaining the STM images

The spin-polarized STM images shown in Fig. 8.1 and Fig. 8.2 suggest a truly three-dimensional spin-spiral as the magnetic ground state of the Mn double layer on the W(110) surface. It is composed of a $c(2 \times 2)$ antiferromagnetic state with magnetic moments aligned to the $[1\bar{1}0]$ direction and a cycloidal spin-spiral state rotating along the $[001]$ direction. The resulting spin-structure is sketched in Fig. 8.3 (b). It corresponds to a magnetic state that has been introduced in section 5.2 and characterized as *conical spin spiral* state. It is described by

$$\mathbf{S}_n = S (\cos \theta, \cos(\phi + \tau) \sin \theta, \sin(\phi + \tau) \sin \theta), \quad (8.1)$$

where \mathbf{S}_n represents the magnetic moment of the n th atom and S is its absolute value. The angle θ describes the canting of the magnetic moment and is known as *cone angle* while angle ϕ determines the *rotation angle*. The phase in which the magnetic moments in the Mn surface and subsurface layer can rotate with respect to

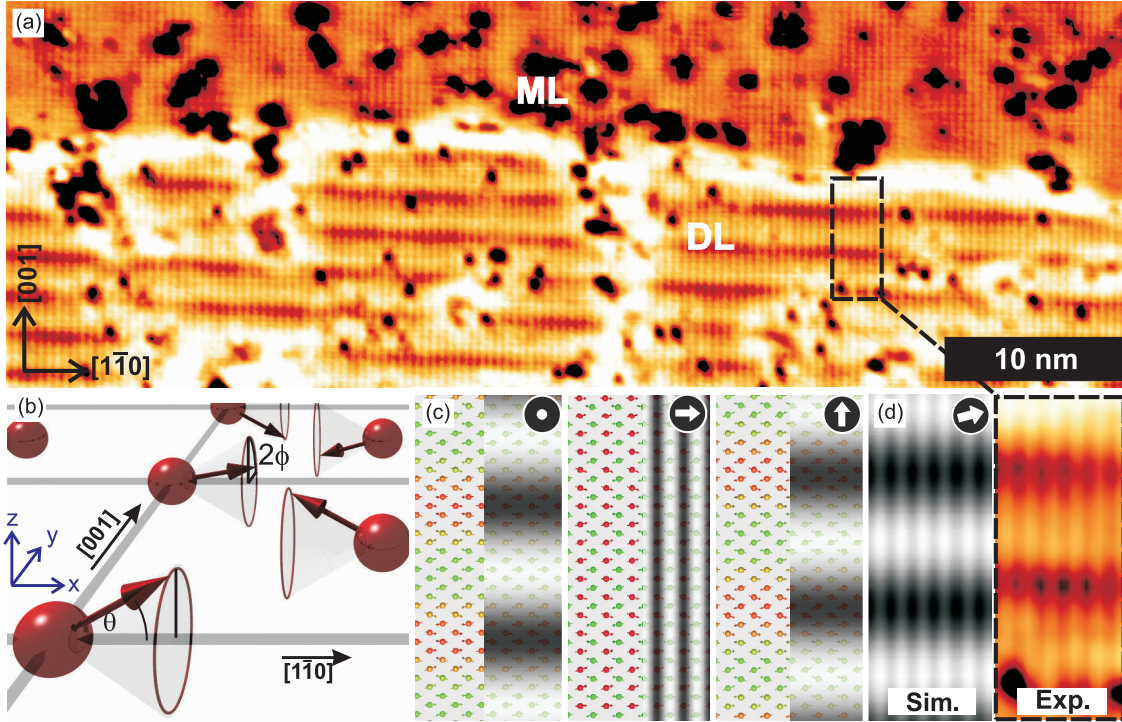


Figure 8.3: Larger area of the constant-current image of the Mn monolayer and double layer compared to the one shown in Fig. 8.2 and measured with an in-plane magnetized tip. ($I = 2$ nA, $U = -10$ mV, $B = 0$ T, $T = 8$ K) (b) Sketch of a conical spin-spiral of the double layer Mn on W(110). For reasons of simplicity the magnetic moments of the topmost layer are displayed solely. (c) Simulated spin-polarized STM images within a simple model based on the spin-polarized Tersoff-Hamann model [62] for different tip magnetization directions superimposed to a ball model of the conical spin structure of (b) for $\theta = 30^\circ$ and $\phi = \phi_{exp} = 24^\circ$. The color scale ranging from red to green indicates the projection of the Mn moments onto the tip magnetization direction (indicated by the white thick arrow). (d) Simulation with an in-plane tip magnetization enclosing an angle of 20° from the $[1\bar{1}0]$ direction and magnified view of the area surrounded by the black broken line in (a).

each other is given by the *phase angle* τ . Based on this spin structure spin-polarized STM images were simulated within a simple model depending on the independent orbital approximation [55, 62] for the tip magnetization \mathbf{m}_T being aligned to the three principal crystallographic axes as shown in Fig. 8.3 (c). Considering the tip magnetization aligned to either the $[001]$ direction or perpendicular to the film plane results in horizontal stripes known from the measurements displayed in Fig. 8.1. Here, the horizontal stripes are caused by the long-range modulation of the spin spiral propagating in the $[001]$ direction. Adjusting the tip's magnetization to the $[1\bar{1}0]$ direction reproduces the fine vertical stripes observed in Fig. 8.2.

Since in a STM experiment without external magnetic field the tip magnetization direction cannot be assigned to coincide with one of the principal axes, further spin-polarized STM images have been simulated with a slightly canted tip as it is shown in Fig. 8.3 (d). The canting of the magnetization component of the tip leads to a superposition of the contrasts obtained for the $[1\bar{1}0]$ and the $[001]$ direction, respectively. Therefore, the resulting spin-polarized STM image contains the fine stripes along $[001]$ as well as the long-range modulation producing the (horizontal) stripes along $[1\bar{1}0]$. Such a contrast is in good agreement with the experimental observations and thus the proposed conical spin-spiral state can explain the measurements. However, the question arises what is the mechanism of such an intriguing magnetic state, which has not been discovered before at a surface. In order to tackle this problem, first-principles calculations of the electronic structure have been performed as described in the following sections.

8.3 Computational Details

The first-principles calculations have been carried out applying the FLAPW method and using the experimental lattice constant of W ($a = 3.165 \text{ \AA}$). For the collinear calculations an asymmetric film was considered consisting of seven layers of W and two layers on Mn. A wavevector cut-off of $k_{max} = 3.6 \text{ a.u.}^{-1}$ has been used for the basis functions, and 24 \mathbf{k}_{\parallel} points in the irreducible wedge of the two-dimensional Brillouin zone have been employed. The structural relaxations have been performed by means of force minimization within the GGA [33]. The energetically most favorable collinear calculation was found to be the row-wise antiferromagnetic II state (see Fig. 8.4) with an inward relaxed distance by 2.5% between the W-interface and the Mn subsurface layer corresponding to an interlayer distance of $d_{W-Mn} = 2.180 \text{ \AA}$. The interlayer distance between the Mn subsurface and the Mn surface layer is $d_{Mn-Mn} = 1.998 \text{ \AA}$ corresponding to an inward relaxation of 10.6%. The magnetic properties as well as the spin-spiral calculations have been examined within the LDA [122].

The flat spin-spirals were calculated scalar-relativistically using the structural relaxations of the row-wise antiferromagnetic II state and an asymmetric film of five layers of W and two layers of Mn. In order to calculate the spin spirals self-consistently, the generalized Bloch theorem has been employed [79, 80, 81]. Calculations with a film consisting of seven layers of W and two layers of Mn have been performed to test the influence of the slab thickness. However, the results were found to be in good agreement with the results for the seven layer film. The 484 \mathbf{k}_{\parallel} points were distributed in the entire two-dimensional Brillouin zone of the $p(1 \times 1)$ unit cell for the full energy dispersion plotted in Fig. 8.5 (a). Spin spirals close to the row-wise antiferromagnetic II state (see inset in Fig. 8.5(a)) have been computed using a mesh of 961 \mathbf{k}_{\parallel} points. For the flat spin-spirals the wave vector cut-off has

been $k_{max} = 3.6 \text{ a.u.}^{-1}$.

Calculations of the conical spin spirals have been carried out in the $c(2 \times 2)$ unit cell (compare with Fig. 8.4) using an asymmetric film comprising seven layers of W with two layers of Mn on top. 280 \mathbf{k}_{\parallel} points have been employed and the wave-vector cut-off was $k_{max} = 3.6 \text{ a.u.}^{-1}$. Convergence tests concerning k -point density and wave-vector cut-offs have been made for 560 \mathbf{k}_{\parallel} points and $k_{max} = 3.8 \text{ a.u.}^{-1}$ giving the same results.

Spin-orbit coupling was taken into account in second variation [105] for collinear configurations in order to obtain the magneto-crystalline anisotropy energy using 1260 \mathbf{k}_{\parallel} points in the full two-dimensional Brillouin zone. The Dzyaloshinskii-Moriya interaction has been considered by treating the SOC in first order perturbation for non-collinear magnetic structures as introduced in section 6.6 [112]. Starting from the self-consistently calculated spin spirals, the Dzyaloshinskii-Moriya interaction has been obtained by using 2025 \mathbf{k}_{\parallel} points for flat spin spirals and 1026 \mathbf{k}_{\parallel} points for conical spin-spirals. The computation of the local density of states in the vacuum has been accomplished making use of 280 \mathbf{k}_{\parallel} points and $k_{max} = 3.8 \text{ a.u.}^{-1}$.

8.4 Magnetic Properties of the Mn Double Layer on W(110)

A first step towards understanding the magnetic properties of the Mn double layer on the W(110) surface is taken by studying the collinear configurations illustrated in Fig. 8.4. There are four configurations: (i) the ferromagnetic configuration (FM) with all magnetic moments aligned parallel, (ii) the layered antiferromagnetic configuration (LAFM), where the magnetic moments within one layer align parallel while the layers couple antiparallel, and two row-wise antiferromagnetic structures formed by an antiferromagnetic checkerboard arrangement in each Mn layer resulting in either (iii) a parallel (RW-AFM I) or (iv) an antiparallel alignment (RW-AFM II) of the magnetic moments along the [001] direction.

From the total energy calculations it becomes clear that the Mn double layer prefers an antiparallel alignment of the atoms since the RW-AFM II state is lowest in energy. The LAFM state ($\Delta E = +34 \text{ meV}$) and the RW-AFM I state ($\Delta E = +62 \text{ meV}$) are higher in energy but still energetically more favorable than the FM state ($\Delta E = +137 \text{ meV}$). This is further reflected in the exchange constants up to the third neighbor, which were extracted from these total energy differences. They result in $J_1 = -20.6 \text{ meV}$ for the interlayer nearest-neighbor exchange, $J_{2,eff} = -6.9 \text{ meV}$ for the intralayer nearest-neighbor exchange and $J_3 = -5.2 \text{ meV}$ for the interlayer next-nearest-neighbor exchange (cf. Fig 8.4). The negative values indicate a tendency towards antiferromagnetism within the Heisenberg model.

Furthermore, by including the SOC into the calculations the magneto-crystalline anisotropy of this system is obtained. It was found that for the RW-AFM II state the preferred magnetization axis (easy axis) is the $[1\bar{1}0]$ direction. Aligning the

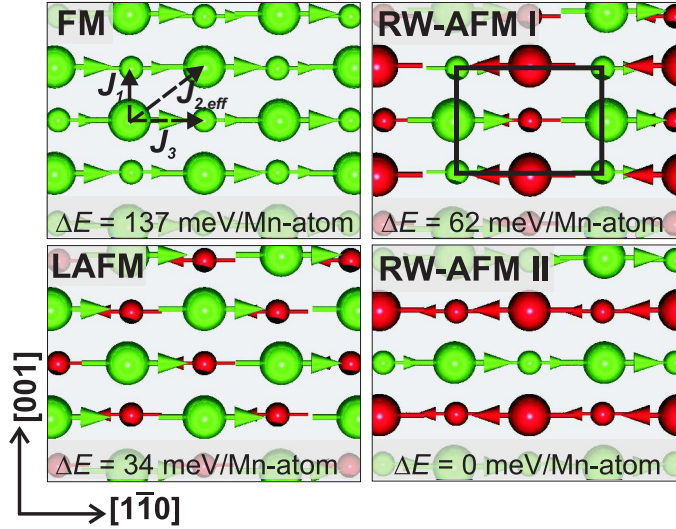


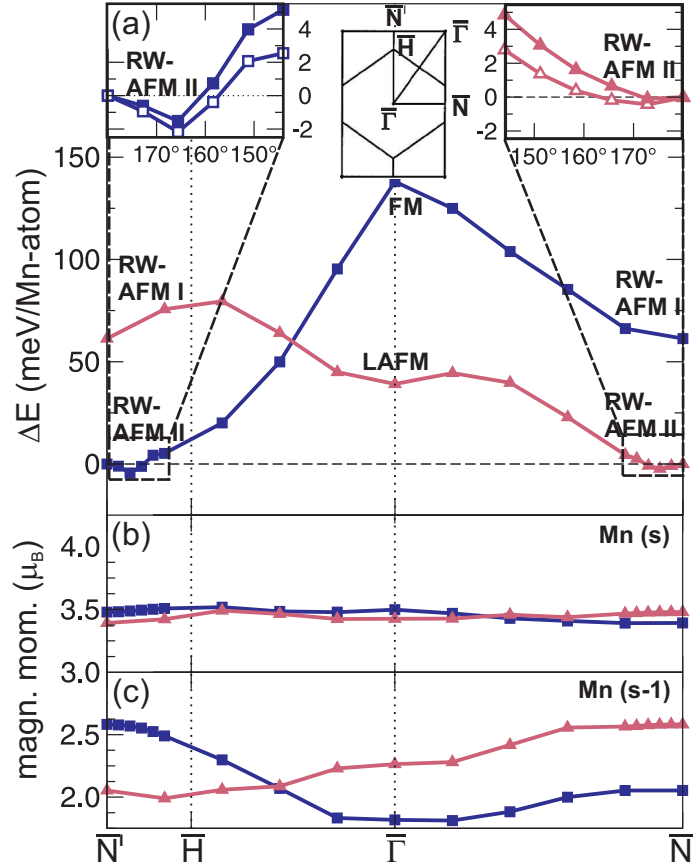
Figure 8.4: Top view of the considered collinear magnetic configurations of the Mn double layer on the W(110) surface. The large spheres represent the Mn atoms of the surface layer, while the small spheres indicate the Mn subsurface atoms. The magnetic unit cell used in the calculations is sketched by a black rectangle. Arrows specify the Heisenberg exchange constants up to the third-nearest neighbor.

magnetization to the $[110]$ and $[001]$ direction resulted in energy differences of $\Delta E_{SOC} = +1.8$ meV and $\Delta E_{SOC} = +0.5$ meV, respectively, revealing the direction perpendicular to the film plane as the hard axis.

In order to check for instabilities against non-collinear magnetism, the energy dispersion $E(\mathbf{q})$ of flat spin spirals has been computed according to Eq. (8.1) with $\tau = 0^\circ$ and $\theta = 90^\circ$ starting from the FM and LAFM configurations. The result is presented in Fig. 8.5. The spin-spiral vectors \mathbf{q} have been chosen along the high-symmetry lines in the two-dimensional Brillouin zone (see inset in Fig. 8.5).

The starting configurations were the FM and LAFM state and at the high symmetry points \bar{N} and \bar{N}' the RW-AFM I and RW-AFM II state were obtained. The energy differences of the spin-spiral dispersion at the high-symmetry points of the two-dimensional Brillouin zone ($\Delta E_{LAFM} = +39$ meV, $\Delta E_{RW-AFM I} = +61$ meV, $\Delta E_{FM} = +139$ meV) agree with those extracted from the calculation of the collinear configurations. In the vicinity of the RW-AFM II state at the high symmetry point \bar{N}' (see inset in Fig. 8.5(a)) the energy dispersion curve reveals an energy minimum of -1.5 meV with respect to the RW-AFM II configuration. The corresponding spin-spiral vector describes a spin spiral with a rotation angle of 166° between magnetic moments of adjacent atomic rows along the $[001]$ direction. Close to the RW-AFM II state at the \bar{N} point the spin-spiral dispersion curve is shallow. Hence, the energy difference between the 173° spin spiral and the RW-AFM II state is within the computational accuracy.

Figure 8.5: (a) Calculated energy dispersion of spin spirals along the $\bar{\Gamma} - \bar{H} - \bar{N}'$ and the $\bar{\Gamma} - \bar{N}$ direction, respectively, of the two-dimensional Brillouin zone (see middle inset) starting from the FM (filled squares) and the LAFM configuration (filled triangles). The insets show the energy dispersion close to \bar{N}' and \bar{N} for a larger k -point density. Open symbols represent calculations including the Dzyaloshinskii-Moriya interaction. (b)-(c) Magnetic moments of the Mn atoms of the surface (b) and the subsurface layer (c).



While the magnetic moments in the Mn surface layer are basically constant at a value of $3.5 \mu_B$, the moments in the subsurface layer vary from $1.8 \mu_B$ for the FM state at the $\bar{\Gamma}$ point to $2.6 \mu_B$ in the RW-AFM II state at the \bar{N} and \bar{N}' point. In fact, the formation of a magnetic moment increases the energy gain and thus the magnetic moment is largest in the ground state or spin structures close to it.

Based on the calculation of the flat spin spirals, spin-polarized STM images have been simulated within the spin-polarized Tersoff-Hamann model [61] in order to compare with the experimental observations. The simulations displayed in Fig. 8.6 correspond to spin spirals along the $\bar{\Gamma} - \bar{H} - \bar{N}'$ high symmetry line. The spin-polarized STM image at the $\bar{\Gamma}$ point, i.e., the FM state (cf. Fig. 8.6 (a)), displays a pattern that resembles the chemical unit cell in Fig. 8.1 (c), since all magnetic moments are aligned in parallel and are electronically equivalent. Introducing a rotation of the spin by a small angle of 36° between adjacent magnetic moments as in Fig. 8.6 (b) results in a modulation of the contrast along the $[001]$ direction similar to the one observed in Fig. 8.1 (a) and (b). However, the increase of the rotation angle (72°) leads to a smaller periodicity in the modulation (cf. Fig. 8.6 (c)). For a rotation of 144° as presented in Fig. 8.6 (d) the resulting contrast changes significantly compared to the ones in Fig. 8.6 (a) to (c). Nevertheless, it

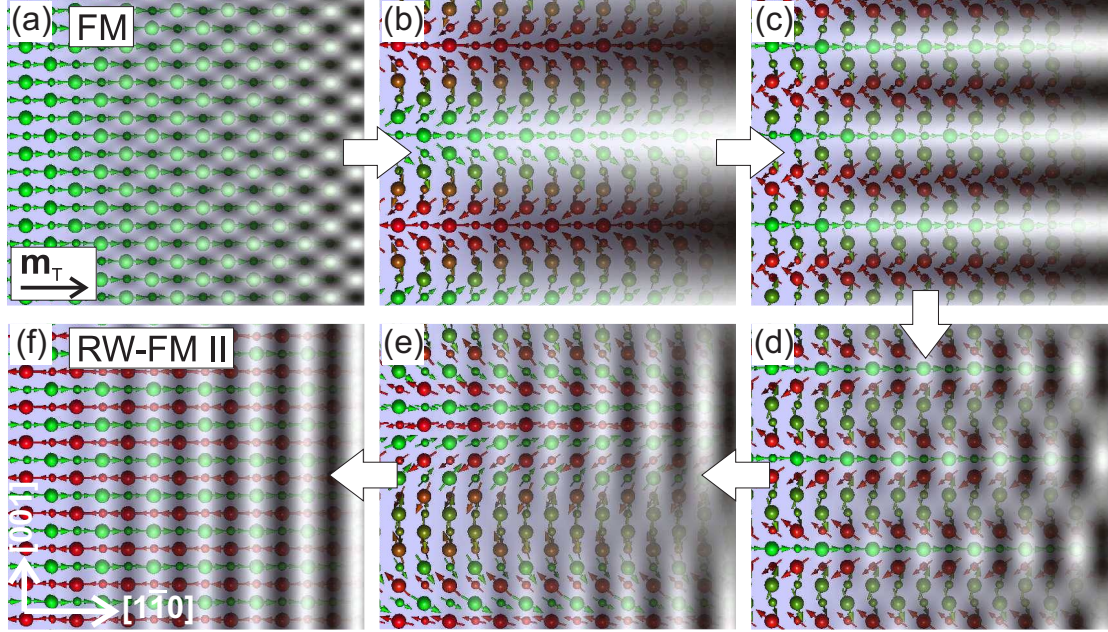
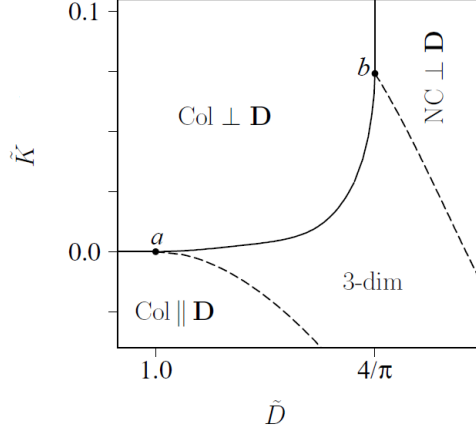


Figure 8.6: Simulated spin-polarized STM images of flat spin spirals within the Tersoff-Hamann model for a tip with an in-plane magnetization along $[1\bar{1}0]$. The spin-spiral vector \mathbf{q} is propagating in the $\bar{\Gamma} - \bar{H} - \bar{N}'$ direction starting from (a) the FM state and resulting in (f) the RW-AFM II state. The magnetic structure in (e) corresponds to the flat 166° spiral state obtained from the energy minimum in Fig. 8.5 in the vicinity of \bar{N}' . For better visibility the rotation plane is chosen in the film plane. However, the spin spirals considered for the calculation of the Dzyaloshinskii-Moriya interaction are cycloidals rotating in the $[001]$ - $[110]$ plane.

is still different from those observed experimentally in Fig. 8.2, since the magnetic moments do not only alter along the $[1\bar{1}0]$ direction but also along $[001]$. The same applies for the spin-polarized STM contrast in Fig. 8.6 (e) that corresponds to the image of a 166° spin spiral obtained from the energy minimum close to \bar{N}' in the curve in Fig. 8.5 (a). Finally, the antiparallel alignment of adjacent magnetic moments as in Fig. 8.6 (f) leads to a pattern of fine stripes along the $[001]$ direction which is typical of the local antiferromagnetic order as found in the RW-AFM II state. However, neither the RW-AFM II configuration nor the flat spin spiral, which corresponds to the energy minimum in Fig. 8.5 (a), produce a spin-polarized STM contrast that resembles the experimental observations in Figures 8.1 or 8.2. Thus, they are not capable of explaining the experimental results. As demonstrated in section 8.2 the suggested conical spin spiral reproduces the pattern observed in the spin-polarized STM experiment as displayed in Fig. 8.3 (d). Therefore, the mechanisms that allow for the occurrence of a three-dimensional spin structure will be investigated thoroughly in the next sections.

Figure 8.7: Phase diagram based on a micromagnetic model as introduced in Ref. [136] for the dimensionless parameters \tilde{K} and \tilde{D} , which describe the relation between the anisotropy and the Dzyaloshinskii-Moriya interaction. The diagram shows the collinear phases where the magnetic moment is either parallel (Col \parallel \mathbf{D}) or perpendicular (Col \perp \mathbf{D}) to \mathbf{D} . The non-collinear phases contain structures with the rotation plane perpendicular to \mathbf{D} (NC \perp \mathbf{D}) or those describing a truly three-dimensional path in spin space (3-dim). Figure taken from [136].



8.5 Conical Spin Spirals Induced by Spin-Orbit Coupling

There are two different mechanisms that are capable of inducing a conical spin-spiral state in a system such as the double layer Mn on the W(110) surface. For instance, the interplay of the Heisenberg exchange, the Dzyaloshinskii-Moriya interaction and the magnetocrystalline anisotropy can give rise to three-dimensional spin structures as it has been predicted theoretically by M. Heide et al. [136] based on a micromagnetic model that considers the following Hamiltonian

$$\mathcal{H} = - \sum_{ij} J_{ij} \mathbf{S}_i \cdot \mathbf{S}_j + \sum_{ij} \mathbf{D}_{ij} (\mathbf{S}_i \times \mathbf{S}_j) + \sum_i K_i (S_i^z)^2, \quad (8.2)$$

which includes the Heisenberg exchange J_{ij} (first term), the Dzyaloshinskii-Moriya interaction \mathbf{D}_{ij} (second term) and the magnetocrystalline anisotropy K_i (third term). Furthermore, it makes use of the dimensionless parameters $\tilde{K} = (K_D - K_y)/(|K_z - K_y|)$ and $\tilde{D} = D/\sqrt{A|K_z - K_y|}$ where A refers to the exchange related spin stiffness, D is related to the Dzyaloshinskii vector and K_D , K_z and K_y are the anisotropy constants. The occurrence of a three-dimensional spin structure depends on the strength of these interactions. For example, if the anisotropy term dominates, i.e., \tilde{D} is small, the resulting ground state is collinear with the magnetization either parallel or perpendicular to the Dzyaloshinskii vector \mathbf{D} as displayed in the phase diagram of Fig. 8.7. In contrast, the predominance of the exchange and the Dzyaloshinskii-Moriya interaction leads to a large \tilde{D} and the magnetization rotates in a plane perpendicular to \mathbf{D} . In this case further distinctions have to be made concerning the direction of the Dzyaloshinskii vector. If it coincides with the hard axis, the system forms a cycloidal spin spiral rotating in the plane perpendicular to \mathbf{D} . On the other hand, if \mathbf{D} is parallel to the easy axis, three-dimensional struc-

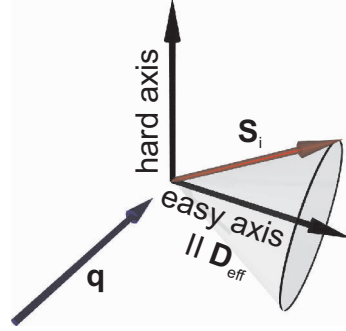


Figure 8.8: Sketch of the spin S_i rotating on a cone. The Dzyaloshinskii-Moriya interaction is represented by the effective Dzyaloshinskii vector D_{eff} . The Heisenberg exchange introduces a spin spiral in the direction of vector q . The magnetocrystalline anisotropy defines the easy and the hard axis.

tures can form and the scenario sketched in Fig. 8.8 can take place leading to a conical spin-spiral state: a spin spiral prefers a cycloidal rotation perpendicular to the effective Dzyaloshinskii vector D_{eff} and propagates in the direction indicated by the vector q . At the same time, the magnetic easy axis coincides with D_{eff} while the rotation plane of the spin spiral contains the hard axis. In order to avoid the energetically unfavorable magnetic axis, the spin S_i tilts towards the easy axis and spans a cone.

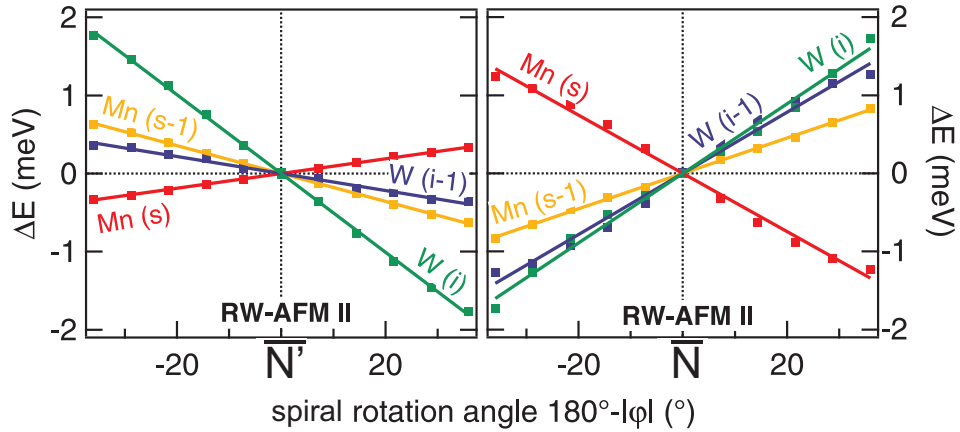


Figure 8.9: Layer resolved contributions of the Dzyaloshinskii-Moriya interaction close to the RW-AFM II state at N' and N , respectively. The surface layer of Mn is indicated by Mn(s) and the subsurface layer by Mn(s-1). The W interface and the W layer below are denoted by W(i) and W(i-1), respectively. The data points (squares) represent the outcome upon the inclusion of the SOC effect via first order perturbation theory in the DFT calculations. Linear fits have been applied (straight lines) in order to obtain the values of the Dzyaloshinskii-Moriya term.

In order to study if this mechanism is responsible for the conical spin structure observed in the Mn double layer on the W(110) surface, the parameters \tilde{K} and \tilde{D} will be evaluated in the following. The anisotropy constants $K_D = 0$ meV, $K_y = +0.5$ meV, $K_z = 1.8$ meV and the exchange related spin stiffness $A = -20.6$ meV

	D at \bar{N} (meV)	D at \bar{N}' (meV)
Mn (s)	+0.29	-1.11
Mn (s-1)	-0.56	+0.67
W (i)	-1.57	+1.32
W (i-1)	-0.34	+1.16
total	-1.80	+1.93

Table 8.1: Contributions of the Dzyaloshinskii-Moriya term D for the Mn surface and subsurface layer, Mn (s) and Mn (s-1), as well as the W interlayer W (i) and the W layer below the interface W (i-1). The values have been obtained by fitting the results of the flat spin-spiral calculations linearly (compare with Fig. 8.9).

have been obtained from the collinear calculations. The Dzyaloshinskii-Moriya term is provided by including the SOC in the calculations of the flat spin-spirals in the vicinity of the \bar{N}' and the \bar{N} point (see insets in Fig. 8.5). From these calculations its strength for the Mn double layer has been determined by means of a linear fit, i.e., $E_{SOC} = D \cdot q$, as $D = -1.80$ meV and $D = 1.93$ meV at the \bar{N}' and \bar{N} point, respectively. In fact, these values are not small but the Dzyaloshinskii-Moriya interaction alters the energetics only slightly without shifting the minimum of the energy dispersion curve close to \bar{N}' . Therefore, it does not change the physical picture.

The layer resolved contribution of the Dzyaloshinskii-Moriya interaction reveals that the main part of D stems from the W atoms due to its large SOC strength (cf. Fig. 8.9 and table 8.1). Even small magnetic moments are sufficient to cause a strong contribution to the Dzyaloshinskii-Moriya interaction. The polarization of the substrate is largest in the layer that is closest to the magnetic film. Thus, the W atoms of the interface layer contribute the major part to the Dzyaloshinskii-Moriya interaction.

The analysis of the Dzyaloshinskii-Moriya interaction allows for the evaluation of the micromagnetic model. The insertion of the above values results in $\tilde{K} = -0.385$ and $\tilde{D} = 0.373$. The comparison with the phase diagram in Fig. 8.7 exhibits that micromagnetic model predicts a collinear magnetic ground state with the moments perpendicular to \mathbf{D}_{eff} for the Mn double layer on W(110), which does not agree with the experimental results. Obviously, the occurrence of a conical spin spiral as ground state in this system cannot be explained within this model based on the interplay of the exchange interaction, the Dzyaloshinskii-Moriya interaction and the anisotropy.

8.6 Conical Spin Spirals Induced by Higher-Order Spin Interactions

The conical spin spiral observed in the Mn double layer on W(110) is evidently not due to the mechanism introduced in the previous section. However, as pointed out in sections 4.2 and 7.3, spin interactions beyond the Heisenberg exchange, namely the biquadratic and the four-spin interaction, can lift the degeneracy of spin structures that are energetically equivalent within the Heisenberg picture. These interactions represent the second mechanism that could give rise to a conical spin-spiral ground state. For transition metal systems it has been shown theoretically that the higher-order spin interactions are important in bulk systems [132, 133] and in ultrathin films [121, 123, 137]. Furthermore, the crucial role of the four-spin interaction in surface magnetism has been recently demonstrated in theory and experiment for an Fe monolayer on the Ir(111) surface [16].

In order to check whether conical spin spirals can indeed be more favorable than the RW-AFM II state or flat spin spirals, their total energy has been directly calculated using the FLAPW method. Since the spin structure suggested by the experiment is an antiferromagnetic configuration superimposed to a spin-spiral state, the calculations require a $c(2 \times 2)$ unit cell as it is indicated in Fig. 8.10. In this case the starting configuration is the RW-AFM II state. In a first step, only the canting of the magnetic moment with respect to the surface plane will be considered. The rotation due to the spin spiral will be introduced afterwards based on the optimum canting angle.

As a start, the magnetic moments, which are aligned along the $[1\bar{1}0]$ direction, are canted with respect to the film plane by the angle θ (see sketch in Fig. 8.10) while taking into account the phase angle τ (compare with Eq. (8.1)) between the moments in the surface and the subsurface layer. Assigning the value of τ to 0° , 90° and 180° results in the configurations I to III sketched in the upper row of Fig. 8.10 (a) to (c).

Upon canting of the magnetic moments an energy minimum is observed for configuration I (Fig. 8.10 (a)), i.e., $\tau = 0^\circ$, and a cone angle of $\theta = 30^\circ$ (see Fig. 8.11). It is by 10.0 meV/Mn-atom lower in energy than the RW-AFM II state. For configuration II (Fig. 8.10 (b)), i.e., $\tau = 90^\circ$, the energy gain is 8.4 meV/Mn-atom for $\theta = 25^\circ$. Configuration III (Fig. 8.10 (c)), i.e., $\tau = 180^\circ$, has the overall smallest energy gain with 5.1 meV/Mn-atom for $\theta = 30^\circ$.

In order to identify the interaction giving rise to the canting of the magnetic moments, the total energy of the DFT calculations, in which all magnetic interactions are implicitly included in the exchange-correlation potential, can be mapped to a model that includes the Heisenberg exchange as well as the higher-order spin interactions. Since the Heisenberg exchange is constant for all pairs of parallel magnetic moments \mathbf{S}_i and \mathbf{S}_j in the RW-AFM II state (see Fig. 8.4), the energy change for

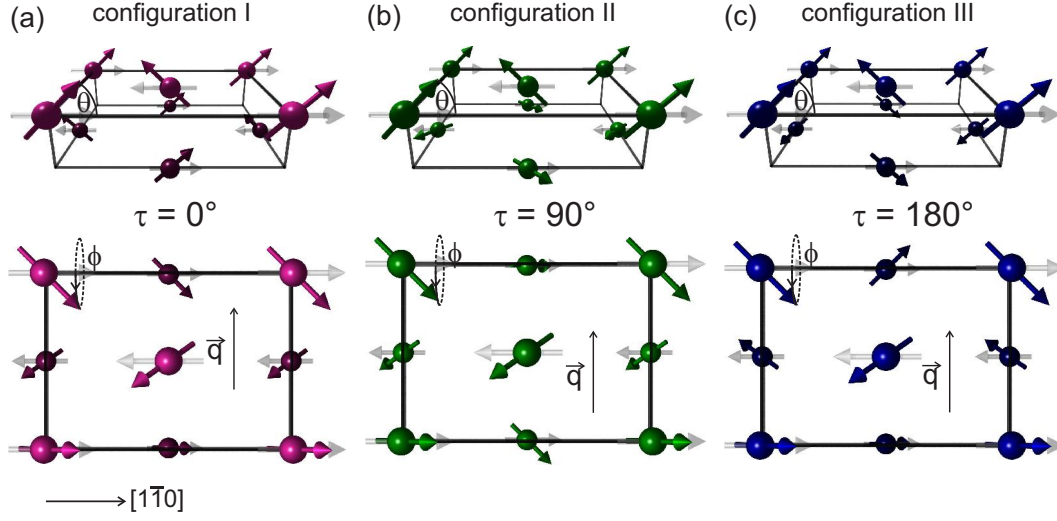


Figure 8.10: Sketches of the conical spin-spiral states for (a) $\tau = 0^\circ$ (configuration I), (b) $\tau = 90^\circ$ (configuration II) and (c) $\tau = 180^\circ$ (configuration III). The upper row displays the side view of the canted non-rotating spin structures. The bottom row shows the top view of the configurations including the rotation by ϕ .

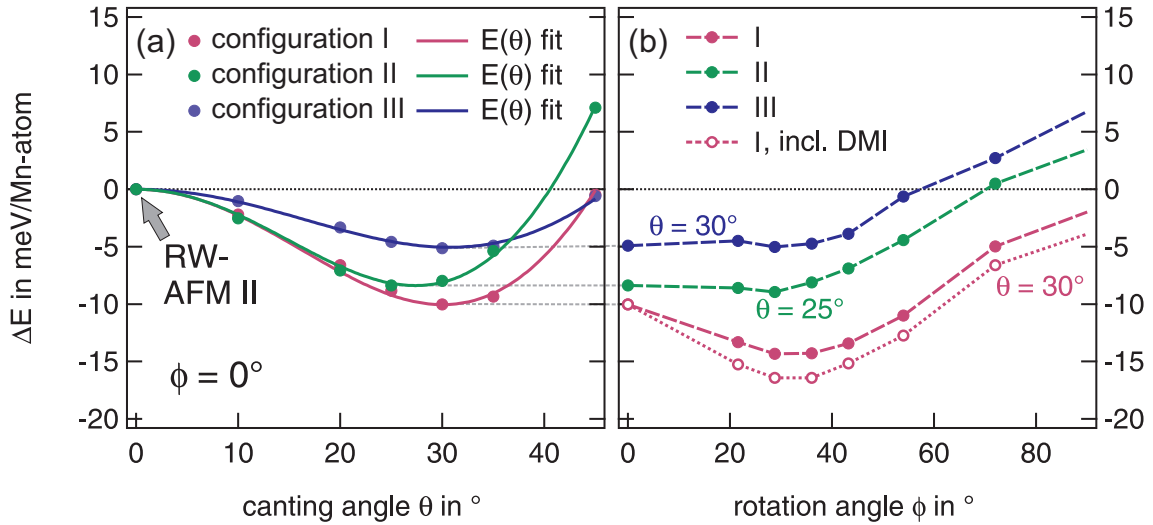


Figure 8.11: (a) Total energy of the configurations in Fig. 8.10 (a), (b) and (c) with respect to the RW-AFM II state as a function of the canting angle θ . Symbols denote the results of the calculations. Lines indicate the fits of the Heisenberg exchange and the higher spin interactions to the calculations. (b) Total energy with respect to the RW-AFM II state as a function of the rotation angle ϕ . The canting angle is kept fixed at $\theta = 30^\circ$ for configurations I and III and at $\theta = 25^\circ$ for configuration II. Open circles denote calculations including the DMI.

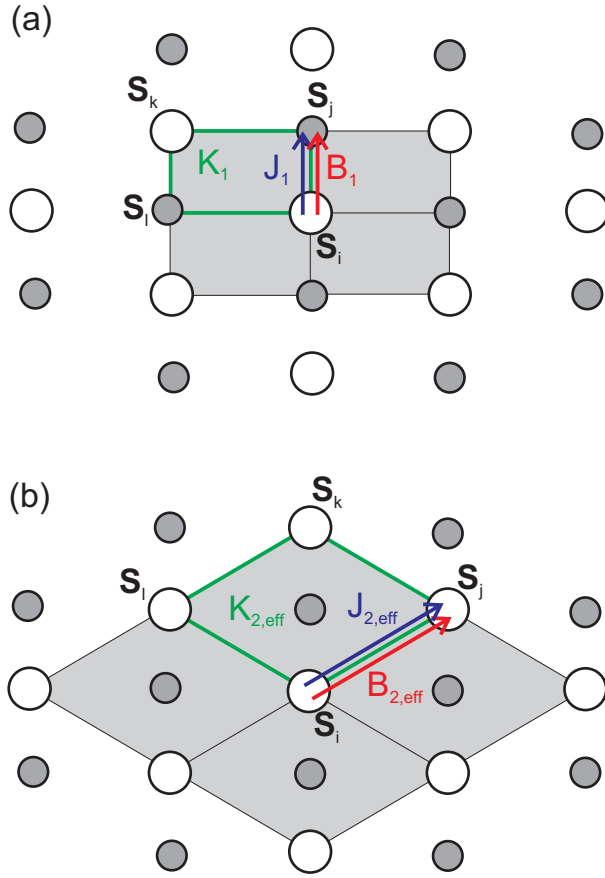


Figure 8.12: (a),(b) Sketch of the Mn double layer. Large white circles denote the Mn atoms of the surface layer while gray circles represent the Mn atoms of the subsurface layer. $\mathbf{S}_i, \mathbf{S}_j, \mathbf{S}_k,$ and \mathbf{S}_l refer to the spins of four Mn atoms. The Heisenberg exchange, J , and the bi-quadratic exchange, B , are depicted as blue and red arrows, respectively, considering the (a) nearest neighbors and (b) next-nearest neighbors. The four-spin interaction, K , is indicated by (a) a green rectangle for the nearest neighbors and (b) a green rhombus for the next-nearest neighbors.

configuration I, Fig. 8.10 (a), is

$$E_{exch}(\theta) = (2J_1 + 4J_{2,eff})S^2 \cos(2\theta) \quad (8.3)$$

due to the canting of \mathbf{S}_i and \mathbf{S}_j in Fig. 8.12 (a) for the nearest neighbors (J_1) and Fig. 8.12 (b) for the next-nearest neighbors ($J_{2,eff}$). Here, the index 'eff' refers to the effective intralayer neighbor exchange (cf. Fig. 8.12 (b)). Since the decomposition into a surface and a subsurface contribution is very complex, the constants are treated as one effective constant that applies for both layers at the same time.

However, the dependence on $\cos(2\theta)$ leads to an energy minimum for $\theta = 0^\circ$ taking the strong antiferromagnetic exchange into account, i.e., the Heisenberg exchange is minimized for collinear magnetic structures and thus cannot explain the energy minimum upon canting of the magnetic moments. For the higher-order spin interactions up to the next-nearest neighbors, on the other hand, the angular dependence results in

$$E_{biq}(\theta) = (B_1 + 2B_{2,eff})S^4 \cos(4\theta) \quad (8.4)$$

configuration I	$a = (2J_1 + 4J_{2,eff})S^2$	-37.7 (meV)
	$b = (-B_1 - 2B_{2,eff} - 4K_{2,eff})S^4$	+19.1 (meV)
configuration II	$a = (J_1 + 4J_{2,eff})S^2 - (B_1 + 8K_1)S^4$	-54.2 (meV)
	$b = (-1/4B_1 - 2B_{2,eff} - K_1 - 4K_{2,eff})S^4$	+23.5 (meV)
configuration III	$a = (4J_{2,eff})S^2 - 4K_1S^4$	-18.4 (meV)
	$b = (-2B_{2,eff} - 2K_1 - 4K_{2,eff})S^4$	+9.5(meV)

Table 8.2: Fitted values of the Heisenberg exchange and the higher-order spin interactions.

in the case of the biquadratic exchange and

$$E_{4-spin}(\theta) = 4K_{2,eff}S^4 \cos(4\theta) \quad (8.5)$$

for the four-spin interaction (cf. Fig. 8.12). Since $\cos 4\theta$ exhibits a minimum at $\theta = 45^\circ$, the higher-order spin interactions provide a sound explanation of the energy gain due to the canting. The angular dependence of the other two configurations is evaluated in a similar way. However, in all three configurations the Heisenberg exchange follows a $\cos(2\theta)$ while the higher-order spin interactions also provide a $\cos(4\theta)$ -dependent contribution. Therefore, a fitting function of the following form

$$E(\theta) = a \cos(2\theta) + b \cos(4\theta) \quad (8.6)$$

has been used for all three energy curves in Fig. 8.11. In this way, the constants related to the Heisenberg exchange and the higher-order spin interactions can be extracted as presented in table 8.2. From Fig. 8.11 (a) it is evident that the DFT calculation can be well fitted by this relation. The constants given in table 8.2 depend strongly on each other and thus complicate the extraction of single values for the exchange or the higher-order spin interactions. However, the absolute values of the fitting constants b for all three configurations are only about two times smaller than that of the fitting parameters a , which are basically dominated by the Heisenberg exchange. This is a further demonstration of the importance of the higher-order spin interactions in this system.

Based on the optimum canting angle of $\theta = 30^\circ$ for configuration I and III as well as $\theta = 25^\circ$ for configuration II a homogenous rotation along the [001] direction has been introduced as sketched in Fig. 8.10. In this manner, the spins are rotated in the [001]-[110] plane by ϕ , which is related to the length of the spin-spiral vector \mathbf{q} . For configuration I an additional energy gain of 4.6 meV is observed leading to a spin-spiral state with $\phi = 32^\circ$, while configuration III loses energy with increasing ϕ . In the case of configuration II the energy reduces by about 0.6 meV only before it experiences a strong increase.

Furthermore, SOC has been included in the spin-spiral calculations of configuration (a) for $\theta = 30^\circ$ leading to an additional energy gain of 2.1 meV for $\phi = 32^\circ$ due to the Dzyaloshinskii-Moriya interaction.

Finally, from the calculations it can be concluded that the Mn double layer on the W(110) surface exhibits a conical spin spiral with a rotation angle of $\phi = 32^\circ$ that is in good agreement with the experimental value of about $\phi_{exp} = 24^\circ$. The overall energy gain is about 16.7 meV with respect to the RW-AFM II state, which is clearly more favorable compared to the energy difference of 1.5 meV resulting from the calculation of the flat spin spirals (Fig. 8.5). However, the experimental confirmation of the phase angle of $\tau = 0^\circ$ as well as the cone angle of $\theta = 30^\circ$ is difficult. Therefore, an approach will be presented in section 8.8 that allows for the estimation of the cone angle θ by the comparison of the corrugation amplitudes obtained for the $[\bar{1}\bar{1}0]$ and $[001]$ direction, respectively.

8.7 Simulation of spin-polarized STM images

Based on the results of the DFT calculations spin-polarized STM images were simulated for the ground state of the Mn double layer on the W(110) surface considering various tip magnetization directions (Fig. 8.13). In particular, the images resulting from tip magnetization directions that are deviating from the three crystallographic axes were taken into account. For a tip with a magnetization component tilting from the $[\bar{1}\bar{1}0]$ direction towards $[001]$ (Fig. 8.13 (a)) the similarity to the experimental results (cf. Fig. 8.3 (a)) obtained with an in-plane magnetized STM tip is obvious, since the images show fine vertical lines and at the same time long-ranged horizontal stripes. The same applies for a tip magnetized in between the $[\bar{1}\bar{1}0]$ and the $[110]$ direction (Fig. 8.13 (b)). Solely in the case of a tip magnetization direction between $[001]$ and $[110]$ the fine vertical stripe pattern is missing as only the $[\bar{1}\bar{1}0]$ component of the magnetization exhibits local antiferromagnetic order. Therefore, the images resemble the experimental ones in Fig. 8.1, where the STM tip has been magnetized normal to the film plane. Furthermore, the simulated STM images based on the DFT calculations confirm the simulations carried out within a simple model based on the Tersoff-Hamann model (cf. Fig. 8.3).

In order to study the influence of the phase angle τ onto the magnetic contrast, spin-polarized STM images were calculated based on the electronic structure of the system obtained from the DFT calculations for a tip magnetization direction of 45° with respect to the $[\bar{1}\bar{1}0]$ direction. This was done to reproduce the superimposed contrast as in the experiment (cf. Fig. 8.3 (a)). The resulting images are displayed in Fig. 8.14 (a). All of them show the fine vertical stripes indicating the local antiferromagnetic order and, at the same time, horizontal stripes due to the spin-spiral state. At first glance the three contrasts look identical. However, having a closer look reveals that the contrast for configuration I is slightly more blurred than the

ones of configurations II and III. This behavior becomes more obvious if the line profiles are taken into account. Since the phase angle only plays a role along $[1\bar{1}0]$, the line profiles along that direction (Fig. 8.14 (b)) are identical for all phases as they represent the antiferromagnetic order of the $[1\bar{1}0]$ component of the magnetization. The line profiles coinciding with the $[001]$ direction, on the other hand, show discrepancies between the three configurations. For configuration I the largest amplitude in the line profile is observed while a phase of configuration III causes a small amplitude. This behavior is due to the fact that for configuration I magnetic moments of both Mn layers still possess almost parallel magnetization components along the $[001]$ direction. This leads to an enhancement of the magnetization density. However, for configuration III magnetic moments of both layers are almost antiparallel arranged along the $[001]$ direction. Thus, the magnetization density ex-

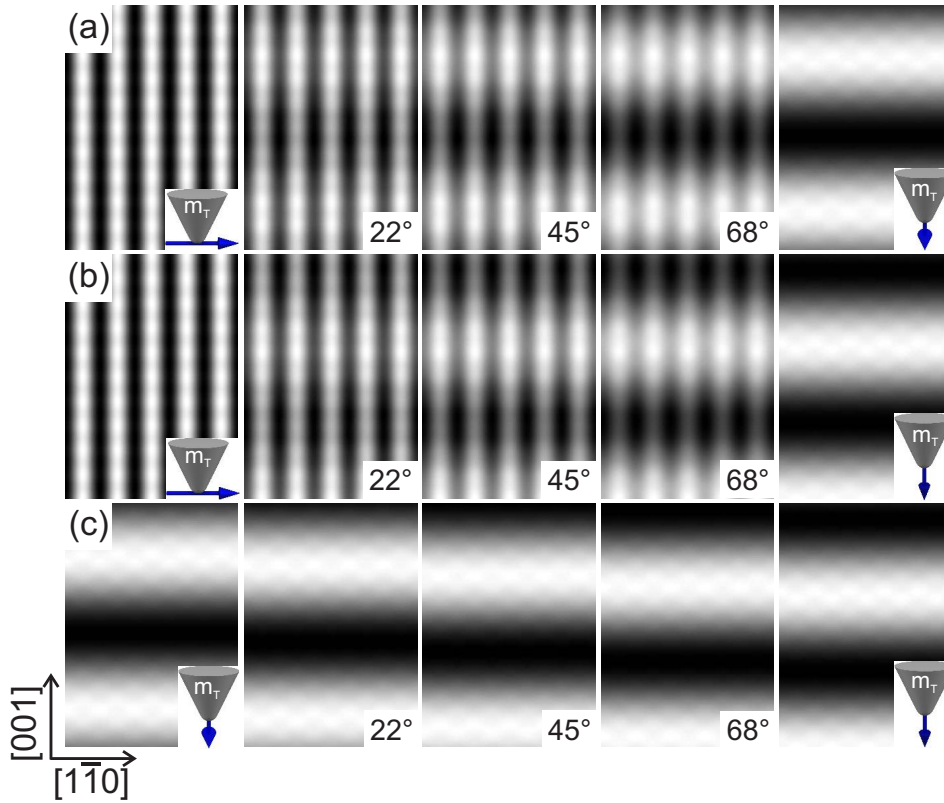


Figure 8.13: Simulated spin-polarized STM images of the conical spin spiral state of the Mn double layer on W(110) based on the full DFT calculations for different tip magnetization directions for the case of $\tau = 0^\circ$, $\theta = 30^\circ$ and $\phi = 30^\circ$. Here, the tip magnetization direction varies from (a) $[1\bar{1}0]$ to $[001]$, (b) $[1\bar{1}0]$ to $[110]$ and (c) $[001]$ to $[110]$. The images in the three middle columns illustrate the resulting STM images of tips with a magnetization component deviating from the main axes by 22° , 45° and 68° . The spin-polarization of the tip is $P_T = 0.5$. The tip-sample distance has been chosen as 6\AA .

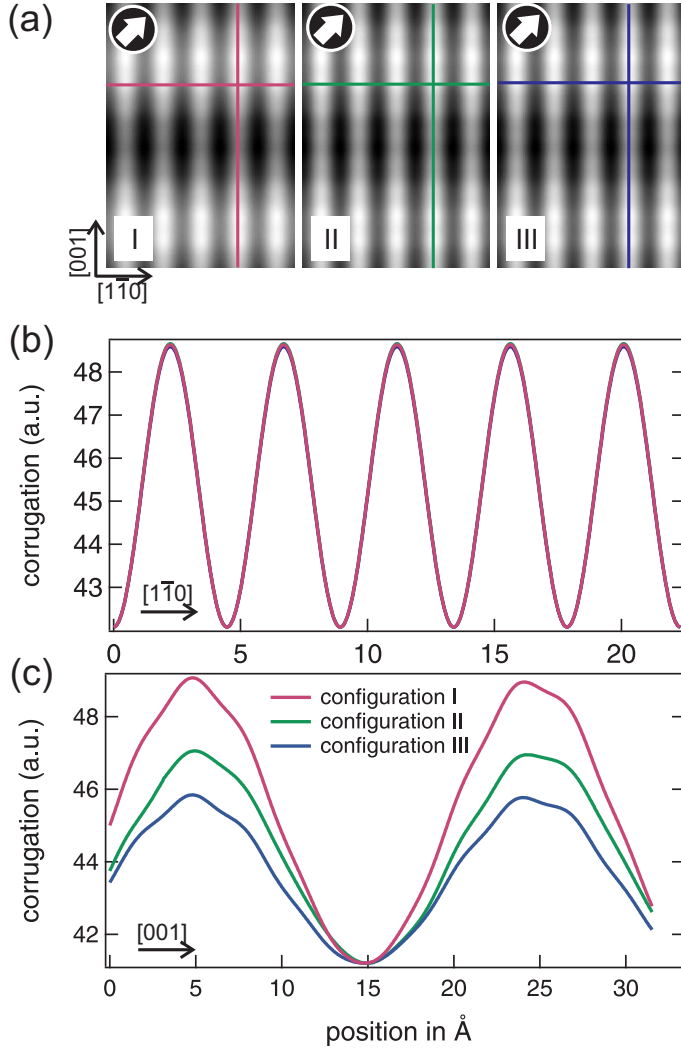


Figure 8.14: (a) Spin-polarized STM images calculated based on the DFT calculations at 6 Å in the vacuum for configurations I, II and III with a cone angle of $\theta = 30^\circ$ and a rotation angle of $\phi = 30^\circ$. The tip magnetization is tilted by 45° with respect to the $[1\bar{1}0]$ direction and the polarization is $P_T = 0.5$. (b)-(c) Line profiles of all three configurations calculated along the horizontal lines (b) and the vertical lines (c) indicated in (a).

periences a compensation and a subsequent reduction due to the choice of the phase angle. Since the configuration with configuration II resembles an intermediate of the above cases, it is reasonable to find its amplitude in between.

As mentioned above, the canting of the tip magnetization leads to a superposition of the magnetic contrasts expected for the magnetization component corresponding to the principal crystallographic axes. Since both cases, i.e., Fig. 8.13 (a) and (b), resemble each other, it is beyond the simulations to draw conclusions concerning the alignment of the tip magnetization in the experiments. Moreover, the unknown cone angle of the spin-spiral state in the experiment represents yet another uncertainty, since it has an influence on the corrugation amplitude in the line profiles taken along the $[1\bar{1}0]$ and the $[001]$ direction, respectively. However, this aspect will be further investigated in the next section.

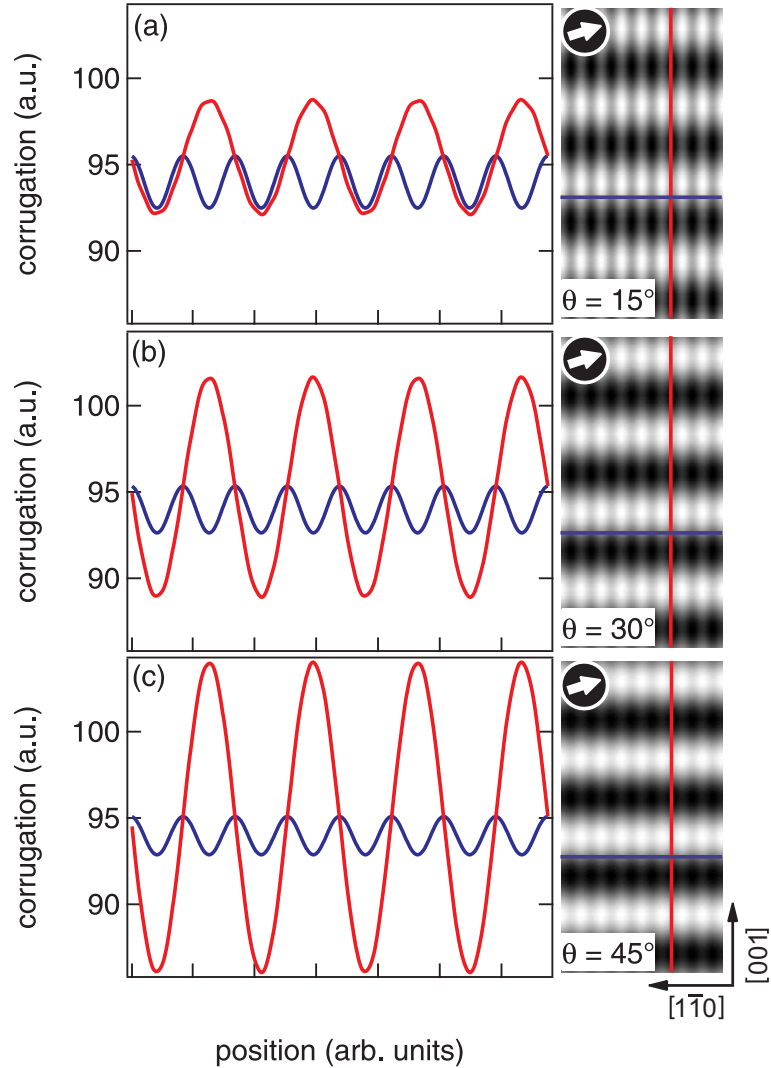


Figure 8.15: Line profiles and STM images simulated within a simple model based on the generalized Tersoff-Hamann model for different cone angles $\theta = 15^\circ$ (a), $\theta = 30^\circ$ (b) and $\theta = 45^\circ$ (c). The rotation angle corresponds to the experimental one ($\phi = 24^\circ$) and the tip-sample distance is 8 Å. The red (blue) line profiles in (a), (b) and (c) are calculated along the red (blue) lines indicated in the STM images. The tip magnetization direction is tilted from the $[1\bar{1}0]$ direction by 18° .

8.8 Corrugation Amplitudes

During a surface scan at a fixed constant current the tip of a STM experiences small variations in the height. The maximum difference in the tip height as a function of the lateral position \mathbf{r}_{\parallel} of the tip within the unit cell is called *corrugation amplitude* Δz . In section 7.4.2 it was shown that simulated STM line profiles allow for the identification of the tip magnetization direction. Furthermore, in Fig. 8.14 it became evident that the line profiles along the $[1\bar{1}0]$ and the $[001]$ direction are different. In order to study the effect of the cone angle on the line profiles and thus on the corrugation amplitude along the $[1\bar{1}0]$ and $[001]$ direction, spin-polarized STM images as well as line profiles have been simulated for the double layer Mn on W(110) within the simple model that is based on the independent orbital approximation [55, 62] and the spin-polarized Tersoff-Hamann model [61] as

introduced in section 4.3.3. Figures 8.15 (a) to (c) display the results for the cone angles $\theta = 15^\circ$, $\theta = 30^\circ$ and $\theta = 45^\circ$. The simulated STM images (right panel) agree well with those obtained from the DFT calculations (cf. figures 8.13 and 8.14) and the experimental ones (cf. Fig. 8.2) since they all show the fine stripe pattern along the $[1\bar{1}0]$ direction superimposed to the modulation along $[001]$. The blue line profiles, on the other hand, were computed along the $[1\bar{1}0]$ direction and illustrate the local antiferromagnetic order, where an antiparallel aligned magnetic moment is represented by a minimum and a parallel alignment corresponds to a maximum. Calculating line profiles along the $[001]$ direction results in the red lines, which represent the corrugation due to the spin-spiral rotation. By varying the cone angle the ratio of both corrugation amplitudes changes as well. For $\theta = 15^\circ$ the corrugation amplitude of the $[001]$ direction is about twice the size of the corrugation amplitude obtained in the $[1\bar{1}0]$ direction. Enlarging the cone angle to $\theta = 30^\circ$ leads to an increase of the ratio to five over one since the projection of the magnetic moment onto the tip magnetization direction decreases in the $[1\bar{1}0]$ direction while it increases in the $[001]$ direction. This tendency becomes apparent for $\theta = 45^\circ$, too. Here, the ratio of the corrugation amplitudes rises to eight over one. Hence, the relation of the corrugation amplitudes depends strongly on the size of the cone angle. This fact can be exploited in order to determine the cone angle experimentally. Since the corrugation amplitude responds sensitively to the magnetization direction of the tip the latter has to be kept fixed, and, of course, it needs to be known, which can be achieved in an experiment by a rotatable magnetic field [128].

Based on the spin-polarized Tersoff-Hamann model [61] and the independent-orbital approximation [55, 62] the ratio of the corrugation amplitudes is derived for the Mn double layer on W(110). The corrugation amplitude is typically of the order of $\Delta z \approx 0.10 \text{ \AA}$. Keeping in mind that the tip-sample distance z_0 ranges from about 5 to 12 \AA the corrugation amplitude is rather small [65]. As pointed out in section 4.3.3 the corrugation amplitude is given by

$$\Delta z(\mathbf{r}_{\parallel}) = \frac{\Delta I(\mathbf{r}_{\parallel}, z_0)}{2\kappa I_0(z_0)} \quad (8.7)$$

where z_0 denotes an average tip-sample distance, $I_0(z_0)$ is a lateral constant part and $\Delta I(\mathbf{r}_{\parallel}, z_0)$ is a small variation that depends on the lattice by

$$\Delta I(\mathbf{r}_{\parallel}, z_0) \propto \exp \left[-2z_0 \sqrt{\frac{2m_e}{\hbar^2} \phi_{work} + \left(\frac{\mathbf{G}_i}{2} \right)^2} \right]. \quad (8.8)$$

Here, \mathbf{G}_i denotes the reciprocal lattice vector that is inversely proportional to the lattice vector a_i , i.e., $\mathbf{G}_i = \frac{2\pi}{a_i}$. ϕ_{work} is the work function which is typically between 4 and 5 eV for transition metals. In the following ϕ_{work} is chosen as 4.8 eV due

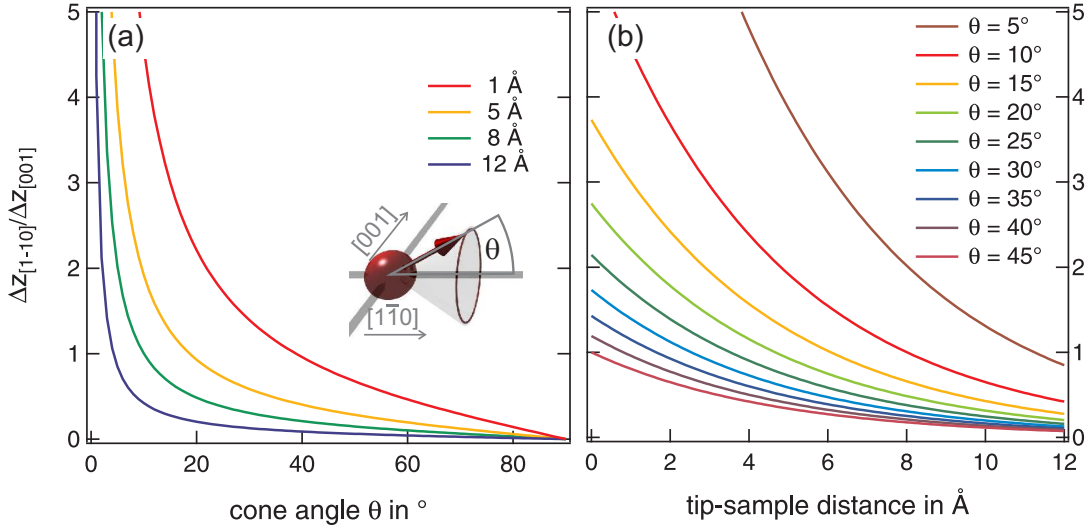


Figure 8.16: The relation of the corrugation amplitudes for (a) fixed tip-sample distances z_0 and (b) fixed cone angles θ . The tip magnetization direction is aligned to $[1\bar{1}0]$ and $[001]$ for $\Delta z_{[1\bar{1}0]}$ and $\Delta z_{[001]}$, respectively.

to the work function of the Mn double layer on W(110) which is 4.75 eV. In the case of the Mn double layer on W(110) the lattice vectors a_i correlate with the magnetic periodicity along the $[1\bar{1}0]$ direction, $a_1 = 3.1652 \text{ \AA}$, and the $[001]$ direction, $a_2 = 24 \text{ \AA}$, respectively.

In order to determine the relation of the corrugation amplitudes of the $[1\bar{1}0]$ and the $[001]$ direction for the present case of a conical spin spiral, the angular dependence of the corrugation amplitudes needs to be calculated. According to Eq. (8.1) the magnetization of the sample is given by

$$\mathbf{m}_S = S_n \begin{pmatrix} \cos \theta \\ \sin \theta \cos(\phi + \tau) \\ \sin \theta \sin(\phi + \tau) \end{pmatrix}. \quad (8.9)$$

The magnetization of the tip is defined as

$$\mathbf{m}_{T,[1\bar{1}0]} = S_T \begin{pmatrix} 1 \\ 0 \\ 0 \end{pmatrix} \quad (8.10)$$

for the tip magnetization direction aligned to $[1\bar{1}0]$ and

$$\mathbf{m}_{T,[001]} = S_T \begin{pmatrix} 0 \\ 1 \\ 0 \end{pmatrix} \quad (8.11)$$

along [001]. Therefore, the dependence of the corrugation on the cone angle θ corresponds to

$$\mathbf{m}_{T,[1\bar{1}0]} \cdot \mathbf{m}_S \propto \cos \theta \quad \text{along } [1\bar{1}0] \quad \text{and} \quad \mathbf{m}_{T,[001]} \cdot \mathbf{m}_S \propto \sin \theta \quad \text{along } [001]. \quad (8.12)$$

With $\Delta z_{[1\bar{1}0]} \propto \cos \theta$ and $\Delta z_{[001]} \propto \sin \theta$ the ratio results in

$$\frac{\Delta z_{[1\bar{1}0]}}{\Delta z_{[001]}} = \cot(\theta) \cdot \frac{\exp\left(-2z_0 \sqrt{\frac{2m_e}{\hbar^2} \cdot \phi_{\text{work}} + \left(\frac{\pi}{a_1}\right)^2}\right)}{\exp\left(-2z_0 \sqrt{\frac{2m_e}{\hbar^2} \cdot \phi_{\text{work}} + \left(\frac{\pi}{a_2}\right)^2}\right)}. \quad (8.13)$$

It has been calculated for either a fixed tip-sample distance z_{dist} (Fig. 8.16(a)) or a fixed cone angle θ (Fig. 8.16(b)).

Both figures, Fig. 8.16(a) and (b), show that for large cone angles and large tip-sample distances the ratio of the corrugation amplitudes becomes nearly zero, i.e., $\Delta z_{[001]}$ becomes very large. First of all, this is due to the fact that magnetic configurations described by a small lattice vector a_i decay faster with increasing tip-sample distance than those with a large lattice vector as it is seen from Eq. (8.8). Secondly, with increasing cone angle the projected magnetization component in the $[1\bar{1}0]$ direction becomes smaller. Therefore, the study of the cone angle is quite complex since it requires a well-known tip magnetization direction and a sufficiently small tip-sample distance. Up to now there is no direct experimental confirmation of the theoretical cone angle of $\theta = 30^\circ$. However, with a ratio of about four over one for $\Delta z_{[001]}$ versus $\Delta z_{[1\bar{1}0]}$ obtained in spin-polarized STM experiments [138] the cone angle of the spin-spiral state found in a double layer Mn on W(110) can be estimated to be between 30° and 45° if the tip-sample distance is assumed as 8 \AA . Therefore, an optimum cone angle of 30° as found in the DFT calculations is consistent with the experimental data.

8.9 The Tunneling Anisotropic Magnetoresistance Effect in a Conical Spin-Spiral State

The conical spin-spiral ground state of the Mn double layer on the (110) surface of W is well suited for the study of a transport effect due to SOC which is known as tunneling anisotropic magnetoresistance (TAMR). In contrast to the junctions used for the tunneling magnetoresistance effect (TMR), a magnetic tunnel junction needs to comprise only one magnetic electrode opposed to a nonmagnetic electrode in order to give rise to the TAMR effect. Due to changes in the electronic structure the TAMR causes a magnetization-direction-dependent change in the tunneling resistance. It has first been observed in another ultra-thin film system – the double layer of Fe on the W(110) surface – where it has been demonstrated that the SOC

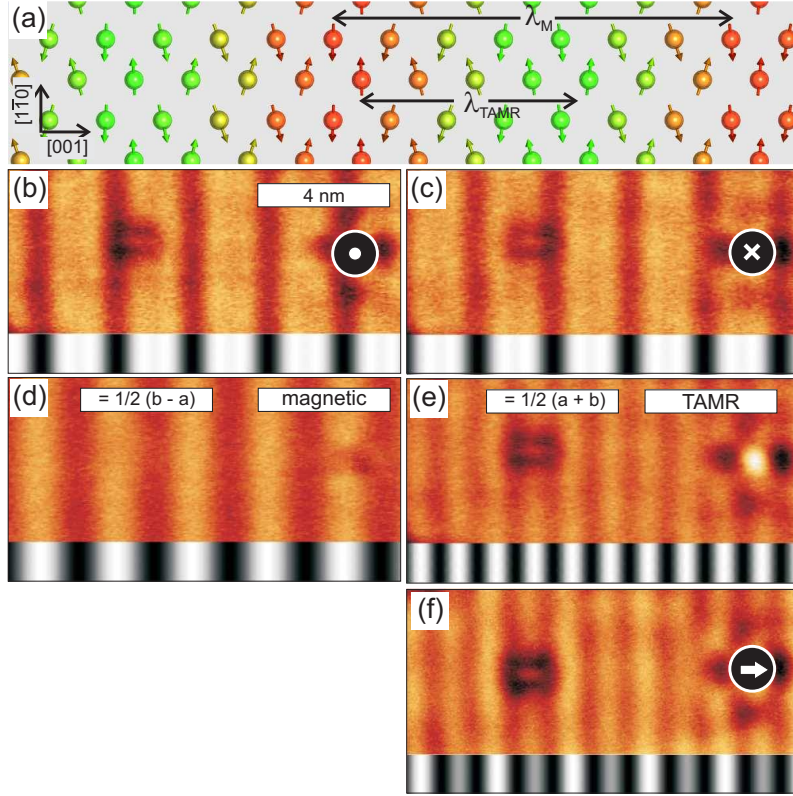


Figure 8.17: Spin-polarized STM measurements and simulations ($P = 0.1, \gamma = 0.2$) (a) Top view of the magnetic ground state. Red and green symbols denote negative and positive z components of the magnetization, respectively. (b),(c) Spin-polarized dI/dU maps of the same sample area with oppositely out-of-plane magnetized tips (spin-polarized tip that aligns with external magnetic field at $B = +2$ T and $B = -2$ T). (d) Difference and (e) sum of the images in (b) and (c). (f) Spin-polarized dI/dU maps of the same area with an in-plane magnetized tip ($B = 0$ T). All spin-polarized STM images: $I = 1$ nA, $U = -40$ mV, $T = 9$ K

induced changes in the local density of states in the vacuum allow for the resolution of magnetic domain walls on the nanometer scale using nonmagnetic STM tips [19]. The TAMR effect will be introduced in more detail in the next chapter, where it will be explored at the limit of single atoms. Here, it will be shown how it can be used to image the conical spin spiral of the Mn double layer on W(110).

While neglecting SOC non-collinear configurations such as the conical spin spiral are characterized by a constant variation of the magnetization direction from one atom to the other. Therefore, every spin of this structure experiences the same local environment, and the spins are electronically equivalent. As a consequence, every modulation observed in the LDOS can be directly related to the SOC effect. For instance, spin-polarized STM measurements carried out in the group of Prof. Wiesendanger at the University of Hamburg with an out-of-plane magnetized tip

show characteristic bright and dark stripes as displayed in Fig. 8.17 (b). By reversing the magnetization direction of the spin-polarized STM tip the pattern in Fig. 8.17 (c) displays a phase shift of about half the magnetic periodicity ($\lambda_{\text{TAMR}} = \lambda_M/2 = 1.2 \text{ nm}$) with respect to the pattern in Fig. 8.17 (b). In order to analyze the electronic and the magnetic contributions separately, the images Fig. 8.17 (b) and Fig. 8.17 (c) have been subtracted and added up resulting in the magnetic (Fig. 8.17 (d)) and electronic signal (Fig. 8.17 (e)). The latter is due to the TAMR effect and the variation of the local density of states is related to the angle θ of the spin direction on the cone of the spiral via $\cos^2 \theta$. The spin-polarized contribution, on the other hand, scales with the cosine of the angle between the tip's and the atom's magnetization. The rotation of the magnetization direction of the tip from out-of-plane to in-plane results in the images shown in Fig. 8.17 (f), which display a shift of the magnetic contrast of $\pm\lambda_M/4$. This is due to the fact that the TAMR contrast is pinned to the spin structure while the spin-polarized contribution to a STM image changes upon rotation of the tip magnetization direction.

In conclusion, the study of the TAMR in the double layer Mn on W(110) illustrated that the conical spin spiral can be investigated using a nonmagnetic STM tip. This is due to the magnetization-direction dependent changes in the electronic structures.

8.10 Conclusions

In this chapter the magnetic ground state of two monolayers of Mn on the W(110) surface has been investigated. A strong tendency towards antiferromagnetic order accompanied by an instability against non-collinear magnetic order has been observed in this system that allows for three-dimensional spin structures, i.e., conical spin spirals. Here, such a conical spin-spiral state has been found, which exhibits a cone angle of $\theta = 30^\circ$ and a spin-spiral rotation angle of $\phi = 32^\circ$. The latter corresponds to a period length of 1.8 nm, which is in reasonable agreement with the results of spin-polarized STM experiments.

Two mechanisms that give rise to such spin arrangements have been under consideration. It was found that the higher-order spin interactions, i.e., the biquadratic exchange and the four-spin interaction induce a canting of the magnetic moments with respect to the film plane. Furthermore, the Heisenberg exchange introduces a rotation that propagates along the [001] direction. The resulting conical spin-spiral exhibits local antiferromagnetic order and explains the experimentally obtained spin-polarized STM images. The conical spin spiral of the Mn double layer on W(110) is the first observation of such a spin structure at a surface. Moreover, the occurrence of this three-dimensional magnetic configuration can be directly ascribed to the higher-order spin interactions, which are typically neglected in transition metals. Here, it is demonstrated that the spin interactions beyond the Heisenberg picture

can play an important role in such systems.

The further examination of the influence of the tip magnetization direction on the spin-polarized STM contrasts has been carried out based on simulated STM images calculated within the Tersoff-Hamann model. In order to allow for the identification of the cone angle the corrugation amplitudes corresponding to the modulation along the $[1\bar{1}0]$ and $[001]$ direction, respectively, as well as their ratio have been studied. Finally, the influence of the SOC on a conical spin spiral in terms of the tunneling anisotropic magnetoresistance has been investigated.

9 Tunneling Anisotropic Magnetoresistance at the Single Atom Limit

In 1975 M. Jullière discovered the tunneling magnetoresistance (TMR) [60] – a magnetoresistive effect that occurs due to spin-dependent tunneling in nanosize magnetic tunnel junctions. As illustrated schematically in Fig. 9.1 (a) the latter consist of two ferromagnetic layers that are separated by a thin insulating layer through which the electrons can tunnel from one ferromagnetic electrode to the other. According to Jullière’s model the tunneling takes place considering the following assumptions (i) the spin of the tunneling electrons is conserved and (ii) the conductance G is proportional to the product of the densities of states of the ferromagnets in the parallel (P) or antiparallel (AP) alignment, respectively. By applying an external magnetic field the magnetizations of the electrodes can be switched from parallel (high tunneling probability) to antiparallel (low tunneling probability). While the experiments of M. Jullière had to be realized at very low temperatures [60] the TMR effect at room temperature was achieved in the 90s by Moodera [139] and Miyazaki [140]. This allows for the application of the TMR effect in read heads of modern hard disk drives. Furthermore, the discovery of the TMR gave rise to the development of the magnetoresistive random-access memory (MRAM) – a non-volatile random-access memory technology. Due to SOC the resistance can become anisotropic, i.e., it depends on the magnetization direction of the tunnel junction with respect to the crystallographic axes as sketched in Fig. 9.1 (b). For the observation of this effect the junction needs only a single magnetic electrode separated from a nonmagnetic electrode by an insulating layer. Due to magnetization-direction dependent changes in the electronic structure the tunneling current between these electrodes exhibits differences for a film that is magnetized either out-of-plane (\perp) or in-plane (\parallel) [19, 25, 141, 142]. This effect has been established as tunneling anisotropic magnetoresistance (TAMR). The TAMR offers an alternative route towards spintronic devices as it circumvents the restriction of coherent spin-dependent transport [25] in contrast to the TMR.

The TAMR has first been observed in STM measurements of a double-layer film of Fe on the W(110) surface [19]. It also occurs in planar tunnel junctions that involve ferromagnetic semiconductors [25]. Furthermore, the application of magnetic transition-metal electrodes allows for the operation of such nanoscale devices at room temperature [143, 144]. Other experiments have been conducted concerning the TAMR in metal-semiconductor Fe/GaAs/Au junctions [145] and transition-metal

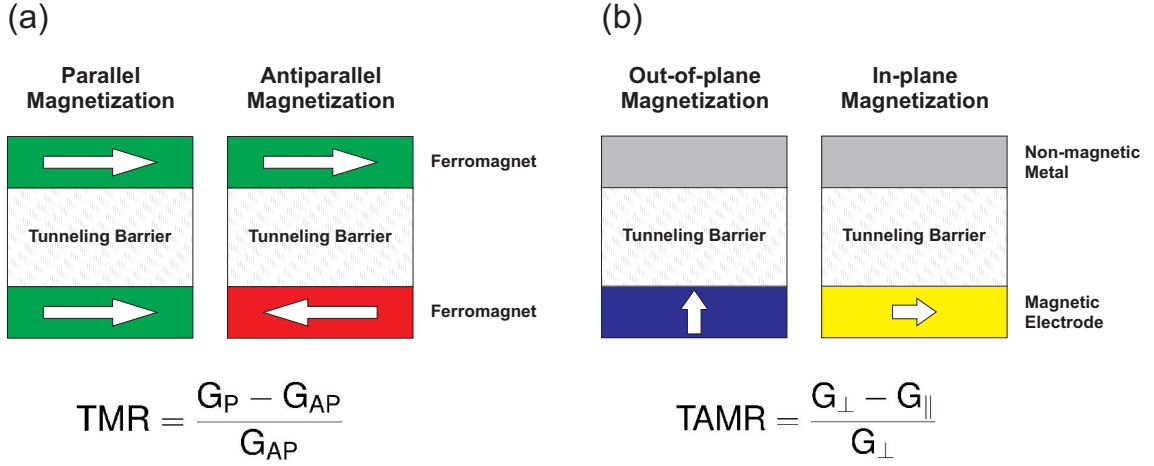


Figure 9.1: (a) Sketch of the TMR: the electrons tunnel between two ferromagnets that are separated by an insulating layer, e.g., vacuum. The tunneling current depends on the magnetic alignment of the electrodes, i.e., either parallel (P) or antiparallel (AP). The TMR is defined from the conductances in the parallel (G_P) and antiparallel (G_{AP}) alignment. (b) Sketch of the TAMR: the tunnel junction comprises a nonmagnetic and a magnetic electrode that are separated by a tunneling barrier. The conductance is subject to the magnetization orientation in the magnetic layer, i.e., perpendicular (G_{\perp}) or parallel (G_{\parallel}) to the surface.

electrodes separated by oxides [146]. By combining $3d$ and $5d$ transition metals it was possible to enhance the TAMR by two orders of magnitude up to some 10%. Due to theoretical predictions of a large TAMR effect in antiferromagnetic $3d$ - $5d$ bimetallic alloys [147] attempts are being made towards antiferromagnetic electrodes [148].

So far planar structures such as multilayers of magnetic and nonmagnetic materials of a few nanometer thickness as electrodes have been investigated almost exclusively. It is still under debate how the TAMR scales in the limiting case of a single atom. In Ni and Co break-junctions it has been predicted that the TAMR reaches up to 200% due to tip-resonant states and exhibits characteristic bias-dependent oscillations on a mV range [149]. Nanoscale contacts that were produced by the controllable breaking of a nanowire structure (break junction technique) while monitoring the electrical resistance of the junctions also exhibited large TAMR values between 20% to 100% [150]. For break junctions formed via electromigration values up to 25% have been observed for the TAMR and significant changes in the angular dependencies of the dI/dV for bias voltages on the scale of a few mV [151]. However, the direct comparison of theoretical and experimental results has always been a major issue in explaining the origin of the TAMR as the hitherto existing approaches for the fabrication of nanoscale contacts did not allow for microscopically well-defined contacts.

In this chapter, it is shown that STM experiments on single adatoms deposited on ultrathin films allow to study the TAMR at the single-atom limit and to compare

it with electronic structure calculations. Since the adsorbed atoms are subject to the local exchange interaction, their magnetic moments align to the moments of the neighboring atoms in the film. Thus, they exhibit in-plane magnetization if the adsorption site is on the domain wall and out-of-plane magnetization if they are adsorbed on the domain. In this way, it is possible to explore the TAMR without applying an external magnetic field and enable the comparison of theoretical and experimental results.

In the following, the TAMR effect at the single-atom limit will be investigated systematically. First of all, the double-layer Fe film on the W(110) surface will be examined concerning its role as a magnetic template for the adatoms. It reveals a nanoscale domain structure. By depositing a Co atom to either the domain or the domain wall of the Fe double layer it presents an out-of-plane and in-plane magnetization direction, respectively. Densities of states are calculated in the vacuum for both magnetizations of the Co adatom and compared to the experimental spectra. The direct comparison of theory and experiment as well as the analysis of the orbital symmetry of the electronic states provides insight into the origin of the TAMR. It is further explained within the framework of a simple model that considers the coupling of two atomic states at a surface. By choosing a heavier adatom such as a nonmagnetic Ir atom for the adsorption to the Fe DL, the SOC effect in the single atom contact will be enhanced. Due to hybridization effects the Ir atom is spin-polarized and reveals a magnetic moment that aligns to those of the neighboring atoms of the Fe film. Furthermore, the Ir atom exhibits a huge TAMR compared to the single Co atom due to magnetization-direction dependent changes of the electronic structure. Finally, the influence of the magnetic template onto the TAMR effect in the Co adatom is explored by changing the nanoscale domain structure of the Fe DL on W(110) [19, 26, 27] with the more rapidly rotating spin-orbit induced spin-spiral ground state of the Mn monolayer on W(110) [9]. Due to the alignment with the magnetic moments of the nearest neighbor Mn atoms the magnetization direction of the Co adatom can take every angle that is provided by the Mn spin spiral. Also in this case the TAMR is explored by analyzing the orbital character of the states that contribute to the vacuum density of states.

Parts of this chapter have been published in Physical Review Letters [152].

9.1 TAMR of the Fe Double-Layer on W(100)

As mentioned above, there are two ways to study how the electronic structure of a system depends on the orientation of the magnetization. On the one hand, a strong external magnetic field can be applied in order to constrain the magnetic moments of the sample to the hard magnetization directions. This approach faces complications regarding the sensitivity of the experimental setup or a deformation of the contacts due to magnetostatic or magnetostrictive forces. On the other hand,

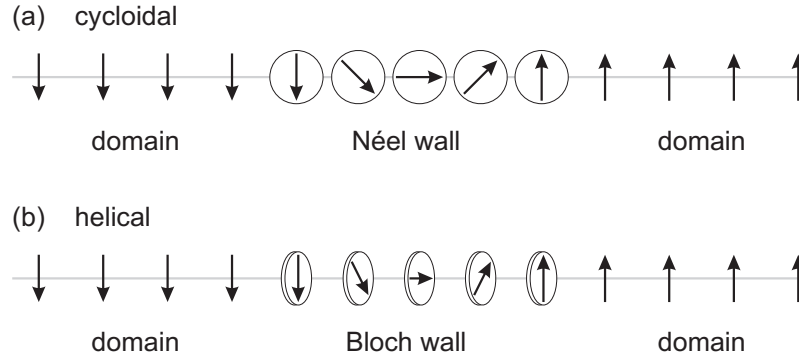


Figure 9.2: (a) Néel wall: the transition between two domains happens via a cycloidal spin spiral, i.e., the spin-rotation axis is perpendicular to the propagation direction. (b) Bloch wall: the transition between two domains happens via a helical spin spiral, i.e., the spin-rotation axis is parallel to the propagation direction.

the sample itself can provide a local frame for the magnetization by exhibiting, for instance, a domain structure. For a film consisting of two monolayers of Fe deposited on the (110) surface of W such a nanoscale domain structure has been observed experimentally [19, 26, 27]. The transition from an 'up' magnetized domain to a 'down' magnetized domain happens via the domain wall, where the magnetic moments reorient gradually. Figure 9.2 illustrates the two types of domain walls. In a *Néel wall* the axis of the spin rotation is perpendicular to the propagation direction resulting in a cycloidal spin-spiral state (cf. Fig. 9.2 (a)). In a *Bloch wall* the magnetic moments rotate in a helical fashion, i.e., the propagation direction and the spin rotation axis are parallel (cf. Fig. 9.2 (b)). However, the double-layer Fe film on W(110) exhibits Néel walls since the moments of the Fe atoms rotate right-handed cycloidal from one domain to another via the [001] direction (cf. Fig. 9.3), which is driven by the DMI [10, 128, 129].

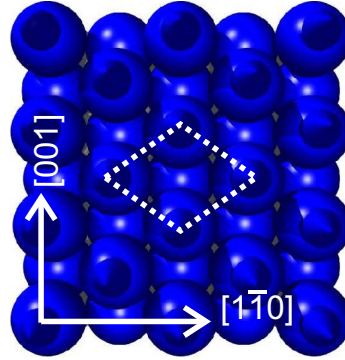
Further studies of this system revealed that spectra acquired above the domain via scanning tunneling spectroscopy show small deviations of a few percent compared to those obtained above the domain wall [19]. DFT studies of the electronic structure explained the differences with a magnetization-direction dependent hybridization gap between the d_{xy+zx} and the d_{z^2} states of the minority channel leading to a magnetization-direction dependent contribution to the tunneling current, i.e., the TAMR effect.

In the following, the double layer of Fe on the W(110) surface is investigated with regard to its function as a substrate for the single atoms.

Computational Details

The calculations have been carried out employing a symmetric film consisting of five layers of W with two monolayer of Fe on each side. As a starting point the experimental lattice constant of W has been used ($a_0 = 3.165 \text{ \AA}$) and the structural

Figure 9.3: Top-view of the double-layer Fe film on the W(110) surface. The blue spheres with arrows refer to the Fe atoms and their magnetic moments, respectively. For better visibility the arrows have been omitted in the sub-surface Fe layer. The magnetic unit cell is indicated by a dotted white line.



relaxations have been accomplished within the GGA [33] while neglecting SOC. The interlayer distance between the Fe sublayer and the W substrate relaxes inwards by 17%, i.e., 2.042 Å, with respect to the bulk lattice constant of W. The distance between the Fe surface layer and the Fe sublayer decreased to a value of 1.768 Å, i.e., a reduction of 22% compared to the bulk W distance. The studies of the electronic structure have been performed within the LDA [122] including SOC via a second variational approach [105]. For the sampling of the two-dimensional BZ 18 \mathbf{k}_{\parallel} -points in the irreducible wedge have been used for the convergence as well as 962 \mathbf{k}_{\parallel} -points in the full two-dimensional BZ for the calculation of the local density of states (LDOS). The plane-wave cutoff has been set to $k_{max} = 3.9 \text{ a.u.}^{-1}$.

9.1.1 Calculation of the TAMR of the Double Layer Fe on W(110)

In order to gain insight into the electronic structure of the Fe double-layer film, Fig. 9.4 (a) displays the spin-resolved LDOS calculated in the topmost layer of the Fe film. In this system the magnetic moments in the domain walls rotate from 'up' to 'down' and *vice versa* via the [001] direction and form a Néel wall that is driven by the DMI. Therefore, the spin-quantization direction used in the calculation of the LDOS aligns either perpendicular (\perp) or parallel (\parallel) to the surface plane and represents the magnetization in the domain and the domain walls, respectively. The curves in the majority and the minority spin channel present a similar profile but at the same time they are shifted with respect to each other due to the exchange splitting. The latter allows for the formation of a magnetic moment, which is $2.9 \mu_B$ in the Fe surface atoms and $2.32 \mu_B$ in atoms of the subsurface layer. Due to the exchange splitting the densities of states in the majority spin channel exhibit full occupation since the major part of the states is located below the Fermi level. On the other hand, the densities of states in the minority channel are shifted towards higher energies and thus imply only partly occupation of the states. Furthermore, in the energy range of $E_F - 0.6 \text{ eV}$ and $E_F + 1 \text{ eV}$ the densities of the minority spin states are larger than those of the majority spin hinting at a predominance of spin down states in the vacuum density of states.

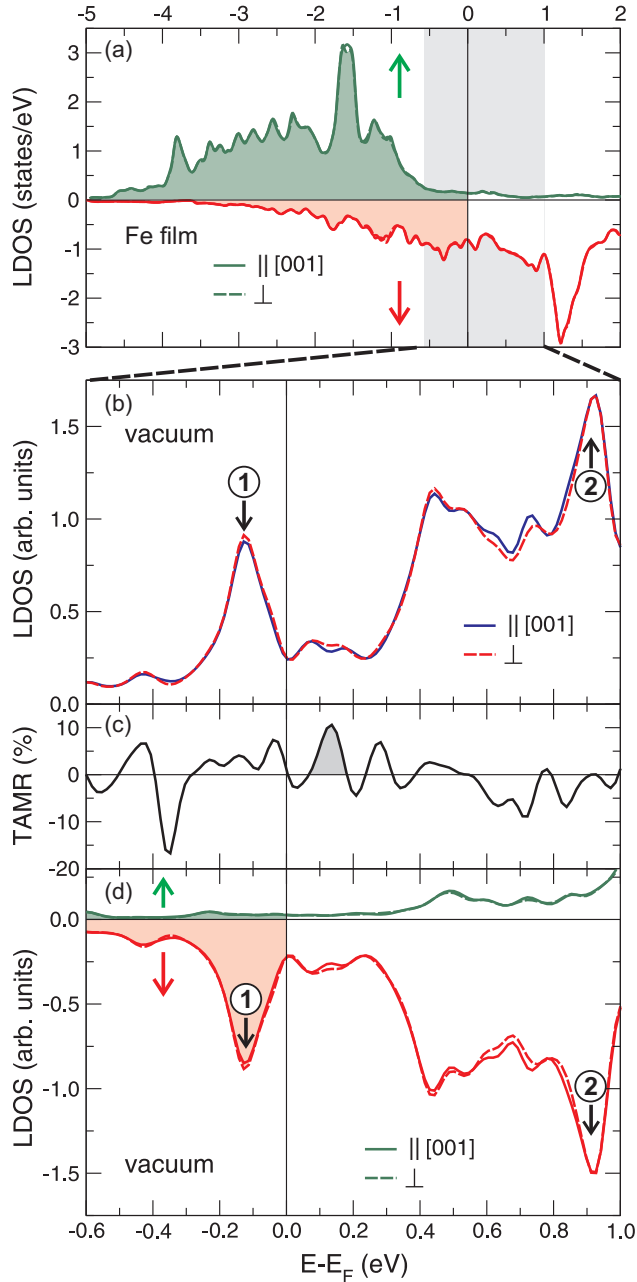


Figure 9.4: (a) LDOS in the Fe DL on W(110) calculated for a magnetization perpendicular (dashed lines) to the film plane and parallel to the [001] (solid lines) direction in the majority (\uparrow) and minority (\downarrow) spin channel. (b) The spin-averaged LDOS in the vacuum calculated at 10 Å above the in-plane (blue solid line) and out-of-plane (red dashed line) magnetized Fe film. (c) Calculated TAMR effect of the vacuum LDOS in (b) according to Eq. (9.1). (d) Spin-resolved vacuum LDOS of the in-plane (solid) and out-of-plane (dashed) magnetized Fe film.

In the MT spheres differences in the electronic structure due to the different magnetization directions are barely observable in the LDOS¹. This is quite different in the vacuum as presented in Fig. 9.4 (b). Both curves exhibit a similar shape including two distinctive peaks located at -0.13 eV and $+0.93$ eV with respect

¹In order to illustrate them, the anisotropy of the LDOS might be plotted. Since the following discussion restricts to the changes in the vacuum LDOS, the information of the TAMR in the MT spheres has been neglected in this case.

to the Fermi level, which can be identified with those at -0.08 V and $+0.7$ V of the experimental spectroscopy data in reference [19] and are a characteristic of the double-layer Fe film on W(110). Nevertheless, the densities of states show small deviations depending on the magnetization direction. These discrepancies originate from an anisotropy in the LDOS due to SOC, which causes the TAMR effect. It is quantified by applying the following equation

$$\text{TAMR} = \frac{\text{LDOS}_{\perp} - \text{LDOS}_{\parallel}}{\text{LDOS}_{\perp}} \quad (9.1)$$

to the vacuum densities of states in Fig. 9.4 (b). The resulting curve in Fig. 9.4 (c) reveals numerous oscillations as a function of energy with values ranging between -17% and $+11\%$.

In the following, the discussion of the TAMR focuses on the shaded feature at $+0.14$ eV above the Fermi energy (E_F), which allows to distinguish domains and domain walls in STM experiments using bare W tips [19]. It is due to an increase in the perpendicular magnetized LDOS_{\perp} with respect to LDOS_{\parallel} . Furthermore, the spin-resolved vacuum densities of states in Fig. 9.4 (d) show that this feature stems from the minority spin channel just as the major part of the vacuum LDOS. The decomposition of the density of states in the MT sphere of a Fe surface atom according to the orbital symmetry reveals that states of d_{z^2} character dominate the vacuum LDOS. This is by no means surprising since their shape and the orientation perpendicular to the surface allows for a slow decay into the vacuum. In contrast, orbitals that possess a planar symmetry and are aligned parallel to the surface such as d_{xy} and $d_{x^2-y^2}$ barely extend into the vacuum and decay more quickly with increasing distance. However, in the case of the TAMR feature at $E_F + 0.14$ eV the d_{z^2} orbitals mix with the hybridized states of d_{xy} and d_{yz} character leading to a reduction of LDOS_{\parallel} in comparison to LDOS_{\perp} . Thus, the obtained theoretical results agree well with the experimental data in [19].

The above analysis of the Fe double layer on the W(110) presents an ideal basis for the following study of the TAMR in the single-atom limit. Adatoms can be deposited either on the domain or the domain wall revealing different magnetization directions due to exchange coupling with the Fe atoms. Analogously to the case of the Fe double layer on W(110), the comparison of vacuum densities of states obtained for an in-plane magnetization, i.e., along [001] and perpendicular to the surface will reveal differences resulting in the TAMR due to the mixing of d states with different orbital character.

9.2 Co Adatom on Fe/W(110)

As mentioned at the beginning of this chapter, the TAMR effect has not been discussed in nanoscale structures on the basis of a direct comparison of experimental

and theoretical data for the same well-defined system. In this section a single Co adatom on the double-layer film of Fe on the W(110) surface is investigated in terms of STM measurements and DFT calculations. Here, one takes advantage of the fact that Co adatoms couple ferromagnetic to the Fe double layer. Therefore, their magnetic moments are oriented parallel to the magnetization of the local environment, i.e., perpendicular to the film plane for a Co atom adsorbed on the domain and parallel to the film plane in the case of a Co atom residing on the domain wall. In this way, no external magnetic field is needed in order to rotate the magnetization of the Co atom that exhibits a moment of $1.81 \mu_B$ for both magnetization directions. Bias-dependent oscillations of the TAMR on a scale of 100 mV and values of up to 12% have been observed in the STM experiment. The origin of this effect is explained based on first-principles calculations that reveal the hybridization of Co d states of different orbital symmetry depending on the magnetization direction due to SOC. A direct consequence of the spin-orbit induced mixing of states are magnetization-direction dependent changes in the LDOS that explain the observed TAMR.

Experimental Observation of the TAMR

The experiments were performed in the group of Prof. Berndt at the University of Kiel with a home-built STM operated at 7 K and in ultrahigh vacuum with a base pressure of 10^{-9} Pa. W(110) surfaces were cleaned by oxidation cycles at 1400 K and brief annealing at 2200 K. Room temperature exposure of clean W(110) to an Fe atom flux from an electron beam evaporator and subsequent annealing at 500 K results in a closed Fe film on top of a Fe wetting layer (Fig. 9.5(a)) [153]. Single Co atoms were deposited onto Fe-covered W(110) at 10 K. Figure 9.5 (b) shows that Co atoms adsorb to magnetic domains and domain walls, which are imaged with high and low contrast, respectively. The contrast is due to different magnetization directions, whose signature is imprinted on the probed electronic structure via the spin-orbit interaction [19]. Magnetic domains exhibit an out-of-plane (\perp) magnetization while the central regions of domain walls are in-plane (\parallel) magnetized. W tips were fabricated from polycrystalline wire, which was chemically etched *ex vacuo* and annealed *in vacuo* prior to mounting to the STM. Special care was taken to preserve a non-spin-polarized current during the experiments. To this end spectroscopy and maps of dI/dV were acquired from double-layer Fe islands, which in case of a spin-polarized tunneling current give rise to clear spin contrast [19].

The tunneling spectra shown in Fig. 9.6 (a) were obtained with W tips for Co adatoms, which are adsorbed either on the domains or on the domain walls of the Fe film. Due to the strong exchange coupling of the Co adatom and the underlying Fe film the direction of the magnetic moment of Co is orientated out-of-plane for Co adatoms on the domains and in-plane for Co adatoms on the domain walls.

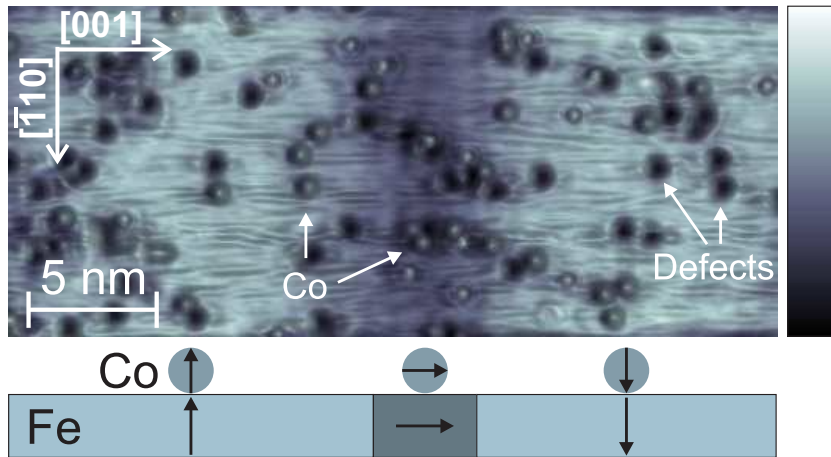
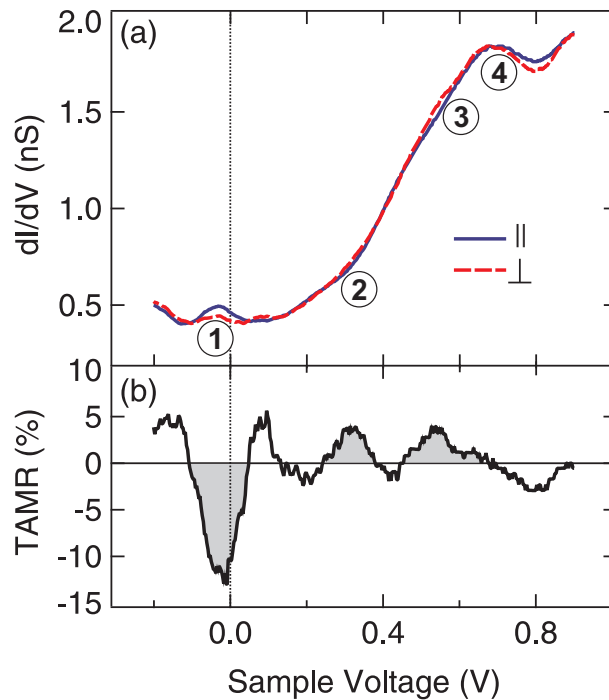


Figure 9.5: Pseudo-three-dimensional representation of a constant-current STM image (1 nA, 0.07 V) of Co atoms adsorbed on a double-layer Fe film on W(110). To visualize the magnetic domains and domain walls, the topography data have been colored with the simultaneously recorded dI/dV map. The color scale ranges from 5 (dark) to 14 nS (bright). The sketch at the bottom of the figure shows the alignment of the Co magnetic moment with the Fe magnetization.

Figure 9.6: (a) dI/dV spectra obtained using STM with W tips on Co adatoms on domains (dashed line) and on domain walls (solid line) of an Fe double layer on W(110). The feedback loop had been disabled at 0.9 V and 1 nA prior to spectroscopy. To facilitate comparison with calculations (Fig. 9.8) some spectroscopic features are labeled 1–4. (b) Tunneling anisotropic magnetoresistance determined from the spectra in (a). The TAMR ($\text{TAMR} = ((dI/dV)_\perp - (dI/dV)_\parallel) / (dI/dV)_\perp$) at the features 1 to 4 are shaded for easier comparison with Fig. 9.8.



We observe that the two types of spectra show only little differences. There is a pronounced feature in the unoccupied states at about 0.7 V above the Fermi energy and a smaller one in the occupied states at -0.02 V. Between these major peaks two smaller features appear as small shoulders in the spectra. The differences of the

two curves can be quantified by calculating the TAMR defined as

$$\text{TAMR} = \frac{((dI/dV)_{\perp} - (dI/dV)_{\parallel})}{(dI/dV)_{\perp}}, \quad (9.2)$$

which is plotted in Fig. 9.6(b). The TAMR displays numerous oscillations in sign as a function of bias voltage and reaches values of up to 13 %.

Computational Details

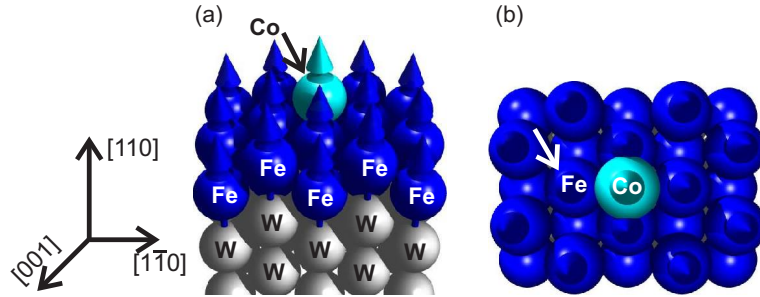


Figure 9.7: (a) Side-view of the $c(4 \times 4)$ unit cell used in the calculations. Gray spheres represent atoms of the nonmagnetic W substrate. Magnetic atoms are indicated by blue (Fe) and cyan (Co) spheres that include arrows. (b) Top-view of the unit cell. The white arrow points at the Fe atom for which the orbital decomposition has been calculated.

The calculations have been performed within the FLAPW method using a symmetric slab consisting of five layers of W with two layers of Fe on each side. The Co atom has been added on each side at the hollow site position centering the $c(4 \times 4)$ unit cell. Structural relaxations have been taken from references [154, 155]. The electronic structure of the system has been studied within the LDA [122]. Spin-orbit coupling was included by means of a second variational approach [105]. 12 \mathbf{k}_{\parallel} -points in the irreducible wedge of the two-dimensional Brillouin zone and a plane-wave cutoff of $k_{max} = 3.9 \text{ a. u.}^{-1}$ were used. The LDOS has been calculated using 468 \mathbf{k}_{\parallel} -points in the entire Brillouin zone.

9.2.1 TAMR of the Co Adatom on the Double Layer Fe on W(110)

Figure 9.8 (a) shows the calculated LDOS in the MT sphere of the Co adatom for the majority and the minority spin channel revealing almost full occupation in the majority spin states. However, due to the exchange splitting the LDOS in the minority spin channel is shifted towards higher energies. The resulting magnetic moment of the Co atom is $1.81 \mu_B$ and independent of the magnetization direction. Furthermore, this shift leads to a predominance of the minority spin states around the Fermi level within an energy range of $E_F - 0.5 \text{ eV}$ to $E_F + 2 \text{ eV}$. A comparison

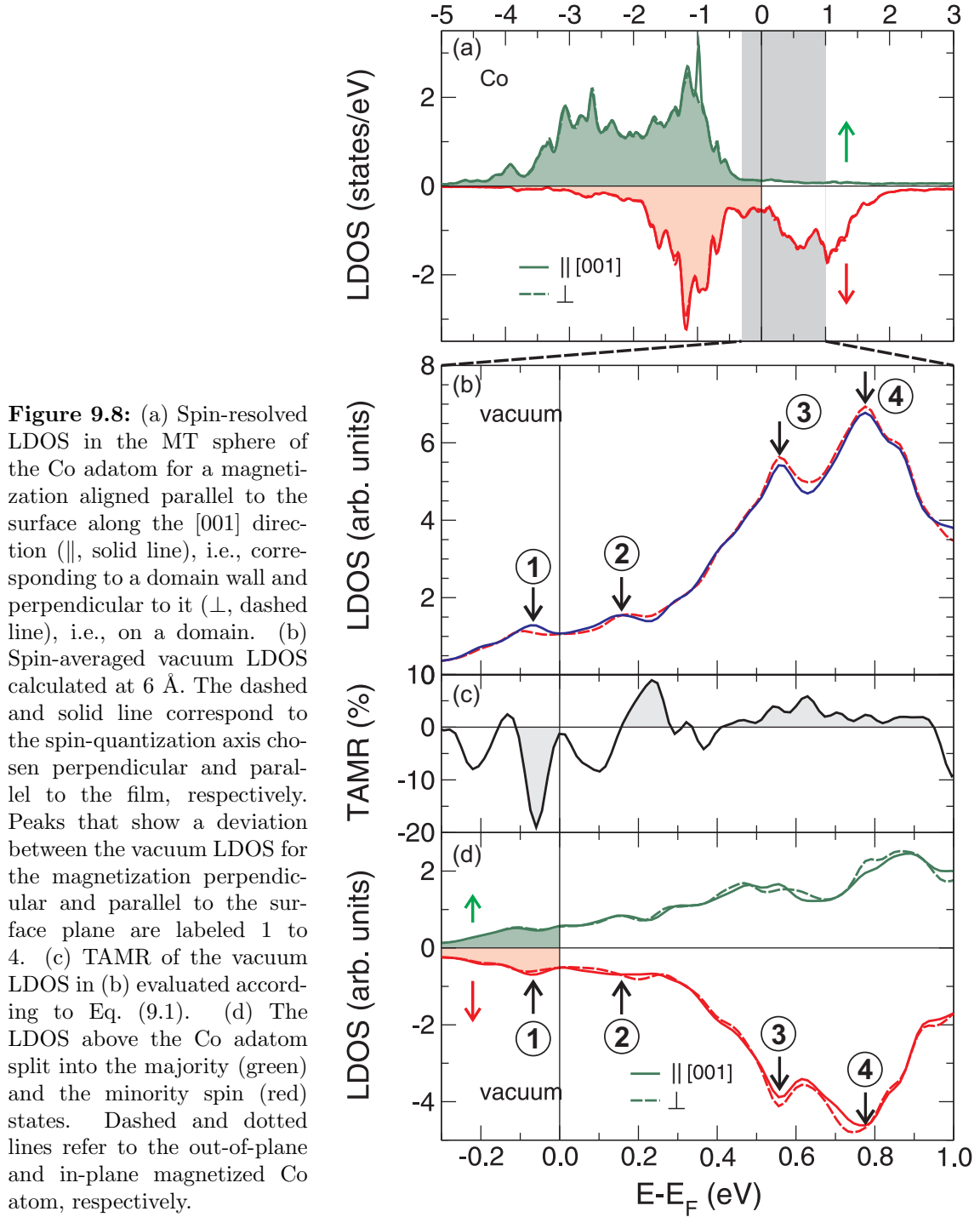


Figure 9.8: (a) Spin-resolved LDOS in the MT sphere of the Co adatom for a magnetization aligned parallel to the surface along the [001] direction (\parallel , solid line), i.e., corresponding to a domain wall and perpendicular to it (\perp , dashed line), i.e., on a domain. (b) Spin-averaged vacuum LDOS calculated at 6 Å. The dashed and solid line correspond to the spin-quantization axis chosen perpendicular and parallel to the film, respectively. Peaks that show a deviation between the vacuum LDOS for the magnetization perpendicular and parallel to the surface plane are labeled 1 to 4. (c) TAMR of the vacuum LDOS in (b) evaluated according to Eq. (9.1). (d) The LDOS above the Co adatom split into the majority (green) and the minority spin (red) states. Dashed and dotted lines refer to the out-of-plane and in-plane magnetized Co atom, respectively.

of the LDOS calculated for a Co atom being adsorbed on the domain, i.e., a magnetization direction perpendicular to the surface (\perp , dashed line) and on the domain wall, i.e., parallel to the [001] direction (\parallel , solid line) [10] indicates a few changes

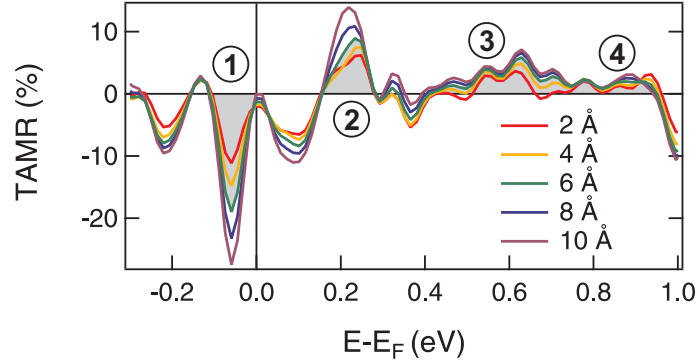


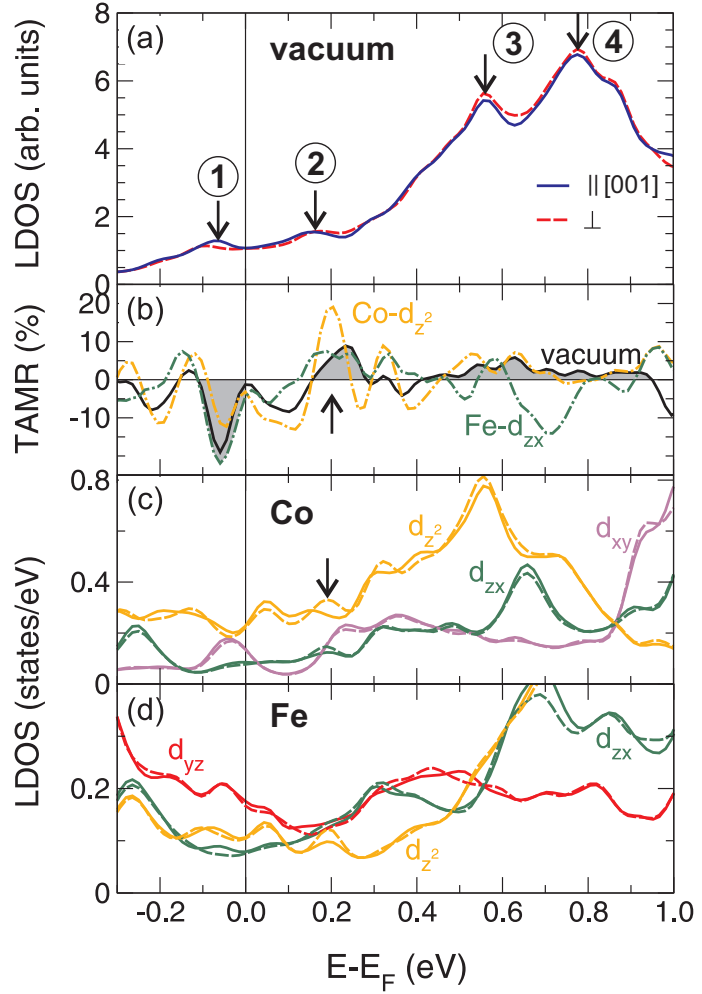
Figure 9.9: Distance dependence of the TAMR effect obtained for LDOS_{\parallel} and LDOS_{\perp} . The distance ranges from 2 Å (red) to 10 Å (violet) above the Co atom.

in the electronic structure. For instance in the majority channel a strong peak at -1 eV below the Fermi energy is observed for the atom that is magnetized parallel to the surface, which is absent in the LDOS of the perpendicular magnetized Co adatom. However, due to the large scale of the plot the changes in the LDOS of the Co adatom obtained for different magnetization directions are barely visible within the energy range of the experimental data, i.e., $E_F - 0.3$ eV to $E_F + 1$ eV. This is different for the LDOS calculated at 6 Å above the Co adatom in Fig. 9.8 (b). They can be qualitatively compared with the tunneling spectra displayed in Fig. 9.6 (a). Located at the energies of -0.07 , $+0.16$, $+0.56$ and $+0.78$ eV with respect to the Fermi level, four peaks 1 to 4 may be distinguished, which can be identified with those found in the experimental data in Fig. 9.6 (a) at -0.02 , $+0.32$, $+0.52$ and $+0.70$ V.

Similar to the experimental dI/dV spectra the calculated LDOS in the vacuum for the different magnetizations exhibits small deviations due to the anisotropy, which is directly related to the TAMR (cf. Eq. (9.1)). Figure 9.8 (c) displays the TAMR effect where features at the positions of peaks 1 to 4 have been shaded for clarity. The energy dependent oscillations show a positive value for peaks 2 to 4, i.e., the vacuum LDOS is enhanced for the perpendicular magnetization of the Co adatom. Peak 1, on the other hand, results in a negative TAMR since the vacuum LDOS for the in-plane magnetized Co adatom is larger. However, at the position of peak 1 the calculated TAMR values range from -19% to $+9\%$, which is in reasonable agreement with the experimental results of -12% to $+5\%$. Furthermore, the overall behavior of the TAMR is in accordance with the experiment (cf. Fig. 9.6 (b)).

Plotting the vacuum LDOS of the majority and the minority spin separately reveals that for energies above $+0.3$ eV with respect to the Fermi level the minority spin states exhibit a larger LDOS compared to the majority spin states, which is due to different vacuum decay properties of the s , p and d orbitals that contribute to the vacuum LDOS [154]. However, since the profile of the vacuum LDOS in the

Figure 9.10: (a) The vacuum LDOS calculated at 6 Å above the Co atom adsorbed on the double layer Fe on the W(110) surface. The dashed and solid line correspond to the spin-quantization axis chosen perpendicular and parallel to the film. Peaks that show a deviation between the vacuum LDOS for the magnetization perpendicular and parallel to the surface are denoted by arrows. (b) TAMR of the vacuum LDOS (black line) shown in (a). The TAMR of the d_{z^2} states of the Co atom shown in (c) is indicated by a yellow dashed-dotted line. The green dashed-dotted line represents the TAMR of the d_{zx} states of the Fe atom shown in (d). (c)–(d) Orbitally decomposed LDOS of the minority states in the muffin-tin of the Co atom and the adjacent Fe atom, respectively. Dashed and solid lines correspond to a spin-quantization axis chosen perpendicular or parallel to the surface, respectively.



minority channel resembles that of the spin-averaged vacuum LDOS in Fig. 9.8 (b), it can be concluded that the deviations caused by the TAMR stem from minority spin states.

The TAMR effect depends on changes in the electronic structure. Therefore, it exhibits a distance dependence, which is due to the different decaying lengths of the states. For instance, more localized states decay faster with increasing distance while delocalized states extend far into the vacuum. This can lead to an enhancement of TAMR features for large distances as shown in Fig. 9.9 at the energies of peak 1 and 2. For peak 1 the TAMR effect has a value of about -11% at 2 Å above the Co atom. Increasing the distance to 10 Å almost triples the TAMR effect down to -28% . Additionally, the occurrence of changes in sign depends on the distance from the Co adatom, too. While at a distance of 10 Å the flat part of the TAMR reveals no change in sign for the energy range of peaks 3 and 4, a reduction of the distance results in two more sign reversals close to 0.50 eV and 0.67 eV. However, a

tip-sample distance of 2 Å does not correspond to the tunneling regime, but can be explored experimentally in the contact regime.

The TAMR effect originates from the spin-orbit induced mixing of electronic states with different orbital character. Therefore, it is useful to analyze the mechanism behind it in terms of an orbital decomposition of the density of states (cf. Fig. 9.10 (c)). Given that the LDOS of the majority spin channel is low around the Fermi level (cf. 9.8 (d)) only the d states of the minority channel are taken into account. Comparing the d -orbitals of the Co atom (Fig. 9.10 (c)) to the vacuum LDOS (Fig. 9.10 (a)) demonstrates that the electronic states that contribute to the changes at the positions of peaks 2 to 4 are mainly of d_{z^2} character. However, peak 1 cannot be ascribed to the d_{z^2} states of the Co atom. Its occurrence can only be explained by the hybridization of states of the Co atom and the adjacent Fe atom (cf. Fig. 9.7 (b)). At the Co atom feature 1 is of d_{xy} character while it is of d_{zx} type in the Fe film.

The small deviations due to different magnetization directions, \perp and \parallel , are likewise present in the orbital decomposition of the LDOS at the Co and the Fe atom. In Fig. 9.10 (b) their TAMR effects (Co: yellow line; Fe: green line) are compared to the total TAMR effect (black line) of the vacuum LDOS. For the features at peaks 2 to 4 the d_{z^2} states of the Co atom reproduce the trend of the total TAMR in most instances, while the minimum at peak 1 agrees well with TAMR of the Fe- d_{zx} states. Hence, it is necessary to consider the electronic structure of the Fe atoms as well as the Co atom in order to understand the origin of the TAMR effect at feature 1 in this system.

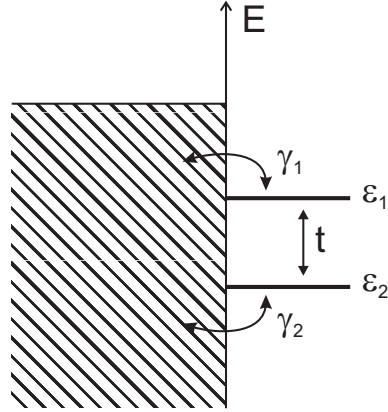
9.2.2 Model of the TAMR

The results above demonstrate that the anisotropy of the LDOS is directly related to changes in the electronic structure due to SOC. These changes originate from the mixing of d states with different orbital character such as d_{z^2} and the d_{zx} states. This is easily seen for peak 2 (cf. Fig. 9.10 (a) and (c)) at the Co atom: the LDOS_{\perp} of the d_{z^2} states exhibits an enhancement as well as a shift towards higher energies with respect to the d_{z^2} states of the in-plane magnetization direction. Furthermore, a small peak occurring in the LDOS_{\perp} of the d_{zx} states at the same energy hints to a hybridization between the states with an orbital character of d_{z^2} and d_{zx} . Calculating the difference between the d_{z^2} states of \perp and \parallel magnetization according to Eq. (9.1) results in a TAMR curve with similar behavior compared to the TAMR of the vacuum LDOS (cf. Fig. 9.10 (b)).

In order to capture the essence of the TAMR effect, a simple model based on the Green's function $G(E)$ is introduced in the following. It describes two localized atomic states at a surface that interact via SOC (cf. Fig. 9.11):

$$(E \cdot \mathbb{1} - \mathcal{H} - \Sigma) G(E) = \mathbb{1}. \quad (9.3)$$

Figure 9.11: Sketch of two states at the energies ε_1 and ε_2 that couple to a surface and interact via the hopping t between them. γ_1 and γ_2 specify the broadening of the peaks due to hybridization with the substrate.



Here, \mathcal{H} is the Hamilton matrix

$$\mathcal{H} = \begin{pmatrix} \varepsilon_1 & -t \\ -t & \varepsilon_2 \end{pmatrix} \quad (9.4)$$

with the energies ε_1 and ε_2 of the two states as well as the hopping t between them, which depends on the spin-quantization axis due to spin-orbit interaction. The diagonal elements $i\gamma_1$ and $i\gamma_2$ of the non-hermetian self-energy matrix

$$\Sigma = \begin{pmatrix} i\gamma_1 & 0 \\ 0 & i\gamma_2 \end{pmatrix} \quad (9.5)$$

describe the broadening of the peaks due to the hybridization of the atomic states with the substrate. Inserting \mathcal{H} and Σ gives the following equation:

$$\begin{pmatrix} E - \varepsilon_1 - i\gamma_1 & t \\ t & E - \varepsilon_2 - i\gamma_2 \end{pmatrix} \begin{pmatrix} G_{11}(E) & G_{12}(E) \\ G_{21}(E) & G_{22}(E) \end{pmatrix} = \mathbf{1}. \quad (9.6)$$

The LDOS $D_1(E)$ and $D_2(E)$ of the two states are given by the diagonal elements G_{11} and G_{22} of the 2×2 Green's function matrix using

$$D_i(E) = -\frac{1}{\pi} \text{Im} G_{ii}(E). \quad (9.7)$$

After inverting the matrix the Green's function reads

$$\begin{pmatrix} G_{11}(E) & G_{12}(E) \\ G_{21}(E) & G_{22}(E) \end{pmatrix} = \frac{1}{(E - \varepsilon_1 - i\gamma_1)(E - \varepsilon_2 - i\gamma_2) - t^2} \begin{pmatrix} E - \varepsilon_1 - i\gamma_1 & t \\ t & E - \varepsilon_2 - i\gamma_2 \end{pmatrix}. \quad (9.8)$$

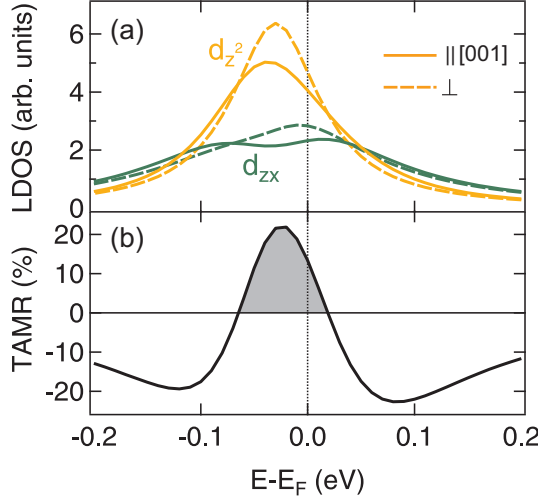


Figure 9.12: (a) LDOS obtained for a simple model of two atomic surface states that exhibit different orbital symmetry, d_{z^2} (yellow) and d_{zx} (green), and couple via SOC. The dashed (solid) line corresponds to the magnetization perpendicular (parallel) to the film plane. (b) Anisotropy of the LDOS (TAMR) calculated according to Eq. (9.1) for the d_{z^2} state in (a).

Then, the LDOS of state 1 and 2 result in

$$D_1(E) = -\frac{1}{\pi} \left[\gamma_1 (E - \varepsilon_2)^2 + \gamma_1 \gamma_2^2 + \gamma_2 t^2 \right] \times \left[(E - \varepsilon_1)^2 (E - \varepsilon_2)^2 + \gamma_1^2 \gamma_2^2 + t^4 + 2\gamma_1 \gamma_2 t^2 - 2t^2 (E - \varepsilon_1)(E - \varepsilon_2) + \gamma_1^2 (E - \varepsilon_2)^2 + \gamma_2^2 (E - \varepsilon_1)^2 \right]^{-1} \quad \text{and} \quad (9.9)$$

$$D_2(E) = -\frac{1}{\pi} \left[\gamma_2 (E - \varepsilon_1)^2 + \gamma_1^2 \gamma_2 + \gamma_1 t^2 \right] \times \left[(E - \varepsilon_1)^2 (E - \varepsilon_2)^2 + \gamma_1^2 \gamma_2^2 + t^4 + 2\gamma_1 \gamma_2 t^2 - 2t^2 (E - \varepsilon_1)(E - \varepsilon_2) + \gamma_1^2 (E - \varepsilon_2)^2 + \gamma_2^2 (E - \varepsilon_1)^2 \right]^{-1}, \quad \text{respectively.} \quad (9.10)$$

In order to quantify the model of the TAMR, the peaks of the d_{z^2} and d_{zx} states at +0.19 eV in the Co atom, Fig. 9.10 (c), are revisited. Their broadening ($\gamma_1 = 0.05$ eV, $\gamma_2 = 0.11$ eV) as well as their energy difference ($\varepsilon_1 - \varepsilon_2 = -0.03$ eV) are chosen accordingly. The mixing t of two minority spin states (\downarrow) with d_{z^2} and d_{zx} symmetry is given by the matrix element

$$|\langle \downarrow, d_{zx} | \mathcal{H}_{SOC} | d_{z^2}, \downarrow \rangle| = \frac{1}{2} \sqrt{3} \sin \theta \sin \phi, \quad (9.11)$$

where $\mathcal{H}_{SOC} = \xi \mathbf{L} \cdot \mathbf{S}$ is the Hamilton operator of SOC (cf. Eq. (6.7) with the SOC constant ξ , angular momentum \mathbf{L} and spin \mathbf{S} [99]). It vanishes for a magnetization out-of-plane ($\phi = 90^\circ$ and $\theta = 0^\circ$) and becomes maximal for an in-plane magnetization ($\phi = 90^\circ$ and $\theta = 90^\circ$). As mentioned in chapter 6 the strength of SOC,

ξ , is on the order of about 50 meV for 3d-transition metals [99]. Thus, the mixing parameter t is chosen as 0 meV for the \perp magnetization direction and 40 meV for the \parallel magnetization direction. Fig. 9.12 (a) displays the result of the model derived above. The LDOS of the d_{z^2} and the d_{zx} states are enhanced for the \perp magnetization and, furthermore, exhibit a small energy shift in the position of the peak with respect to the LDOS of the in-plane magnetization. This is in agreement with the results of the DFT calculations in Fig. 9.10 (c). The model TAMR in Fig. 9.12 is obtained by taking only the d_{z^2} states into account. The resulting shape is similar to the one of a single d_{z^2} peak as indicated by an arrow in Fig. 9.10 (b). It shows a sign reversal at lower and higher energies. With values up to 20% the model TAMR is in good agreement with the TAMR of the Co d_{z^2} states (22%) obtained in the electronic structure calculations. However, the TAMR values of the vacuum LDOS are smaller due to the neglect of the s - and p states within the model.

Conclusions

In this section, the TAMR of a single Co atom adsorbed on a double layer of Fe on the W(110) has been investigated. With values ranging between -19% to $+9\%$ the TAMR based on first-principles calculations compares reasonable with the experimental values ranging from -12% to $+5\%$. The origin of the TAMR has been ascribed to the mixing of 3d states with different orbital character in the Co atom. The main contribution to the vacuum LDOS originates from the d_{z^2} states of the minority spin channel in the Co atom that mix with d resonances and thus lead to a magnetization-direction dependence of the LDOS in the vacuum. The features of the TAMR were captured in a model of two interacting atomic states.

9.3 Non-magnetic Single Iridium Adatom on the Double Layer Fe on W(110)

So far, the focus has been on single magnetic atoms adsorbed on a magnetic thin film such as the Co atom in the section before. Indeed, such an atom exhibits a large magnetic moment of up to $1.8 \mu_B$, but the SOC effect is weak in elements of the 3d series. A way to increase the TAMR effect is to choose a heavier element from the 5d series instead of a 3d metal to be adsorbed on the Fe film. Spin-polarization due to the magnetic thin film allows the formation of a sufficiently large magnetic moment in the 5d adatom. In the following, it is demonstrated by the example of an Ir adatom how this strategy heads to a giant TAMR effect on the order of up to 60 %.

Computational Details

The *ab initio* calculations have been performed using a symmetric slab consisting of five layers of W with two layers of Fe on each side while employing the experimental lattice constant of W, $a = 3.165 \text{ \AA}$. The Ir atom is centered within a $c(4 \times 4)$ unit cell on both sides of the slab (cf. inset in Fig. 9.13 (a)). Structural relaxations have been carried out via force minimization for the Ir adatoms and the Fe atoms of the film within the GGA [33]. The equilibrium interlayer distance between the Ir atom and the next-nearest Fe atom is reduced by 28%, i.e., 1.61 \AA , compared to the W bulk. The analysis of the electronic structure has been carried out within the LDA [122] if not stated otherwise. The SOC effect has been included by applying a second variational approach [105] using 12 \mathbf{k}_{\parallel} -points in the irreducible wedge of the two-dimensional Brillouin zone. A plane-wave cutoff of $k_{max} = 3.9 \text{ a.u.}^{-1}$ has been used. The LDOS in the muffin-tin as well as in the vacuum has been computed using 280 \mathbf{k}_{\parallel} -points in the entire Brillouin zone.

9.3.1 Spin-Polarization of the Ir Adatom on the Double Layer Fe on W(110)

As mentioned above, the hybridization between the Fe atoms of the double-layer film and the Ir adatom lead to a spin-polarization of the latter. This is observed by comparing the spin-resolved local densities of states in the MT spheres of the adjacent Fe atoms, Fig. 9.13 (a), to that of the Ir atom in Fig. 9.13 (b). Several peaks located at $E_F - 3.6 \text{ eV}$ and $E_F - 0.75 \text{ eV}$ in the majority channel (green) as well as $E_F + 1.5 \text{ eV}$ in the minority channel (red) occur in both the Fe atoms and the Ir atom and hint at hybridized states. Recalling the LDOS calculated in the Fe film in section 9.1.1 (cf. Fig. 9.4 (a)) shows that the exchange splitting of the spin channels changes slightly if an Ir atom is deposited onto the film. The resulting magnetic moment of the Fe atom 4 in the inset of Fig. 9.13 (a) amounts to $+2.72 \mu_B$ in the GGA [33] and $+2.62 \mu_B$ within the LDA [122], i.e., it is reduced with respect to the Fe moment of $2.9 \mu_B$ in the surface layer of the double-layer film. However, the LDOS of the Ir atoms exhibits likewise an exchange splitting as observed in Fig. 9.13 (b), which leads to magnetic moments of $+0.87 \mu_B$ within the GGA and $+0.77 \mu_B$ within the LDA. Evidently, for both exchange-correlation potentials the Ir atom is significantly spin-polarized. Furthermore, it follows from Fig. 9.13 (b) that the minority spin states dominate at lower energies while close to the Fermi level states of the majority spin govern the LDOS. This tendency is further illustrated by calculating the spin-polarization in the Ir adatom according to

$$P_{Ir} = \frac{(\text{LDOS}_{\uparrow} - \text{LDOS}_{\downarrow})}{(\text{LDOS}_{\uparrow} + \text{LDOS}_{\downarrow})} . \quad (9.12)$$

Fig. 9.13 (b) represents the resulting curve. It exhibits several sign reversals for the spin-polarization in the Ir atom. In the energy range of $E_F - 1 \text{ eV}$ and $E_F + 1 \text{ eV}$

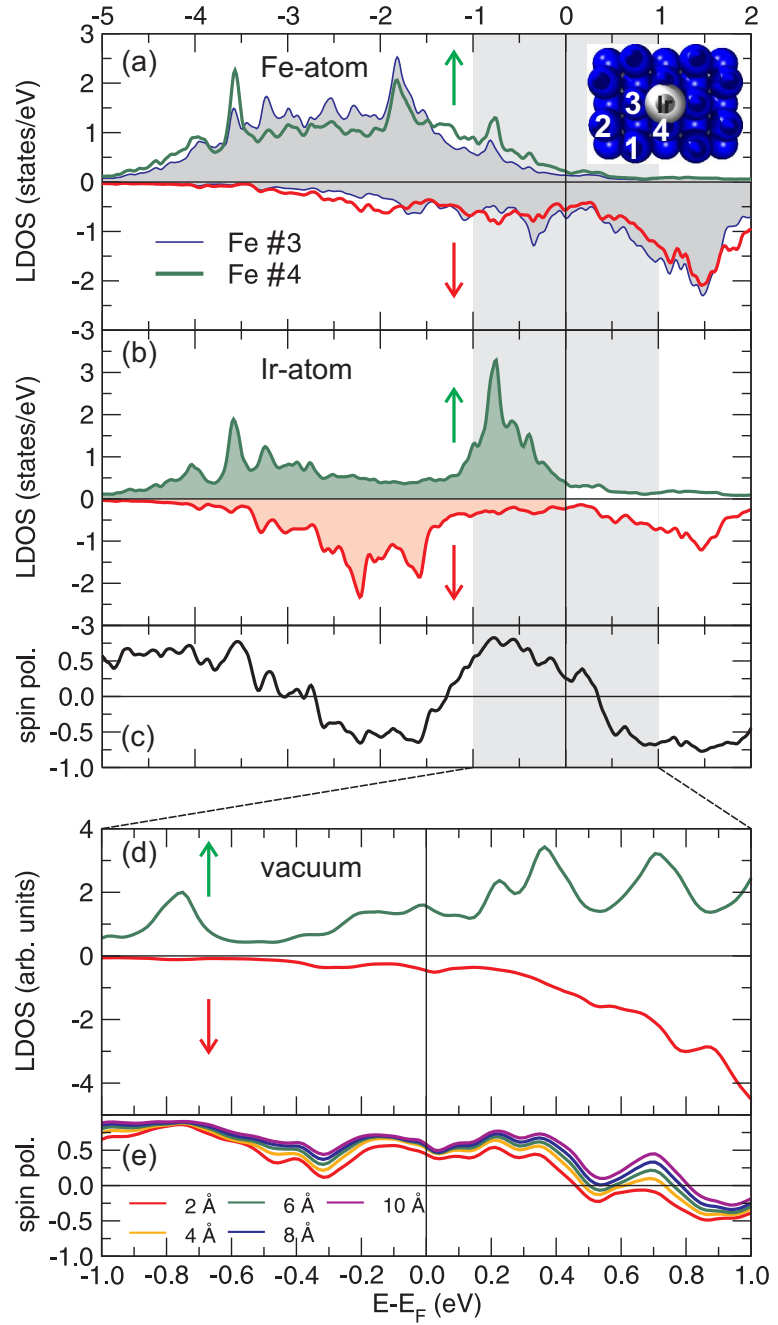


Figure 9.13: (a) LDOS in the MT spheres of the neighboring Fe atoms 3 and 4 (see inset) in the majority and minority spin channel. (b) Spin-dependent LDOS calculated in the MT sphere of the Ir atom. (c) Spin-polarization of the LDOS in (b) according to Eq. (9.3.1). (d) LDOS in the vacuum calculated at 6 Å above the Ir atom. Green and red lines correspond to the majority (\uparrow) and minority (\downarrow) spin channels. (e) Spin-polarization of the vacuum LDOS calculated in a range of 2 Å (red line) to 10 Å (violet line) above the Ir atom according to Eq. (9.3.1).

it is maximum at $E_F - 0.77$ eV and a value of $P_{Ir} = 0.82$. The sign of the spin-polarization changes at $E_F + 0.35$ eV leading to a minimum value of $P_{Ir} = -0.69$ at $E_F + 0.85$ eV. At 6 Å above the Ir adatom a similar behavior is observed. The vacuum LDOS presented in Fig. 9.13 (d) reveals a dominance of majority spin states for energies up to $E_F + 0.54$ eV. For higher energies the LDOS in the minority channel increases. This is also visible in the spin-polarization in the vacuum, which

has been evaluated in Fig. 9.13 (e) for distances ranging from 2 Å to 10 Å above the Ir adatom. For the major part of the energy range it shows positive values of about $P_{Ir,vac} = 0.5$ with maximum values of up to 0.9 nearly independent of the distance. Nevertheless, the transition from positive spin-polarization values to negative ones depends clearly on the distance. In the case of small distances such as 4 Å the spin-polarization changes its sign first at 0.49 eV above the Fermi level, becomes positive again at $E_F + 0.61$ eV and reverses finally at $E_F + 0.73$ eV. For larger distances of 10 Å, on the other hand, the transition from positive to negative values is observed at $E_F + 0.81$ eV without an additional sign reversal at lower energies. However, magnetic single-atom junctions consisting of Co or Cr atoms on double-layer Fe islands on the W(110) surface exhibit asymmetries in the conductance of up to +0.28 and -0.24, respectively [154]. Considering the maximum asymmetry of 0.9 observed above the Ir atom, which is about three times larger as that of the Co and Cr adatoms the application of 5d elements in single atom contacts can be an alternative route towards large spin-valve effects.

9.3.2 The TAMR Effect of the Ir Adatom on the Double Layer Fe on W(110)

However, the Ir adatom does not only exhibit a significant spin-polarization but exhibits also a giant anisotropy of its LDOS, which will result in a huge TAMR effect. Figure 9.14 (a) shows the spin-averaged local densities of states evaluated in the vacuum for three different magnetization directions of the Ir atom. In this case the spin-quantization axes in the calculations have been chosen not only along the [001] direction (LDOS_{cycl}) and the normal to the film plane (LDOS_⊥), but also along the other in-plane direction, i.e., $[1\bar{1}0]$ direction (LDOS_{hel}). Here, the change from an out-of-plane to an in-plane magnetization via the [001] direction corresponds to a cycloidal rotating domain wall, i.e., a Néel wall. The rotation via the other in-plane direction, i.e., the $[1\bar{1}0]$ direction, on the other hand, describes a helical rotating domain wall also known as Bloch wall. As stated in section 9.1 the double-layer Fe film exhibits a Néel wall inducing a preferable rotation of the magnetization from perpendicular to the [001] direction in the Ir atom. Here, the other type of domain wall will be considered in order to illustrate how the TAMR will depend on the type of the wall.

In contrast to the vacuum densities of states of the Co adatom (cf. 9.8 (b)) the three curves in Fig. 9.14 (a) present large differences throughout the energy range of $E_F - 1$ eV to $E_F + 1$ eV. Three peaks may be distinguished at the energies of -0.63 eV (1), +0.4 eV (2) and +0.76 eV (3). While the peaks labeled 2 and 3 occur in the LDOS of all magnetization directions, peak 1 appears solely in the vacuum for a spin-quantization axis along the perpendicular and $[1\bar{1}0]$ in-plane direction, i.e., helical magnetized Ir atom. Because of the absence of peak 1 in the LDOS for the cycloidal domain wall, the corresponding TAMR_{cycl} exhibits values between -51% and +69% as displayed in Fig. 9.14 (b). On the other hand, the TAMR for the

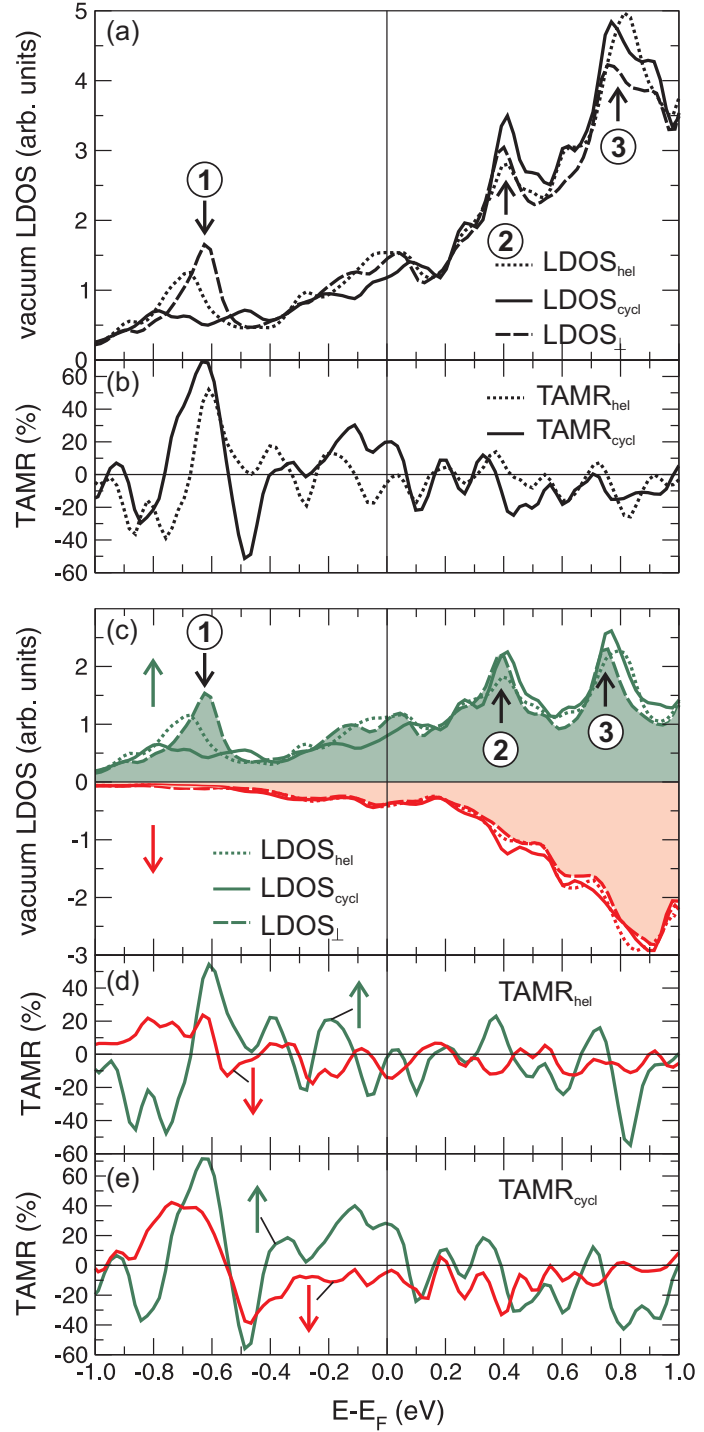


Figure 9.14: (a) Spin-averaged LDOS in the vacuum at 6 Å above the Ir for different magnetization directions, i.e., either normal to the surface (dashed line), $LDOS_{\perp}$, or parallel to the film plane aligned to the $[1\bar{1}0]$ (dotted line), $LDOS_{hel}$, and the $[001]$ direction (solid line), $LDOS_{cycl}$, respectively. (b) TAMR effect calculated for the vacuum densities of states in (a) according to Eq. (9.1). The TAMR of a helical rotating spin structure, i.e., from out-of-plane to in-plane along $[1\bar{1}0]$ is represented by a dotted line, $TAMR_{hel}$, while that of a cycloidal rotating domain wall, i.e., from out-of-plane to in-plane along $[001]$ is indicated by a solid line, $TAMR_{cycl}$. (c) Spin-dependent vacuum LDOS for three different magnetizations of the Ir adatom. (d)-(e) TAMR of the curves presented in (c) for the majority (green) and minority spin channel (red).

helical domain wall reveals only slightly smaller values between -39% and $+52\%$ due to a shift towards lower energies in the position of peak 1 in $LDOS_{hel}$. As observed in the double-layer Fe film (Fig. 9.4 (c)) and the Co adatom (figures 9.8 (c) and 9.10

(b)) the TAMR curves maintain their oscillatory behavior as a function of energy in Fig. 9.14 (b). For instance, in the vicinity of the Fermi energy $\text{TAMR}_{\text{cycl}}$ shows considerable positive values of up to +30% and drops down to -22% at $E_F + 0.1$ eV. Also at the positions of peak 2 and 3 the TAMR curves descend to values of about -25%. However, the most prominent TAMR values are related to changes in the vacuum densities of states at peak 1.

A closer look at the vacuum density of states plotted in terms of the majority and minority spin for the three different magnetizations directions as in Fig. 9.14 (c) shows that peak 1 stems mainly from states of the majority spin states. As stated above, the contribution of the minority states to the vacuum LDOS increases for energies above the Fermi level. This is further observed in the spin analysis of the TAMR in figures 9.14 (d) and 9.14 (e), where the TAMR curves of the majority spin present a similar shape compared to that of the spin-averaged ones in Fig. 9.14 for energies smaller than E_F . Thus, it can be safely concluded that the TAMR effect at peak 1 originates from states of majority spin.

In order to understand the changes in the electronic structure that give rise to the huge TAMR effect, the orbital decomposition of the LDOS in the Ir atom is analyzed. In Fig. 9.15 the case of a helical rotating domain wall is examined, i.e., for a magnetization direction perpendicular to the surface and parallel to the $[1\bar{1}0]$ direction. While both local densities of states in Fig. 9.15 (a) exhibit peak 1 it is smaller in size and slightly shifted towards lower energies in LDOS_{hel} in comparison to LDOS_{\perp} . This results in a huge oscillation between $E_F - 1$ eV and $E_F - 0.5$ eV in TAMR_{hel} , Fig. 9.15 (b). Although the d_{zx} and the d_{z^2} orbitals in Fig. 9.15 (c) and (d), respectively, show a distinct feature for both magnetization directions at the position of peak 1 the SOC matrix elements $|\langle \uparrow, d_{zx} | \mathcal{H}_{\text{SOC}} | d_{z^2}, \uparrow \rangle| = \frac{1}{2}\sqrt{3} \sin \theta \sin \phi$ [99] that describe their mixing vanish for both, the in-plane ($\theta = 90^\circ$, $\phi = 0^\circ$) and out-of-plane direction ($\theta = 0^\circ$, $\phi = 0^\circ$). In the case of a hybridization between d_{z^2} states and those of d_{yz} symmetry the matrix elements take the form $|\langle \uparrow, d_{yz} | \mathcal{H}_{\text{SOC}} | d_{z^2}, \uparrow \rangle| = \frac{1}{2}\sqrt{3} \sin \theta \cos \phi$ [99]. They only vanish for the out-of-plane magnetization direction and become maximal for the in-plane magnetized Ir adatom and thus lead to the huge TAMR effect between $E_F - 1$ eV and $E_F - 0.5$ eV.

Figure 9.16 (a) shows the vacuum density of states for the cycloidal rotating domain wall, i.e., an Ir atom with magnetization perpendicular to the surface and parallel to $[001]$ in-plane direction. As mentioned before, peak 1 is absent in the LDOS above the in-plane magnetized Ir atom in the cycloidal domain wall. This leads to a huge single peak in the $\text{TAMR}_{\text{cycl}}$ at $E_F - 0.63$ eV, Fig. 9.16(b), with changes of sign at both higher and lower energies. It is likewise due to the mixing of d_{z^2} and d_{zx} states that occur as single peaks in the LDOS of the perpendicular magnetized atom and as double peaks if the Ir atom is adsorbed on the Néel wall (cf. Fig 9.16 (c) and (d)).

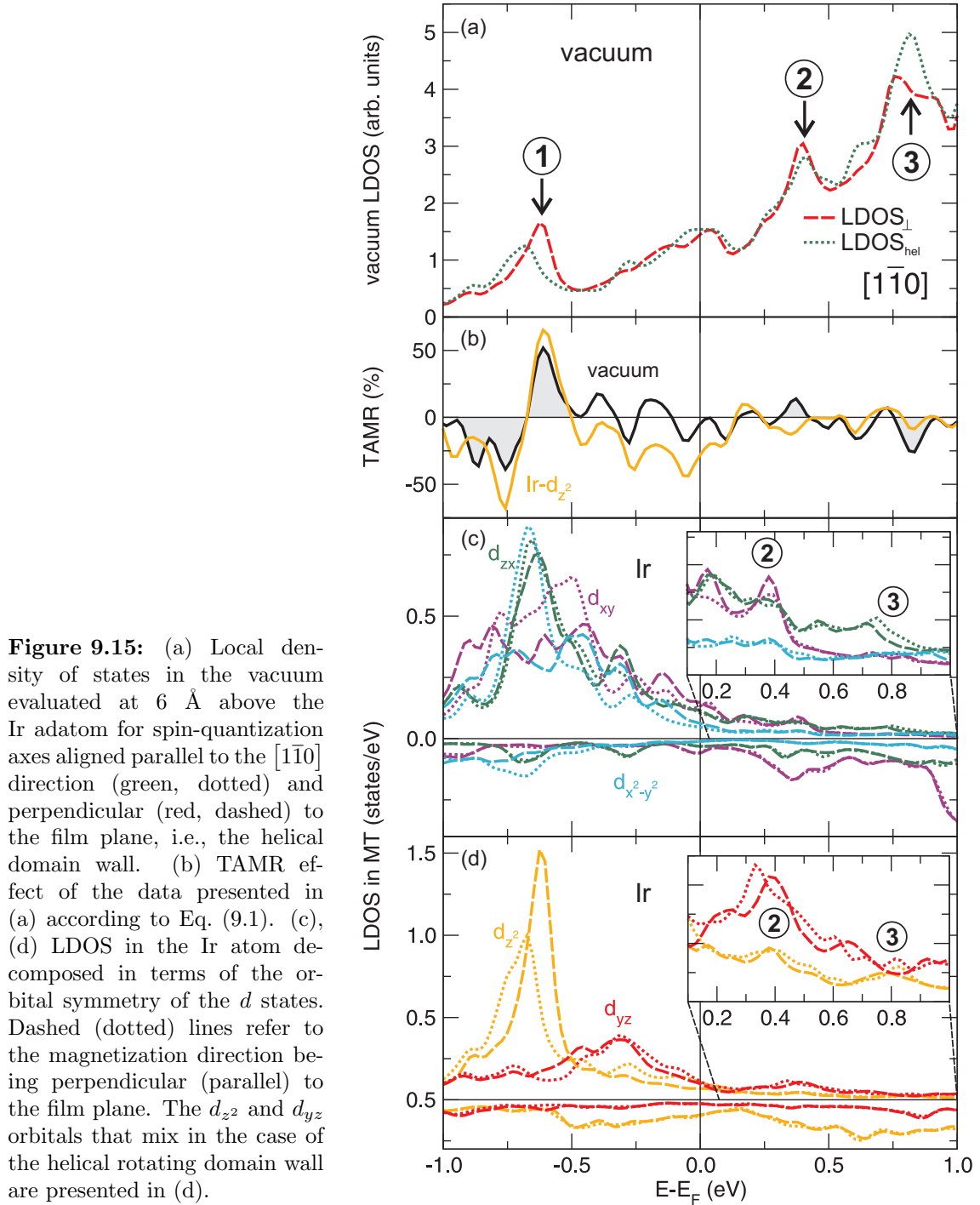


Figure 9.15: (a) Local density of states in the vacuum evaluated at 6 Å above the Ir adatom for spin-quantization axes aligned parallel to the $[1\bar{1}0]$ direction (green, dotted) and perpendicular (red, dashed) to the film plane, i.e., the helical domain wall. (b) TAMR effect of the data presented in (a) according to Eq. (9.1). (c), (d) LDOS in the Ir atom decomposed in terms of the orbital symmetry of the d states. Dashed (dotted) lines refer to the magnetization direction being perpendicular (parallel) to the film plane. The d_{z^2} and d_{yz} orbitals that mix in the case of the helical rotating domain wall are presented in (d).

The different behavior of the TAMR for an Ir atom adsorbed on a helical and a cycloidal rotating domain wall, respectively, can be explained on the basis of the simple model introduced in section 9.2.2. For the helical rotation of the magnetization

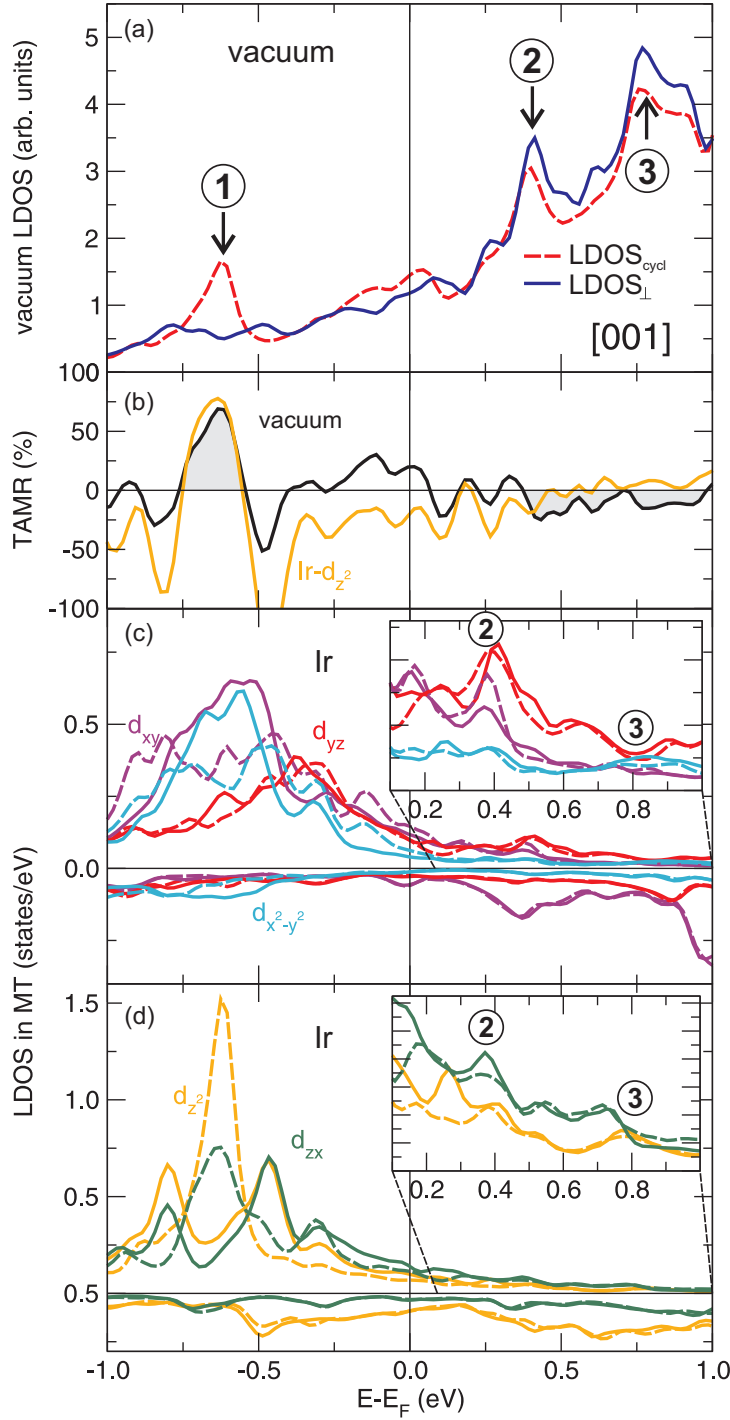
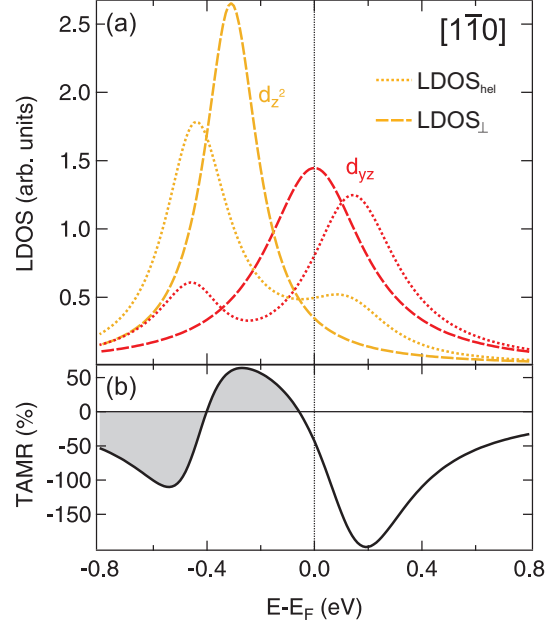


Figure 9.16: (a) Local density of states in the vacuum evaluated at 6 Å above the Ir adatom for spin-quantization axes aligned parallel to the film plane along the [001] direction (blue, solid) and perpendicular to the film plane (red, dashed), i.e., the cycloidal domain wall. (b) TAMR effect of the data presented in (a) according to Eq. (9.1). (c), (d) LDOS in the Ir atom decomposed by the orbital symmetry of the d states. Dashed (solid) lines refer to the magnetization direction being perpendicular (parallel) to the film plane. The d_{z^2} and d_{zx} orbitals that mix in the case of the cycloidal rotating domain wall are presented in (d).

direction this is done by considering the broadening of the d_{yz} peak at $E_F - 0.31$ eV ($\gamma_2 = 0.22$ eV) as well as that of the d_{z^2} states at $E_F - 0.63$ eV ($\gamma_1 = 0.12$ eV) in Fig. 9.15 (c) and (d), respectively. One needs to recall the matrix element of the

Figure 9.17: (a) LDOS obtained for the simple model of two atomic surface states that exhibit different orbital symmetry, d_{z^2} (yellow) and d_{yz} (red), and couple via SOC as introduced in section 9.2.2. The dashed (dotted) line corresponds to the magnetization perpendicular (parallel along $[\bar{1}\bar{1}0]$) to the film plane, i.e., helical rotating domain wall. (b) Anisotropy of the LDOS (TAMR_{hel}) calculated according to Eq. (9.1) for the d_{z^2} state in (a).



mixing d_{yz} and d_{z^2} states [99]:

$$|\langle \uparrow, d_{yz} | \mathcal{H}_{SOC} | d_{z^2}, \uparrow \rangle| = \frac{1}{2} \sqrt{3} \sin \theta \cos \phi. \quad (9.13)$$

and remember that it vanishes for the perpendicular magnetization ($\theta = 0^\circ, \phi = 0^\circ$) and becomes maximal for the magnetization aligned to the $[\bar{1}\bar{1}0]$ direction ($\theta = 90^\circ, \phi = 0^\circ$). Considering a significantly larger SOC in the Ir adatom compared to that of the Co adatom ($t = 40$ meV) $t = 0$ and $t = 250$ meV are used for the magnetization direction perpendicular and parallel to the surface, respectively. The resulting model is illustrated in Fig. 9.17 (a). Since their energy difference is relatively large with about $\varepsilon_1 - \varepsilon_2 = 0.31$ eV the overlap between the d_{yz} and d_{z^2} peaks is small leading to only a minor interaction between those states. This agrees well with the LDOS obtained from the DFT calculations as presented in Fig. 9.15 (d). Also the shift in the position of the peaks for the model LDOS_{hel} compares well with the *ab initio* results. It is due to the large SOC constant of $t = 250$ meV. Moreover, changing the magnetization from out-of-plane to in-plane results in a reduction of the height of the peaks, which is likewise observed in the DFT results. By evaluating the TAMR_{hel} from the model d_{z^2} states via Eq. (9.1) yields a curve similar in shape to the TAMR_{hel} observed in Fig. 9.15 (b). Starting from smaller energies it presents negative values for a range of several hundreds of meV and shows a sign reversal at the intersection of LDOS_∥ and LDOS_⊥. Furthermore, it compares well with the TAMR_{hel} computed from only the d_{z^2} states and presented as a yellow line in Fig. 9.15 (b).

In the case of the cycloidal rotating domain wall the peak of the d_{z^2} states at

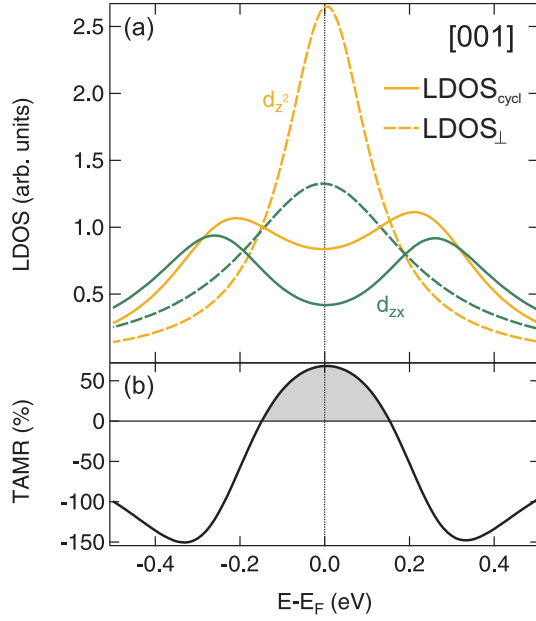


Figure 9.18: (a) LDOS obtained for the simple model of two atomic surface states that exhibit different orbital symmetry, d_{z^2} (yellow) and d_{zx} (green), and couple via SOC as introduced in section 9.2.2. The dashed (solid) line corresponds to the magnetization perpendicular (parallel along [001]) to the film plane, i.e., cycloidal rotating domain wall. (b) Anisotropy of the LDOS (TAMR_{cycl}) calculated according to Eq. (9.1) for the d_{z^2} state in (a).

$E_F - 0.63$ eV ($\gamma_1 = 0.12$ eV) as well as that of the d_{zx} states at $E_F - 0.64$ eV ($\gamma_2 = 0.24$ eV) have been taken into account for the simple model. Their matrix element has been introduced as

$$|\langle \uparrow, d_{zx} | \mathcal{H}_{SOC} | d_{z^2}, \uparrow \rangle| = \frac{1}{2} \sqrt{3} \sin \theta \sin \phi \quad (9.14)$$

and as it has been stated in section 9.2.2 it vanishes for the perpendicular magnetization ($\theta = 0^\circ, \phi = 0^\circ$) and is maximal for the magnetization aligned to [001], i.e., $\theta = 90^\circ$ and $\phi = 90^\circ$. Thus, the SOC strengths that have been used for the helical rotating domain wall, $t = 0$ and $t = 250$ meV, are employed for the magnetization direction perpendicular and parallel to the surface, respectively. In Fig. 9.18 (a) the resulting peaks are illustrated. Due to their small energy difference of $\varepsilon_1 - \varepsilon_2 = 0.01$ eV they overlap over a large energy range and thus the interaction between them is increased compared to that of the helical rotating domain wall. Thus, the rotation of the magnetization from out-of-plane to in-plane results in a reduction - or better - a splitting of the peaks, which is also observed in the LDOS shown in Fig. 9.18 (d). Therefore, the curves of the d_{z^2} and the d_{zx} states exhibit a double peak structure including a minimum at the position of peak 1 if the magnetization coincides with the [001]. By considering only the d_{z^2} states of the model (cf. Fig. 9.18 (a)) the TAMR_{cycl} has been calculated according to Eq. (9.1). It is presented in Fig. 9.18 (b) and resembles the large TAMR_{cycl} effect of the *ab initio* results as shown in Fig. 9.16 (b). It exhibits a strong peak with sign reversals at high and low energies. Furthermore, the model TAMR_{cycl} agrees well with the TAMR_{cycl} obtained from first-principles if the latter is restricted to the d_{z^2} states.

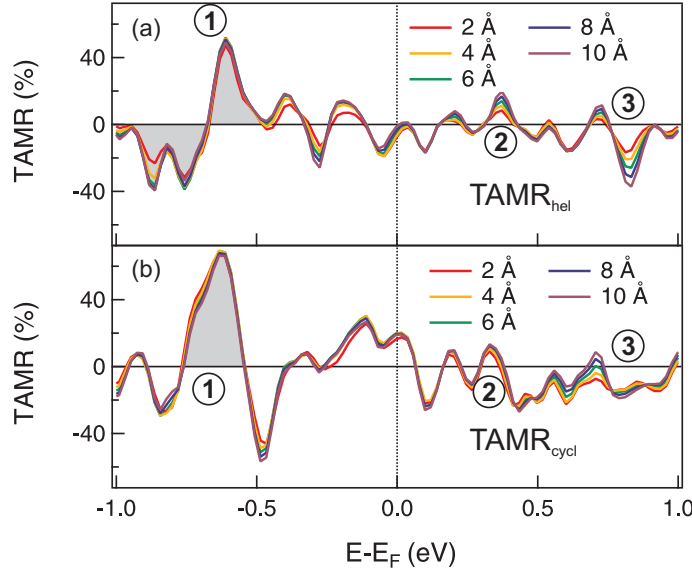


Figure 9.19: Distance dependence of the TAMR effect of (a) $LDOS_{hel}$ and (b) $LDOS_{cycl}$ with respect to $LDOS_{\perp}$. The distance ranges from 2 Å (red) to 10 Å (violet) above the Ir atom.

Apparently, the splitting of the peaks in the vacuum LDOS of the Ir atom on the double-layer Fe film on the W(110) depends on the in-plane magnetization direction of the adatom and thus on the magnetization direction of the Fe film. Because the magnetization in this system has been chosen to model the Bloch and the Néel wall, respectively, the adsorption of a nonmagnetic atom on domains and the domain walls can be used to distinguish between the two types. Since the identification of the in-plane magnetization and the distinction between a helical or cycloidal rotating domain wall is complicated and needs, for instance, the application of a three-dimensional magnetic field in a spin-polarized STM measurement [128] the presented results can be used as an alternative method in order to determine the type of a domain wall in spin-polarized STM measurements.

In the case of an Ir adatom on Fe/W(110) the distance dependence of the TAMR is subject to its size as can be extracted from Fig. 9.19 (a) and (b). At the position of the strongest effect the variation of the distance barely causes the TAMR to change. Only for energies above the Fermi level at the positions of peak 2 and 3 the anisotropy of the vacuum densities changes considerably with respect to the distance. For $TAMR_{cycl}$ even a sign reversal occurs at 0.71 eV above E_F . However, the TAMR of the Ir adatom is qualitatively nearly independent to variations of the height.

Finally, the TAMR can be investigated concerning its spatial distribution as presented in Fig. 9.20. Here, the cross-sectional plots bisect the film along the $[1\bar{1}0]$ direction within an energy range of 30 meV at the position of peak 1. In both cases,

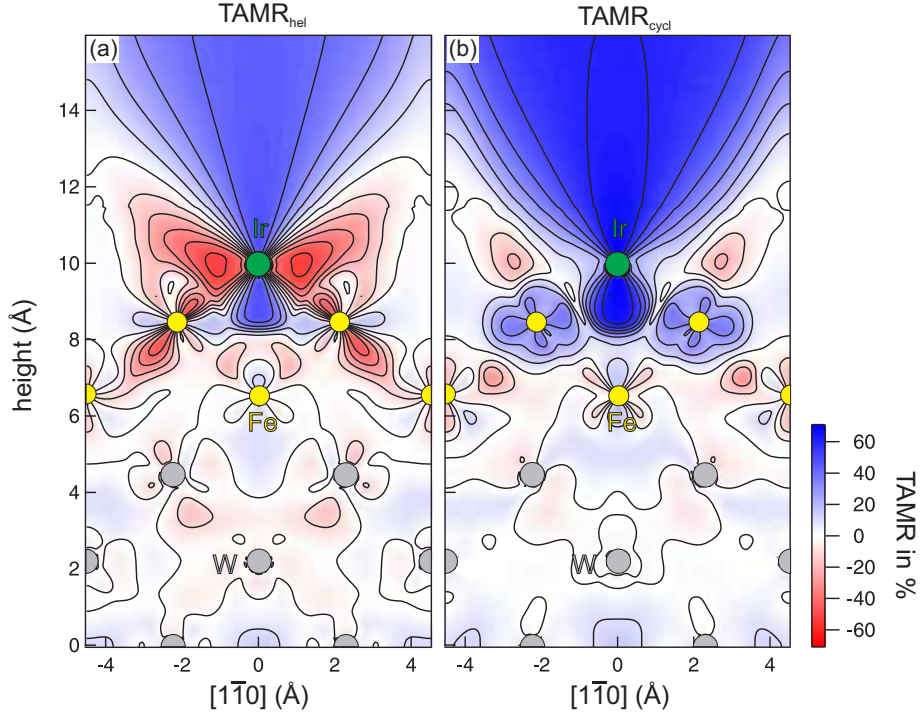


Figure 9.20: Spatial distribution of the TAMR illustrated as cross sections along the $[1\bar{1}0]$ crossing the center of the Ir atom. The Ir, Fe and W atoms are indicated as colored circles. The TAMR has been yielded from LDOS_{hel} in (a) as well as $\text{LDOS}_{\text{cycl}}$ in (b) with respect to LDOS_{hel} within the energy interval between $E_F - 0.67$ eV and $E_F - 0.54$ eV.

TAMR_{hel} and $\text{TAMR}_{\text{cycl}}$, the cross sections reveal large TAMR values in the area of the Ir adatom and slightly smaller values at the Fe atoms of the topmost layer. While the illustration of $\text{TAMR}_{\text{cycl}}$ in Fig. 9.20 (b) shows almost exclusively positive values, TAMR_{hel} in Fig. 9.20 (a) displays small areas parallel to the film plane with large negative values in the vicinity of the Ir atom. In both plots the hybridization with the Fe atoms of the topmost layer becomes clear and a huge conical shaped area can be observed above the Ir atom. It is due to the dominance of d_{z^2} orbitals at the Ir adatom and stretches far into the vacuum. It demonstrates that the TAMR mainly stems from states of d_{z^2} character that lead to the large values of +69% and +52% for TAMR_{hel} and $\text{TAMR}_{\text{cycl}}$, respectively.

Influence of the Exchange-Correlation Potential

The choice of the exchange-correlation potential can have an effect on the calculated electronic properties since it only approximates the exact self-energy [156, 157]. For instance, due to the choice of the exchange-correlation potential the position of the peaks in densities of states can shift. For that reason, the TAMR in a single Ir atom adsorbed on the Fe double layer is investigated in Fig. 9.21 concerning the influence

of the exchange-correlation potential.

In figures 9.21 (a) and (b) the vacuum densities of states are compared for the three different magnetization directions obtained within the LDA and the GGA, respectively. At first glance there have only been small changes at peak 3. While its appearance has been slightly altered its position has barely changed. The change of the exchange-correlation potential has evidently a minor influence onto peak 3, which is mainly of d_{z^2} and d_{yz} or d_{zx} symmetry. Peak 2 on the contrary underwent a large change and is reduced within the GGA. Furthermore, it has shifted towards smaller energies for LDOS_\perp , while in LDOS_{hel} and $\text{LDOS}_{\text{cycl}}$ its position changed about 100 meV towards higher energies.

Also within the GGA peak 1 provides the strongest TAMR effect with values

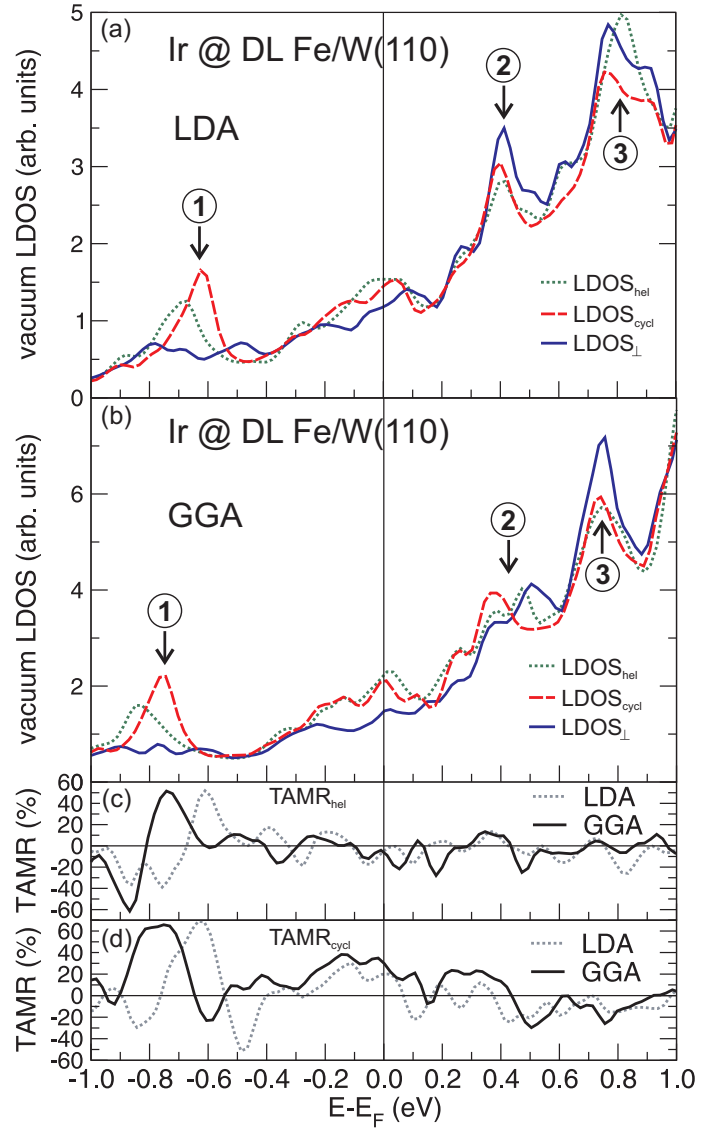


Figure 9.21: The vacuum LDOS calculated within (a) the LDA and (b) the GGA at 6 Å above the Ir adatom on the double layer Fe on W(110) for the magnetization direction along $[1\bar{1}0]$ (green dotted), $[001]$ (blue solid) and perpendicular to the film (red dashed). (c)-(d) The TAMR effect of the Ir atom calculated within the LDA (gray dotted) and the GGA (black solid) of (c) LDOS_{hel} and LDOS_\perp and (d) $\text{LDOS}_{\text{cycl}}$ and LDOS_\perp .

ranging from -61% to $+52\%$ and -23% to $+66\%$ for TAMR_{hel} and $\text{TAMR}_{\text{cycl}}$, respectively. It is basically of d_{z^2} and d_{zx} or d_{yz} symmetry, i.e., the charge density stretches perpendicular to the surface and far into the vacuum. Nevertheless, it shifts by about 120 meV towards lower energies. As Fig. 9.20 demonstrates, the strong TAMR effect emerges from the hybridization of the Ir atom and the topmost layer of the Fe film. Therefore, the shift of peak 1 is due to a reduction of the magnetic moments of the next-nearest neighboring Fe atoms from $2.73 \mu_B$ to $2.62 \mu_B$ upon changing from the GGA to the LDA.

The TAMR of the curves presented in Fig. 9.21 (a) and (b) is given in Fig. 9.21 (c) and (d). Due to its nature as a result of the SOC effect it has been expected that the TAMR experiences at least some smaller changes. However, in the case of the Ir atom the TAMR effect is qualitatively independent of the exchange-correlation potential and so are all conclusions drawn in the previous sections.

Conclusions

In this section the TAMR was discussed for a nonmagnetic single atom from the $5d$ series. An Ir atom resembles the Co atom chemically, but exhibits a stronger SOC at the same time. Due to hybridization with the atoms of the topmost Fe layer a magnetic moment of $+0.77 \mu_B$ has been induced in the Ir atom leading to a spin-polarization of up to 0.9. This is about three times larger as the values of up to 0.28 observed in Co adatoms on Fe double-layer island on W(110) [154]. The huge spin-polarization and the strong SOC lead to a TAMR effect that has been amplified by factors of three to four. It gives huge values up to 69% compared to the TAMR of maximum 19% found in the single Co atom. The origin of the huge TAMR effect has been ascribed to the mixing of d_{z^2} states with those of d_{zx} symmetry and the large SOC constant ξ of Ir on the order of 250 meV. Finally, the influence of the exchange-correlation potential onto the TAMR effect has been analyzed.

In comparison to +19% observed in a single Co atom the TAMR effect in the Ir atom experiences an amplification of a factor of 2.7 and 3.6, respectively, due to the strong SOC effect.

9.4 Co Adatom on the Mn monolayer on W(110)

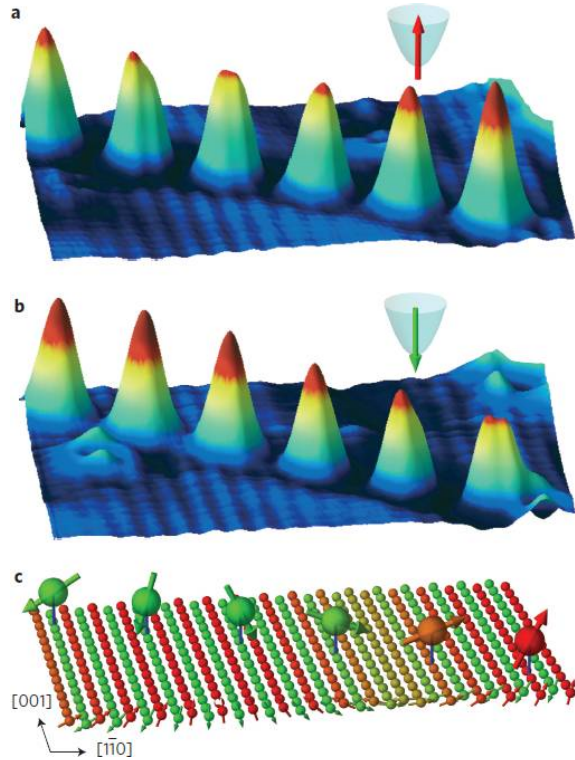


Figure 9.22: (a),(b) Perspective STM images (-10 mV, 2 nA) of a chain of Co atoms adsorbed on a monolayer of Mn on the W(110) surface obtained with an up and down magnetized tip. (c) Sketch of the scenario displayed in (a) and (b). This figure has been taken from reference [158].

So far atoms adsorbed on a nanoscale domain structure have been studied. In this section the well characterized Mn monolayer on the W(110) surface will act as a template for a single Co adatom. The characteristic of the Mn monolayer on W(110) is the spin-orbit driven spin-spiral ground state propagating along the $[1\bar{1}0]$ direction with an angle of about 174° between neighboring magnetic moments and thus resulting in an almost antiferromagnetic local order [9]. Recently, it was discovered that the single Co atom is coupled ferromagnetic to the underlying magnetic thin film via Heisenberg exchange allowing for the spin to be set to any direction that is accessible in the Mn spin-spiral state [158]. A chain of Co atoms has been formed in a STM experiment via atom manipulation along the atomic rows of the magnetic template. Thereby, it is possible to study their spin-polarized LDOS in the vacuum with up and down magnetized STM tips (cf. Fig. 9.22). In line profiles acquired along the $[1\bar{1}0]$ direction changes in height and shape have been observed depending on the angle θ between the tip magnetization direction and the magnetic moment of the respective Co atom. It was found that the height follows not only a cosine as expected from the TMR effect, i.e., the spin-polarized current, but in order to fit the experimental results, a higher order correction proportional to $\cos^2 \theta$ was needed. It has been speculated whether the $\cos^2 \theta$ contribution can be assigned to SOC, i.e., the TAMR. However, with a value of 36% extracted from the experiment the Co

adatom would present a considerable TAMR. Hence, the purpose of the following discussion is to shed light onto the occurrence of this effect in a single Co atom on the Mn monolayer on the W(110) surface.

Computational Details

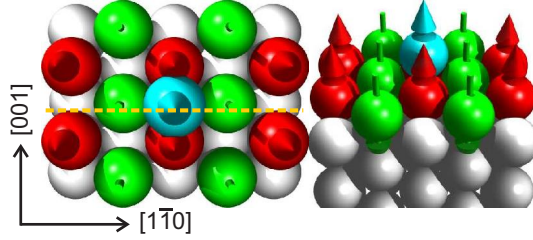


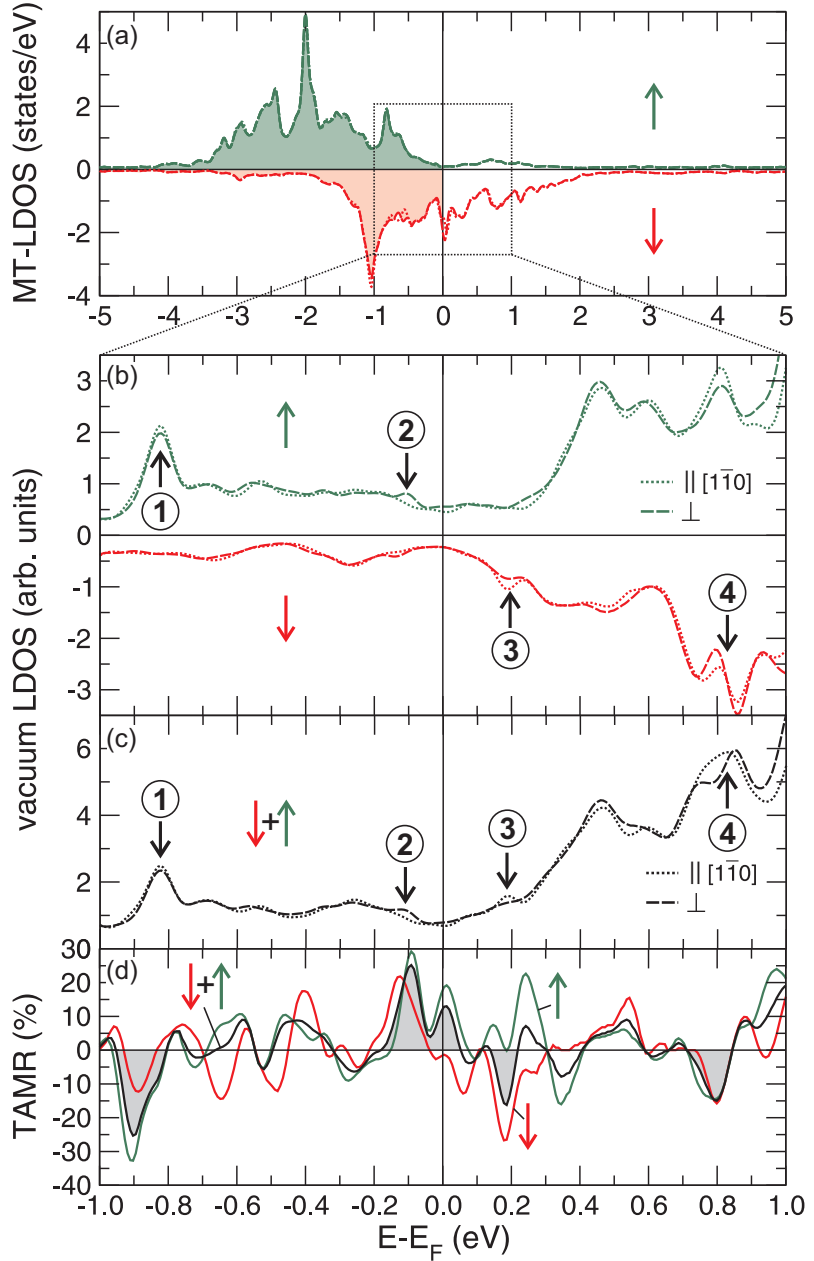
Figure 9.23: Top and perspective view of the employed unit cell. Grey spheres represent the W substrate atoms while the Mn atoms are depicted as red (green) spheres with arrows that are antiparallel (parallel) to the magnetic moment of the Co atom (turquoise).

FLAPW calculations have been carried out using the film setup including the relaxations given in reference [158], i.e., symmetric slab consisting of five layers of W with one layer of Mn on each side. In order to model the local antiferromagnetic order, the magnetic moments of the Mn atoms have been arranged in the checkerboard configuration using a $c(4 \times 4)$ unit cell, where the Co atom has been deposited in the hollow site at the center (cf. Fig. 9.23). The electronic structure has been studied within the GGA [33] as in reference [158] without SOC, so that a direct comparison is possible. The inclusion of the SOC effect happened by means of second variation [105] using 24 \mathbf{k}_{\parallel} -points in the irreducible wedge of the two-dimensional Brillouin zone and a plane-wave cutoff of $k_{max} = 3.9$ a. u.⁻¹. The LDOS (LDOS) was calculated using 468 \mathbf{k}_{\parallel} -points in the entire Brillouin zone.

9.4.1 Spin Analysis of the Co Adatom on the Single Layer Mn on W(110)

Figure 9.24 (a) displays the spin-resolved LDOS in the MT sphere of the Co atom that has been adsorbed on the monolayer film of Mn on the W(110) surface. The main part of the LDOS in the majority spin channel is located below the Fermi level and exhibits full occupation. The minority LDOS, on the other hand, is bisected by the Fermi energy, which implies that the minority spin channel is only partly filled. This exchange splitting results in a magnetic moment of $1.62 \mu_B$ of the Co atom. Around the Fermi level the LDOS at the Co atom seems to be dominated by the minority spin states. However, the vacuum LDOS in the minority spin channel is reduced with respect to that of the majority spin – a behavior, which has been likewise observed in the experimental and theoretical data of reference [158]. It has been explained based on the hybridized s , p_z and d_{z^2} states at the Fermi level, which

Figure 9.24: (a) LDOS calculated in the MT sphere of the Co atom for the majority (\uparrow , green lines) and minority (\downarrow , red lines) spin. The LDOS for an in-plane (out-of-plane) magnetization of the Co adatom and the Mn monolayer is denoted by a dotted (dashed) line. (b) LDOS evaluated within the vacuum at 6 Å above the Co atom adsorbed on an in-plane (out-of-plane) magnetized film. The majority (minority) channel is represented by green (red) lines. (c) Spin-averaged vacuum LDOS obtained by adding the LDOS of the majority and the minority spin in (b). (d) TAMR calculated for the curves in (b) and (c). While the TAMR of the majority and minority spin states is depicted as green and red line, the TAMR of the spin-averaged vacuum LDOS is illustrated as a black line. The shaded areas correspond to the features labeled in (b) and (c).



are maximum above the Co atom in the majority channel, while the minority channel comprises essentially d_{zx} states that exhibit a minimum above the Co atom [158]. Figure 9.24 (b) shows how the localization of the different states influences the LDOS in the vacuum. The pronounced peak exhibited by the minority spin states at the Co atom close to the Fermi level, Fig. 9.24 (a), is absent in the vacuum, Fig. 9.24 (b). In addition, the minority channel loses its predominance in the vacuum in the major part of the considered energy range due to the mechanism named above. In addition,

Fig. 9.24 (b) illustrates the differences that occur in vacuum densities calculated above Co atoms with different magnetization directions, i.e., aligned to the $[\bar{1}\bar{1}0]$ direction (LDOS_{\parallel}) and perpendicular to the surface (LDOS_{\perp}), respectively. Both types of curves show a similar profile, but at the same time reveal small deviations that also emerge in the spin-averaged density of states in the vacuum in Fig. 9.24 (c). The most distinct features are located at -0.82 eV, -0.11 eV, $+0.19$ eV and $+0.83$ eV and labeled 1 to 4. While feature 3 clearly stems from states of the minority spin features, 1, 2 and 4 are present in both spin channels (cf. Fig. 9.24 (b)). This is further observed in the TAMR depicted in Fig. 9.24 (d), where the anisotropy of the spin-averaged (black line) as well as the spin-resolved (minority (red) and majority spin (green)) densities of states in the vacuum are displayed. The anisotropy of the LDOS, i.e., the TAMR, has been calculated just as in Eq. (9.1) and exhibits values ranging from -25% to $+25\%$ (black line). Strong TAMR features related to peaks 1 to 4 in the vacuum LDOS are indicated by shaded areas. The features at peaks 1, 3 and 4 are caused by an enhanced LDOS of the in-plane magnetized film and result in negative values of the TAMR. Peak 2, on the other hand, evokes a maximum in the TAMR close to E_F due to a lower LDOS_{hel} with respect to LDOS_{\perp} . The spin analysis of the TAMR exhibits that the large effects close to peaks 1, 2 and 4 emerge likewise from states of the minority and majority channel while the TAMR close to peak 3 is mainly stemming from states in the minority channel as indicated in Fig. 9.24 (b).

9.4.2 The TAMR of the Co Adatom on the Single Layer Mn on W(110)

The evaluation of the spin contribution to the TAMR in Fig. 9.24 (d) revealed that at the energies of peak 1 and 2 it reaches values of -25% and $+25\%$, respectively. This is even larger than in the case of the single Co atom adsorbed on the Fe double-layer film with theoretical values of -19 to $+9\%$. Furthermore, it is in a reasonable agreement with the value of 36% obtained from the experimental results for STM measurements at low bias voltages of -10 mV [158]. The orbital decomposition of the LDOS in the Co atom in Fig. 9.25 (c) exhibits that the states of d_{z^2} character dominate the majority channel as it has been observed in [158]. For instance, at the position of peak 2 the LDOS in the vacuum in Fig. 9.25 (a) is low in the vicinity of E_F and displays a small peak that appears in LDOS_{\perp} but is absent in LDOS_{\parallel} . Having a closer look at the orbital character of the density of states at the Co atom at the energy of -0.09 eV reveals that the d_{yz} as well as the d_{z^2} states in the majority spin channel present likewise a small peak for the out-of-plane magnetized film, which does not exist for the in-plane magnetization direction. Furthermore, the minority states contribute to the TAMR at peak 2 by a spin-orbit induced mixing of the minority $d_{x^2-y^2}$ states with those of d_{yz} symmetry in the majority spin channel. While the TAMR at the peaks 1, 2 and 4 originates mainly from states of d_{z^2} character, it stems from the minority d_{yz} states at peak 3.

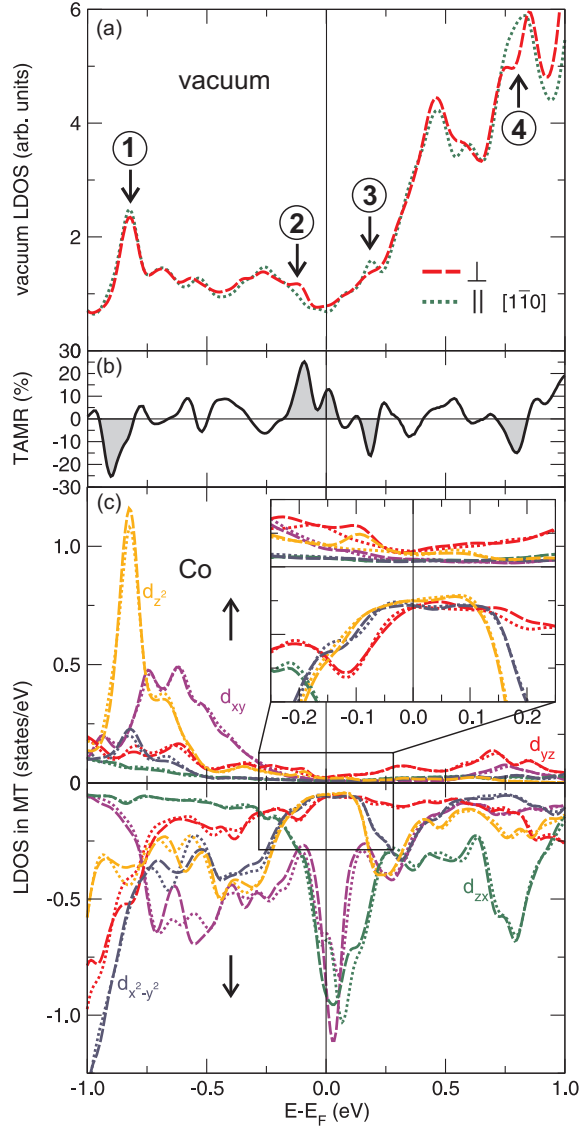


Figure 9.25: (a) The vacuum LDOS evaluated at 6 Å above the Co atom for the in-plane (green, dotted) and out-of-plane (red, dashed) magnetized Mn film. (b) TAMR calculated for the curves in (a) according to Eq. (9.1). Shaded areas correspond to the features labeled in (a). (c) Orbital decomposition of the LDOS at the Co atom for the in-plane and out-of-plane spin quantization.

Figure 9.26 shows cross-sections of the majority and the minority spin of the in-plane (Fig. 9.26(a)) and out-of-plane (Fig. 9.26 (b)) magnetized film calculated along the yellow line in Fig. 9.23. The energy range has been chosen within 10 meV above the Fermi energy for a better comparison with the calculations in reference [158]. According to Serrate et al. [158] the circular shape of the majority LDOS at the Co atom is because of the d_{z^2} states that dominate the charge density close to the Fermi energy. They are rotationally symmetric perpendicular to the surface and result in a maximum above the central Mn row. Further amplification is due to the hybridization with states of s and p_z symmetry. In the minority channel, on the other hand, the shape of the LDOS at the Co adatom resembles a double lobe with its node being aligned to the central Mn row due to the predominance of states with

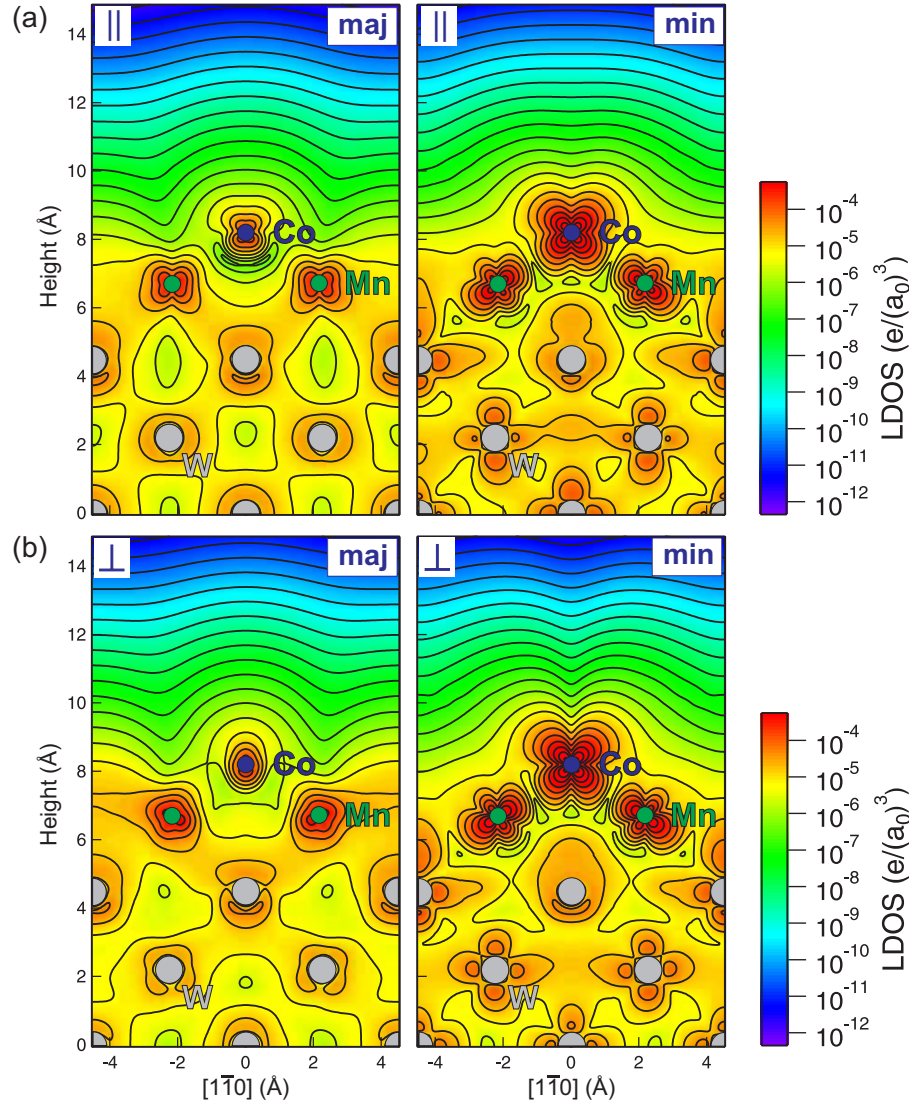


Figure 9.26: Cross sectional plots of (a) LDOS_{\parallel} and (b) LDOS_{\perp} along the orange line in Fig. 9.22 in the energy range between E_F and $E_F + 10$ meV. The left (right) panel displays the electrons with majority (minority) spin.

d_{zx} symmetry. This leads to an overall reduction of the electronic density and to a much quicker decay into the vacuum. For this reason, the vacuum local densities of states (figures 9.24 (c) and 9.25 (a)) are mainly dominated by the majority spin channel even though there is a huge peak in the minority d states of the Co atom (cf. Fig. 9.25 (c)). The comparison of the LDOS in the majority channel obtained for the in-plane and out-of-plane magnetized film (left panels in Fig. 9.26 (a) and (b)) reveals that the charge density of the perpendicular to the surface magnetized Co atom stretches farther into the vacuum than in the case of LDOS_{\parallel} . A similar

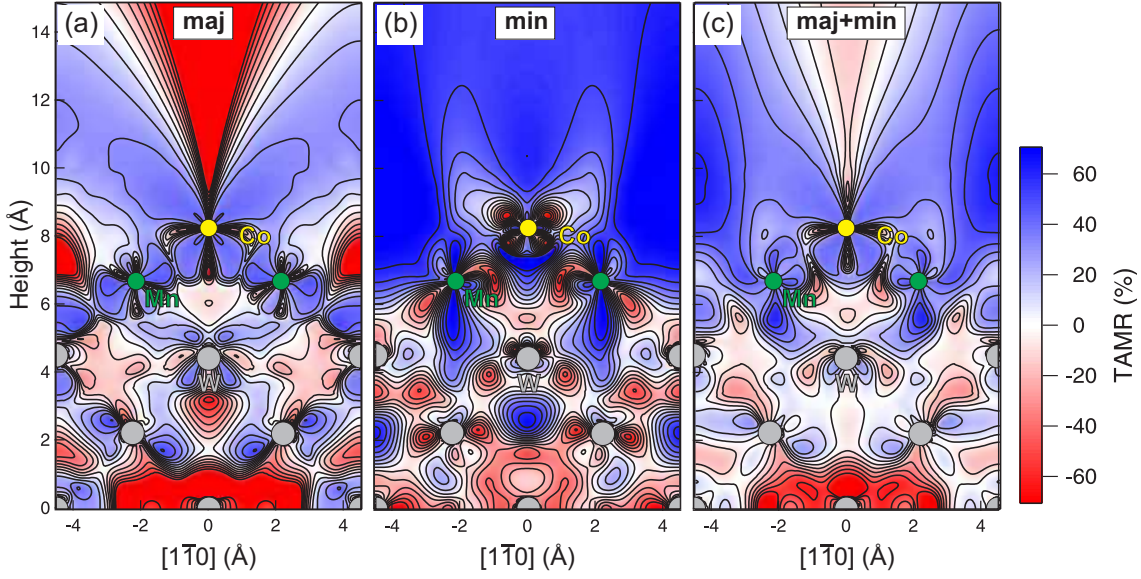


Figure 9.27: Cross sectional plots of the TAMR obtained from (a) the majority spin states, (b) the minority spin states and (c) the mixed spin states of LDOS_{\parallel} and LDOS_{\perp} along the orange line in Fig. 9.22 in the energy range between E_F and $E_F + 10$ meV.

behavior is observed in the minority channel (right panels in Fig. 9.26 (a) and (b)), where the dip of the node that is centered above the Co atom is diminished in LDOS_{\perp} with respect to LDOS_{\parallel} . This corresponds to the enhancement found in the vacuum LDOS in Fig. 9.24 (b).

Finally, the deviations found in the cross sections of figures 9.26 (a) and (b) allow for the calculation of the TAMR according to Eq. (9.1). Figure 9.27 presents the resulting plots. In the energy range of E_F and $E_F + 10$ meV in Fig 9.24 (d), where the LDOS and the TAMR have been integrated over the entire two-dimensional unit cell, the spin-averaged TAMR displays positive values of up to +13 %. In the minority channel the TAMR drops to -2% , whereas for the majority spin states it reaches +19%. The plots in Fig. 9.27 show a similar scenario but larger absolute TAMR values due to the cross-section, where only a line crossing the center of the two-dimensional unit cell is considered (cf. the yellow line in Fig. 9.23). The majority spin states, Fig. 9.27 (a), exhibit negative TAMR values located in a two lobe shaped area normal to the surface and centered at the position of the Co atom. The Mn atoms of the topmost layer, on the other hand, reveal positive TAMR values in a pear-shaped area perpendicular to the surface. Also, above the Co adatom the TAMR is positive due to the d_{z^2} symmetry of the states. In the minority channel this is different (cf. Fig. 9.27 (b)). While in the area above the Mn atoms of the surface layer the TAMR is positive, it exhibits negative values above the Co atom because of the strong enhancement of LDOS_{\perp} with respect to LDOS_{\parallel} in the d_{zx} and d_{yz} states in Fig. 9.25 (c). However, the spin-averaged TAMR in Fig. 9.27 (c) is

still negative above the Co atom. At the same time it reveals positive values within elongated areas above the W atoms of the interface layer. They result in +13 % for the spin-averaged TAMR due to the dominance of the majority spin states at 6 Å in the vacuum.

Conclusions

In this section the TAMR effect has been investigated for a single Co atom adsorbed on the Mn monolayer on W(110). This substrate is characterized by a spin-orbit driven spin-spiral ground state that allows for any direction of the Co magnetic moment provided by the underlying spin-spiral due to strong local exchange coupling. By rotating the magnetization direction from in-plane to out-of plane in the first-principles calculation changes in the vacuum density of states have been observed that range from -25% to +25%. Hence, a single Co atom adsorbed on a Mn monolayer exhibits an even larger TAMR effect than a Co atom adsorbed on the Fe double-layer film. Furthermore, it agrees well with the experimental value of 36 % evaluated from the line profiles in reference [158]. Thus, the $\cos^2 \theta$ variation of height and shape of the peaks can be ascribed to the TAMR. The changes observed in the electronic structure have been explained based on the mixing of d orbitals with different symmetry. This leads to differences in height and shape of the partial charge density at the Fermi energy above the Co atom. Since a distinct TAMR feature emerges from states close to the Fermi energy, this effect is accessible even in the limiting case of small bias voltages.

10 Summary

In this thesis, a density functional theory study of non-collinear magnetism and spin-orbit coupling effects on nanostructures such as ultrathin magnetic films and adatoms at surfaces has been presented. The investigation of magnetism at the nanoscale is of great importance in the field of spintronics. Non-collinear magnetic structures of the size of a few atoms or even in the single-atom limit might represent the building blocks of information carriers in future spintronic devices. Therefore, it is important to understand the mechanisms behind the formation of non-collinear spin structures and the influence of spin-orbit coupling on such nanoscale structures. The calculations were performed using one of the most accurate methods, namely the full-potential linearized plane wave method [23, 24], that is based on density functional theory [20, 21] as implemented in the FLEUR code [22]. After introducing the theoretical concepts and the applied methods in chapters 2 to 6 three different topics have been addressed.

In chapter 7 a Cr monolayer on the Pd(111) surface has been investigated as a prototype system for spin frustration on a triangular lattice. Two-dimensional antiferromagnets such as Cr monolayers are characterized by an antiparallel alignment of neighboring magnetic atoms due to the exchange coupling. On a triangular lattice the antiferromagnetic ordering between nearest neighbors can lead to a topological frustration of the spins resulting in a non-collinear spin structure, such as the 120° Néel state. It has been predicted for Cr monolayers on the (111) surfaces of Ag and Cu [118, 119] and experimentally observed in a monolayer of Mn on Ag(111) [120]. Here, the Pd(111) surface acts as a substrate for the Cr monolayer. By performing structural relaxations it was found that the Cr monolayer favors a row-wise antiferromagnetic alignment by about 162 meV/Cr atom in the fcc stacking with respect to the hcp stacking if only collinear configurations are considered. The magnetic phase space has been scanned by means of spin-spiral calculations along the high-symmetry lines of the two-dimensional Brillouin zone. For an unsupported Cr monolayer on the Pd(111) lattice constant as well as the Cr monolayer on Pd(111) a global minimum was obtained at the \bar{K} point, which corresponds to the 120° Néel state with an energy difference of about 39 meV/Cr atom and 27 meV/Cr atom, respectively, in comparison to the row-wise antiferromagnetic alignment of the spins. By mapping the *ab initio* results onto the Heisenberg model the exchange constants could be extracted. Cr on Pd(111) reveals a clear dominance of the antiferromagnetic nearest neighbor exchange over the second and third nearest neighbor exchange interaction. Also spin interactions beyond pair-wise exchange have been

taken into account by calculating a superposition state of spin spirals: the $3Q$ state, which has been found to be about 24 meV/Cr atom more unfavorable than the row-wise antiferromagnetic configuration. Thus, the Néel presents the magnetic ground state of the monolayer Cr on Pd(111). In order to compare the DFT results with the spin-polarized STM measurements images have been simulated within the spin-polarized Tersoff-Hamann model [61] for different in-plane magnetizations of the tip. Thereby, the predicted Néel state was confirmed. A quantitative comparison of simulated and experimental line profiles allowed for the determination of the in-plane tip magnetization direction in the spin-polarized STM experiments.

A more complex magnetic nanoscale structure has been presented in chapter 8 dedicated to the double layer of Mn on W(110). Besides Cr, Mn represents the other $3d$ transition metal for which two-dimensional antiferromagnetism is expected due to the tendency towards antiferromagnetic exchange coupling. For example, this has been observed for the Mn monolayer on W(110) [9], where the magnetic moments of neighboring atoms are almost antiparallel aligned. The small tilting angle between the magnetic moments is due the Dzyaloshinskii-Moriya interaction, which prefers a non-collinear magnetic ground state and thus induces a spin spiral. In this system, the importance of the Dzyaloshinskii-Moriya interaction at a surface has been demonstrated for the first time. As has been shown in this thesis also the Mn double layer prefers an antiparallel coupling of nearest neighbor magnetic moments leading to an antiferromagnetic checkerboard spin arrangement within the layers. Additionally, the surface and subsurface layer couple antiferromagnetic resulting in a parallel alignment of the spins along the $[\bar{1}10]$ direction and antiferromagnetic order along the $[001]$ direction. Among the considered collinear states this configuration is by about 137 meV/Mn atom energetically more favorable than an entirely ferromagnetic spin arrangement. From these calculations the conclusion was drawn that the Mn double layer on W(110) exhibits a preference of antiferromagnetism. By scanning the magnetic phase space via the calculation of flat spin-spirals along the high-symmetry lines of the two-dimensional Brillouin zone a tendency towards non-collinear magnetic order was observed for this system. However, the resulting flat spin-spiral state was only about 1.5 meV/Mn atom more favorable in energy than the preferred collinear antiferromagnetic configuration. By simulating spin-polarized STM images within a simple model based on the spin-polarized Tersoff-Hamann model [62] it was demonstrated that this spin-spiral state could not explain the results obtained in the spin-polarized STM measurements. Furthermore, it was shown that the experimental STM contrast could only be reproduced by a transverse conical spin spiral state. In this structure the antiparallel aligned magnetic moments of neighboring atoms rotate on a cone with the propagation direction of the spin spiral being perpendicular to the magnetization direction. By mapping the DFT results onto an extended Heisenberg model it was demonstrated that the canting of the magnetic moments is induced by exchange interactions beyond nearest neighbors, namely the four-spin interaction and the biquadratic exchange. The

rotation, on the other hand, originates from the Heisenberg exchange and is stabilized by the Dzyaloshinskii-Moriya interaction. The resulting spin structure is about 16.7 meV/Mn atom lower in energy than the collinear antiferromagnetic state and exhibits a cone angle of $\theta = 30^\circ$ as well a rotation angle of $\phi = 32^\circ$. This finding presents the first observation of a conical spin-spiral state in an ultrathin film and demonstrates the crucial role of the higher-order spin interactions in surface magnetism.

By means of spin-polarized STM images simulated within the spin-polarized Tersoff-Hamann model [61] the influence of the tip magnetization direction onto the observed pattern has been studied. Thus, it was demonstrated that for complex magnetic structures it might be preferable to vary the tip magnetization direction according to the three crystallographic axes in order to detect every pattern originating from the magnetic structure. Furthermore, the experimental determination of the cone angle is a non-trivial task. Therefore, the relation of the corrugation amplitudes, i.e., the maximum difference in the tip height during an STM measurement in dependence on the cone angle has been studied in the present work utilizing the spin-polarized Tersoff-Hamann model and the independent-orbital approximation [62] in order to provide an informative basis for future spin-polarized STM measurements. Finally, the tunneling anisotropic magnetoresistance (TAMR) has been investigated in the double layer Mn on W(110). This effect leads to magnetization-direction dependent changes in the electronic structure and can be detected by means of spin-polarized and non-spin-polarized scanning tunneling microscopy. Since it is pinned to the electronic structure, the TAMR contrast does not vary with respect to the rotation of the tip magnetization direction. For instance, in a non-spin-polarized STM measurement it provides the possibility to distinguish magnetic structures such as domains and domain walls without the use of an external field [19].

Finally, the TAMR is investigated for single adatoms on ultrathin magnetic films on W(110) in chapter 9. Single magnetic and nonmagnetic atoms present the smallest possible logical unit in a future spintronic device. A major issue in the study of the TAMR is the direct comparison of theoretical and experimental results. By considering single atoms adsorbed on magnetic ultrathin films with a non-collinear spin structure the direction of the adatom's magnetic moment can be controlled via the adsorption site and the exchange coupling with the neighboring atoms of the underlying film. In addition, the experiments can be carried out without the use of an external magnetic field thereby circumventing problems such as a potential deformation of the contacts. First, the TAMR has been studied for a double layer of Fe on W(110), which presents the substrate for the single atoms. The Fe double layer exhibits a nanoscale domain structure on W(110) with magnetic moments that rotate right-handed and cycloidal via the [001] direction in the Néel type domain walls [10, 128, 129]. By rotating the spins in the Fe film from out-of-plane to in-plane along the [001] direction the local densities of states in the vacuum exhibit deviations depending on the magnetization direction. They can be quantified via

the TAMR. It is defined as the difference between the local densities of states for the two magnetization directions divided by the densities of states of one of the configurations. It reveals energy dependent oscillations in sign ranging from -17% to $+11\%$ for the Fe double layer on W(110). The TAMR feature that can be related to the experiments from Bode et al. [19], who found a significant deviation in the dI/dU signals measured above the domain and the domain wall at $U = 0.07$ V, is located at $+0.14$ eV above the Fermi energy and is of the order of 11% . Upon the decomposition of the density of states in the muffin tin spheres of the Fe atoms, the TAMR feature can be ascribed to the spin-orbit induced mixing of d_{z^2} states with the hybridized d_{xy} and d_{yz} orbitals in the minority spin channel.

In the next step, the TAMR has been studied for single Co adatoms on the Fe double layer on W(110). Here, it presents a similar range of values between -19% and $+9\%$ which agrees with the experimental values of -12% to $+5\%$ observed in STM measurements. The strongest TAMR feature is located at 0.07 eV below the Fermi level and has a strength of -19% . It stems from the hybridization of minority spin states in the Co atom and the Fe atoms of the underlying film and is of d_{xy} character at Co and d_{yz} in the Fe film. In order to capture the essence of the TAMR, a simple model has been introduced that describes the mixing of two atomic states at a surface by means of the Green's functions. It illustrates the concept of spin-orbit induced mixing of states with different orbital character and by revisiting the d_{z^2} and d_{zx} states in the Co adatom obtained from DFT calculations the resulting model TAMR agrees well with the TAMR of the DFT results. However, by choosing an Ir adatom instead of a Co adatom the TAMR effect can be increased to values of up to 70% . Due to hybridization with the adjacent Fe atoms of the film the Ir adatom reveals an induced magnetic moment of $+0.77 \mu_B$ and $+0.87 \mu_B$ within the LDA [31] and the GGA [33], respectively. In comparison to the magnetic moment of the Co adatom, i.e., $1.81 \mu_B$ obtained within the LDA [31], the magnetic moment of the Ir adatom is half as large. Nevertheless, it exhibits a spin-polarization of up to 0.9 , which is about three times larger than that of the Co adatom on Fe/W(110) [154]. Thus, the use of $5d$ elements instead of those of the $3d$ series does not only result in a larger TAMR but might also present a new route towards larger spin-valve effects. Furthermore, the TAMR of the Ir adatom has not only been studied for the case of a cycloidal rotating domain wall, i.e., the Néel wall, but also for a Bloch wall, which exhibits a helical rotation from 'up' to 'down' via the $[1\bar{1}0]$ direction. In both cases, the TAMR exhibits large values that range from -51% to $+69\%$ and from -39% to $+52\%$ in the cycloidal and helical domain wall, respectively. At the same time the TAMR of the cycloidal domain wall can be distinguished from that of the helical domain wall due to the spin-orbit induced splitting of the peaks. In the case of a cycloidal domain wall, the mixing of d_{z^2} states with those of d_{zx} symmetry leads to a pronounced peak at -0.63 eV with respect to the Fermi energy for the out-of-plane magnetized adatom, which is absent in the vacuum local density of states of the in-plane magnetization direction. In the case of the helical domain wall, the mixing

of d_{z^2} states with those of d_{yz} symmetry results in peaks for both magnetization directions that differ slightly in height and energy position. Therefore, it may be possible to make use of the TAMR in single atoms in order to determine the domain wall type in STM experiments.

Finally, the TAMR of a Co adatom on the monolayer Mn on W(110) has been investigated. As mentioned before, the monolayer Mn on W(110) exhibits a spin-orbit driven spin-spiral state with almost antiparallel alignment of neighboring magnetic moments propagating along the $[\bar{1}10]$ direction [9]. Due to the ferromagnetic coupling of the Co adatom and the adjacent Mn atoms of the film the magnetic moment of the adatom can be set to any magnetization direction that is accessible in the spin spiral [158]. For this system, the TAMR ranges from -25% to $+25\%$ and a large feature at 0.09 eV below the Fermi level can be ascribed to the mixing of the d_{z^2} states with d_{yz} orbitals of both spin channels. Moreover, the TAMR value of $+25\%$ agrees well with the value of $+36\%$ extracted from spin-polarized STM experiments [158].

In conclusion, the magnetism of nanostructures at surfaces has been investigated in this thesis. It was demonstrated that not only the frustration of Heisenberg exchange coupling but also spin-interactions beyond pair-wise exchange, such as the four-spin interaction and the biquadratic exchange, can induce non-collinear magnetic structures. In particular, it has been demonstrated that the Mn double layer on W(110) exhibits a conical spin-spiral state due to higher-order spin interactions. This shows that such terms can play a crucial role for magnetic nanostructures at surfaces. Furthermore, it was shown that the formation of such non-collinear magnetic structures can be further stabilized by the Dzyaloshinskii-Moriya interaction. Another central topic of this thesis was the study of the TAMR on the basis of single atoms on magnetic thin films concerning a future application in spintronic devices. It was demonstrated that the use of single atoms adsorbed on ultrathin magnetic films allow for a direct comparison of theoretical and experimental results. TAMR values of up to 25% have been observed in Co adatoms. Furthermore, the use of a Ir instead of a Co as adatom gives TAMR values of up to 70%. Therefore, choosing a $5d$ element in the tunnel junction shows promising results since both, the TAMR and the spin-valve effect can be explicitly enhanced compared to that of an adatom of the $3d$ series.

11 Bibliography

- [1] Data sheet, Hitachi GST Travelstar 5K500.B.
- [2] M. N. BAIBICH, J. M. BROTO, A. FERT, F. N. VAN DAU, F. PETROFF, P. ETIENNE, G. CREUZET, A. FRIEDERICH and J. CHAZELAS, *Giant Magnetoresistance of (001)Fe/(001)Cr Magnetic Superlattices*, Phys. Rev. Lett. **61**, 2472 (1988).
- [3] G. BINASCH, P. GRÜNBERG, F. SAURENBACH and W. ZINN, *Enhanced magnetoresistance in layered magnetic structures with antiferromagnetic interlayer exchange*, Phys. Rev. B **39**, 4828 (1989).
- [4] A. BERGER, in *40th Springschool, Spintronics – From GMR to Quantum Information*.
- [5] S. A. WOLF, D. D. AWSCHALOM, R. A. BUHRMAN, J. M. DAUGHTON, S. VON MOLNÁR, M. L. ROUKES, A. Y. CHTCHELKANOVA and D. M. TREGGER, *Spintronics: A Spin-Based Electronics Vision for the Future*, Science **294**, 1488 (2001).
- [6] A. FERT, V. CROS and J. SAMPAIO, *Skyrmions on the track*, Nature Nanotechnology **8**, 152 (2013).
- [7] I. E. DZHALOSHINSKII, *Thermodynamic theory of weak ferromagnetism in antiferromagnetic substances*, Sov. Phys. JETP **5**, 1259 (1957).
- [8] T. MORIYA, *Anisotropic Superexchange Interaction and Weak Ferromagnetism*, Phys. Rev. **120**, 91 (1960).
- [9] M. BODE, M. HEIDE, K. VON BERGMANN, P. FERRIANI, S. HEINZE, G. BIHLMAYER, A. KUBETZKA, O. PIETZSCH, S. BLÜGEL and R. WIESENDANGER, *Chiral magnetic order at surfaces driven by inversion asymmetry*, Nature **447**, 190 (2007).
- [10] M. HEIDE, G. BIHLMAYER and S. BLÜGEL, *Dzyaloshinskii-Moriya interaction accounting for the orientation of magnetic domains in ultrathin films: Fe/W(110)*, Phys. Rev. B **78**, 140403 (2008).

- [11] S. EMORI, U. BAUER, S.-M. AHN, E. MARTINEZ and G. S. D. BEACH, *Current-driven dynamics of chiral ferromagnetic domain walls*, ArXiv e-prints (2013).
- [12] T. H. R. SKYRME, *A Unified Field Theory of Mesons and Baryons*, Nuclear Physics **31**, 556 (1962).
- [13] S. MÜHLBAUER, B. BINZ, F. JONIETZ, C. PFLEIDERER, A. ROSCH, A. NEUBAUER, R. GEORGII and P. BÖNI, *Skyrmion Lattice in a Chiral Magnet*, Science **323**, 915 (2009).
- [14] A. NEUBAUER, C. PFLEIDERER, B. BINZ, A. ROSCH, R. RITZ, P. G. NIKLOWITZ and P. BÖNI, *Topological Hall Effect in the A Phase of MnSi*, Phys. Rev. Lett. **102**, 186602 (2009).
- [15] C. PAPPAS, E. LELIÈVRE-BERNA, P. FALUS, P. M. BENTLEY, E. MOSKVIN, S. GRIGORIEV, P. FOUQUET and B. FARAGO, *Chiral Paramagnetic Skyrmion-like Phase in MnSi*, Phys. Rev. Lett. **102**, 197202 (2009).
- [16] S. HEINZE, K. VON BERGMANN, M. MENZEL, J. BREDE, A. KUBETZKA, R. WIESENDANGER, G. BIHLMAYER and S. BLÜGEL, *Spontaneous atomic-scale magnetic skyrmion lattice in two dimensions*, Nature Physics **7**, 713 (2011).
- [17] F. JONIETZ, S. MÜHLBAUER, C. PFLEIDERER, A. NEUBAUER, W. MÜNZER, A. BAUER, T. ADAMS, R. GEORGII, P. BÖNI, R. A. DUINE, K. EVERSCHOR, M. GARST and A. ROSCH, *Spin Transfer Torques in MnSi at Ultralow Current Densities*, Science **330**, 1648 (2010).
- [18] X. YU, N. KANAZAWA, W. ZHANG, T. NAGAI, T. HARA, K. KIMOTO, Y. MATSUI, Y. ONOSE and Y. TOKURA, *Skyrmion flow near room temperature in an ultralow current density*, Nature Communications **3**, 988 (2012).
- [19] M. BODE, S. HEINZE, A. KUBETZKA, O. PIETZSCH, X. NIE, G. BIHLMAYER, S. BLÜGEL and R. WIESENDANGER, *Magnetization-Direction-Dependent Local Electronic Structure Probed by Scanning Tunneling Spectroscopy*, Phys. Rev. Lett. **89**, 237205 (2002).
- [20] P. HOHENBERG and W. KOHN, *Inhomogeneous Electron Gas*, Phys. Rev. **136**, B864 (1964).
- [21] W. KOHN and L. J. SHAM, *Self-Consistent Equations Including Exchange and Correlation Effects*, Phys. Rev. **140**, A1133 (1965).
- [22] www.flapw.de.

-
- [23] E. WIMMER, H. KRAKAUER, M. WEINERT and A. J. FREEMAN, *Full-potential self-consistent linearized-augmented-plane-wave method for calculating the electronic structure of molecules and surfaces: O₂ molecule*, Phys. Rev. B **24**, 864 (1981).
- [24] H. KRAKAUER, M. POSTERNAK and A. J. FREEMAN, *Linearized augmented plane-wave method for the electronic band structure of thin films*, Phys. Rev. B **19**, 1706 (1979).
- [25] C. GOULD, C. RÜSTER, T. JUNGWIRTH, E. GIRGIS, G. M. SCHOTT, R. GI-RAUD, K. BRUNNER, G. SCHMIDT and L. W. MOLENKAMP, *Tunneling Anisotropic Magnetoresistance: A Spin-Valve-Like Tunnel Magnetoresistance Using a Single Magnetic Layer*, Phys. Rev. Lett. **93**, 117203 (2004).
- [26] M. BODE, O. PIETZSCH, A. KUBETZKA, S. HEINZE and R. WIESEN-DANGER, *Experimental Evidence for Intra-Atomic Noncollinear Magnetism at Thin Film Probe Tips*, Phys. Rev. Lett. **86**, 2142 (2001).
- [27] O. PIETZSCH, A. KUBETZKA, M. BODE and R. WIESENDANGER, *Real-Space Observation of Dipolar Antiferromagnetism in Magnetic Nanowires by Spin-Polarized Scanning Tunneling Spectroscopy*, Phys. Rev. Lett. **84**, 5212 (2000).
- [28] L. H. THOMAS, *The calculation of atomic fields.*, Math. Proc. of the Cambridge Phil. Soc. **23**, p. 542 (1927).
- [29] E. FERMI, *Un metodo statistico per la determinazione di alcune priorieta dell'atome*, Rend. Accad. Naz. Lincei **6**, 602 (1927).
- [30] M. LEVY, *Universal variational functionals of electron densities, first-order density matrices, and natural spin-orbitals and solution of the v-representability problem*, Proceedings of the National Academy of Sciences **76**, 6062 (1979).
- [31] U. V. BARTH and L. HEDIN, *A local exchange-correlation potential for the spin-polarized case*, J. Phys.C: Solid State Physics **5**, 1629 (1972).
- [32] M. M. PANT and A. K. RAJAGOPAL, *Theory of inhomogeneous magnetic electron gas*, Solid State Comm. **10**, 1157 (1972).
- [33] Y. ZHANG and W. YANG, *Comment on 'Generalized Gradient Approximation Made Simple'*, Phys. Rev. Lett. **80**, 890 (1998).
- [34] D. D. JOHNSON, *Modified Broyden's method for accelerating convergence in self-consistent calculations*, Phys. Rev. B **38**, 12807 (1988).

- [35] M. WEINERT, E. WIMMER and A. J. FREEMAN, *Total-energy all-electron density functional method for bulk solids and surfaces*, Phys. Rev. B **26**, 4571 (1982).
- [36] W. E. PICKETT, *Pseudopotential methods in condensed matter applications*, Computer Physics Reports **9**, 115 (19).
- [37] J. C. SLATER, *Wave Functions in a Periodic Potential*, Phys. Rev. **51**, p. 846 (1937).
- [38] O. K. ANDERSEN, *Linear methods in band theory*, Phys. Rev. B **12**, 3060 (1975).
- [39] D. D. KOELLING and G. O. ARBMAN, *Use of energy derivative of the radial solution in an augmented plane wave method: application to copper*, Journal of Physics F Metal Physics **5**, 2041 (1975).
- [40] D. SINGH, *Ground-state properties of lanthanum: Treatment of extended-core states*, Phys. Rev. B **43**, 6388 (1991).
- [41] J. STOER, *Numerische Mathematik 1*, Springer-Verlag, Berlin (1994).
- [42] P. E. BLÖCHL, O. JEPSEN and O. K. ANDERSEN, *Improved tetrahedron method for Brillouin-zone integrations*, Phys. Rev. B **49**, 16223 (1994).
- [43] D. J. CHADI and M. L. COHEN, *Special Points in the Brillouin Zone*, Phys. Rev. B **8**, 5747 (1973).
- [44] H. J. MONKHORST and J. D. PACK, *Special points for Brillouin-zone integrations*, Phys. Rev. B **13**, 5188 (1976).
- [45] S. H. VOSKO and J. P. PERDEW, *Theory of the Spin Susceptibility of an Inhomogeneous Electron Gas via the Density Functional Formalism*, Canadian Journal of Physics **53**, 1385 (1975).
- [46] O. GUNNARSSON, *Band model for magnetism of transition metals in the spin-density-functional formalism*, Journal of Physics F: Metal Physics **6**, 587 (1976).
- [47] J. F. JANAK, *Uniform susceptibilities of metallic elements*, Phys. Rev. B **16**, 255 (1977).
- [48] U. K. POULSEN, J. KOLLÁR and O. K. ANDERSON, *Magnetic and cohesive properties from canonical bands*, Journal of Physics F: Metal Physics **6**, L241 (1976).

-
- [49] A. R. WILLIAMS, R. ZELLER, V. L. MORUZZI, C. D. GELATT and J. KÜBLER, *Covalent magnetism: An alternative to the Stoner model*, Journal of Applied Physics **52**, 2067 (1981).
- [50] S. BLÜGEL, T. BRÜCKEL and C. M. SCHNEIDER, *Magnetism goes Nano*, Schriften des Forschungszentrum Jülich, Reihe Materie und Material (2005).
- [51] M. TAKAHASHI, *Half-filled Hubbard model at low temperature*, J. Phys. C: Solid State Phys **10**, 1289 (1977).
- [52] M. PAJDA, J. KUDRNOVSKÝ, I. TUREK, V. DRCHAL and P. BRUNO, *Ab initio calculations of exchange interactions, spin-wave stiffness constants, and Curie temperatures of Fe, Co, and Ni*, Phys. Rev. B **64**, 174402 (2001).
- [53] K. TERAKURA, N. HAMADA, T. OGUCHI and T. ASADA, *Local and non-local spin susceptibilities of transition metals*, Journal of Physics F: Metal Physics **12**, 1661 (1982).
- [54] G. BINNIG, H. ROHRER, C. GERBER and E. WEIBEL, *Surface Studies by Scanning Tunneling Microscopy*, Phys. Rev. Lett. **49**, 57 (1982).
- [55] C. J. CHEN, *Introduction to Scanning Tunneling Microscopy*, Oxford University Press, New York (1993).
- [56] Y. YOSHIDA, S. SCHRÖDER, P. FERRIANI, D. SERRATE, A. KUBETZKA, K. VON BERGMANN, S. HEINZE and R. WIESENDANGER, *Conical Spin-Spiral State in an Ultrathin Film Driven by Higher-Order Spin Interactions*, Phys. Rev. Lett. **108**, 087205 (2012).
- [57] M. BODE, M. GETZLAFF, A. KUBETZKA, R. PASCAL, O. PIETZSCH and R. WIESENDANGER, *Temperature-Dependent Exchange Splitting of a Surface State on a Local-Moment Magnet: Tb(0001)*, Phys. Rev. Lett. **83**, 3017 (1999).
- [58] M. WAŚNIEWSKA, S. SCHRÖDER, P. FERRIANI and S. HEINZE, *Real space observation of spin frustration in Cr on a triangular lattice*, Phys. Rev. B **82**, 012402 (2010).
- [59] R. WIESENDANGER, I. V. SHVETS, D. BÜRGLER, G. TARRACH, H. J. GÜNTERODT, J. M. D. COEY and S. GRÄSER, *Topographic and Magnetic-Sensitive Scanning Tunneling Microscope Study of Magnetite*, Science **255**, 583 (1992).
- [60] M. JULLIERE, *Tunneling between ferromagnetic films*, Physics Letters A **54**, 225 (1975).

- [61] D. WORTMANN, S. HEINZE, P. KURZ, G. BIHLMAYER and S. BLÜGEL, *Resolving Complex Atomic-Scale Spin Structures by Spin-Polarized Scanning Tunneling Microscopy*, Phys. Rev. Lett. **86**, 4132 (2001).
- [62] S. HEINZE, *Simulation of spin-polarized scanning tunneling microscopy images of nanoscale non-collinear magnetic structures*, Applied Physics A: Materials Science & Processing **85**, 407 (2006).
- [63] J. BARDEEN, *Tunnelling from a Many-Particle Point of View*, Phys. Rev. Lett. **6**, 57 (1961).
- [64] J. TERSOFF and D. R. HAMANN, *Theory and Application for the Scanning Tunneling Microscope*, Phys. Rev. Lett. **50**, 1998 (1983).
- [65] J. TERSOFF and D. R. HAMANN, *Theory of the scanning tunneling microscope*, Phys. Rev. B **31**, 805 (1985).
- [66] V. P. LABELLA, H. YANG, D. W. BULLOCK, P. M. THIBADO, P. KRATZER and M. SCHEFFLER, *Atomic Structure of the GaAs(001) – (2 × 4) Surface Resolved Using Scanning Tunneling Microscopy and First-Principles Theory*, Phys. Rev. Lett. **83**, 2989 (1999).
- [67] S. HEINZE, S. BLÜGEL, R. PASCAL, M. BODE and R. WIESENDANGER, *Prediction of bias-voltage-dependent corrugation reversal for STM images of bcc (110) surfaces: W(110), Ta(110), and Fe(110)*, Phys. Rev. B **58**, 16432 (1998).
- [68] S. HEINZE, R. ABT, S. BLÜGEL, G. GILAROWSKI and H. NIEHUS, *Scanning Tunneling Microscopy Images of Transition-Metal Structures Buried Below Noble-Metal Surfaces*, Phys. Rev. Lett. **83**, 4808 (1999).
- [69] C. J. CHEN, *Theory of scanning tunneling spectroscopy*, Journal of Vacuum Science Technology A: Vacuum, Surfaces, and Films **6**, 319 (1988).
- [70] C. J. CHEN, *Microscopic view of scanning tunneling microscopy*, Journal of Vacuum Science Technology A: Vacuum, Surfaces, and Films **9**, 44 (1991).
- [71] C. J. CHEN, *Origin of atomic resolution on metal surfaces in scanning tunneling microscopy*, Phys. Rev. Lett. **65**, 448 (1990).
- [72] S. HEINZE, M. BODE, A. KUBETZKA, O. PIETZSCH, X. NIE, S. BLÜGEL and R. WIESENDANGER, *Real-Space Imaging of Two-Dimensional Antiferromagnetism on the Atomic Scale*, Science **288**, 1805 (2000).

-
- [73] A. R. SMITH, R. YANG, H. YANG, W. R. LAMBRECHT, A. DICK and J. NEUGEBAUER, *Aspects of spin-polarized scanning tunneling microscopy at the atomic scale: experiment, theory, and simulation*, Surface Science **561**, 154 (2004).
- [74] P. H. DEDERICHS, S. BLÜGEL, R. ZELLER and H. AKAI, *Ground States of Constrained Systems: Application to Cerium Impurities*, Phys. Rev. Lett. **53**, 2512 (1984).
- [75] V. P. ANTROPOV, M. I. KATSNELSON, B. N. HARMON, M. VAN SCHILFGAARDE and D. KUSNEZOV, *Spin dynamics in magnets: Equation of motion and finite temperature effects*, Phys. Rev. B **54**, 1019 (1996).
- [76] V. P. ANTROPOV, M. I. KATSNELSON, M. VAN SCHILFGAARDE and B. N. HARMON, *AbInitio Spin Dynamics in Magnets*, Phys. Rev. Lett. **75**, 729 (1995).
- [77] O. N. MRYASOV, A. I. LIECHTENSTEIN, L. M. SANDRATSKII and V. A. GUBANOV, *Magnetic structure of FCC iron*, Journal of Physics: Condensed Matter **3**, 7683 (1991).
- [78] M. UHL, L. SANDRATSKII and J. KÜBLER, *Electronic and magnetic states of γ -Fe*, Journal of Magnetism and Magnetic Materials **103**, 314 (1992).
- [79] C. HERRING, *Magnetism*, Academic, New York (1966).
- [80] L. M. SANDRATSKII, *Energy Band Structure Calculations for Crystals with Spiral Magnetic Structure*, physica status solidi (b) **136**, 167 (1986).
- [81] P. KURZ, F. FÖRSTER, L. NORDSTRÖM and S. BLÜGEL, *Ab initio treatment of noncollinear magnets with the full-potential linearized augmented plane wave method*, Phys. Rev. B **69**, 24415 (2004).
- [82] N. W. ASHCROFT and N. D. MERMIN, *Solid State Physics*, Holt, Rinehart and Wilson (1976).
- [83] P. KURZ, *Non-collinear Magnetism at Surfaces and in Ultrathin Films*, Ph.D. thesis, RWTH Aachen (2000).
- [84] L. M. SANDRATSKII and P. G. GULETSKII, *Symmetrised method for the calculation of the band structure of noncollinear magnets*, Journal of Physics F: Metal Physics **16**, L43 (1986).
- [85] L. SANDRATSKII and P. GULETSKII, *Energy band structure of BBC iron at finite temperatures*, Journal of Magnetism and Magnetic Materials **79**, 306 (1989).

- [86] J. KUBLER, K. H. HOCK, J. STICHT and A. R. WILLIAMS, *Density functional theory of non-collinear magnetism*, Journal of Physics F: Metal Physics **18**, 469 (1988).
- [87] J. KUBLER, K.-H. HOCK, J. STICHT and A. R. WILLIAMS, *Local spin-density functional theory of noncollinear magnetism (invited)*, Journal of Applied Physics **63**, 3482 (1988).
- [88] J. STICHT, K.-H. HCK and J. KBLER, *Non-collinear itinerant magnetism: the case of Mn 3 Sn*, Journal of Physics: Condensed Matter **1**, 8155 (1989).
- [89] O. N. MRYASOV, V. A. GUBANOV and A. I. LIECHTENSTEIN, *Spiral-spin-density-wave states in fcc iron: Linear-muffin-tin-orbitals band-structure approach*, Phys. Rev. B **45**, 12330 (1992).
- [90] L. NORDSTRÖM and D. J. SINGH, *Noncollinear Intra-atomic Magnetism*, Phys. Rev. Lett. **76**, 4420 (1996).
- [91] P. KURZ, F. FÖRSTER, L. NORDSTRÖM, G. BIHLMAYER and S. BLÜGEL, *Ab initio treatment of noncollinear magnets with the full-potential linearized augmented plane wave method*, Phys. Rev. B **69**, 024415 (2004).
- [92] L. NÉEL, *L'approche á la saturation de la magnétostriction*, J. Phys. Rad. **15**, 376 (1954).
- [93] Y. A. BYCHKOV and E. I. RASHBA, *Oscillatory effects and the magnetic susceptibility of carriers in inversion layers*, J. Phys. C: Solid State Phys. **15**, 6039 (1984).
- [94] Y. A. BYCHKOV and E. I. RASHBA, *Properties of a 2D electron gas with lifted spectral degeneracy*, Sov. Phys. JETP Lett. **39**, 78 (1984).
- [95] M. UCHIDA, Y. ONOSE, Y. MATSUI and Y. TAKURA, *Real-space observation of helical spin order*, Science **311**, 359 (2006).
- [96] D. D. KOELLING and B. N. HARMON, *A technique for relativistic spin-polarised calculations*, J. Phys. C: Solid State Physics **10**, 3107 (1977).
- [97] G. BAYM, *Lectures On Quantum Mechanics*, Lecture Notes and Supplements in Physics, Westview Press (1974).
- [98] J. D. JACKSON, *Klassische Elektrodynamik*, Gruyter, 3 ed. (2002).
- [99] E. ABATE and M. ASDENTE, *Tight-Binding Calculation of 3d Bands of Fe with and without Spin-Orbit Coupling*, Phys. Rev. **140**, A1303 (1965).

-
- [100] P. BRUNO, in *24. IFF-Ferienkurs, Magnetismus von Festkörpern und Grenzflächen*, p. 24.1, Forschungszentrum Jülich GmbH (1993).
- [101] P. BRUNO, *Dipolar magnetic surface anisotropy in ferromagnetic thin films with interfacial roughness*, Journal of applied physics **64**, 3153 (1988).
- [102] P. BRUNO, *Tight-binding approach to the orbital magnetic moment and magnetocrystalline anisotropy of transition-metal monolayers*, Phys. Rev. B **39**, 865 (1989).
- [103] S. BLÜGEL, *Magnetische Anisotropie und Magnetostraktion*, www.fz-juelich.de/iff/staff/Bluegel_S/Lectures, Vorlesungsskript.
- [104] M. METHFESSEL and J. KÜBLER, *Bond analysis of heats of formation: application to some group VIII and IB hydrides*, J. Phys. F: Met. Phys. pp. 141–161 (1982).
- [105] C. LI, A. J. FREEMAN, H. J. F. JANSEN and C. L. FU, *Magnetic anisotropy in low-dimensional ferromagnetic systems: Fe monolayers on Ag(001), Au(001), and Pd(001) substrates*, Phys. Rev. B **42**, 5433 (1990).
- [106] A. R. MACKINTOSH and O. K. ANDERSEN, *Electrons at the Fermi Surface* (1980), Cambridge University Press, Cambridge.
- [107] A. OSWALD, R. ZELLER, P. J. BRASPENNING and P. H. DEDERICHS, *Interaction of magnetic impurities of Cu and Ag*, J. Phys. F: Met. Phys. **15**, 193 (1985).
- [108] A. I. LIECHTENSTEIN, M. I. KATSNELSON, V. P. ANTROPOV and V. A. GUBANOV, *Local spin density functional approach to the theory of exchange interactions in ferromagnetic metals and alloys*, Journal of Magnetism and Magnetic Materials **67**, 65 (1987).
- [109] S. J. YOUN, W. MANNSTADT and A. J. FREEMAN, *Analytic Spin-Orbit Coupling Matrix Element Formulae in FLAPW Calculations*, J. Comp. Phys. **172**, 387 (2001).
- [110] A. CRÉPIEUX and C. LACROIX, *Dzyaloshinsky-Moriya interactions induced by symmetry breaking at a surface*, J. Magn. Magn. Mater. **182**, 341 (1998).
- [111] P. W. ANDERSON, *New Approach to the Theory of Superexchange Interactions*, Phys. Rev. **115**, 2 (1959).
- [112] M. HEIDE, G. BIHLMAYER and S. BLÜGEL, *Describing Dzyaloshinskii-Moriya spirals from first principles*, Physica B: Cond. Mat. **404**, 2678 (2009).

- [113] S. BLÜGEL, D. PESCIA and P. H. DEDERICHS, *Ferromagnetism versus antiferromagnetism of the Cr(001) surface*, Phys. Rev. B **39**, 1392 (1989).
- [114] R. WIESENDANGER, H.-J. GÜNTHERODT, G. GÜNTHERODT, R. J. GAMBINO and R. RUF, *Observation of vacuum tunneling of spin-polarized electrons with the scanning tunneling microscope*, Phys. Rev. Lett. **65**, 247 (1990).
- [115] M. KLEIBER, M. BODE, R. RAVLIĆ and R. WIESENDANGER, *Topology-Induced Spin Frustrations at the Cr(001) Surface Studied by Spin-Polarized Scanning Tunneling Spectroscopy*, Phys. Rev. Lett. **85**, 4606 (2000).
- [116] B. SANTOS, J. PUERTA, J. I. CERDA, R. STUMPF, K. VON BERGMANN, R. WIESENDANGER, M. BODE, F. MCCARTY and F. DE LA FIGUERA, *Structure and magnetism of ultra-thin chromium layers on W(110)*, New Journal of Physics **10**, 013005 (2008).
- [117] P. FERRIANI, S. HEINZE, G. BIHLMAYER and S. BLÜGEL, *Unexpected trend of magnetic order of 3d transition-metal monolayers on W(001)*, Phys. Rev. B **72**, 024452 (2005).
- [118] S. HEINZE, P. KURZ, D. WORTMANN, G. BIHLMAYER and S. BLÜGEL, *Complex Magnetism in Ultra-Thin Films: Atomic-Scale Spin Structures and Resolution by Spin-Polarized Scanning Tunneling Microscopy*, Applied Physics A **75**, 25 (2002).
- [119] P. KURZ, G. BIHLMAYER and S. BLÜGEL, *Noncollinear magnetism of Cr and Mn monolayers on Cu(111)*, Journal of Applied Physics **87**, 6101 (2000).
- [120] C. L. GAO, W. WULFHEKEL and J. KIRSCHNER, *Revealing the 120° Antiferromagnetic Néel Structure in Real Space: One Monolayer Mn on Ag(111)*, Phys. Rev. Lett. **101**, 267205 (2008).
- [121] B. HARDRAT, A. AL-ZUBI, P. FERRIANI, S. BLÜGEL, G. BIHLMAYER and S. HEINZE, *Complex magnetism of iron monolayers on hexagonal transition metal surfaces from first principles*, Phys. Rev. B **79**, 094411 (2009).
- [122] S. H. VOSKO, L. WILK and M. NUSAIR, *Accurate spin-dependent electron liquid correlation energies for local spin density calculations: a critical analysis*, Canadian Journal of Physics **58**, 1200 (1980).
- [123] P. KURZ, G. BIHLMAYER, K. HIRAI and S. BLÜGEL, *Three-Dimensional Spin Structure on a Two-Dimensional Lattice: Mn / Cu(111)*, Phys. Rev. Lett. **86**, 1106 (2001).
- [124] M. BODE, *Spin-polarized scanning tunnelling microscopy*, Reports on Progress in Physics **66**, 523 (2003).

-
- [125] R. SCHMIDT, C. LAZO, H. HÖLSCHER, U. H. PI, V. CACIUC, A. SCHWARZ, R. WIESENDANGER and S. HEINZE, *Probing the Magnetic Exchange Forces of Iron on the Atomic Scale*, Nano Letters **9**, 200 (2009).
- [126] S. KRAUSE, L. BERBIL-BAUTISTA, G. HERZOG, M. BODE and R. WIESENDANGER, *Current-Induced Magnetization Switching with a Spin-Polarized Scanning Tunneling Microscope*, Science **317**, 1537 (2007).
- [127] P. FERRIANI, K. VON BERGMANN, E. Y. VEDMEDENKO, S. HEINZE, M. BODE, M. HEIDE, G. BIHLMAYER, S. BLÜGEL and R. WIESENDANGER, *Atomic-Scale Spin Spiral with a Unique Rotational Sense: Mn Monolayer on W(001)*, Phys. Rev. Lett. **101**, 027201 (2008).
- [128] S. MECKLER, N. MIKUSZEIT, A. PRESSLER, E. Y. VEDMEDENKO, O. PIETZSCH and R. WIESENDANGER, *Real-Space Observation of a Right-Rotating Inhomogeneous Cycloidal Spin Spiral by Spin-Polarized Scanning Tunneling Microscopy in a Triple Axes Vector Magnet*, Phys. Rev. Lett. **103**, 157201 (2009).
- [129] S. MECKLER, O. PIETZSCH, N. MIKUSZEIT and R. WIESENDANGER, *Micro-magnetic description of the spin spiral in Fe double-layer stripes on W(110)*, Phys. Rev. B **85**, 024420 (2012).
- [130] R. COLDEA, S. M. HAYDEN, G. AEPPLI, T. G. PERRING, C. D. FROST, T. E. MASON, S.-W. CHEONG and Z. FISK, *Spin Waves and Electronic Interactions in La₂CuO₄*, Phys. Rev. Lett. **86**, 5377 (2001).
- [131] F. L. PRATT, P. J. BAKER, S. J. BLUNDELL, T. LANCASTER, S. OHIRAKAWAMURA, C. BAINES, Y. SHIMIZU, K. KANODA, I. WATANABE and G. SAITO, *Magnetic and non-magnetic phases of a quantum spin liquid*, Nature **471**, 612 (2010).
- [132] S. LOUNIS and P. H. DEDERICHS, *Mapping the magnetic exchange interactions from first principles: Anisotropy anomaly and application to Fe, Ni, and Co*, Phys. Rev. B **82**, 180404 (2010).
- [133] R. SINGER, F. DIETERMANN and M. FÄHNLE, *Spin Interactions in bcc and fcc Fe beyond the Heisenberg Model*, Phys. Rev. Lett. **107**, 017204 (2011).
- [134] K. VON BERGMANN, M. MENZEL, D. SERRATE, Y. YOSHIDA, S. SCHRÖDER, P. FERRIANI, A. KUBETZKA, R. WIESENDANGER and S. HEINZE, *Tunneling anisotropic magnetoresistance on the atomic scale*, Phys. Rev. B **86**, 134422 (2012).

- [135] O. PIETZSCH, A. KUBETZKA, D. HAUDE, M. BODE and R. WIESENDANGER, *A low-temperature ultrahigh vacuum scanning tunneling microscope with a split-coil magnet and a rotary motion stepper motor for high spatial resolution studies of surface magnetism*, Review of Scientific Instruments **71**, 424 (2000).
- [136] M. HEIDE, G. BIHLMAYER, P. MAVROPOULOS, A. BRINGER and S. BLUEGEL, *Spin Orbit Driven Physics at Surfaces, Ψ_k* , Scientific Highlight of the Month (2006).
- [137] P. FERRIANI, I. TUREK, S. HEINZE, G. BIHLMAYER and S. BLÜGEL, *Magnetic Phase Control in Monolayer Films by Substrate Tuning*, Phys. Rev. Lett. **99** (2007).
- [138] Y. Yoshida, private communication.
- [139] J. S. MOODERA, L. R. KINDER, T. M. WONG and R. MESERVEY, *Large Magnetoresistance at Room Temperature in Ferromagnetic Thin Film Tunnel Junctions*, Phys. Rev. Lett. **74**, 3273 (1995).
- [140] T. YAOI, S. ISHIO and T. MIYAZAKI, *Dependence of magnetoresistance on temperature and applied voltage in a $82\text{Ni-Fe/Al-Al}_2\text{O}_3/\text{Co}$ tunneling junction*, Journal of Magnetism and Magnetic Materials **126**, 430 (1993).
- [141] A. MATOS-ABIAGUE and J. FABIAN, *Anisotropic tunneling anisotropic magnetoresistance and tunneling anisotropic magnetoresistance: spin-orbit coupling in magnetic tunnel junctions*, Phys. Rev. B **79**, 155303 (2009).
- [142] A. MATOS-ABIAGUE, M. GMITRA and J. FABIAN, *Angular dependence of the tunneling anisotropic magnetoresistance in magnetic tunnel junctions*, Phys. Rev. B **80**, 045312 (2009).
- [143] A. B. SHICK, F. MACA, J. MASEK and T. JUNGWIRTH, *Prospect for room temperature tunneling anisotropic magnetoresistance effect: Density of states anisotropies in CoPt systems*, Phys. Rev. B **73**, 024418 (2006).
- [144] A. N. CHANTIS, K. D. BELASHCHENKO, E. Y. TSYMBAL and M. VAN SCHILFGAARDE, *Tunneling Anisotropic Magnetoresistance Driven by Resonant Surface States: First-Principles Calculations on an Fe(001) Surface*, Phys. Rev. Lett. **98**, 046601 (2007).
- [145] J. MOSER, A. MATOS-ABIAGUE, D. SCHUH, W. WEGSCHEIDER, J. FABIAN and D. WEISS, *Tunneling Anisotropic Magnetoresistance and Spin-Orbit Coupling in Fe/GaAs/Au Tunnel Junctions*, Phys. Rev. Lett. **99**, 056601 (2007).

-
- [146] L. GAO, X. JIANG, S.-H. YANG, J. D. BURTON, E. Y. TSYMBAL and S. S. P. PARKIN, *Bias Voltage Dependence of Tunneling Anisotropic Magnetoresistance in Magnetic Tunnel Junctions with MgO and Al₂O₃ Tunnel Barriers*, Phys. Rev. Lett. **99**, 226602 (2007).
- [147] A. B. SHICK, S. KHMELEVSKIY, O. N. MRYASOV, J. WUNDERLICH and T. JUNGWIRTH, *Spin-orbit coupling induced anisotropy effects in bimetallic antiferromagnets: A route towards antiferromagnetic spintronics*, Phys. Rev. B **81**, 212409 (2010).
- [148] B. G. PARK, J. WUNDERLICH, X. MARTI, V. HOLÝ, Y. KUROSAKI, M. YAMADA, H. YAMAMOTO, A. NISHIDE, J. HAYAKAWA, H. TAKAHASHI, A. B. SHICK and T. JUNGWIRTH, *A spin-valve-like magnetoresistance of an antiferromagnet-based tunnel junction*, Nature Mat. **10**, 347 (2011).
- [149] J. D. BURTON, R. F. SABIRIANOV, J. P. VELEV, O. N. MRYASOV and E. Y. TSYMBAL, *Effect of tip resonances on tunneling anisotropic magnetoresistance in ferromagnetic metal break-junctions: A first-principles study*, Phys. Rev. B **76**, 144430 (2007).
- [150] M. VIRET, M. GABUREAC, F. OTT, C. FERMON, C. BARRETEAU, G. AUTES and R. GUIRADO-LOPEZ, *Giant anisotropic magneto-resistance in ferromagnetic atomic contacts*, Eur. Phys. J. B **51**, 1 (2006).
- [151] K. I. BOLOTIN, F. KUEMMETH and D. C. RALPH, *Anisotropic Magnetoresistance and Anisotropic Tunneling Magnetoresistance due to Quantum Interference in Ferromagnetic Metal Break Junctions*, Phys. Rev. Lett. **97**, 127202 (2006).
- [152] N. NÉEL, S. SCHRÖDER, N. RUPPELT, P. FERRIANI, J. KRÖGER, R. BERNDT and S. HEINZE, *Tunneling Anisotropic Magnetoresistance at the Single-Atom Limit*, Phys. Rev. Lett. **110**, 037202 (2013).
- [153] A. KUBETZKA, M. BODE, O. PIETZSCH and R. WIESENDANGER, *Spin-Polarized Scanning Tunneling Microscopy with Antiferromagnetic Probe Tips*, Phys. Rev. Lett. **88**, 057201 (2002).
- [154] N. NÉEL, P. FERRIANI, M. ZIEGLER, S. HEINZE, J. KRÖGER and R. BERNDT, *Energy-resolved spin-polarized tunneling and exchange coupling of Co and Cr atoms on Fe islands on W(110)*, Phys. Rev. B **85**, 155406 (2012).
- [155] P. FERRIANI, C. LAZO and S. HEINZE, *Origin of the spin polarization of magnetic scanning tunneling microscopy tips*, Phys. Rev. B **82**, 054411 (2010).

- [156] J. P. PERDEW and M. LEVY, *Physical Content of the Exact Kohn-Sham Orbital Energies: Band Gaps and Derivative Discontinuities*, Phys. Rev. Lett. **51**, 1884 (1983).
- [157] B. KOHLER, P. RUGGERONE and M. SCHEFFLER, *Ab initio study of the anomalies in the He-atom-scattering spectra of H/Mo(110) and H/W(110)*, Phys. Rev. B **56**, 13503 (1997).
- [158] D. SERRATE, P. FERRIANI, Y. YOSHIDA, S.-W. HLA, M. MENZEL, K. VON BERGMANN, S. HEINZE, A. KUBETZKA and R. WIESENDANGER, *Imaging and manipulating the spin direction of individual atoms*, Nature Nanotechnology **5**, 127202 (2010).

List of Abbreviations

E_F	Fermi energy
AFM	antiferromagnet
APW	augmented plane wave method
BZ	Brillouin zone
DFT	density functional theory
DMI	Dzyaloshinskii-Moriya interaction
DOS	density of states
fcc	face centered cubic
FLAPW	full-potential linearized augmented plane wave method
FM	ferromagnetic
GGA	generalized gradient approximation
GMR	giant magnetoresistance
hcp	hexagonal close packed
IR	interstitial region
LAFM	layered antiferromagnet
LAPW	linearized augmented plane wave method
LDA	local density approximation
LDOS	local density of states
LEED	low-energy electron-diffraction
LSDA	local spin density approximation
MAE	magnetocrystalline anisotropy energy
ML	monolayer
ML	monolayer
MRAM	magnetoresistive random-access memory
MT	muffin tin
RKKY	Ruderman-Kittel-Kasuya-Yoshida interaction
RW-AFM	row-wise antiferromagnet
SOC	spin-orbit coupling
SP-STM	spin-polarized scanning tunneling microscopy/scanning tunneling microscope
TAMR	tunneling anisotropic magnetoresistance
TMR	tunneling magnetoresistance
UML	unsupported monolayer

Veröffentlichungen und Konferenzbeiträge

Veröffentlichungen

- M. Waśniowska, S. Schröder, P. Ferriani, and S. Heinze
Real-space observation of spin frustration in Cr on a triangular lattice
Physical Review B **82**, 012402 (2010)
- Y. Yoshida, S. Schröder, P. Ferriani, D. Serrate, A. Kubetzka, K. von Bergmann, S. Heinze, and R. Wiesendanger
Conical spin-spiral state in an ultra-thin film driven by higher-order spin interactions
Physical Review Letters **108**, 087205 (2012)
- K. von Bergmann, M. Menzel, D. Serrate, Y. Yoshida, S. Schröder, P. Ferriani, A. Kubetzka, R. Wiesendanger, and S. Heinze
Tunneling anisotropic magnetoresistance on the atomic scale
Physical Review B **86**, 134422 (2012)
- N. Néel, S. Schröder, N. Ruppelt, P. Ferriani, J. Kröger, R. Berndt, and S. Heinze
Tunneling anisotropic magnetoresistance at the single-atom limit
Physical Review Letters **110**, 037202 (2013)

Konferenzbeiträge und Poster

Vorträge

- **25.03.2010** S. Schröder, P. Ferriani, S. Heinze
Non-collinear magnetism in the double layer Mn/W(110)
DPG Frühjahrstagung der Sektion Kondensierte Materie, Regensburg, Deutschland
- **30.08.2011** S. Schröder, Y. Yoshida, P. Ferriani, D. Serrate, K. von Bergmann, A. Kubetzka, R. Wiesendanger, S. Heinze
Conical spin-spiral state in the Mn double layer on W(110)
European Conference on Surface Science, Wrocław, Polen

- **02.11.2011** S. Schröder, Y. Yoshida, P. Ferriani, D. Serrate, K. von Bergmann, A. Kubetzka, R. Wiesendanger, S. Heinze
Conical spin-spiral state in an ultra-thin film driven by higher-order spin interactions
56th Annual Conference on Magnetism and Magnetic Materials, Scottsdale, Arizona, USA

Poster

- **21.07.2009** S. Schröder, M. Waśniowska, P. Ferriani, S. Heinze
Topological spin frustration in the Cr monolayer on Pd(111)
20th International Colloquium on Magnetic Films and Surfaces, Freie Universität, Berlin, Deutschland
- **14.09.2010** S. Schröder, P. Ferriani, S. Heinze
Non-collinear magnetism in the double layer Mn/W(110)
 Ψ_k Conference 2010, Berlin, Deutschland
- **18.03.2011** S. Schröder, P. Ferriani, S. Heinze
Spin-structure of the Mn double layer on W(110)
DPG Frühjahrstagung der Sektion AMOP und der Sektion Kondensierte Materie, Dresden, Deutschland

Wissenschaftliche Aktivitäten

- **09.03.-20.03.2009** 40th IFF Springschool
Spintronics – From GMR to Quantum Information
Forschungszentrum Jülich, Deutschland
- **17.05.-28.05.2010** Spring College on Nanoscience
The Abdus Salam International Centre for Theoretical Physics
Trieste, Italien

Lebenslauf

PERSÖNLICHE DATEN

Silke Schröder
Griegstraße 31
22763 Hamburg
geboren am 21.01.1983 in Hamburg
deutsch

SCHULAUSBILDUNG

1989-1993 Grundschule Hainholz, Elmshorn
1993-2002 Elsa-Brändström-Schule, Elmshorn
06/2002 Allgemeine Hochschulreife

STUDIUM

10/2002-10/2004 Grundstudium Physik an der Universität Hamburg
10/2004-06/2008 Hauptstudium Physik an der Universität Hamburg
04/2007-06/2008 Diplomarbeit am Institut für Angewandte Physik,
Universität Hamburg
*Elektronische und magnetische Effekte der Spin-Bahn-Kopplung
auf nicht-kollineare magnetische Strukturen an Oberflächen*
06/2008 Diplom Physik

PROMOTION

09/2008-06/2013 Promotion Physik
First-Principles Study of Non-Collinear Magnetism and Spin-Orbit Driven Physics in Nanostructures at Surfaces
09/2008-08/2009 am Institut für Angewandte Physik, Universität Hamburg
09/2009-06/2013 am Institut für Theoretische Physik und Astrophysik, Christian-Albrechts Universität zu Kiel

Danksagung

An dieser Stelle möchte ich mich bei allen bedanken, die mich in den letzten Jahren begleitet, gefördert, unterstützt und somit zum Gelingen dieser Arbeit beigetragen haben.

Mein erster Dank geht an Prof. Dr. Stefan Heinze, da er die Durchführung dieser Arbeit in seiner Gruppe für mich überhaupt erst möglich gemacht hat. Zudem verstand er es mich über die Jahre hinweg stets zu motivieren und von Anfang an für die Spintronik zu begeistern. Hierfür und für die intensive Betreuung möchte ich ihm herzlichst danken.

Bei Dr. Paolo Ferriani möchte ich mich für seine Hilfe und Unterstützung bedanken, insbesondere wenn es mit den Rechnungen nicht voranging. Darüber hinaus gilt ihm als Gründungsmitglied unserer Fahrgemeinschaft mein tiefster Dank dafür, dass er uns sein Auto zur Verfügung gestellt und es unseren Fahrkünsten anvertraut hat. Schließlich möchte ich ihm noch für das Korrekturlesen dieser Arbeit danken.

Für die Übernahme des Zweitgutachtens der Dissertation möchte ich an dieser Stelle Prof. Dr. Eckhard Pehlke ganz herzlich danken. Prof. Dr. Wolfgang Duschl gilt mein Dank für die Übernahme des Prüfungsvorsitzes. Bei Prof. Dr. Berndt möchte ich mich dafür bedanken, dass er sich als Prüfer für die Disputation zur Verfügung stellt.

Der Gruppe 'Rastersonormethoden' von Prof. Dr. Roland Wiesendanger am Institut für Angewandte Physik der Universität Hamburg danke ich für die erfolgreiche Zusammenarbeit und die schöne Zeit in Hamburg. Besonderer Dank gilt hierbei Dr. Marta Waśniowska, Dr. Yasuo Yoshida, Dr. Kirsten von Bergmann, Dr. André Kubetzka, Dr. David Serrate und Dr. Matthias Menzel für viele ergiebige Diskussionen und die Durchführung der Experimente.

Ebenfalls bedanken möchte ich mich bei Prof. Dr. Richard Berndt, Prof. Dr. Jörg Kröger, Dr. Nicolas Néel und Nico Ruppelt für die schöne Zusammenarbeit und die experimentellen Ergebnisse.

Bei Prof. Dr. Stefan Blügel und Dr. Gustav Bihlmayer möchte ich mich für viele wertvolle Tipps im Umgang mit FLEUR bedanken. Weiterhin danke ich den Mitgliedern der Gruppe Quantum Theory of Materials des Peter Grünberg Instituts für die Gestaltung des Rahmenprogramms bei diversen Konferenzen.

Allen ehemaligen und aktuellen Mitgliedern der Gruppe 'Theory of Spintronics' möchte ich ebenfalls danken für die schöne Zeit, die ich in dieser Gruppe verbringen durfte. Meinen Kollegen Dr. Cesar Lazo, Dr. Björn Hardrat, Dr. Alexander Thiess, Dr. Urs Wilke, Franziska Schubert, Gregor Michalicek und Simon Fichtner möchte ich für die gute Büroatmosphäre und viele interessante Gespräche danken. Besonderer Dank gilt Cesar und Dr. Bertrand Dupé für das Korrekturlesen dieser Arbeit.

Ich danke den Mitarbeitern des Instituts für Theoretische Physik und Astrophysik an der Universität Kiel für die angenehme Arbeitsatmosphäre.

Bodo Krause-Kyora und Dr. Simone Knief danke ich für ihre Unterstützung beim parallelen Rechnen auf den Linuxclustern in Hamburg beziehungsweise Kiel.

Weiterhin bedanke ich mich auch beim Norddeutschen Verbund für Hoch- und Höchstleistungsrechnen (HLRN) für die zur Verfügung gestellte Rechenzeit.

Mein ganz besonderer Dank geht an meine Eltern, meine Familie und meine Freunde, deren Liebe und Unterstützung ich mir immer sicher sein konnte.

Eidesstattliche Erklärung

Hiermit versichere ich an Eides statt, dass die vorliegende Dissertation – abgesehen von der Beratung durch meinen wissenschaftlichen Lehrer und der Verwendung der angegebenen Hilfsmittel – nach Inhalt und Form meine eigene ist.

Sie hat weder ganz noch teilweise an einer Stelle im Rahmen eines Prüfungsverfahrens vorgelegen. Die hier vorgestellten Ergebnisse sind in Teilen bereits in wissenschaftlichen Fachzeitschriften veröffentlicht worden. Eine ausführliche Publikationsliste findet sich auf S. 173 ff.

Diese Arbeit ist unter Einhaltung der Regeln guter wissenschaftlicher Praxis der Deutschen Forschungsgemeinschaft entstanden.

Kiel, den